Structural, Electronic and Kinetic Studies on Organometallic Intercalates of Metal Dichalcogenides

by

Heng Vee Wong

A thesis submitted in part fulfillment
of the requirements for the degree of
Doctor of Philosophy
at the University of Oxford

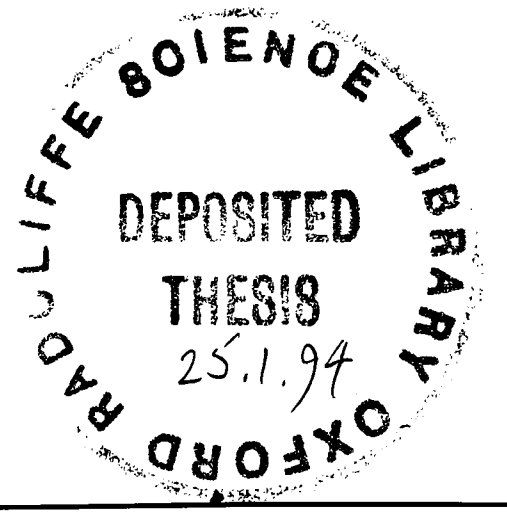

Keble College
Oxford

October 1993

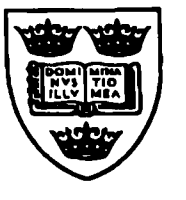

The work described in this thesis was carried out in the Inorganic Chemistry Laboratory, South Parks Road, Oxford, from October 1990 to September 1993 under the supervision of Dr Dermot O'Hare. All the work is my own unless stated to the contrary, and has not been previously been submitted for any degree at this, or any other, university.

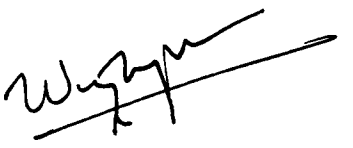

To my Pa who would have loved to see this,
and to Mom, who will.

Abstract

Structural, Electronic and Kinetic Studies on Organometallic Intercalates of Metal Dichalcogenides

Heng Vee Wong
Keble College

submitted for D. Phil.
Trinity Term, 1993

Large single crystals of the metal dichalcogenide hosts ZrS_2 and SnX_2 (X = S, Se) have been successfully intercalated with a variety of organometallic guests { $Co(\eta\text{-}C_5H_5)_2$, $Cr(\eta\text{-}C_5H_5)_2$, $Co(\eta\text{-}C_5H_4CH_3)_2$, $Mo(\eta\text{-}C_6H_6)_2$, $Mo(\eta\text{-}C_7H_7)(\eta\text{-}C_5H_5)$, $W(\eta\text{-}C_7H_7)(\eta\text{-}C_5H_5)$, $Ti(\eta\text{-}C_8H_8)(\eta\text{-}C_5H_5)$ }. The structural and electronic properties of these materials have been studied, as well as the intercalation kinetics of these organometallic species into the tin dichalcogenides.

X-ray and neutron diffraction experiments have been used to obtain *00l* reflections in order to obtain a one-dimensional profile of electron and neutron scattering in these disordered layered materials (Chapter Two). Refinement of the data shows that for all the organometallic guests, the majority of the intercalant adopts an orientation in which the principal molecular axis lies parallel to the layer planes of the host. These findings are confirmed by ^2H NMR spectroscopy on single crystals of deuterated cobaltocene intercalates of ZrS_2 and $SnSe_2$, where it has been shown that rapid C_5, but not C_2, rotation of the metallocene occurs in the interlamellar van der Waals space.

To study the electronic properties of these intercalates, electrical resistivity and magnetic susceptibility measurements have been performed (Chapter Three). An apparatus has been built to measure the resistivity of these crystal intercalates down to 4.2K. The resistivity measurements show that intercalation of various organometallic complexes confers metallic properties upon ZrS_2 while $SnS_2\{Co(\eta\text{-}C_5H_5)_2\}_{0.3}$ becomes a superconductor with a T_c of 8.3K. The magnetic susceptbility measurements confirm the presence of guest-host charge transfer. Estimates of its extent, as well as the magnitude of the Pauli susceptibility in these intercalates, have been attempted.

Studies on the rate and mechanism for the intercalation of cobaltocene into the disulfides and diselenides of tin have been performed (Chapter Four). An apparatus has been designed and constructed for *in situ* diffraction using synchrotron X-rays in order to monitor the progress of these rapid intercalation reactions. The results indicate that the rate of intercalation of cobaltocene into the tin dichalcogenides is very much dependent on the solvent used, being significantly faster in dimethoxyethane than in toluene. Analyses of the kinetic rate expressions for the tin dichalcogenide intercalation in dimethoxyethane suggests that diffusion of cobaltocene molecules into the interlamellar space constitutes the rate limiting step. The choice of solvent also dramatically affects the mechanism of the intercalation. When a solution of cobaltocene in dimethoxyethane is used, the host transforms directly to the final product but in toluene, staged intermediates are observed during the intercalation process. The apparatus and techniques that have been developed for the *in situ* kinetics experiments are general and permit dynamic structural transformations in air- and moisture-sensitive suspensions of solids to be effectively studied.

Acknowledgement

In the aftermath of this daunting task, it behoves me to thank all the people who have made it possible for me to complete it. My predilection for brevity notwithstanding, the interdisciplinary nature of the work in this thesis makes this list of people rather extensive.

I am grateful to Dermot for introducing me to his special brand of gung-ho effervescence and for letting me enlist in his pioneer batch of D. Phils in the rapidly burgeoning O'Hare Crew. This eclectic collection of individuals have been a source of inspiration and support during my stint at Oxford, particularly the following: John Evans, my tennis buddy and fellow veteran of those memorable Daresbury and Didcot campaigns, for his immeasurable help in all spheres - scientific, social, cultural, recreational - and for his paranoically meticulous proof reading of this thesis. Sue Mason, for all her painstaking NMR work on my crystals but also for inspiring me with her breathtaking transformation from reticent computer illiterate to gregarious guru of the scanner shrine. Steve Barlow, for several solution NMR's and careful but rapid perusal of some of my most "dull and tedious [sic]" chapters. Vince Murphy, for help with synthesis of potential organometallic guests as well as for performing ESR spectroscopy on single crystals of my intercalates (which were unfortunately too difficult for both of us to interpret). Andy Hughes, our erstwhile post-doc till he moved on to greener and more luxuriant pastures from which to continue hacking around on someone else's computer network, for NMR, mass specs, lab history lessons (viz, "In the old days, when I was...") and for hitherto unequalled displays of glassware washing frenzy. Tim Whittaker, for mass specs of some deuterated compounds and our last three batches of Part II's who were responsible for my discovering the solitude but peace of working graveyard shifts.

Many of the projects I attempted, including a fair number of unsuccessful ones in my first year, would not have been possible without the help of the excellent research support staff, both in the ICL and at Daresbury. Within the ICL, I would like to record my thanks to Keith Mayo, Iain Ross and Nenard Vranjes who have helped with all my electronics problems, particularly the temperature controllers for the multiple zone furnaces and various components for the conductivity apparatus. Dr Pete Trevellick developed the software for both these projects. Also, Jim Kench and Ann Douglas of Microanalytical Services for patiently analysing countless samples of my "dull black powder" or "equally dull black crystals". To the Glassblowers, Martin Miles, Teri Westlake, and the recently-retired Geoff Wilkinson, I shall always be grateful; their prodigious skills have produced every single bit of intricate glassware that I have ever needed in my stint here, regardless of quantity or degree of difficulty. Chris Burras and his merry men (Dave Paul and Howard Lillyman) have made my basement forays not only fruitful but enjoyable, while Mr Brogden's combination of bizarre humour and cheery demeanour made "shopping at stores" a real pleasure.

Outside the ICL, the technical support staff of Daresbury Laboratory have been immensely helpful, in particular, Messrs Rathbone and Nield, whose eleventh-hour improvisational talents made it possible for John and me to perform our maiden experiments with our *in situ* kinetics rig on schedule. Simon Clark was the catalyst for much of the kinetics work and is therefore instrumental for my being able to write a large portion of this thesis.

Not being cognisant of much physics beyond first-year university level, I have also benefited a great deal from discussions with Dr Jonathan Hodby, Steve Hazell (Clarendon Labs) and Dr Mohammed Kurmoo (The Royal Institution, London). "Mo" was also responsible for starting me off on single crystal conductivity measurements and Steve spent countless hours trying to mount contacts onto my misbehaving crystals for Hall measurements.

None of the work in this thesis, nor indeed my presence in Oxford, would have been possible without the magnanimity of the Rhodes Trust, under whose auspices I received a scholarship to study here. My family, especially my mother, have been unwavering in their support throughout my long absence from home; this has allowed me to pursue my education with undivided attention and an unladen heart.

On an equally important front, my friends in Oxford have helped me tremendously, getting me out of labs for fresh air and bolstering my spirits on many a frustrating day with both food for thought as well as the more gastronomically palatable type. Amongst others, these include Eric, Kee Chuan, Sharon, Li Yen, Alison, Pin^2 and the Platt's. Most of all however, two very exceptional people whose understanding and love have helped me cross the huge gulf between being merely content and truly happy: my brother Yu and my special friend JC.

Abbreviations used:

Bz = (η-C_6H_6)

Cht = (η-C_7H_7)

Cot = (η-C_8H_8)

Cp = (η-C_5H_5)

Cp' = (η-$C_5H_4Me_3$)

d^{10}-$CoCp_2$ = $Co(\eta$-$C_5D_5)_2$

d^8- toluene = $C_6D_5(CD_3)$

DME = dimethoxyethane

EDD = Energy Dispersive Diffraction

MX_2 = metal dichalcogenide

TABLE OF CONTENTS

CHAPTER ONE

GENERAL INTRODUCTION

CHAPTER ONE

GENERAL INTRODUCTION

1.1. Introduction

Intercalation compounds are solids into which guest atoms have been inserted. The structure of the host may range from three-dimensional framework lattices (e.g. zeolites) through two-dimensional layered compounds (e.g. NbS_2, $MnPS_3$, MoO_3) to one-dimensional chains ($NbSe_3$). Of these, the layered lattices provide the most examples of intercalation and will form the basis for discussion in this chapter.

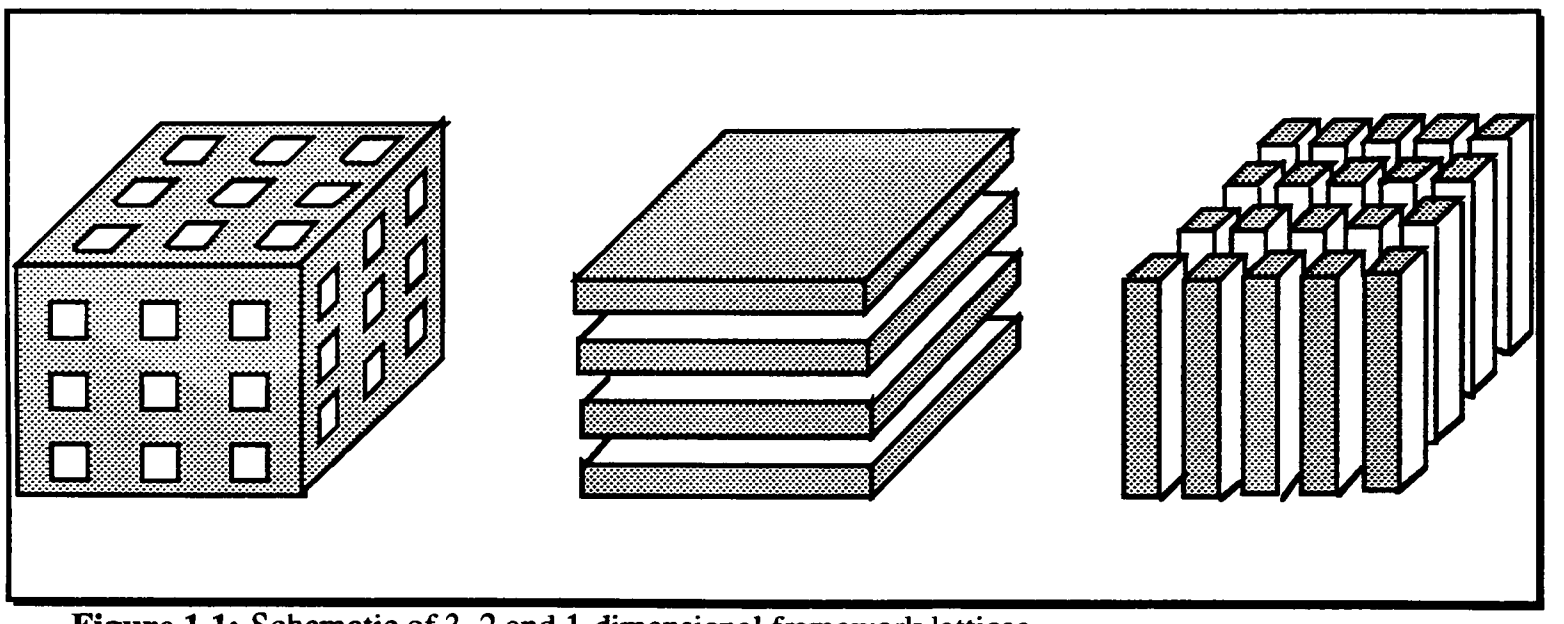

Figure 1.1: Schematic of 3, 2 and 1-dimensional framework lattices

Aside from physical perturbations of the host lattice structure (i.e., interlayer expansion, staging), intercalation often induces changes in magnetic, electrical or optical properties in the host material. These effects arise because intercalation is frequently accompanied by redox processes, whereby electrons are transferred from the guest to the host (e.g. alkali metal intercalates of metal dichalcogenides) or vice versa (e.g. $FeCl_3$-graphite). The potential for tuning these properties by employing a variety of guest-host combinations has led to useful applications for intercalate systems (e.g. reversible solid state batteries)[1, 2]. The subsequent sections will focus on one particular sub-class of layered intercalates, that of the metal dichalcogenides (MX_2). The layout of this chapter will be as follows.

Section **1.2** describes the *general structural features* relevant to layered dichalcogenides such as metal coordination and polytypism. Section **1.3**, on the *intercalation of metal dichalcogenides*, surveys both techniques as well as the types of

intercalants which are amenable to such reactions. Sections **1.4** provides a *rigid band model* for understanding both the *structural* and *electronic* properties of these compounds, details of which are discussed in Sections **1.5** and **1.6** respectively. Section **1.7** focuses on the *kinetics* of intercalation, the issues of interest and our current understanding of the intercalation process, using examples drawn from work performed on both graphite and metal dichalcogenides. Finally, Section **1.8** concludes with an outline for the layout of this thesis.

1.2. General Structural Features

While graphite and boron nitride consist of monolayer sheets of atoms, the unit cell in transition metal chalcogenides comprise three atomic planes in which metal atoms are sandwiched in octahedral or trigonal prismatic holes within close-packed arrays of chalcogen atoms in the *ab* plane. Each "sandwich" layer is held together by either covalent or ionic interlayer bonds (or a combination of both) while adjacent layers are only weakly associated to each other by van der Waals interactions. These weak interlayer associative forces are only a fraction the size of the interlayer bonds, thus giving rise to the layered structures of the metal dichalcogenides. Examples of such MX_2 systems are ZrS_2, NbS_2 and MoS_2.

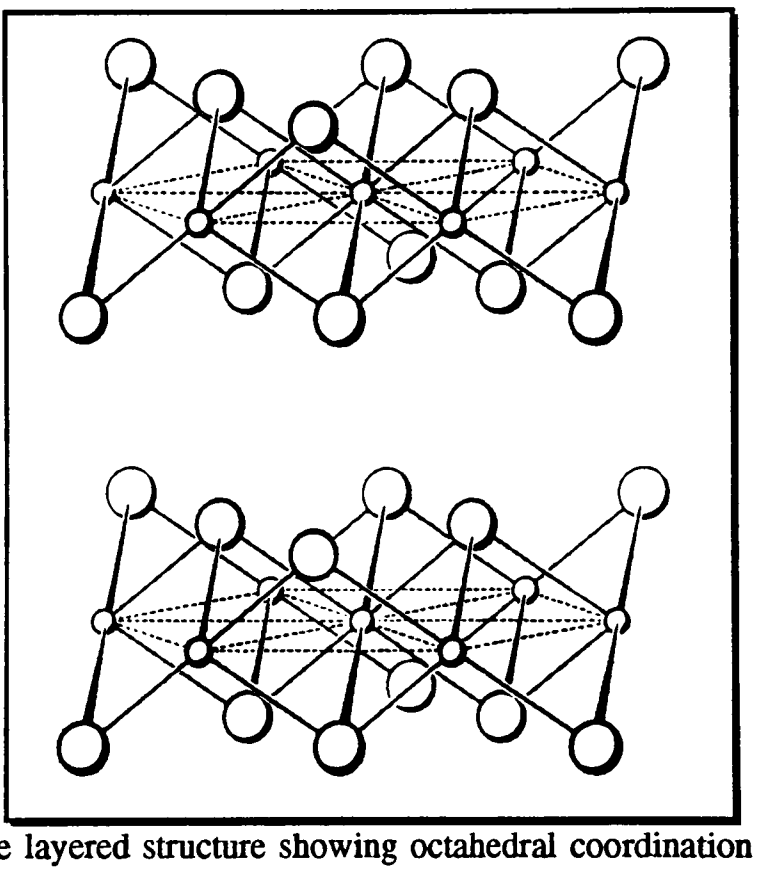

Figure 1.2: CdI_2-type layered structure showing octahedral coordination of the cations (small spheres) to the anions (large spheres).

The crystallographic axes for these compounds are those of standard hexagonal systems with the *a, b* axes parallel and *c* axis perpendicular to the layer planes. Typical values are 3-4Å for the *a* and *b* parameters and *ca.*6Å for the sandwich repeat distance along the *c* axis. The sandwich layers may be stacked in a variety of ways along the *c* axis dimension, resulting in a potentially large number of polytypes. The simplest of these, the

1T-form, can be represented by the mnemonic: *AbC-AbC-AbC...* where the lower case letters denote metal layer positions, upper case letters chalcogen layer positions and the hyphen (-) represents the van der Waals space (see Figure 1.3 below). In this case, each metal atom is octahedrally coordinated to 6 chalcogen atoms, giving rise to a *c/a* ratio of 1.633. Group 4, 6 and 8, as well as some Group 5 metals, adopt this hexagonal close-packed structure.

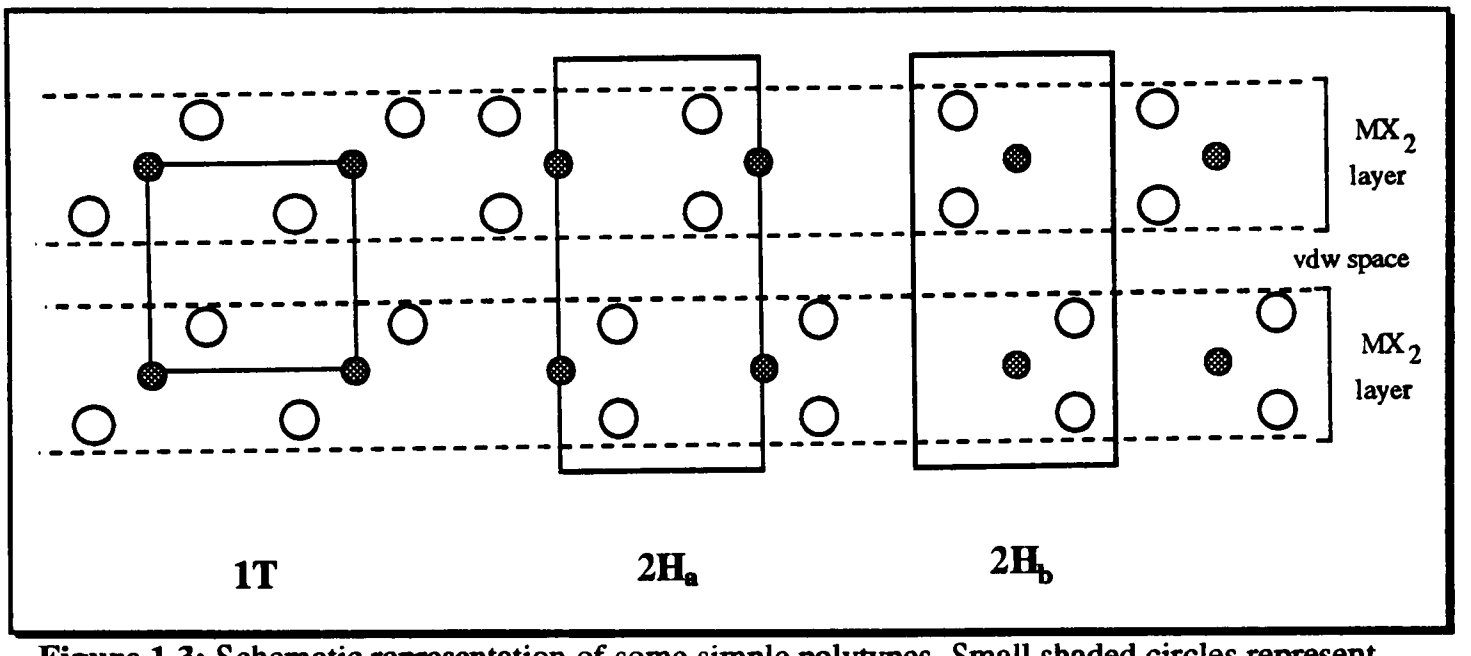

Figure 1.3: Schematic representation of some simple polytypes. Small shaded circles represent metal atoms and open circles represent chalcogen atoms

When the metal atom is trigonal prismatically coordinated to the chalcogens, the polytype can be described as either $2H_a$ or $2H_b$, corresponding to layer sequences of *BaB-CaC-BaB* or *CbC-BcB-CbC* respectively. Permutations of varying proportions of these two forms of metal coordination give rise to a plethora of other polytypes which are discussed in greater detail elsewhere.[3, 4] While the present discussion is confined to metal dichalcogenides, this type of layered structure is by no means unique to the MX_2 solids. Other systems possessing this layered sandwich structure are the metal di-halides, metal phosphorus trichalcogenides and cuprate oxide superconductors.

1.3. Intercalation into Metal Dichalcogenides

1.3.1. General

The weak interlayer forces in metal dichalcogenides allow intercalation of guest species between the MX_2 sandwiches. A wide variety of guests have been inserted, ranging in size from the dimunitive Li^+ cation to bulky organometallic complexes[5] or even macrocyclic ligands such as crown ethers[6]. The common feature that all these intercalants share is that they are good Lewis bases and donate electrons to the host layers upon intercalation (except in the case of intercalation by ion-exchange, where a pre-intercalated cation is directly replaced by an incoming, oxidised form of the guest, without concomitant electron transfer). This topochemical redox process has been

harnessed for use in solid state batteries such as Li/MnO_2 used in photographic equipment. The following section describes some common techniques used in intercalation chemistry.

1.3.2. Techniques for Intercalation

Intercalation techniques can be classified into 5 main groups; (a) direct routes, (b) solvent-mediated intercalation (c) ion-exchange mechanisms (d) electrochemical methods, (e) exfoliation/reformation techniques.

(a) The traditional, and often most expedient method, is by direct reaction of the guest with the host material. Originally employed by Shauftaul[7] in his discovery of H_2SO_4-graphite intercalates, it has been modified so that guests of both vapour and solid phases can be used. The former is the method of choice for many intercalations when the guest is sufficiently volatile while the latter is an extension of traditional high temperature solid state syntheses. Its lack of novelty notwithstanding, direct chemical intercalation remains attractive because of its simplicity, circumventing the complications of solvent co-intercalation or hydrolysis by-products.

(b) In cases where it is inconvenient to deploy a guest in its vapour, liquid or solid phases, it can be solvated before attempting intercalation. Alkali-metals (in liquid ammonia)[8, 9] and various organometallic species (in polar organic solvents, viz, toluene, dimethoxyethane)[5, 10] have been intercalated in this way. By judicious choice of appropriate solvents or careful solvent removal afterwards, problems of solvent co-intercalation can be minimized.

(c) Where kinetic considerations prevent their intercalation (e.g., exceptionally sterically hindered but sufficiently redox active guests) although the thermodynamics are favourable, ion exchange of the bulky guest for another, smaller, mobile, pre-intercalated guest from within the lattice can be a versatile alternative[11]. While useful for a large variety of cations, the primary disadvantages of this method are solvent co-intercalation and hydrolysis of the host lattice, especially when protic solvents are employed.

(d) In a few favourable cases where a solvent of appropriately high conductivity is available and suitable electrodes can be fashioned from both guest and host materials, intercalation can be achieved by electrochemical means[12, 13]. For intercalation into metal dichalcogenides, the host constitutes the cathode while the intercalant (guest) is the anode. Electrons traverse the external circuit from anode to cathode while cations migrate across the electrolyte into the cathode to restore the charge balance. This is the basis of commercially available solid state intercalation batteries such as Li/MnO_2.

(e) The most recently reported method of intercalation is via exfoliation, whereby a layered lattice is first separated into monolayers, exposed to the guest species, then allowed to re-stack itself into its original layered form, thus incorporating the guest in the process. MoS_2 inclusion compounds have been formed by ultrasonic exfoliation in a

variety of metal nitrate solutions, centrifuged and then dried at *ca.* 60°C[14]. Jacobson and Nazar have also used this procedure to intercalate the large cluster cation $(Fe_6S_8(PEt_3)_6)^{3+}$ in TaS_2 by exfoliating $Na_{0.33}TaS_2$ in a N-methyl formamide/H_2O solution, then refluxing the TaS_2 layers in the presence of the Fe cluster[15].

1.3.3. Common Classes of Guests

1.3.3.1. Organic molecules

Organic Lewis bases of various sizes, shapes, ring sizes and chain lengths, from ammonia to pyridine to aliphatic amines have been intercalated in metal dichalcogenides. Short chain amines such as methylamine stack with their long axis parallel to the layers while long chain amines ($>C_{16}$) lie with their chain perpendicular to the layers and form bilayers[16, 17]. This latter conformation close packs the intercalants while maximising interchain hydrophobic interactions. For intermediate chain lengths, (C_4-C_9 aliphatic amines), the chains lie at an oblique angle with respect to the layers, halfway between the perpendicular and parallel orientations. With long chain amines, the interlayer separation can be increased by ten-fold up to *ca.* 60Å as evidenced by the intercalation of n-octadecylamine into 2H-TaS_2[18]. Such a large expansion considerably reduces the layer-layer interactions and these intercalates have been used as a basis for studying physical phenomena such as electrical conductivity and superconductivity in nearly individual layers(see Sections **1.6.3** and **1.6.4** respectively).

1.3.3.2. Alkali metals, transition metals

Alkali metals such as Li, Na, K, Rb, Cs and also simple monovalent metals such as Ag and Cu, readily enter between the layers to form intercalate complexes. For high concentrations of alkali metals and at low temperatures, ordered structures have been observed by electron diffraction[19, 20]. In the Li intercalates, the Li atoms generally occupy octahedral sites within the close-packed chalcogen layers but the structural chemistry of the other alkali metals is more complex as these larger ions can occupy either octahedral or trigonal prismatic sites. In fact, for alkali metals other than Li, few generalizations can be made. The trigonal prismatic phase is stablilized by the larger cations, while in those systems where both types of coordination exist, the octahedral one is the most stable at high alkali concentrations. The change in the *c* lattice parameter with stoichiometry of the guest is also strongly dependant on the type of coordination present. Thus, for octahedrally coordinated ions, the lattice spacing generally expands with increasing metal coordination, whereas the converse is true for trigonal prismatic coordination. The latter case can be rationalised by considering that there is significant repulsion between the sulfur atoms in the trigonal prismatic phase, an unfavourable interaction which can be ameliorated by electrostatic attraction between the alkali metal cations and the anionic host layers.

The pseudo-alkali metals, Cu and Ag, have been intercalated into a number of host dichalcogenides either by direct reactions of the elements at high temperatures[21, 22] or electrochemically at 25°C[12, 13]. The *c* lattice parameter appears independent of the temperature of formation[23]. The key structural feature of these compounds is that the Cu and Ag ions reside in tetrahedral holes within the layers (as opposed to the octahedral or trigonal prismatic sites preferred by the alkali metals). Di Salvo *et al.*, have intercalated a series of post-transition elements (Zn, Cd, Hg, Al, Ga, In, Ge, Sn, Pb, Bi) into TaS_2 at elevated temperatures[21]. However, the reactions are irreversible and probably involve strong metal-sulfur bonding or metal-metal bonding instead of the electrostatic bonding found in classical intercalates like $LiTiS_2$. As such they are not considered true intercalation complexes.

1.3.3.3. Organometallic complexes

The first organometallic intercalates of metal dichalcogenides were reported by Dines in 1975 when he described the intercalation of cobaltocene and chromocene {$CoCp_2$, $CrCp_2$; Cp = (η-C_5H_5)} into 8 different MX_2 lattices[10]. Subsequently, a plethora of organometallic species, both axially symmetric and non-symmetric[5, 24, 25], have been intercalated into these lattices, by direct methods as well as ion-exchange routes[5, 11], these being summarized in Table 1.1.

The criteria for selecting organometallic guests with the greatest likelihood of intercalating into the metal dichalcogenides ZrS_2 and TaS_2 were elucidated by Green and co-workers, from an empirical study conducted in 1976[26]. In it they synthesised 20 new metallocene intercalates which had guests with the following characteristics in common:

(a) They all had sandwich structures with parallel carbocyclic rings. (for an exception to this, see Table 1.1).

(b) Their ionization potentials (I.P.) were less than 6.2eV. Any organometallic complexes with I.P's greater than this threshold were found not to intercalate, including ferrocene (I.P. = 6.88eV), which is structurally similar to cobaltocene (I.P. = 5.5eV) and the most ubiquitous organometallic intercalant to date.

(c) When oxidised, they all formed isolable, stable cations. Thus, although $V(C_6H_6)_2$, has an I.P. of 5.2eV, it does not intercalate into ZrS_2.

The above three criteria are obeyed by the guests in all known organometallic intercalates of metal dichalcogenides to date, the only exception being $ZrS_2\{Ir(PMe_3)_4H\}_{0.15}$, where the guest in this case does not contain parallel carbocylic rings.

These organometallic intercalates are of interest because steric and electronic properties of the guest species can be subtly varied by either metal or ring substitution, allowing the solid-state scientist much finer control over these systems than can be achieved from simply employing elemental or hydrocarbon intercalants. This affords the

possibility of developing numerous novel materials with novel electronic and magnetic properties.

Table 1.1: A summary of the organometallic sandwich compounds which have been successfully intercalated into layered metal dichalcogenide hosts. "*" refers to syntheses in which the product obtained appeared to be impure, and the guest stoichiometry given is almost certainly an overestimate (adapted from O'Hare and Evans, 1993[31].

Host Lattice	Guest	Method of Intercalation	Stoichiometry	interlamellar separation	Δc/Å	Reference
ZrS_2	$CrCp_2$	direct	0.25	11.64	5.81	[26]
	$CoCp_2$	direct	0.25	11.18	5.35	[10]
	$Co(CpMe)_2$	direct	0.25	11.17	5.34	[5]
	$Co(Cp^iPr)_2$	direct	0.15	11.57	5.74	[5]
	$Co(Cp^nBu)_2$	direct	0.13	11.17	5.34	[5]
	$CrBz_2$	direct	0.16	11.73	5.90	[26]
	$MoBz_2$	direct	0.16	11.64	5.81	[26]
	$MoTol_2$	direct	0.13	11.63	5.80	[26]
	$MoMes_2$	direct	0.08, 0.20	11.61, 13.6	5.78, 7.78	[26, 27]
	TiCotCp	direct	0.23	12.23	6.4	[26, 28]
	CrCpBz	direct	0.24	11.9	6.07	[26]
	CrCpCht	direct	0.25	12.0	6.17	[26]
	$Ir(PMe_3)_4H$	direct	0.15		9.2	[24]
1T TaS_2	$CoCp_2$	ion-exchange	0.20	11.38	5.50	[5]
	$Co(CpMe)_2$	direct	0.21	11.59	5.68	[5]
	$Co(Cp^iPr)_2$	direct	0.17	12.05	6.18	[5]
	$Co(Cp^nBu)_2$	direct	0.13	11.44	5.53	[5]
	$CrBz_2$	ion-exchange	0.13	11.95	6.04	[5]
	$MoBz_2$	ion-exchange	0.15	11.89	5.99	[5]
	FeCpBz	ion-exchange	0.16	11.63	5.72	[5]
2H TaS_2	$CoCp_2$	direct	0.25		5.47	[10]

	$CrCp_2$	direct	0.28		5.52	[10]
	$FcC_2H_4NH_2$	ion-exchange	0.19	11.95	5.89	[25]
	$Fe_6S_8(PEt_3)_3$	flocculation	0.05	17.49	11.5	[15]
$TaSe_2$	$CoCp_2$	direct	0.42*		5.45	[10]
	$CrCp_2$	direct	0.25		5.57	[10]
TiS_2	$CoCp_2$	direct	0.2		5.55	[10]
	$CrCp_2$	direct	0.30		5.55	[10]
$TiSe_2$	$CoCp_2$	direct	0.38*		5.52	[10]
$NbSe_2$	$CoCp_2$	direct	0.31		5.53	[10]
	$CrCp_2$	direct	0.20		5.56	[10]
2H SnS_2	$CoCp_2$	direct	0.33		5.35	[10, 29]
$SnSe_2$	$CoCp_2$	direct	0.33	11.51	5.38	[30]
VSe_2	$CoCp_2$	direct	-	-	-	[5]
HfS_2	$CoCp_2$	direct	0.38*		5.52	[10]
	$CrCp_2$	direct	0.20		5.63	[10]

Abbreviations used:
$Cp = \eta^5\text{-}C_5H_5$, $CpMe = \eta^5\text{-}C_5H_4Me$, $Bz = \eta^6\text{-}C_6H_6$, $Tol = \eta^6\text{-}C_6H_5Me$, $Mes = \eta^6\text{-}C_3H_3Me$, $Cht = \eta^7\text{-}C_7H_7$ $Cot = \eta^8\text{-}C_8H_8$

1.4. Electronic Structure - Rigid Band Model

The electronic structure of metal dichalcogenide intercalates can be viewed from a molecular orbital perspective or in terms of band theory. The two are equivalent, since bands are formed from overlap of the metal *d* and chalcogen *s, p* orbitals. The valence band consists mainly of chalcogen character while the conduction band comprises the metal *d* orbitals with crystal field splittings characteristic of its coordination to the chalcogens (viz, octahedral or trigonal prismatic) as illustrated in the Figure 1.4. The band gap thus decreases as the chalcogen is replaced by members further down the group; the band gap varies from several electron Volts for metal disulfides to tenths of an electron Volt for metal ditellurides.

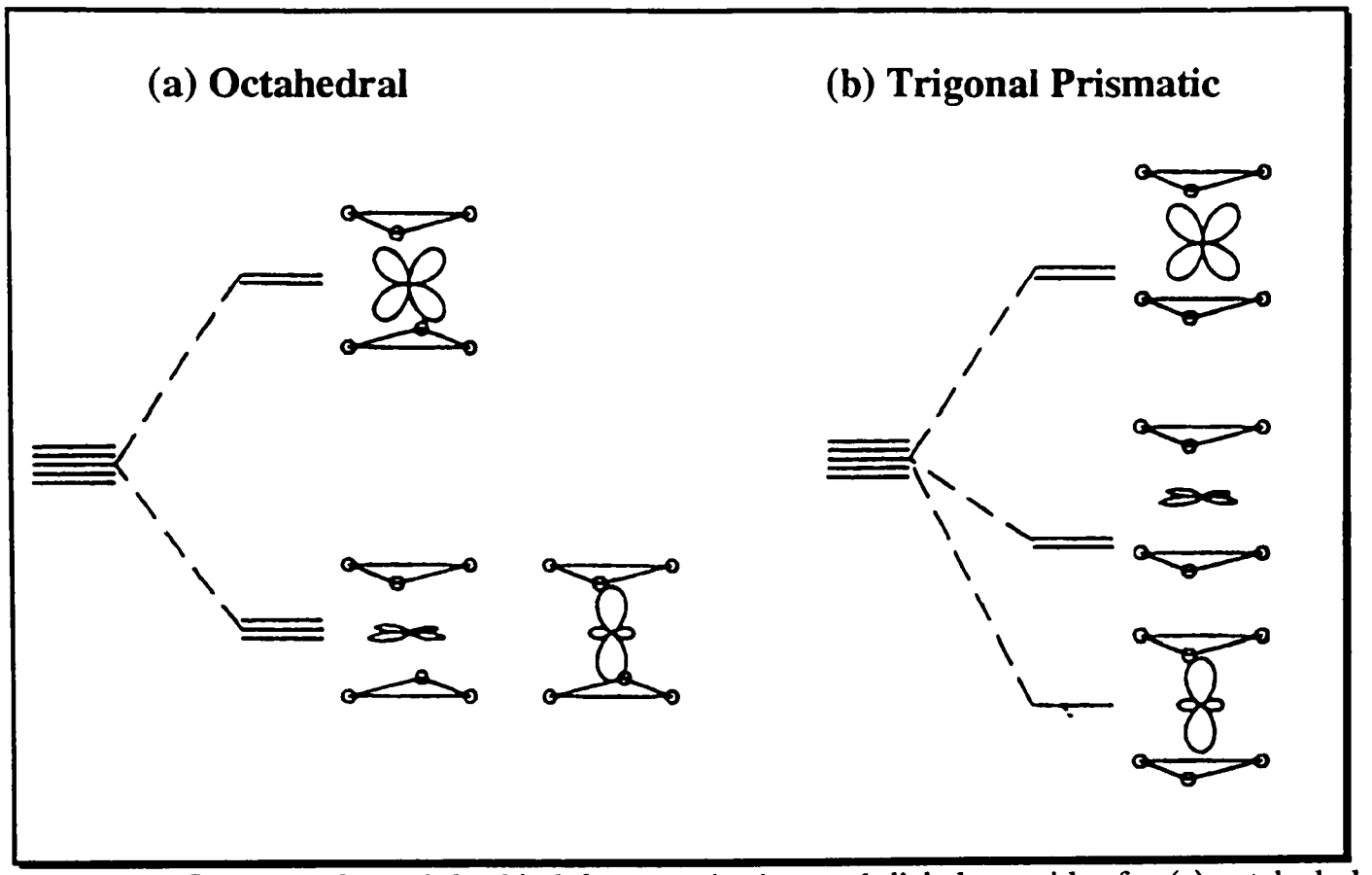

Figure 1.4: Splitting of metal d-orbital degeneracies in metal dichalcogenides for (a) octahedral (b) trigonal prismatic coordination about the metal cation.

Band structures have been calculated for a number of transition metal dichalcogenides and these lead to a band scheme proposed by Liang[32]. The lowest-lying unoccupied energy levels in the host layers are the transistion metal *d* bands, which are either empty or partially filled. Since the local bonding within the sandwiches is little changed upon intercalation, we may usefully describe the changes in electronic properties of the host material within the "rigid band model" which assumes the only change to the host material electronic structure is the increased *d* band filling.The main features of this scheme (see Figure 1.5 below) are that:

(a) Group 4 (d^0) and 6 (d^2) metals adopt octahedral and trigonal prismatic coordination to the chalcogen atoms respectively while Group 5 (d^1) metals can be either octahedrally or trigonally coordinated.

(b) These forms of coordination lead to band occupancies which cause the materials to be semi-conductors {Group 4 (d^0) and 6 (d^2)} and metals/superconductors {Group 5 (d^1)}.

(c) The bands are assumed to be unchanged by the process of intercalation (i.e., they are rigid). Analogous to semiconductor doping, the shape or band structure is approximated as "fixed", even after insertion of the intercalate species and its concomitant charge transfer. The rigid band shape is to be distinguished from band energies, which can, and do, vary upon intercalation.

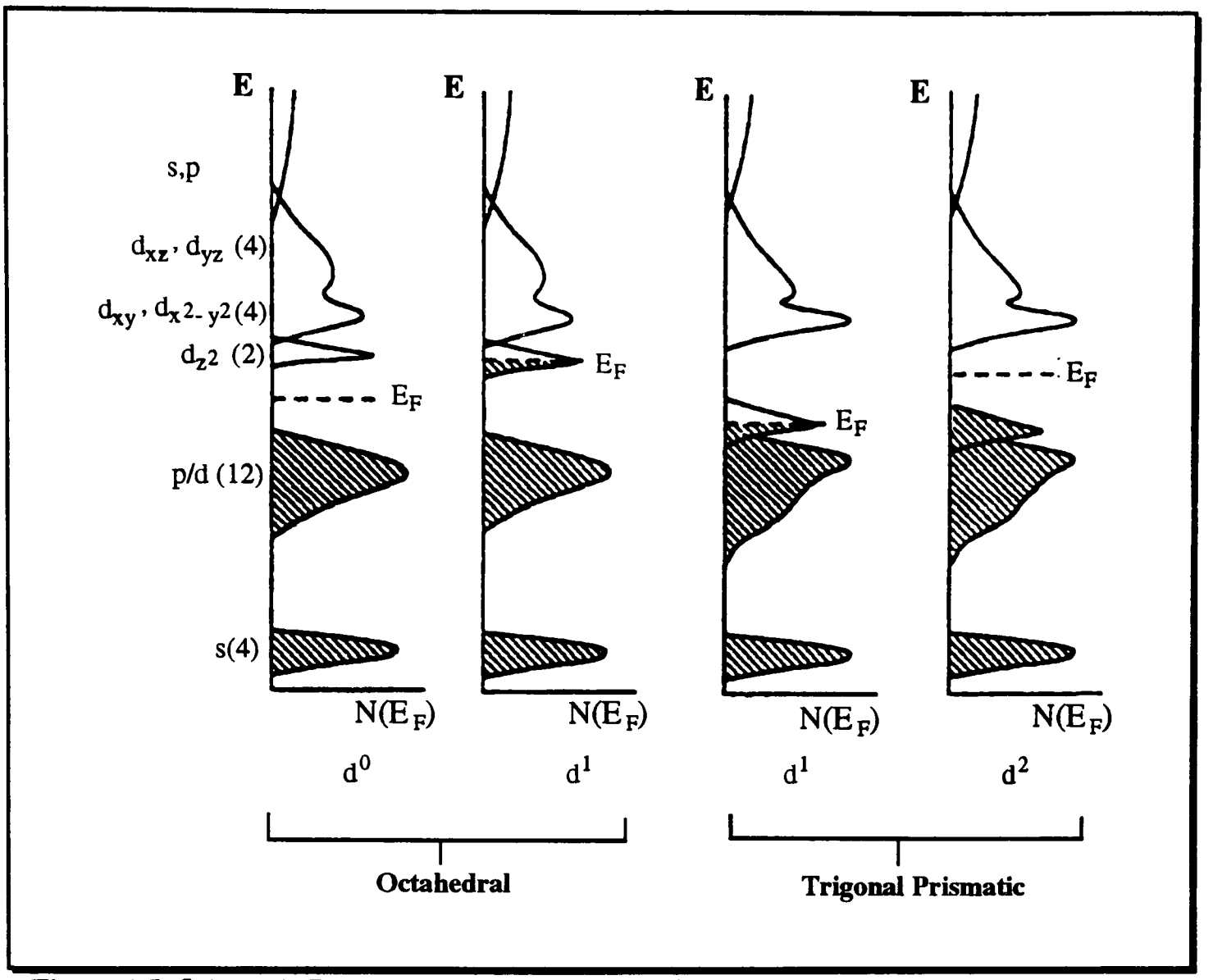

Figure 1.5: Schematic Representation of Rigid Band Model.

Modifications in electrical, magnetic and optical properties (see **1.6**), as well as some of the changes in primary structure (see **1.5**) which occur upon intercalation can be rationalised in terms of electron donation by the guests into the host conduction band.

1.5. Structural Effects of Intercalation

1.5.1. Changes in Secondary Structure

The most obvious structural change of metal dichalcogenides after intercalation of guest species is an increase in interlayer separation, ranging from *ca.* 10% for metal intercalates[23] to more than ten-fold increases for large organic molecules[18]. By contrast, the unit cell dimensions within the *ab* plane are observed to change by only 1-2%. The registry between adjacent layer planes can either remain the same (e.g, $LiTiS_2$ and Group 4 intercalated diselenides[33]) or change noticeably to either a repeatable (e.g $LiZrS_2$[34, 35]) or random sequence[29]. The extent of order in the *ab* plane of the intercalate appears related to the lattice expansion; the larger the interlayer separation, the greater the atttenuation of the van der Waals interactions and hence the greater the disorder between adjacent layer planes.

Host stacking sequences along the *c* axis can also vary to give different *stage levels* of intercalates. Analogous to graphite intercalation compounds, an *n*th stage

intercalate corresponds to a compound in which only every *n*th layer contains guest species. Unlike graphite however, it is not known whether the intercalates are staged directly (Figure 1.6a) or via the Daumas-Herold Domain Model (Figure 1.6b). The domains postulated in the Daumas-Herold model require flexibility of the host layers to accomodate the "kinks" in the stage intercalate and it is unclear whether the stiffness of the MX_2 layers relative to graphite allows the formation of such domains. The relevance and importance of Daumas-Herold domains in the process of intercalation will be discussed in Section **1.7** as well as in Chapter Four.

Another difference between the two classes of intercalates is that since metal dichalcogenides consists of chalcogen-metal-chalcogen sandwiches (as opposed to single layer sheets of carbon), there does not exist the same level of long range forces that give rise to higher-stage compounds found in graphite intercalation compounds.

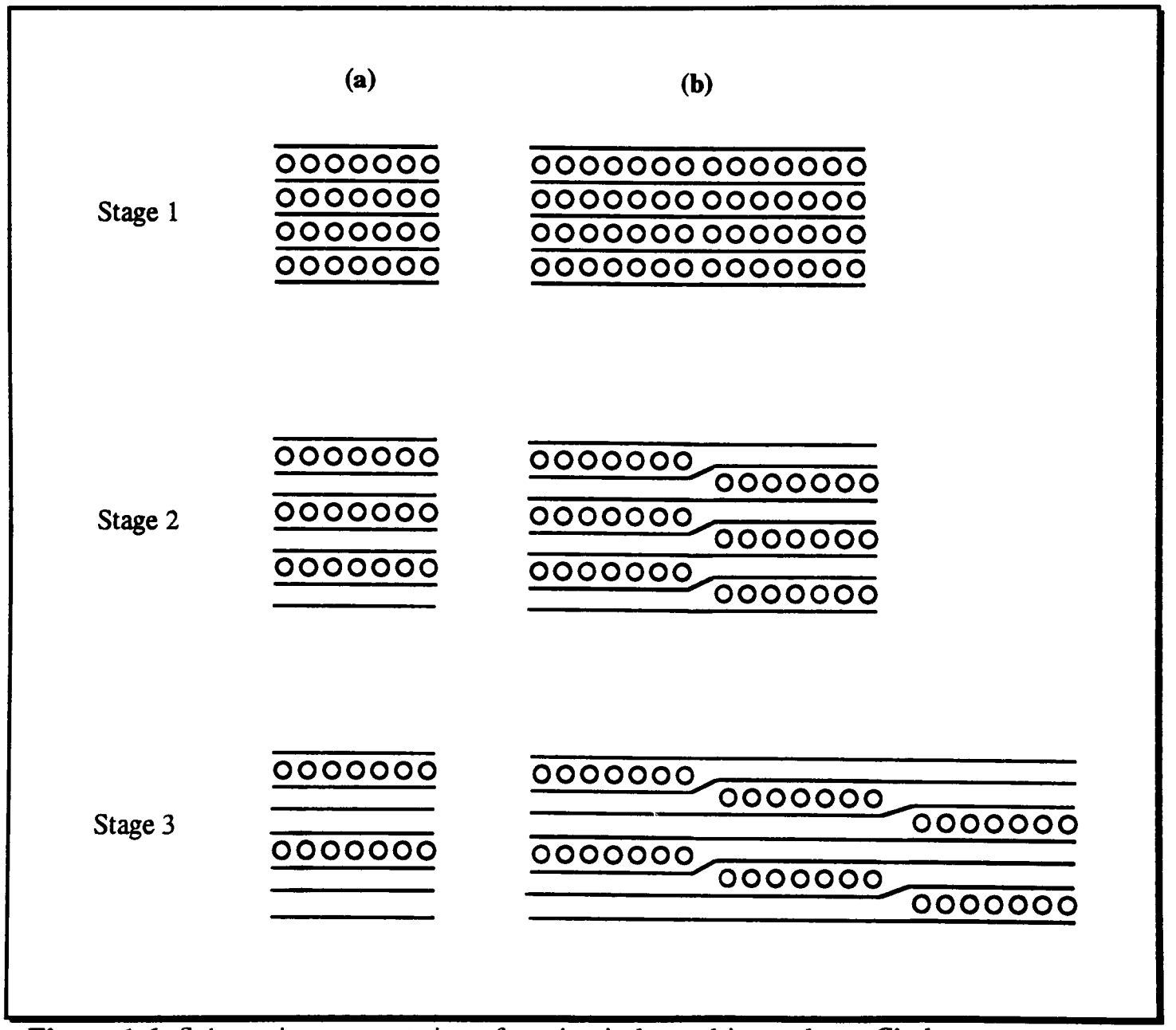

Figure 1.6: Schematic representation of staging in layered intercalates. Circles represent guest species and horizontal lines denote the layer planes of the host. (a) simple model of staged intercalates (b) Daumas-Herold model of staged domains.

1.5.2. Changes in Primary Structure

The local coordination geometry of the metal within a host dichalcogenide layer may also change upon intercalation. For example, octahedrally coordinated Group 5

metal dichalcogenides convert to trigonal prismatic coordination upon intercalation of alkali metals while Group 6 metal dichalcogenides undergo the reverse transition, that is, from trigonal prismatic to octahedral upon intercalation. These changes can be analysed in terms of the rigid band model (see **1.4**) wherein intercalation is accompanied by the donation of an electron into the conduction (d_z^2) band of the host. Thus, when MoS_2 changes metal coordination from trigonal prismatic to octahedral upon intercalation of sodium[36], the main driving force for such a transition is the lowering of the electron occupied d_z^2 band by increasing the *c/a* ratio since this distortion minimizes the total energy of the intercalate system. Another way to look at this shift in energy of the d_z^2 band in relation to its occupation is to regard this as the splitting of energy bands due to Jahn-Teller distortions which lower the energy of the system.

1.5.3. Guest Orientation in the van der Waals space

Since the energies of the guest-guest and guest-host interactions are comparable[37], when the guest species is non-spherical, there arises the question of its orientation, both in the van der Waals space between the layers as well as with respect to the layers. The former has been addressed for both the ammonia and pyridine intercalates of TaS_2 where it was found by neutron scattering[38, 39], X-ray diffraction[40] and NMR[41] studies that the nitrogen is located in the center of the van der Waals gap, and in the case of pyridine, that the plane of the aromatic ring lies perpendicular to the sulfide layers. This contradicts the original assumption that the nitrogen lone pair pointed directly towards the layers for maximal orbital overlap with the host bands (see Figure 1.7). The authors thus proposed an alternative model wherein indirect interaction by donor/acceptor charge transfer ($NH_3 \rightarrow TaS_2$) involving weak covalent mixing between the nitrogen lone pair orbital and electron states of the host layer is responsible for the orientation of the aromatic ring in the interlayer space. Shöllhorn *et al.*, however, subsequently showed that this disposition of the nitrogen lone pairs is favoured because the intercalates contain a proportion of ammonium or pyridinium ions which could interact with the neutral amine within the guest layer plane[39, 42, 43]. Further evidence for the pyridine orientation has been provided by McDaniel *et al.* who examined the dynamics of the ring rotation in both TaS_2[44] and $CdPS_3$[45] using solid state ^{2}H-NMR.

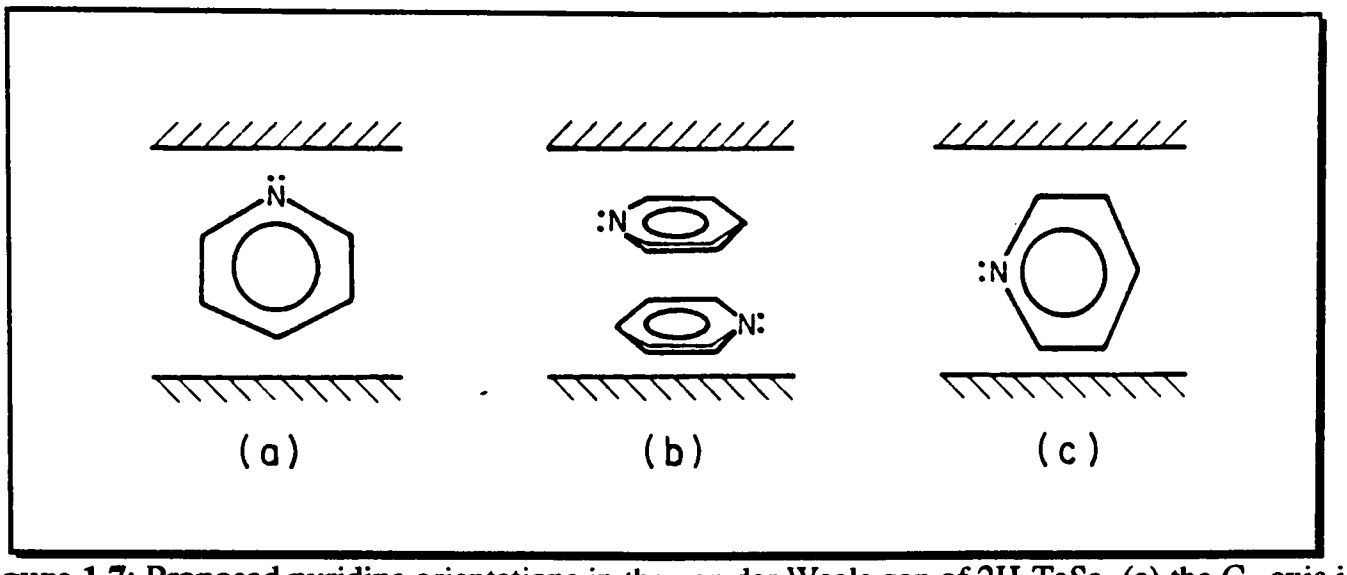

Figure 1.7: Proposed pyridine orientations in the van der Waals gap of 2H-TaS_2. (a) the C_2 axis is perpendicular to the host layers (b) a pyridine bilayer where the molecular planes and the C_2 axes are parallel to the TaS_2 layer; and (c) the C_2 axis is parallel and the molecular plane is perpendicular to the host.

For the metallocene intercalates however, the guest orientation has been the subject of an unresolved debate for nearly two decades[46-48] with differing orientations of the guest reported for different host metal dichalcogenides and indeed even for the same host (TaS_2) at differing temperatures[47].

Dines[10] initiated the controversy on the metallocene orientation within the host layers when he suggested that the guest resided with their principal molecular axis parallel to the layers, using crystallographic parameters for $Co(\eta\text{-}C_5H_5)_2$ which were later shown to be erroneous as they did not take into account the van der Waals radii of the constitutent atoms (see Figure 1.8).

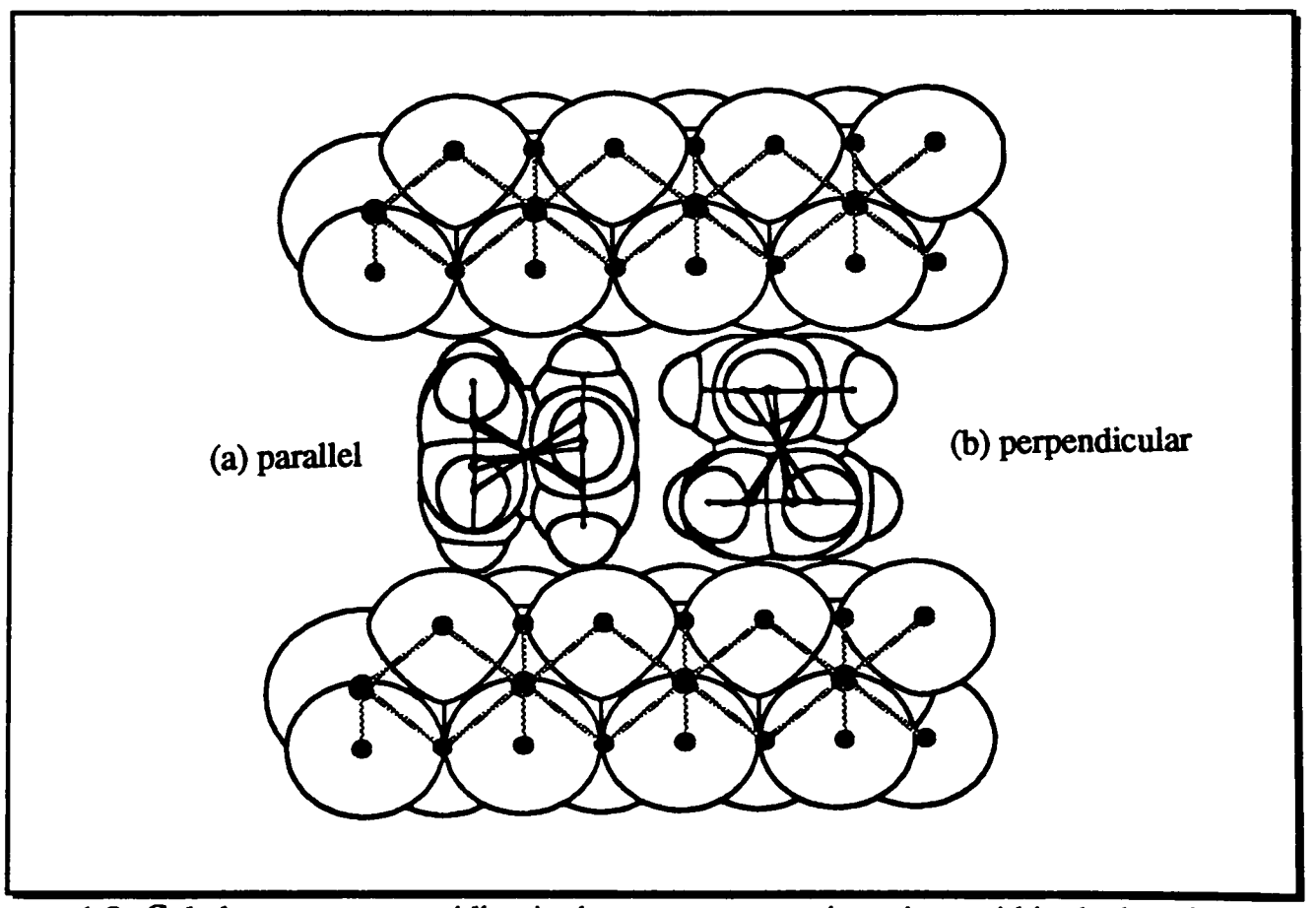

Figure 1.8: Cobaltocene guest residing in the two extreme orientations within the host layers, that is, with the principal metallocene axis either (a) parallel or (b) perpedicular to the *ab* planes of the host.

Silbernagel's ^{1}H-NMR study in 1975 on $TaS_2\{Co(\eta\text{-}C_5H_5)_2\}_{0.25}$ concluded that the C_5 axis of $Co(\eta\text{-}C_5H_5)_2$ lies parallel to the layers[46], an observation corroborated by Davies for the ZrS_2 intercalates[49], where the increasing interlayer lattice expansion was correlated with a series of guests varying in size from $Cr(\eta\text{-}C_5H_5)_2$ to $Cr(\eta\text{-}C_5H_5)(\eta\text{-}C_7H_7)$ but with no significant changes in guest stoichiometries. However, in the same study, he found that various substituted bis(arene)molybdenum intercalates showed similar lattice expansions within the series but very different guest stoichiometries, leading him to conclude that the orientation and stoichiometry of organometallic intercalates depend subtly on the relative importance of guest-guest and guest-host interactions.

The delicate interplay of steric and electronic forces in these systems was reiterated in a detailed solid state ^{2}H NMR study later by Heyes *et al.* in 1987 where he noted that while the $Co(\eta\text{-}C_5H_5)_2$ in TaS_2 exists exclusively with the C_5 axis perpendicular to the layers at temperatures below 230K, at room temperature, the metallocene adopts a mixture of both orientations[47] within the lattice. In contrast, $SnS_2\{Co(\eta\text{-}C_5H_5)_2\}_{0.3}$ was shown, both by single crystal ^{2}H-NMR studies[48]as well as X-ray and neutron diffraction experiments[29], to contain solely $Co(\eta\text{-}C_5H_5)_2$ molecules with their C_5 axis parallel to the layers.

Most recently, solid state NMR work by Mason[50] has confirmed the parallel orientation in $SnSe_2\{CoCp_2\}_{0.3}$ and even suggested a model for the guest packing which can be related to the hexagonal symmetry of the host.

1.6. Electronic Effects of Intercalation

1.6.1. Charge Transfer

There is a wealth of evidence to show that electrons are transferred from guest to host during the intercalation of metal dichalcogenides. The first evidence for oxidation of the guest was provided by Silbernagel[51, 52] who found in a NMR study that the Knight shift of Li in Li_xTiS_2 was between 3 and 12ppm relative to LiI solution, versus a 240ppm shift for Li metal. Moreover, the extent of the shift was inversely related to the stoichiometry of the Li guest, with complete ionization at low x values and *ca.* 80% ionisation for $LiTiS_2$. Similar experimental results were obtained for ^{23}Na in Na_xTiS_2[53] and ^{77}Se in Li_xZrSe_2[54] as well as Li_xTiSe_2[55].

This charge transfer has subsequently been demonstrated, to different extents in all classes of guest species (organic, metallic and organometallic) by a broad spectrum of techniques. Two of the most common techniques to probe the electronic structure in these systems are magnetic susceptibility and electrical resistivity measurements, which are discussed below.

1.6.2. Magnetic Properties

Magnetic susceptibility measurements have been used extensively for detecting the extents of electron transfer to the host conduction band of organic and alkali metal intercalates of the metal dichalcogenides. For example, intercalation of a 2/3 stoichiometry of hydrazine into $TiSe_2$ was observed to increase the temperature-independent susceptibility by 70 x 10^{-6} emu/mole, an increase attributed to Pauli paramagnetic susceptibility arising from increased occupation of the Ti *d* band[56, 57] (see Figure 1.9). Similar observations were made on $LiTiS_2$ and $LiTiSe_2$[58, 59] where transitions from diamagnetic to Pauli paramagnetic behaviour were reported, consistent with complete electron transfer from the lithium guest to the metal *d* band.

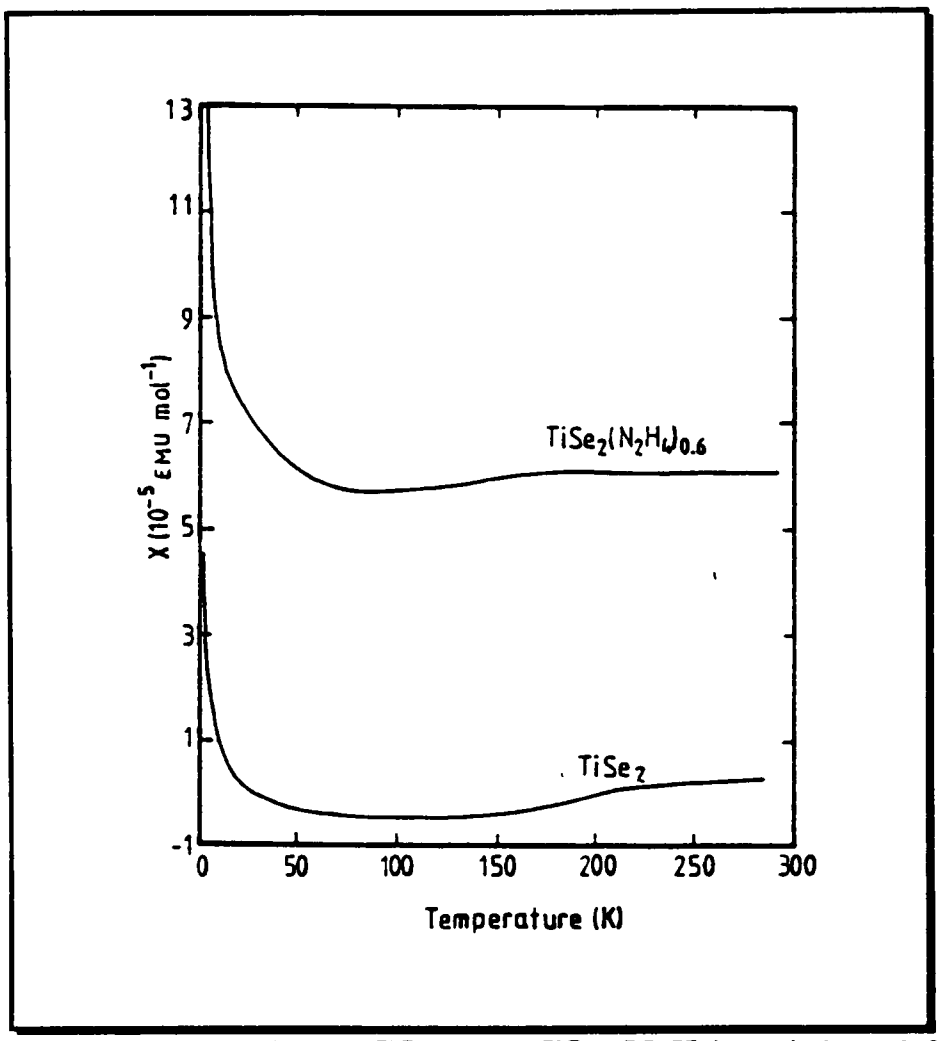

Figure 1.9: Magnetic susceptibility of $TiSe_2$ and $TiSe_2(N_2H_4)_{0.6}$ (adapted from Guy *et al.*, 1982[56].

For organometallic intercalates, the extent of ionization of the guest varies, depending on the host lattice, and can be deduced from magnetic susceptibility measurements. For $TaS_2(CoCp_2)_{0.25}$, the molar susceptibility was found to be 88 x 10^{-6} emu/mole[60], consistent with complete ionization of the guest while $SnS_2(CoCp_2)_{0.3}$ was shown to be a Curie-Weiss paramagnet in the temperature range 4→300K, with μ_{eff} = $0.12\mu_B$, θ = -9.17K[61], suggesting a percentage of unoxidised metallocene was present. This was estimated to be 25% from magnetic studies, in reasonable agreement with photoelectron spectroscopy (PES) measurements which gave 33% $CoCp_2$. Similarly, PES

experiments showed that the ionised and un-ionised $CoCp_2$ exists in a 3:1 ratio in $SnSe_2(CoCp_2)_{0.3}$. These results indicate that the chemical potential of the intercalate continues to increase during intercalation until it matches that of the redox intercalation reaction for $CoCp_2$; further intercalation involves only neutral $CoCp_2$ molecules. The mixed valency of the guest layer is thought to facilitate inter-layer conduction and thus reduce the electronic anisotropy (see Sections. **1.6.3**, **1.6.4**) in these intercalates.

1.6.3. Conductivity

By analogy with the impurity band model for semiconductors, intercalation and its concomitant transfer of electrons into the host conduction band is expected to induce dramatic changes in electrical conductivity of metal dichalcogenides. The conductivities and electronic properties of the host materials have been extensively reviewed by Friend and Yoffe[62]. Essentially, the host materials vary from semiconductors (e.g. ZrS_2, band gap ~1.5eV; TiS_2, band gap ~0.17eV) to metals (e.g., NbS_2 and other Group 5 metal dichalcogenides). Since electrical conductivity can only be measured for crystals of sufficient size on which electrical contacts can be made, the first such studies on this class of compounds were performed on the alkali metal intercalates, where, because of relatively high cation mobilities, intercalation (via alkali metal vapour or electrochemical routes) is straightforward and provides samples of good crystalline quality.

Acrivos showed[63] that the Group 6 semiconductor MoS_2 turns into a good metallic conductor after intercalation with alkali metals and in fact, superconducts at low temperatures[64] (e.g. K_xMoS_2, T_c~6.5K). Other workers extended these studies to show intercalation converted semiconducting Group 4 metal dichalcogenides to metals (e.g., HfS_2/K_xHfS_2) and metallic Group 5 metal dichalcogenides to semiconductors (e.g., 2H-$NbSe_2/K_xNbSe_2$). A wealth of experimental evidence from Friend's group at Cambridge in the 1980's lend support to these findings[65-75], which in the light of the extent of charge transfer to the host bands (see **1.6.1**), are exactly as predicted by the rigid band model. They have also shown that the charge transfer from guest to host is also present in organic amine intercalates, such as hydrazine-$TiSe_2$ where the hydrazine assumes an average valence state of +0.75 between the layers[67] (see Figure 1.10). An added complication, however, is the onset of periodic lattice distortion-charge density waves (PLD-CDW), especially in the Group 5 metal dichalcogenides which cause resistance anomalies inconsistent with the simple band model. However, zirconium dichalcogenides show weak, if any, CDW's, and both $LiZrS_2$ and $LiZrSe_2$ which are isoelectronic with the metallic Group 5 metal dichalcogenides (e.g., NbS_2) in fact show metallic conduction between ca. 70K and 300K[71, 76-78].

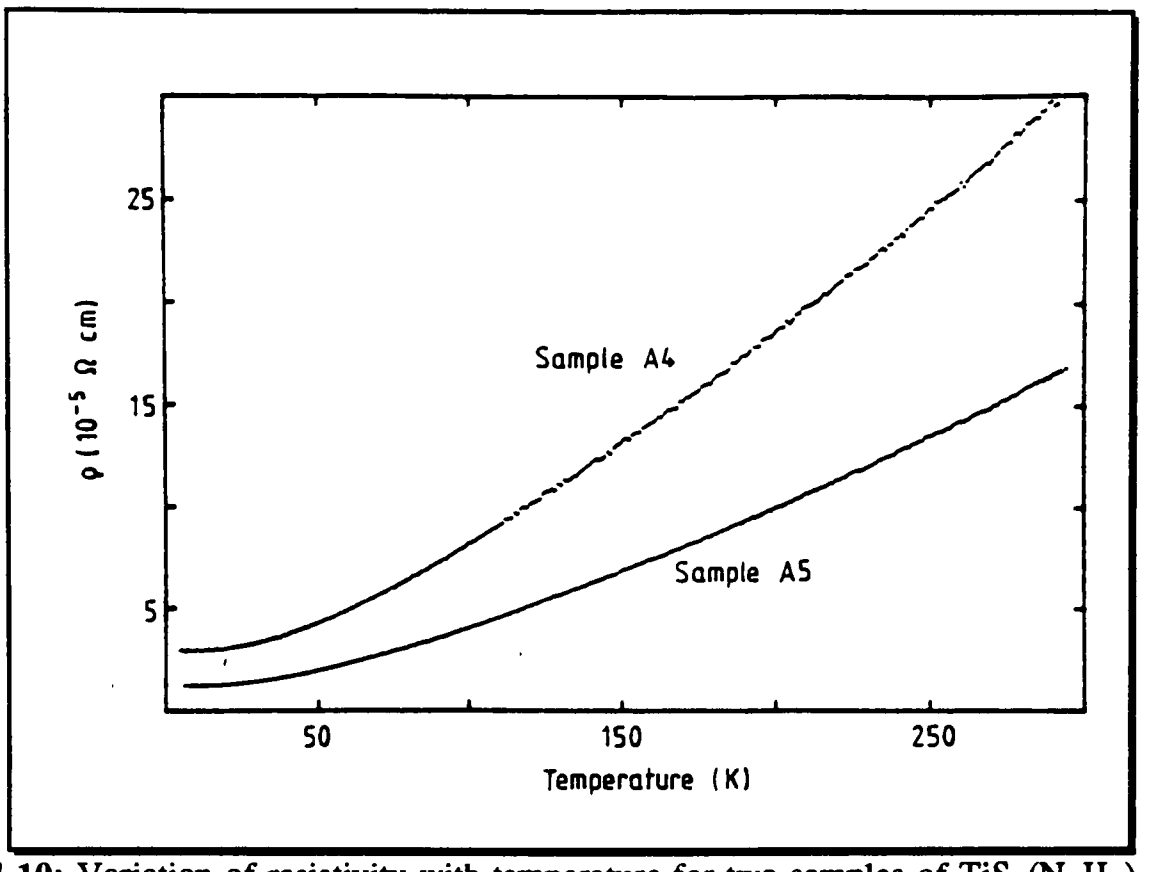

Figure 1.10: Variation of resistivity with temperature for two samples of $TiS_2(N_2H_4)_{0.7}$ (from Sarma *et al.*, 1982[67]).

The anisotropy of these layered compounds is also manifested electrically in that the ratio for conductivity parallel and perpendicular to the layers, $\sigma_{//}/\sigma_{\perp}$, varies from *ca.* 300 in the hosts to *ca.* 10^5 after intercalation[79].

More recently, O'Hare and co-workers showed that in the series $SnSe_xS_{2-x}$ {where $0 \leq x \leq 2$}, intercalation of $CoCp_2$ induced dramatic changes in the conductivity of the hosts; while hosts are all semiconducting, the selenium-rich intercalate single crystals undergo a clear semiconductor-to-metal transition in the stoichiometry range $1.3 < x < 1.85$. In particular, $SnSe_{1.85}S_{0.15}(CoCp_2)_{0.3}$ and $SnSe_2(CoCp_2)_{0.3}$ were shown to be superconductors with $T_c = 5.7K$ and 6.1K respectively[80] . The increase in T_c as sulfur is replaced by selenium can be rationalised in terms of the enhanced degree of electron charge transfer to the empty Sn(5s, 5p) conduction band as suggested by XPES data[81]. The ionized electron from $CoCp_2^+$ would be more effectively screened by the more polarizable selenium than sulfur, leading to greater values for $N(E_F)$ which, according to BCS theory, should yield a higher T_c.

The electrical anisotropy of the $SnSe_xS_{2-x}$ intercalates, in marked contrast to alkali metal and organic intercalates, actually *reduces* upon intercalation, from an intralayer to interlayer conductivity ratio ($\sigma_{//}/\sigma_{\perp}$) of *ca.* 100 to $\sigma_{//}/\sigma_{\perp}$ of *ca.* 10, despite an interlayer expansion of almost 100%[82]. This observation suggests that the organometallic guest somehow interacts electronically with the layers and mediates between them but no detailed studies have probed the exact nature of this interaction, given the difficulties of performing electrical measurements perpendicular to the layers in these plate-like crystals.

1.6.4. Dimensionality of Superconductivity

The existence of superconductivity in metal dichalcogenides and their intercalates have provided scientists with a unique opportunity to study the dimensionality of superconductivity and whether it can persist in individual layers. Several experimental results have been adduced in support of 2-dimensional superconductivity. Di Salvo[83], and later Coleman *et al.*[84] observed that for many long chain amine intercalates of TaS_2, the superconducting transition temperature, T_c, is relatively insensitive to the interlayer expansion induced by varying the aliphatic chain length from C_9 to C_{18}. Should Josephson-type coupling be present, the tunnelling efficiency of the Cooper pairs between the layers would be expected to fall concomitantly with the T_c, as interlayer expansion increases.

Table 1.2: Variation of the superconducting transition temperature, T_c, with increase in interlayer separation, δ, in several alkylamine intercalates of 2H-TaS_2.

Intercalant	δ (Å)	T_c (K)
Ammonia	3.17	4.2
Methylamine	3.32	4.2
Ethylamine	3.53	3.3
Propylamine	3.61	3.0
Butylamine	3.68	2.5
Tributylamine	4.23	3.0
Tridecylamine	36.4	2.5
Tetradecylamine	40.1	2.4
Pentadecylamine	39.0	2.8
Septadecylamine	43.4	2.7
Octadecylamine	50.0	3.0

Further evidence for the absence of Josephson coupling was demonstrated by the insertion of paramagnetic ions such as $CrCp_2^+$ into the interlayer space of 2H-TaS_2[60]. The T_c of this intercalate is virtually identical to that of its diamagnetic cobaltocene analogue, $TaS_2(CoCp_2)_{0.25}$, an observation which shows that Cooper pair-breaking between the layers by the paramagnetic guest is negligible.

Finally, superconductivity has been demonstrated in a unit cell layer of 2H-$NbSe_2$ by Frindt[85] who measured the superconducting T_c as a function of the sample thickness. The T_c (=7.4K) remains constant down to about 40Å after which it falls slightly to *ca.* 5K for a 12Å thick crystal (i.e., two MX_2 layers). Extrapolation of this trend yields a T_c of 3.8K for a single MX_2 layer. Unfortunately, the fact that each layer consists of three

atomic layers (one metal and two dichalcogenide) makes it impossible to conclude that superconductivity has been demonstrated in a truly 2-dimensional system.

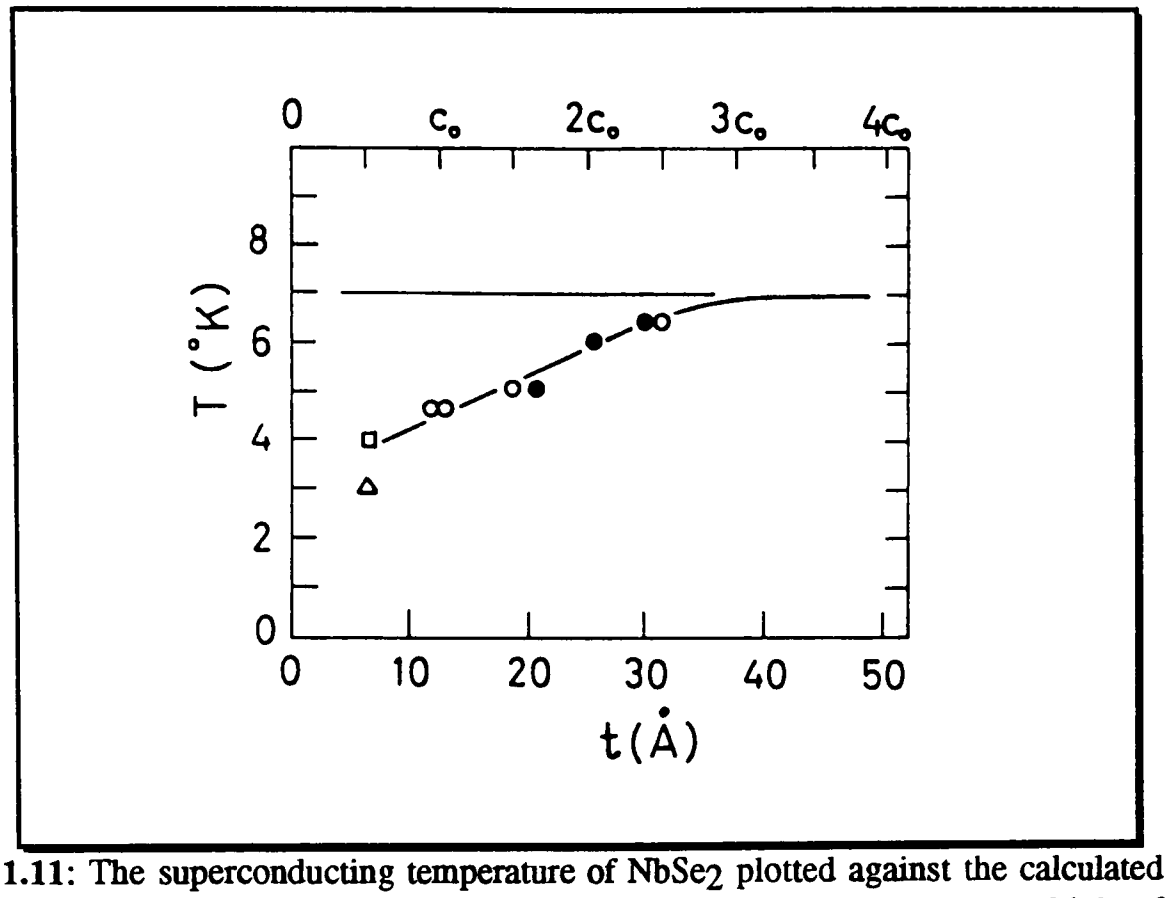

Figure 1.11: The superconducting temperature of $NbSe_2$ plotted against the calculated crystal thickness, t (filled circles).Open circles give crystal thickness to the nearest multiple of single-layer $NbSe_2$. The T_c for NbS_2 (square) and TaS_2 (triangle) are also shown for comparison.

In general, however, the intercalate superconductors have varying degrees of anisotropic properties. One measure of this is the ratio of the upper critical field, measured parallel and perpendicular to the layers, from which the coherence length ratio, $\xi_{//}/\xi_{\perp}$ can be derived. Coleman *et al.*[86] found critical field anisotropies ($H_{c//}/H_{c\perp}$) approaching 60 for $T/T_c < 0.7$ in pyridine and methylamine intercalates of TaS_2 and that their results best fit the theory of dimensional crossover developed by Klemm[87, 88] for highly anisotropic superconductors, based on Josephson tunneling between the layers rather than the anisotropic Ginzburg-Landau theory.

The similarities in superconducting anisotropies between the metal dichalcogenides and the recently discovered high T_c cuprate oxide superconductors has not been ignored and the parallels between the two systems have been reviewed by Liang[89].

1.7. Intercalation Kinetics

1.7.1. Staging Phenomena in Graphite Intercalates

After Schafautl's initial discovery of graphite intercalation compounds in 1841[7], Hoffmann and Frenzel[90] conducted the first systematic studies for stage index determinations on graphite intercalation compounds. Only recently, however, has the interest in graphite intercalates led to a proliferation of work on staging phenomena in

these compounds and their role as intermediates in the kinetics of intercalation.

The Daumas-Herold domain model predicts that intercalation in graphite is through a series of domains nucleating and merging within a layer[91] (see Figure 1.12). Modelling studies[92] have shown that this mechanism most likely proceeds sequentially through staged intermediates n_i, n_{i-1}, n_{i-2}..., n_f(where n_i and n_f are the initial and final stages respectively) rather than directly from host to stage 1 (i.e. fully intercalated) product. Experimental evidence in support of this model is provided by numerous studies[93, 94] In addition, Marcus et al[93] reported the first observation of a fractional stage intercalate of index 4/3.

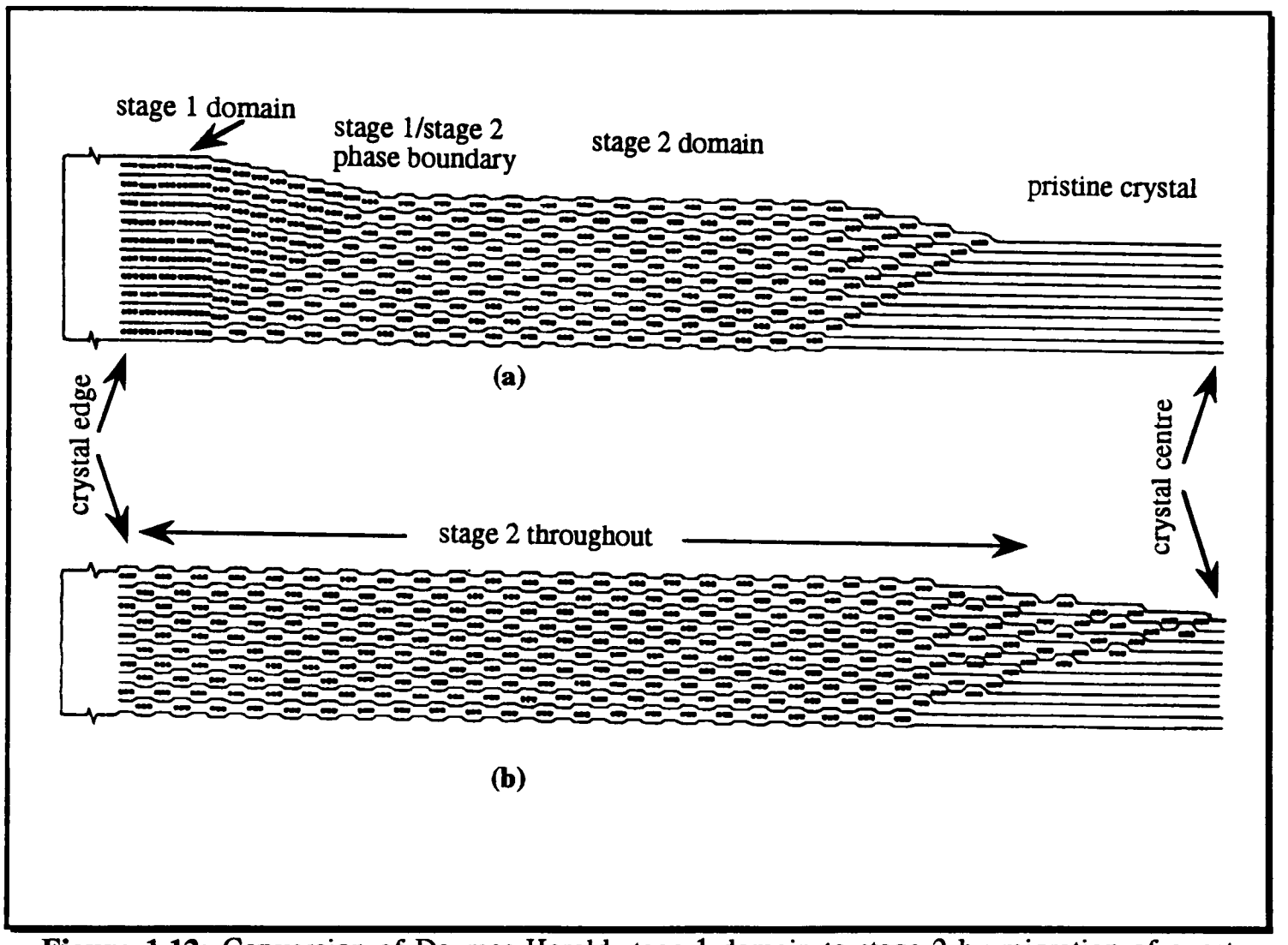

Figure 1.12: Conversion of Daumas-Herold stage 1 domain to stage 2 by migration of guest intercalants towards crystal centre (adapted from Kaluarachchi and Frindt, 1983[95]).

An exception to well defined, sequential stage transitions was demonstrated by Nishitani *et al*, where they showed that for H_2SO_4 intercalates of graphite, the mechanism of staging transitions is governed by the rate of intercalation. For fast electro-intercalations (high overpotential) the mechanism is diffusion-limited while in contrast, slow intercalations are under phase boundary control (that is, they are limited by chemical reaction at the interface). Structurally, the implication is that under diffusion control, more than one staged phase is present as an intermediate while under phase boundary control conditions, the intercalant is uniformly distributed between the layers, that is, only one staged phase predominates at a given time.

1.7.2. Parallels in Metal Dichalcogenide Intercalates

Although less kinetic work has been done on metal dichalcogenides than graphite intercalates because of technical and experimental difficulties (see Chapter 4), many parallels have been drawn between the two systems. The TaS_2-ammonia intercalate has been shown by neutron diffraction experiments[38] to form via the third and second stage intermediates. Similar staging behaviour was shown in TaS_2-pyridine[96] where a disordered second stage phase is the immediate precursor to the first stage phase. Disorder of the second stage phase was simulated by a statistical mixture of 70% second stage and 30% first stage phases. The neutron diffraction data showed for the first time that an intermediate phase with quite constant disorder exists throughout the reaction period and that the transformations, 2H-TaS_2 → 2nd stage and 2nd stage → 1st stage is too quick to be resolved.

As in graphite intercalates, the appearance of higher staged intermediates appears to be a general phenomenon in the reaction mechanism of metal dichalcogenide intercalation, having been observed in both trigonally (viz, 2H-TaS_2[97], 2H-NbS_2[97]) as well as octahedrally coordinated (TiS_2[98, 99], 1T-TaS_2[97]) MX_2 lattices. The intermediate stages in the latter CdI_2-type lattices, however, appear much more transiently and result in products of lower guest stoichiometry with lower negative layer charge densities[97].

1.7.3. Postulated mechanisms of intercalation

From empirical observations that thick crystals intercalate more slowly than thin crystals, intercalation is thought to initiate at the basal planes and proceed inwards. Support for this hypothesis has been provided in graphite intercalates by Hooley, who showed that when the basal planes of oriented pyrolytic graphite are capped with fluorinated tap grease, intercalation was inhibited[100]. Since tap grease had reduced the flexibility of basal planes, Hooley concluded that intercalation must necessarily start at the basal plane edges. Forsman, however, interpreted these results to indicate that basal plane adsorption and oxidation provided the driving force for intercalation[101]. While there is no conclusive evidence yet to support Forsman's theory of basal plane adsorption, it is now generally accepted that in both graphite and metal dichalcogenides, intercalation proceeds by diffusion of phase boundaries from crystal edges towards the centre.

Chianelli *et al.* have demonstrated this for Li_xTiS_2 in some elegant optical micrographs showing a crystal containing a virgin TiS_2 zone encircled by a boundary consisting of Li_xTiS_2[102]. Lerf *et al*[98, 103], in some Time Differentiated Perturbed Angular Correlation (TDPAC) spectroscopy studies of the Ta nuclear quadrupole precession in the lithium intercalates of 2H-TaS_2 and 1T-TaS_2, have also provided convincing evidence for concentrically converging Li intercalated phase boundaries (see Figure 1.13). They note, however, a difference in mechanism between 1T and 2H

polytypes of TaS_2, possibly arising because of the higher crystal quality of the former.

Both polytypes intercalate in phase boundary controlled reactions (concentric cylinder model)[104]but while 2H-TaS_2 intercalation is initiated by extensive nucleation at the crystal edges, 1T-TaS_2 suffers severe nucleation problems at the outset, with the result that a $Li_{0.3}TaS_2$ phase must permeate throughout the crystal before higher concentration phases appear via the concentric cylinder model for 2H-TaS_2[103].

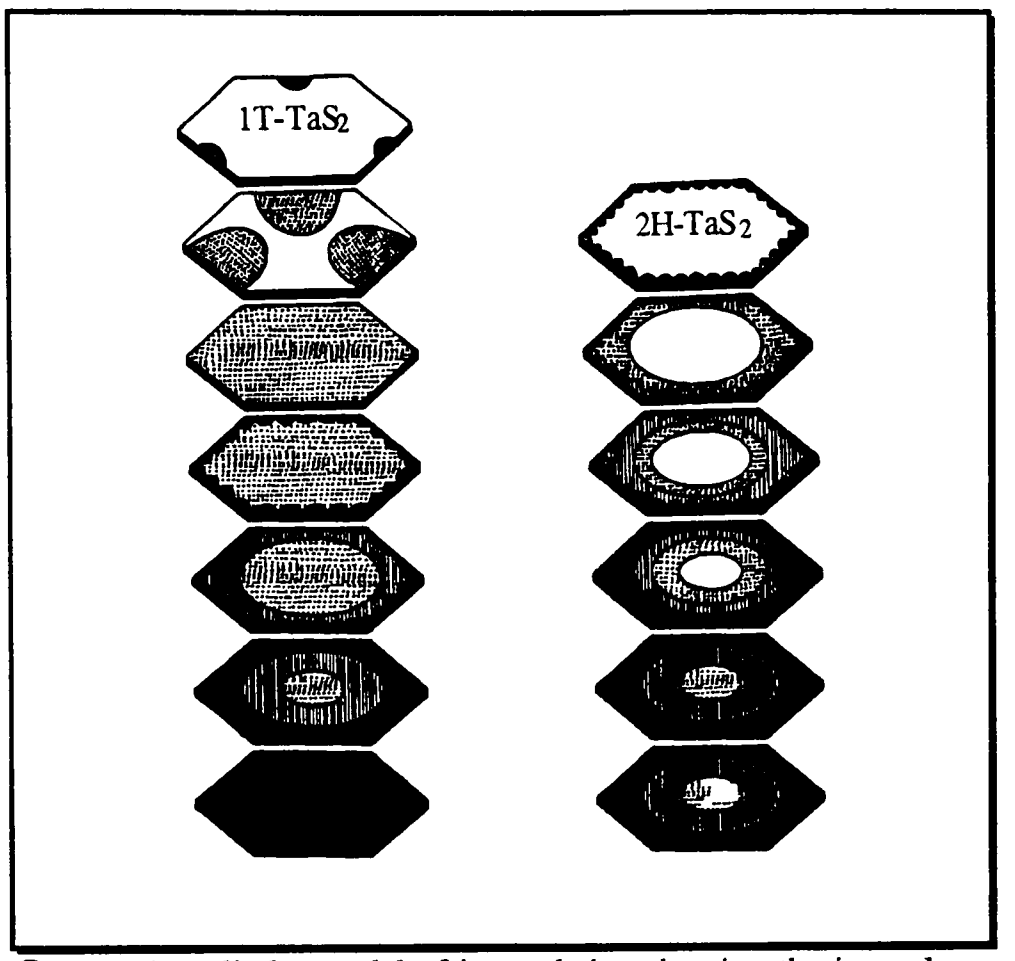

Figure 1.13: Concentric cylinder model of intercalation showing the inward movement of the intercalate phase towards the crystal centre (adapted from Butz and Lerf, 1984[104]).

The transformation between these phases ($Li_{0.3}TaS_2$, $Li_{0.7}TaS_2$, $LiTaS_2$) is not discussed by the authors, but based on energetic considerations, the Daumas-Herold model[91] of stage domains is likely to be operative. The model predicts that every layer is simultaneously permeated with the guest, forming domains of regularly stacked islands which gradually migrate along the intralayer plane, thus giving rise to a moving phase boundary (see Figure 1.12). This mechanism is favoured because transition between stages only involves a *lateral* redistribution of intercalant within a given layer with no motion *perpendicular* to the layers being required, nor de-intercalation of layers to accomodate *n*th→*(n-1)*th and *(n-1)*th→*n*th stage transformations[95].

Phase boundary control has also been illustrated for ammonia intercalates of TaS_2 by Riekel *et al,* who studied, by neutron diffraction, the intercalation of ND_3 into 2H-TaS_2 as well as monitored the rate of ND_3/NH_3 exchange[38]. It thus appears that at least for intercalation of ammonia into TaS_2, the rate determining step is nucleation, rather than the diffusion of the intercalant.

1.8. Conclusions

Clearly, the area of intercalation chemistry is an extremely diverse one; even by restricting our scope to metal dichalcogenide intercalates, the intercalants range from the simple metal atoms to large molecules such as long-chain aliphatic amines, organometallic sandwich complexes or metal clusters. For the larger non-spherically symmetric intercalants, the orientation of the guest within and with respect to the host layers remains poorly understood.

The physical changes conferred on the host by the intercalation of guests into the interlayer space are equally varied; they range from barely noticeable structural variation in the host at one end of the spectrum to superconducting phase transitions at the other, with a plethora of equally unexpected (and in many cases, as yet unexplained) phenomena such as charge density wave supression and two-dimensional magnetic ordering in between. These remarkable variations in physical properties of intercalation compounds provide a rich and hitherto largely untapped vein for chemists, physicists and materials scientists in their search for new sources of synthetic materials.

As yet however, the actual process of intercalation in metal dichalcogenides itself remains a poorly understood phenomenon. Although parallels can be inferred from the significantly greater body of knowledge that is available on graphite intercalation, the metal dichalcogenides, due to their more complex layer structure, provide a more subtle and challenging arena for the scientist. An understanding of the intercalation process and the subtle interplay of guest-host interactions at work in metal dichalcogenides would provide useful insights for the materials scientist in designing novel materials as well as helping them avoid the pitfalls of poor sample quality and unviable intercalations that continue to plague present day research efforts.

1.9. Thesis Objectives

This thesis examines the organometallic intercalates of zirconium and tin dichalcogenides in order to develop an understanding of the 3 areas outlined above:

(a) structure

(b) electronic properties

(c) intercalation kinetics and mechanisms.

Chapter Two describes the application of one-dimensional Fourier analyses on these intercalates using data from neutron and X-ray diffraction of oriented crystal samples. Chapter Three examines the changes, both in magnetic and electrical properties that these layered materials undergo upon intercalation while Chapter Four explores the underlying kinetics and mechanisms of organometallic intercalation, using novel techniques based upon energy-dispersive powder diffraction with a high flux synchrotron X-ray source. Chapter Five provides experimental details of the syntheses of these

materials. Ancillary details and listings of computer programs can be found in Appendices A through C.

References:

1. J. F. Fauvarque, in *Chemical Physics of Intercalation*, ed. S. Flandrois and A. P. Legrand, Plenum Press: New York, 1987, p. 291

2. M. Patriarca, M. A. Voso, B. Scrosati, F. Bonino and M. Lazzari, *Sol. St. Ionics* (1982), **6**, 15-20.

3. R. Schollhorn, in *NATO ASI Series B: Applied Sciences*, ed. A. P. Legrand S. Flandrois, 1987, p. 149-171

4. E. A. Marseglia, *Int. Rev. Phys. Chem.* (1983), **3**, 177-216.

5. R. P. Clement, W. B. Davies, K. A. Ford and M. L. H. Green, *Inorg. Chem.* (1978), **17**, 2754-2758.

6. D. S. Glueck and M. L. H. Green, *Inorg. Chem.* (1992), in press.

7. G. A. Schafautl, *J. Prakt. Chem.* (1841), **21**, 155.

8. D. W. Murphy, S. A. Sunshine and S. M. Zahurak, in *Chemical Physics of Intercalation*, ed. S. Flandrois, A. P. Legrand, Plenum Press: New York, 1987, p. 173

9. J. Rouxel, L. Trichet, P. Chevalier, P. Colombet and O. Abou-Ghaloun, *J. Solid State Chem* (1979), **29**, 311-21.

10. M. B. Dines, *Science* (1975), 1210-11.

11. R. P. Clement, W. B. Davies, K. A. Ford, M. L. H. Green and A. J. Jacobson, *J. of Mol. Catalysis* (1977/78), **3**, 191-194.

12. G. V. Subba-Rao and J. C. Tsang, *Mat. Res. Bull.* (1974), **9**, 921-926.

13. M. S. Wittingham, *J Chem. Soc., Chem. Comm.* (1974), 328-329.

14. M. A. Gee, R. F. Frindt, P. Joensen and S. R. Morrison, *Mat. Res. Bull.* (1986), **21**, 543-549.

15. L. F. Nazar and A. J. Jacobson, *J. Chem. Soc. - Chem. Comm.* (1986), 570-571.

16. R. Schollhorn, *Physica* (1980), **99B**, 89-99.

17. R. Schollhorn, E. Sick and A. Weiss, *Z. Naturforsch.* (1973), **28**, 168.

18. F. R. Gamble, J. H. Osiecki, M. Cais, R. Pisharody, F. J. DiSalvo and T. H. Geballe, *Science* (1971), **174**, 493-497.

19. R. Leonelli, M. Plischke and J. C. Irwin, *Phys. Rev. Lett.* (1980), **45**, 1291.

20. R. M. Suter, M. W. Shafer, P. M. Horn and P. Dimon, *Phys. Rev. Lett.* (1982), **26**, 1495-1498.

21. F. J. DiSalvo, G. W. Hull, L. H. Schwartz, J. M. Voorhoeve and J. V. Waszczak, *J. Chem. Phys.* (1973), **59**, 1922-1929.

22. N. Le Negard, O. Gorochov and G. Collin, *Mat. Res. Bull.* (1975), **10**, 1287.

23. M. S. Wittingham, *Prog. Solid St Chem* (1978), **12**, 41-99.

24. K. Chatakondu, M. L. H. Green, J. Qin, M. E. Thompson and P. J. Wiseman, *Chem Comm* (1988), 223-225.

25. K. Chatakondu, C. A. Formstone, M. L. H. Green, D. O'Hare, J. M. Twyman and P. J. Wiseman, *J. Mat. Chem.* (1991), **1**, 205-212.

26. R. P. Clement, W. B. Davies, K. A. Ford, M. L. H. Green and A. J. Jacobson, *J. Chem. Soc., Chem. Comm.* (1976), 781-2.

27. J. S. O. Evans, *D. Phil. Thesis*. Oxford University, 1993.

28. D. O'Hare, H. V. Wong, S. Hazell and J. W. Hodby, *Adv. Mater.* (1992), **4**, 658-660.

29. D. O'Hare, J. S. O. Evans, P. J. Wiseman and C. K. Prout, *Angew. Chemie - Int. Ed. in English* (1991), **30**, 1156-1158.

30. L. Benes, J. Votinsky, P. Lostak, J. Kalousova and J. Klikorka, *Phys. Stat. Sol. (A)* (1985), **89**, K1-K4.

31. D. O'Hare and J. S. O. Evans, *Comments Inorg. Chem.* (1993), **14**, 155-206.

32. W. Y. Liang, in *Intercalation in Layered Materials*, ed. M. S. Dresselhaus, Plenum Press: New York and London, 1986, p. 31

33. M. S. Wittingham and F. R. Gamble, *Mat. Res. Bull.* (1975), **10**, 363-372.

34. A. LeBlanc, *Mat. Res. Bull* (1974), **9**, 191-?

35. W. R. McKinnon, J. R. Dahn and C. Levy-Clement, *Solid State Comm.* (1984), **50**, 101-104.

36. M. A. Py and R. R. Haering, *Can. J. Phys.* (1983), **61**, 76-84.

37. M. S. Wittingham, *Mater. Res. Bull.* (1978), **13**, 775-82.

38. C. Riekel and R. Schollhorn, *Mat. Res. Bull.* (1976), **11**, 369-376.

39. C. Riekel, D. Hohlween and R. Schollhorn, *J. Chem. Soc., Chem. Comm.* (1976), 863-4.

40. R. R. Chianelli, J. C. Scanlon, M. S. Wittingham and F. R. Gamble, *Inorg. Chem.* (1975), **14**, 1691.

41. F. R. Gamble and B. G. Silbernagel, *J. Chem. Phys.* (1975), **63**, 2544-52.

42. R. Schollhorn and H. D. Zagefka, *Angew. Chem. - Int. Ed. Engl.* (1977), **16**, 199-200.

43. R. Schollhorn, H. D. Zagefka, T. Butz and A. Lerf, *Mat. Res. Bull.* (1979), **14**, 369-76.

44. P. L. McDaniel, T. M. Barbara and J. Jones, *J. Phys. Chem.* (1988), **92**, 626-630.

45. P. L. McDaniel, G. Liu and J. Jones, *J. Phys. Chem.* (1988), **92**, 5055-5058.

46. B. G. Silbernagel, *Chem. Phys. Lett.* (1975), **34**, 298-301.

47. S. J. Heyes, N. J. Clayden, C. M. Dobson, M. L. H. Green and P. J. Wiseman, *J. Chem. Soc., Chem. Comm.* (1987), 1560-1562.

48. C. Grey, J. S. O. Evans, D. O'Hare and S. Heyes, *J. Chem. Soc., Chem Comm.* (1991), 1380-1382.

49. W. B. Davies, *B. A. (Part II) Thesis*. Oxford University, 1976.

50. S. J. Mason, *D. Phil. Thesis*. Oxford University, 1993.

51. B. G. Silbernagel and M. S. Wittingham, *J. Chem Phys.* (1976), **64**, 3670-73.

52. B. G. Silbernagel, *Solid State Comm.* (1975), 361.

53. B. G. Silbernagel and M. S. Wittingham, *Mat. Res. Bull.* (1976), **11**, 29-36.

54. P. Deniard, L. Trichet and Y. Chabre, in *Chemical Physics of Intercalation*, ed. S. F. A. P. Legrand, Plenum Press: New York, 1987, p. 387

55. Y. Chabre and P. Deniard, in *Chemical Physics of Intercalation*, ed. S. F. A. P. Legrand, Plenum Press: New York, 1987, p. 395

56. D. R. P. Guy, R. H. Friend, D. C. Johnson and M. J. Sienko, *J. Phys. C.* (1982), **15**, 1251-5.

57. D. R. P. Guy, R. H. Friend, M. R. Harrison, D. C. Johnson and M. J. Sienko, *J. Phys. C.* (1982), **15**, 1245-9.

58. D. W. Murphy, F. J. DiSalvo, G. W. Hull and J. W. Wasczczak, *Inorg. Chem.* (1976), **15**, 17.

59. L. Bernard, W. Glausinger and P. Colombet, *Solid State Ionics* (1985), **17**, 81-9.

60. F. R. Gamble and A. H. Thompson, *Solid State Comms* (1978), **27**, 379-382.

61. D. O'Hare, W. Jaegermann, D. L. Williamson, F. S. Ohuchi and B. A. Parkinson, *Inorg. Chem.* (1988),

27, 1537-1542.

62. R. H. Friend and A. D. Yoffe, *Adv. Phys.* (1987), **36**, 1-94.

63. J. V. Acrivos, W. Y. Liang, J. A. Wilson and A. D. Yoffe, *J. Phys. C.* (1971), **4**, 418.

64. A. M. Herman, R. B. Somoano, V. Hadek and A. Rembaum, *Solid State Comm.* (1973), **13**, 1065-8.

65. R. H. Friend, S. S. P. Parkin and D. Jerome, *J. Phys. C.* (1982), **15**,

66. M. Sarma, A. R. Beal, S. Nulsen and R. H. Friend, *J. Phys. C.* (1982), **15**, 4367-78.

67. M. Sarma, A. R. Beal, S. Nulsen and R. H. Friend, *J. Phys. C* (1982), **15**, 477-93.

68. P. C. Klipstein and R. H. Friend, *J. Phys. C.* (1984), **17**, 2713-2734.

69. P. C. Klipstein, D. R. P. Guy, A. M. Ghorayeb and R. H. Friend, *Mol. Cryst. Liq. Cryst.* (1985), **121**, 153-156.

70. P. C. Klipstein, R. H. Friend and A. D. Yoffe, *Philos. Mag. B* (1985), **52**, 611.

71. N. Ahmad, P. C. Klipstein, S. D. Obertelli, E. A. Marseglia and R. H. Friend, *J. Phys. C: Solid State Physics* (1987), **20**, 4105-4114.

72. A. M. Ghorayeb and R. H. Friend, *J. Phys. C* (1987), **20**, 4181-4200.

73. P. C. Klipstein and R. H. Friend, *J. Phys. C.* (1987), **20**, 4169-79.

74. P. C. Klipstein, A. G. Bagnall, W. Y. Liang, E. A. Marseglia and R. H. Friend, *J. Phys. C.* (1981), **14**, 4067-81.

75. P. C. Klipstein, M. Sarma, A. R. Beal, S. Nulsen and R. H. Friend, *J. Phys. C.* (1982), **15**, 477-493.

76. Y. Onuki, R. Inada, S. Tanuma, S. Yamanaka and H. Kamimura, *Physica B* (1981), **108**, 1037-8.

77. Y. Onuki, R. Inada, S. Tanuma, S. Yamanaka and H. Kamimura, *J. Phys. Soc. Japan* (1982), **51**, 880.

78. Y. Onuki, S. Yamananka, R. Inada, M. Kido and S. Tanuma, *Syn. Met.* (1983), **5**, 245-55.

79. S. F. Meyer, R. E. Howard, G. R. Stewart, J. V. Acrivos and T. H. Geballe, *J. Chem. Phys.* (1975), **62**, 4411-19.

80. C. A. Formstone, M. Kurmoo, E. T. Fitzgerald, P. A. Cox and D. O'Hare, *J. Mater. Chem.* (1991), **1**, 51-57.

81. C. A. Formstone, E. T. Fitzgerald, P. A. Cox and D. O'Hare, *Inorg. Chem.* (1990), **29**, 3860-3866.

82. D. O'Hare, *Chem. Soc. Rev.* (1992), 121-126.

83. F. J. DiSalvo, R. Schwall, T. H. Geballe, F. R. Gamble and J. H. Osiecki, *Phys. Rev. Lett.* (1971), **27**, 310-313.

84. R. V. Coleman and S. J. Hillenius, *Physica B&C* (1981), **105**, 428-34.

85. R. F. Frindt, *Phys. Rev. Lett.* (1972), **28**, 299-301.

86. R. V. Coleman, G. K. Eiserman, S. J. Hillenius, A. T. Mitchell and J. L. Vicent, *Phys. Rev. B* (1983), **27**, 125-39.

87. R. A. Klemm, M. R. Beasely and A. Luther, *J. Low Temp. Phys.* (1974), **16**, 607-613.

88. R. A. Klemm, A. Luther and M. R. Beasley, *Phys. Rev. B* (1975), **12**, 877.

89. W. Y. Liang, in *Condensed Systems of Low Dimensionality*, ed. J. L. Beeby, Plenum Press: New York, 1991, p. 677-694

90. U. Hoffmann and A. Frenzel, *Z. Elektrochem* (1931), **37**, 613.

91. N. Daumas and A. Herold, *C. R. Acad. Sci. Ser. 6* (1963), **268**, 373.

92. G. Kirczenow, *Syn. Met.* (1985), **12**, 143-8.

93. B. Marcus, J. L. Soubeyroux and P. Tauzin, in *Chemical Physics of Intercalation*, ed. A. P. Legrand and S. Flandrois, Plenum Press: New York, 1987, p. 375

94. H. Suematsu, K. Suda and N. Metoki, *Syn. Met.* (1988), **23**, 7-12.

95. D. Kaluarachchi and R. F. Frindt, *Phys. Rev. B* (1983), **28**, 3663-65.

96. C. Riekel and C. O. Fischer, *J. Solid State Chem.* (1979), **29**, 181-90.

97. C. Riekel, H. Reznik and R. Schollhorn, *J. Solid State Chem.* (1980), **34**, 253-262.

98. T. Butz, H. Saitovitch and A. Lerf, *Chem. Phys. Lett.* (1979), **65**, 146-149.

99. A. H. Thompson, *Phys. Rev. Lett.* (1978), **65**, 146.

100. J. G. Hooley, *Carbon* (1980), **18**, 82-92.

101. W. C. Forsman, *Syn. Met.* (1983), **5**, 77-100.

102. R. Chianelli, J. C. Scanlon and B. M. L. Rao, *J. Solid State Chem.* (1979), **29**, 323-37.

103. P. Ganal, T. Butz and A. Lerf, *Syn. Met.* (1989), **34**, 641-5.

104. T. Butz, A. Lerf and J. O. Besenthal, *Rev. Chim. Min.* (1984), **21**, 556-587.

CHAPTER TWO

STRUCTURAL STUDIES

CHAPTER TWO

STRUCTURAL STUDIES

2.1 Introduction

While extensive scrutiny has been devoted to studying the physical, magnetic and electrical properties of metal dichalcogenide intercalates [1-9], still fundamental questions such as the orientational preferences for metallocene guests in the inter-lamellar space remain largely unresolved and plagued with conflicting evidence. The controversy has been documented in Chapter 1 and will not be repeated here (see **1.5.3**)

The primary problem in structural characterisation of organometallic intercalates is their high degree of disorder inherent in the *ab* plane of the crystals, resulting in broad Bragg peaks from non-*00l* reflections. As a result, traditional methods of crystal structure determination have not been applicable to these systems and, to date, only one full structural study has been attempted, by manually indexing and extraction of intensity information from Weissenberg diffraction photographs[10]. This study demonstrated conclusively that the cobaltocene resides with its principal molecular axis parallel to the host layers, but its labour-intensive nature precluded it from being used to examine the guest orientations in a wider range of organometallic intercalates.

While a full structural determination is time-consuming and not always possible, one-dimensional refinement of both X-ray and neutron diffraction data along the *c* axis is a convenient and useful method for ascertaining the guest orientation, especially when large single crystal samples can be oriented to collect *00l* reflections exclusively. From the integrated intensities of these reflections it is possible to calculate one-dimensional electron density and neutron scattering density profiles respectively, which can be used to deduce the orientation of the guest molecule. The method has been applied by previous researchers in isolated cases such as $TaS_2(Fe_6S_8(PEt_3)_3)$[11] and $SnS_2(CoCp_2)_{0.3}$[10].

Complementary information on the guest dynamics, and by inference, its orientation, can be obtained by solid state deuterium NMR spectroscopy. For example, Heyes *et al.* have shown that in the system 2H-$TaS_2(CoCp_2)_{0.25}$ the cobaltocene undergoes rapid C_5 rotation at temperatures <230K, but that at higher temperatures both C_2 and C_5 rotations are observed[12]. From the variable temperature data between 200 and 340K they inferred that both orientations of cobaltocene exist at high temperatures (>230K). ^2H NMR spectroscopy has also been applied to single crystals of

$SnS_2(CoCp_2)_{0.3}$ by Grey *et al.*, who have shown that only one orientation (that with the principal molecular axis of the metallocene parallel to the layer planes) exists at room temperature[13].

In this chapter, the first two sections introduce the techniques employed, namely, diffraction (Section **2.2**) and ^2H NMR spectroscopy (Section **2.3**). Section **2.4** describes a systematic study of the guest orientation in ZrS_2 intercalated with guests varying in size and shape from prototypical metallocenes ($CoCp_2$, $CrCp_2$) to the larger, mixed ring sandwich complexes such as Ti(η-C_8H_8)(η-C_5H_5) and W(η-C_7H_7)(η-C_5H_4-CH_3). In addition, the $CoCp_2$ orientation in the SnX_2 {X=S, Se} intercalates is examined, including $SnSe_2(CoCp_2)_{0.3}$, the highest temperature superconducting intercalate (T_c=8.3K) reported to date[14]. In Section **2.5**, the results of the diffraction experiments on guest orientation are verified by ^2H NMR spectroscopy for the deuterated intercalates $ZrS_2\{Co(\eta\text{-}C_5D_5)_2\}_{0.25}$ and $SnSe_2\{Co(\eta\text{-}C_5D_5)_2\}_{0.3}$.

2.2 Diffraction

2.2.1. Theory

Both X-rays and neutrons are diffracted by extended crystalline arrays. While X-rays scatter off electrons, neutrons are scattered by atomic nuclei. Nontheless, the basis for both techniques contain many similarities and both cases can be discussed in the same terms.

When a wave impinges on an object, the object becomes a source of secondary waves which "scatters" the incident wave. If a regular array of these objects exists, then the scattered waves will interfere with each other. The overall effect of scattering the incident wave off N point scatterers is given by superpositioning each of the individual scattered waves.

$$\Psi = \sum_{j=1}^{N} \psi_j \qquad (1)$$

where $\psi = f_j \exp(i\alpha_j)$

Rewriting this in Cartesian coordinate vectors, x, y, z:

$$\Psi = \sum_{j=1}^{N} f_j \exp[2\pi i(hx + ky + lz)] \qquad (2)$$

The term f_j is a measure of the scattering power of the jth atom and thus $|\Psi_{hkl}| = |F_{hkl}|$ represents the overall structure factor of the crystal.

Since the intensity of an electromagnetic wave is proportional to the square of its amplitude, the intensity of an X-ray (or neutron) beam, I_{hkl}, diffracting from a crystal is

directly proportional to its structure factor.

$$I_{hkl} = k\,|F_{hkl}|^2 \qquad (3)$$

In principle, if one has suitable phase angle information, one can use diffracted intensity data to obtain values for F_{hkl}. In reality, only its magnitude, $|F_{hkl}|$, is available, due to the phase problem.

2.2.2. X-ray vs Neutron Diffraction

The choice of whether to use X-ray or neutron diffraction data for one-dimensional refinement depends on several factors which arise from the differences between neutrons and X-rays[15]. Neutrons, unlike X-rays, are scattered by atomic nuclei rather than electrons and as such, neutron scattering profiles do not exhibit the $\sin\theta/\lambda$ dependence typical of X-rays. Moreover, because neutrons scatter off nuclei, this can vary dramatically from one isotope to the next (e.g. for the hydrogen and deuterium nuclei, the coherent scattering lengths, b = -0.3741×10^{-12} and 0.6674×10^{-12} cm respectively; see Figure 2.1) As a means of comparison, the neutron scattering lengths for a selection of elements which occur in the organometallic intercalates studied in this chapter are tabulated below:-

Table 2.1: Neutron Scatter Lengths of Selected Elements

Element	Neutron Scattering Length*	Atomic No.
Zr	0.716	40
S	0.2847	16
Co	0.253	27
C	0.6648	6
D	0.6674	1
H	-0.3741	1
Cr	0.3635	24
Mo	0.695	42
Ti	-0.3438	22

* coherent neutron scattering length of bound atoms (10^{-12}cm)

Additionally, the magnetic moment of neutrons allow both nuclear and magnetic scattering information to be obtained when magnetic spins are present in the sample. Finally, the low absorption cross-section of neutrons for certain elements, such as vanadium, allows special sample environment (for example, furnaces and cryostats) which would not be possible in X-ray experiments to be used.

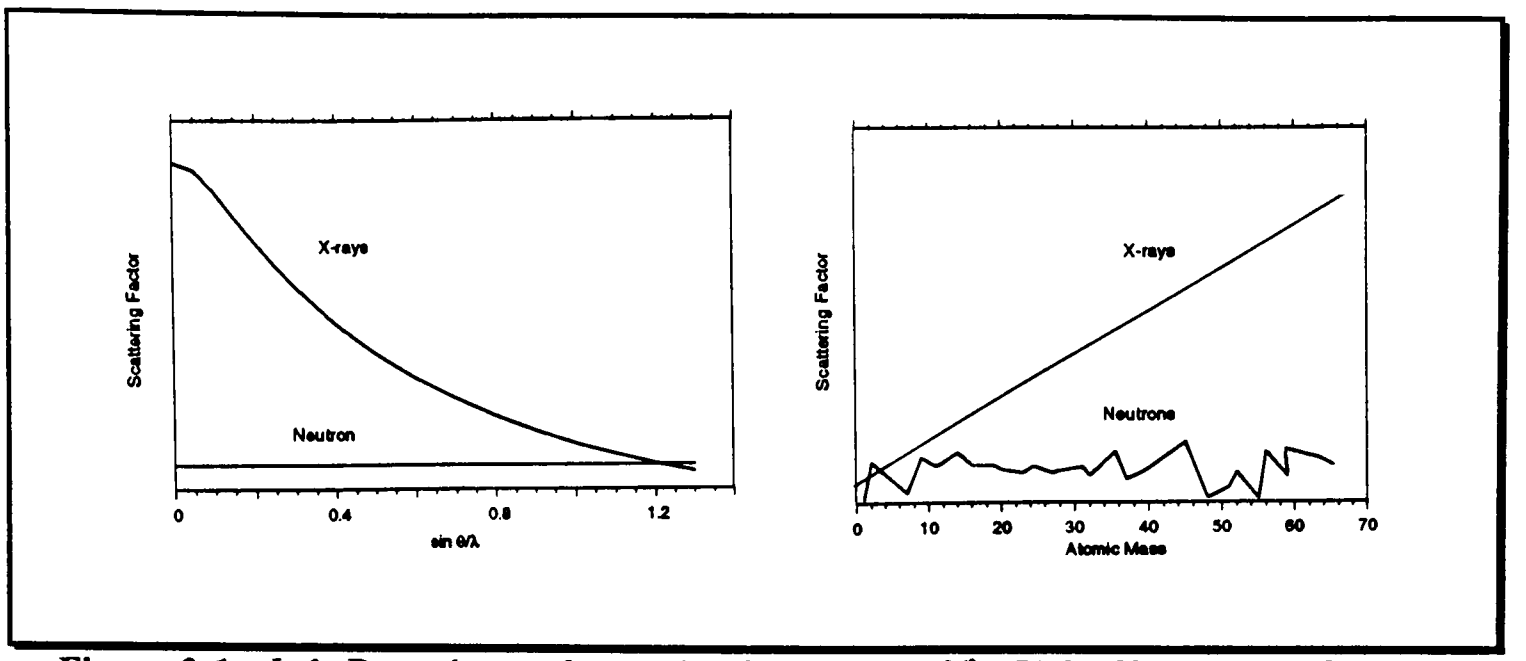

Figure 2.1: *Left:* Dependence of scattering factors on $\sin\theta/\lambda$. *Right:* Variation of X-ray and neutron scattering factors as a function of atomic mass.

In contrast, the disadvantages of using neutrons instead of X-rays are that (a) larger sample sizes are required because of the comparatively lower flux of neutron beams, (b) deuteration of samples is necessary in order to reduce incoherent scattering from hydrogen atoms & (c) there is limited availability of neutron sources.

2.2.3. Data collection and reduction

(a) X-Ray Diffraction

For crystals diffracting in Bragg-Brentano reflection geometry (illustrated in the figure below) alignment of the crystals as shown gives rise to only *00l* reflections since only reciprocal lattice vectors of the form, $\mathbf{k}_{00l}$, intersect the sphere of reflection.

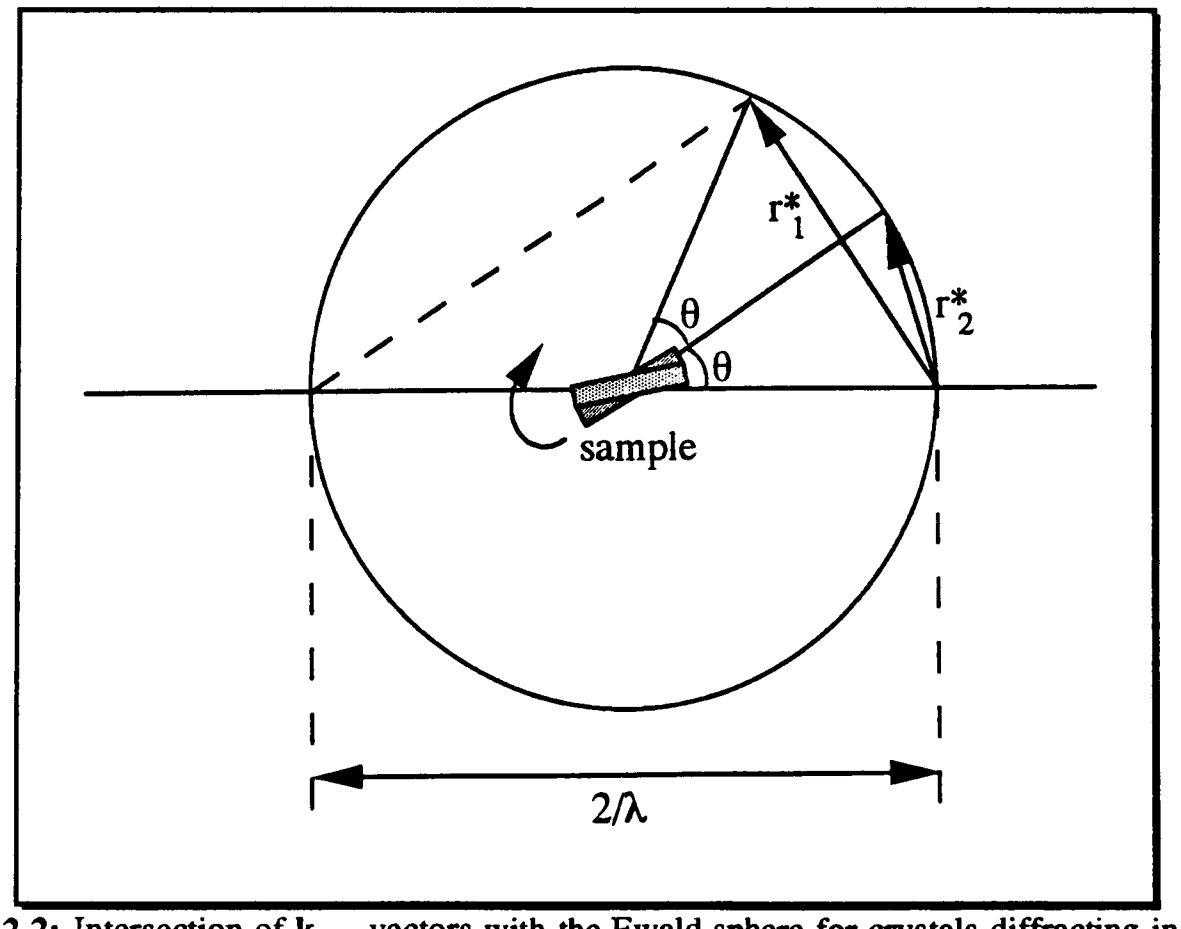

Figure 2.2: Intersection of $\mathbf{k}_{00l}$ vectors with the Ewald sphere for crystals diffracting in Bragg-Brentano geometry.

Since there is considerably more order in organometallic intercalates along the *c* axis than the *a* or *b* directions, one can, by mounting several large crystals of the intercalates parallel to the flat sample holder surface, collect very sharp, intense *00l* reflections.

Crystals of ZrS_2 intercalates were mounted under N_2, using silicone grease in a specially designed air-tight X-ray cell consisting of Capoten supported within an aluminium frame. X-ray diffraction patterns of aligned crystals of the intercalates were recorded (0.002 deg/s) in Bragg-Brentano geometry on a Phillips PW1729 Diffractometer between $2\theta = 4.3° \rightarrow 90°$, so that only *00l* reflections were collected. CuKα radiation (λ = 1.5418Å) was used at 40kV, 30mA. The integrated intensities of the observed reflections, I_{obs}, is related to the structure factors, F_{obs}, by the relation:

$$I_{obs} = k_1 k_2 I_0 LPTE|F_{obs}|^2 \qquad (4)$$

where I_0 = intensity of the incident beam,
$k_1 = e^4/(m^2c^4)$ {a constant arising from Thompson scattering}
$k_2 = \lambda^3\Omega/V^2$ {Ω=vol. of crystal, V=vol. of unit cell}
L = Lorentz factor
P = polarisation factor
T = transmission factor {also known as absorption correction}
E = extinction coefficient {negligible for thin crystals/disordered samples}

Of the factors listed above, only three are important and need to be considered for the experiments described in this chapter: *Lorentz*, *polarisation* and *transmission* factors.

Lorentz corrections are necessary because different sets of lattice planes spend varying amounts of time satisfying the Bragg condition ($\lambda = 2d\sin\theta$) for diffraction as the sample is rotated in the diffractometer. Another way of stating this is in terms of the reciprocal lattice: the Bragg condition is satisfied when the reciprocal lattice nodes cross the sphere of reflection. The time a node is in a diffracting position is dependent on two factors: the position of the node, and the velocity with which it sweeps through the sphere of reflection. For the simple geometry employed in our laboratory diffractometer, the derivation is straightforward.

For a crystal rotating at constant angular velocity ω, the linear velocity component of the reciprocal lattice node P along the radius of the sphere of reflection, $V_n = \omega|r^*|$ and its component along the surface of the Ewald sphere, $V_n = |r^*|\omega\cos\theta$, are shown in Figure 2.3. Substituting $|r^*|$ in terms of Bragg's law, where $|r^*| = 1/d = 2\sin\theta/\lambda$, gives

$$V_n = \frac{\omega}{\lambda} 2\sin\theta\cos\theta = \frac{\omega}{\lambda}\sin 2\theta \qquad (5)$$

Since (ω/λ) is constant for a given diffraction experiment on a crystal, and the amount of time the diffraction condition is satisfied is inversely related to the velocity of the reciprocal lattice node:

$$L = \frac{1}{\sin 2\theta} \qquad (6)$$

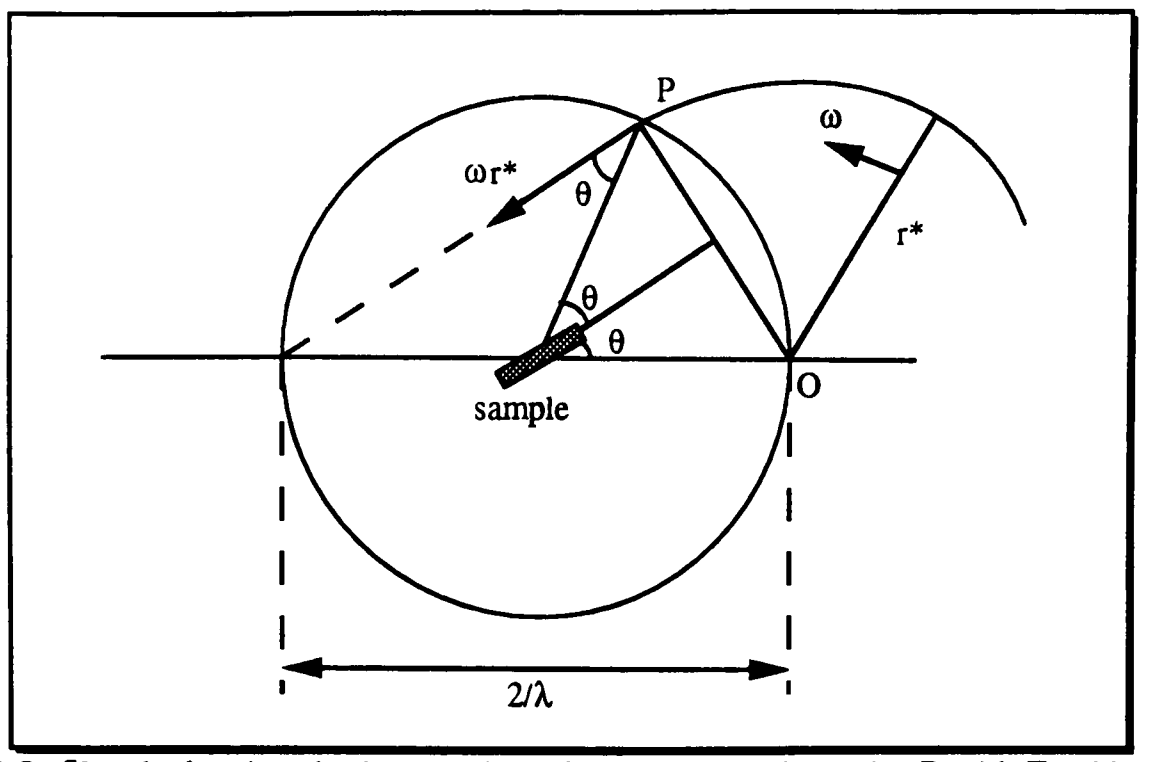

Figure 2.3: Sketch showing the intersection of reciprocal lattice point P with Ewald sphere as crystal is rotated at angular velocity ω.

The polarisation correction depends on the state of polarisation of the incident X-ray beam and on the scattering angle of the diffracted beam. When a non-polarised beam is diffracted by a crystal, the polarisation factor, P, is:

$$P = \frac{1}{2}(1+\cos^2 2\theta). \qquad (7)$$

When the beam is monochromated by selecting Bragg reflections at angle, θ_m, from a monochromator crystal,

$$P = \frac{\cos^2 2\theta.|\cos^n 2\theta_m|+1}{1+|\cos^n 2\theta_m|} \qquad (8)$$

assuming the original beam, monochromated beam and scattered beam all lie in the same plane. For a mosaic monochromator crystal set at 30° such as in the Phillips 1729 Diffractometer used,

$$P = C\,(1+ 0.75\cos^2\theta) \qquad (9)$$

Absorption of X-rays by the diffracting crystal reduces the intensity of the X-ray beam travelling through it by an amount which depends on both the material and the path length of the beam. The intensity of the diffracted beam, I, is given by the relation:

$$I = I_0\, e^{-\mu x} \qquad (10)$$

where μ = linear absorption coefficient
x = total path length

The transmission factor, T, is defined as follows:

$$T = \frac{1}{V}\int_v e^{-\mu(p+q)}dV \qquad (11)$$

where p, q are the path lengths of the incident and diffracted beams respectively.

For the Bragg-Brentano reflection geometry employed, the total path length, x, can be expressed in terms of the thickness of the crystal, t, and the Bragg angle (see

Figure 2.4).

$$x=p+q=(2t)/\sin\theta$$

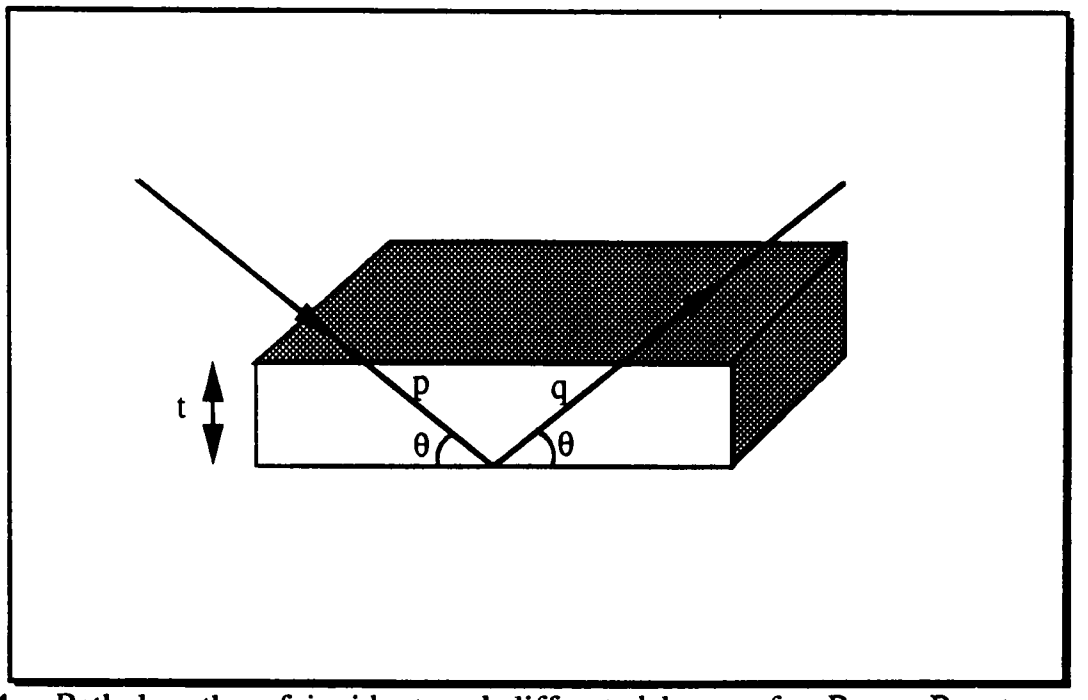

Figure 2.4: Path lengths of incident and diffracted beams for Bragg-Brentano diffraction geometry.

Also, since the crystal is only rotating along one axis, the transmission factor is an integral over only one dimension,

$$T = \frac{1}{x}\int_x e^{-\mu x}dx \qquad (12)$$

In the thin crystal limit, $e^{-2\mu x} \rightarrow 0$ so that

$$T = \frac{1}{2\mu x} \propto \sin\theta \qquad (13)$$

(b) Neutron Diffraction

Room temperature neutron diffraction spectra of aligned crystals of ZrS_2 were acquired on the Liquid and Amorphous Diffractometer (LAD) at the Rutherford Appleton Laboratory, Didcot (see Chapter Five). The crystals were fixed in position by glueing them onto vanadium foil strips using epoxy resin (Araldite), then fixing the foil in place within the vanadium ca^nister using tailor-made vanadium spacers. The ca^nisters were then sealed before removal from the dry N_2 box. On LAD, the vanadium ca^nisters were aligned with a calibrated goniometer, so that the *001* to *008* reflections were successively collected in detector banks 3 to 7.

2.2.4. Refinement of *00l* intensities

The *00l* intensities derived from both the X-ray and neutron experiments, along with cell dimensions and overall guest occupancies, were used to perform subsequent least squares refinements of the guest orientational parameters with PJWB, a FORTRAN77 program written by Dr P. J. Wiseman of the Inorganic Chemistry Laboratory, Oxford[16]. The program utilises Bessel functions to model the electron

density of the rapidly rotating Cp ring as a torus with a radius of 1.15Å. Input cell parameters for the refinement were obtained by least squares analysis of *00l* reflections (using a Choleski matrix inversion method) while guest stoichiometries were fixed at values calculated from elemental C/H analysis of the intercalated crystals. The program refined intensity scale factors, the partitioning of guest occupancies between the two orientations, relative S coordinates (z/c) and isotropic temperature factors. From the structure factors obtained, F_{hkl}, the electron density can be obtained using the relation:

$$\rho(\mathbf{r}) = \frac{1}{V}\sum_{h,k,l=-\infty}^{\infty} F_{hkl}\exp[-2\pi i(hx+ky+lz)] \qquad (14)$$

(where x, y, z are the fractional coordinates of the point defined by the vector **r**.)

If only F_{00l} reflections are used, reverse Fourier transform of F_{hkl} yields the one-dimensional electron density or neutron scattering intensity along the *c* axis.

2.3 Solid State ^{2}H-NMR Spectroscopy

Solid state deuterium NMR spectroscopy is a particularly useful technique for studying molecular motions and order within a wide variety of solid and semi-solid materials. It has been used to study a wide range of compounds such as crystal hydrates[17], liquid crystals[18], polymers[19] and organometallic intercalation compounds[12].

The triple degeneracy of the energy levels of a quadrupolar nucleus, such as deuterium, with I=1, is lifted in a magnetic field by a combination of Zeeman and quadrupolar interactions. The Zeeman interaction arises from the direct coupling of the nuclear spin and the applied magnetic field, while the quadrupolar interaction arises from the coupling between the nuclear charge and the electric field gradient (EFG) at the nucleus. The effects of dipolar, spin-spin coupling and chemical shielding interactions may be neglected, since these interactions are of an order of magnitude smaller than the quadrupolar interaction. For deuterium, the nuclear quadrupole moment is sufficiently small so that the quadrupolar interaction can be considered as a first order perturbation on the Zeeman levels. This is depicted in the figure below for a deuterium nucleus with the principle axis system (PAS) of its EFG tensor oriented at an arbitrary angle, specified by the Euler angle φ, with respect to a static magnetic field, $\mathbf{B}_0$.

The energy separations between these levels, ΔE, can be expressed as a function of two parameters, the deuterium nuclear quadrupolar coupling constant, $\frac{e^2qQ}{h}$, and the asymmetry parameter, η (a measure of the difference between the minor components, eq_{xx} and eq_{yy} of the EFG tensor).

$$\Delta E = \frac{e^2qQ}{h}(3\cos^2\theta - 1 + \eta\sin^2\theta\cos 2\phi) \qquad (15)$$

Since allowed transitions are governed by the spectroscopic selection rule $\Delta m = \pm 1$,

the spectrum of a single deuterium nucleus consists of a doublet, with separation $\Delta\nu$ given by:

$$\Delta\nu = |\Delta E_{+1,0}| - |\Delta E_{0,-1}| = \frac{3e^2qQ}{4h}\{3\cos^2\theta - 1 + \eta\sin^2\theta\cos 2\phi\} \qquad (16a)$$

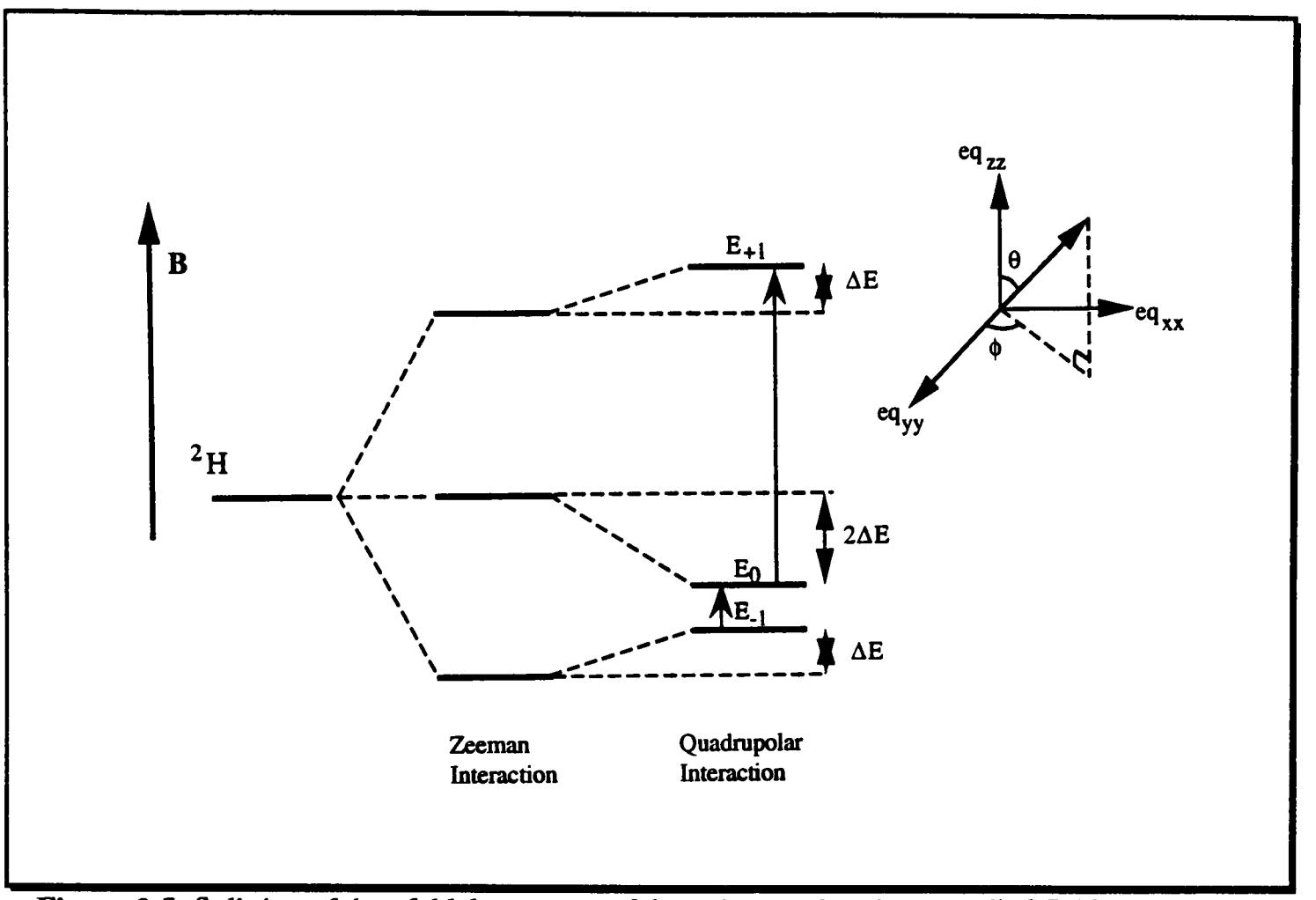

Figure 2.5: Splitting of threefold degeneracy of deuterium nucleus in an applied field. {where $E_{-1} = \gamma(^2H)h\mathbf{B}_0/2\pi + \Delta E$, $E_0 = -2\Delta E$, $E_{+1} = -\gamma(^2H)h\mathbf{B}_0/2\pi + \Delta E$}.

For C-D bonds, the EFG tensor is usually axially symmetric ($eq_{xx} = eq_{yy}$) with its principal component lying along the C-D bond so the expression for $\Delta\nu$ can be simplified:

$$\Delta\nu = \frac{3e^2qQ}{4h}(3\cos^2\theta - 1) \qquad (16b)$$

Hence, for a particular orientation of the C-D bond (or principal component of the EFG tensor), the spectrum shows a doublet with a splitting dependent on θ (the orientation of the C-D bond in the field) and the NQCC. So, for single crystal samples of the type described in this chapter, one can obtain direct information on the orientation of C-D bonds. In contrast, ^{2}H NMR spectra of polycrystalline samples provide a *superposition* of the spectra from all the orientations which are present, the profile being indicative of the extent and rate of motion of the molecular C-D bond.

2.3.1. Effects of Motion on Spectra

Motions with rates comparable to the quadrupolar interaction (10^3-10^7 Hz) partially average the anisotropic EFG tensor, leading to characteristic changes in the ^{2}H NMR profile. For samples whose motions are slow (<10^3 Hz) on the NMR time scale, no

averaging of the EFG tensor occurs, so the spectrum is the same as that for a rigid C-D bond. For molecular motions in the fast exchange limit (>10^8 Hz), the EFG tensor is totally averaged and the spectral profile is characteristic of the averaged tensor components. Between these two extremes, the spectral lineshape can only be determined by explicit calculation of the spin density matrix or Bloch equations modified for molecular dynamics. The spectra are very sensitive to both the rate and nature of motion, showing changes characteristic of these throughout this regime.

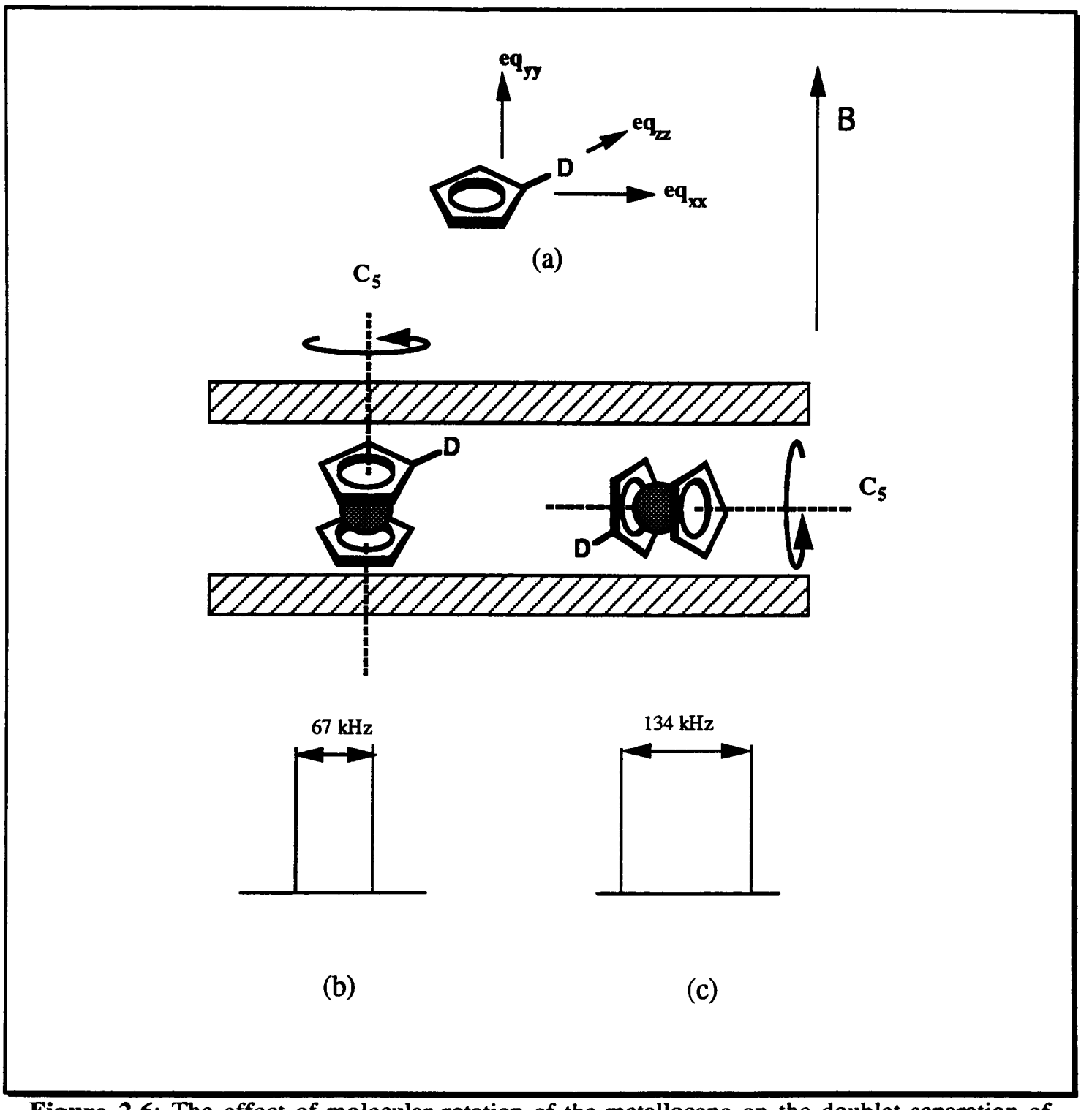

Figure 2.6: The effect of molecular rotation of the metallocene on the doublet separation of deuterium NMR spectra. (a) components of EFG tensor; (b) & (c), doublet splittings expected for ^{2}H NMR for guests oriented as shown in schematic above.

2.4 X-ray and Neutron Diffraction Experiments

The results of one-dimensional analysis performed on diffraction data obtained from ZrS_2 and $SnSe_2$ intercalates are described in this section. The results are preceded

by a description of trial refinements performed in order to verify the accuracy of the refinement program used.

2.4.1. Trial refinements

In order to confirm that using a Bessel function within the refinement program (PJWB) was appropriate for modelling the rapidly rotating Cp rings, the output from two separate input models was compared. The first model (Model A) utilised the Bessel functions to approximate the electron density from the Cp ring as a "doughnut" with a external radius of 1.15Å, while for the second (Model B), the positions of the individual carbon atoms were uniformly staggered in the interlamellar space so that, in essence, a static cobaltocene molecule, with non-eclipsing Cp rings, was used. The two different models are illustrated in the figure below:

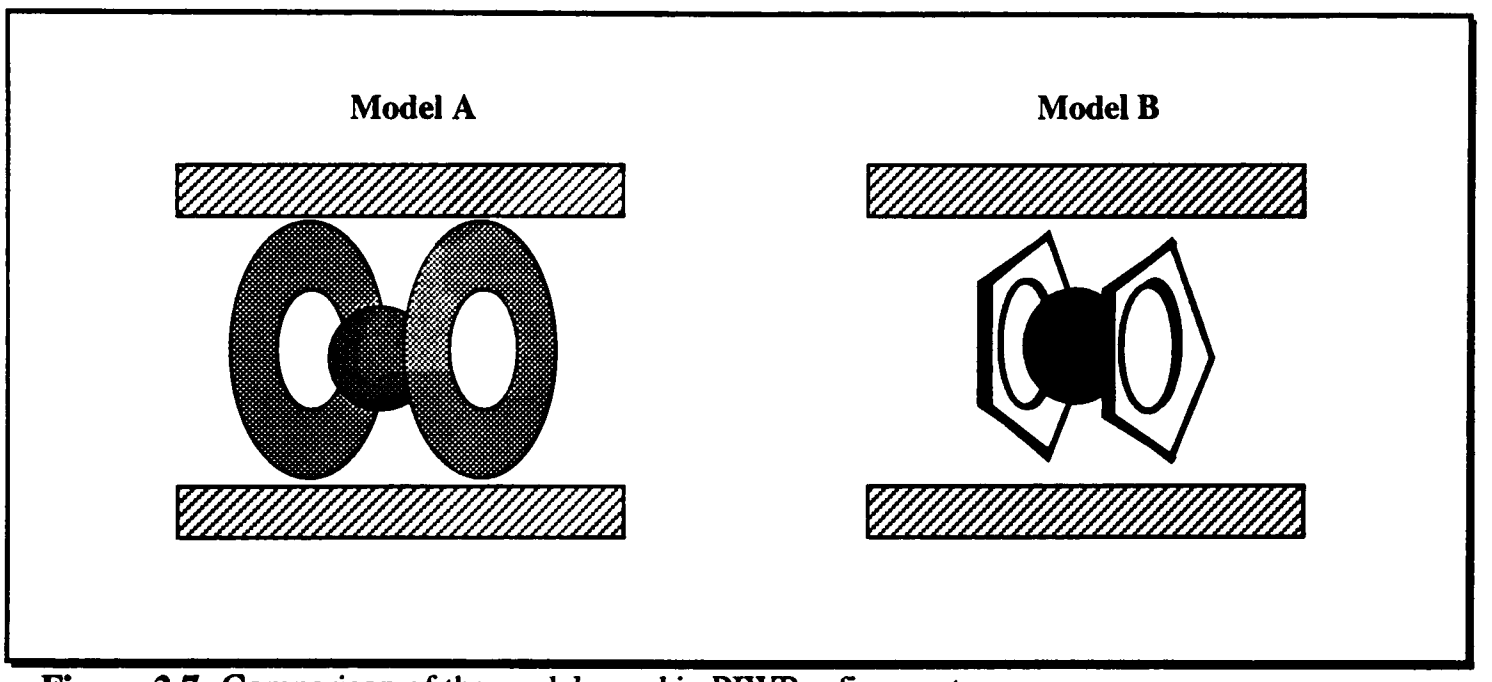

Figure 2.7: Comparison of the models used in PJWB refinements.

A comparison of the calculated structure factors obtained from refinement of the experimental data using the two models described above is shown in Figure 2.8. The good agreement between the output from both models suggests that the use of the Bessel function is an appropriate method for modelling the rapidly rotating carbocyclic rings in the other organometallic intercalates examined.

To confirm the reliability of X-ray data collected on the diffractometer used, intensities of the *00l* reflections for two pristine layered host systems, ZrS_2 and $SnSe_2$, were measured using the protocol described above. Refinement of the data set gave structure factors and relative z-coordinate positions which agree well with the calculated and published[20, 21] values respectively. The comparisons of calculated versus observed structure factors are shown in Figure 2.9, while the calculated one-dimensional electron density along the *c* axis is plotted in Figure 2.10.

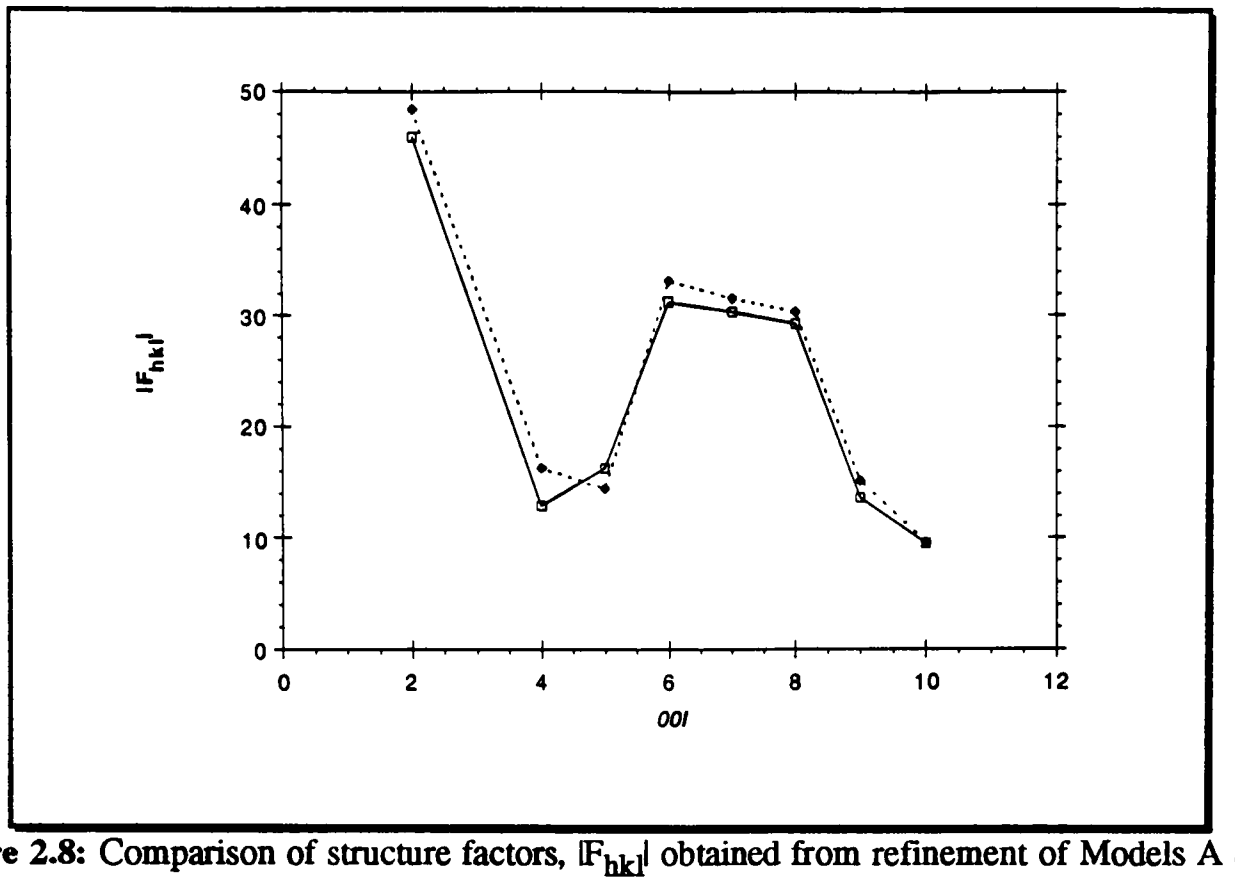

Figure 2.8: Comparison of structure factors, $|F_{hkl}|$ obtained from refinement of Models A & B. Open symbols represent data from Model A and solid symbols represent data from Model B.

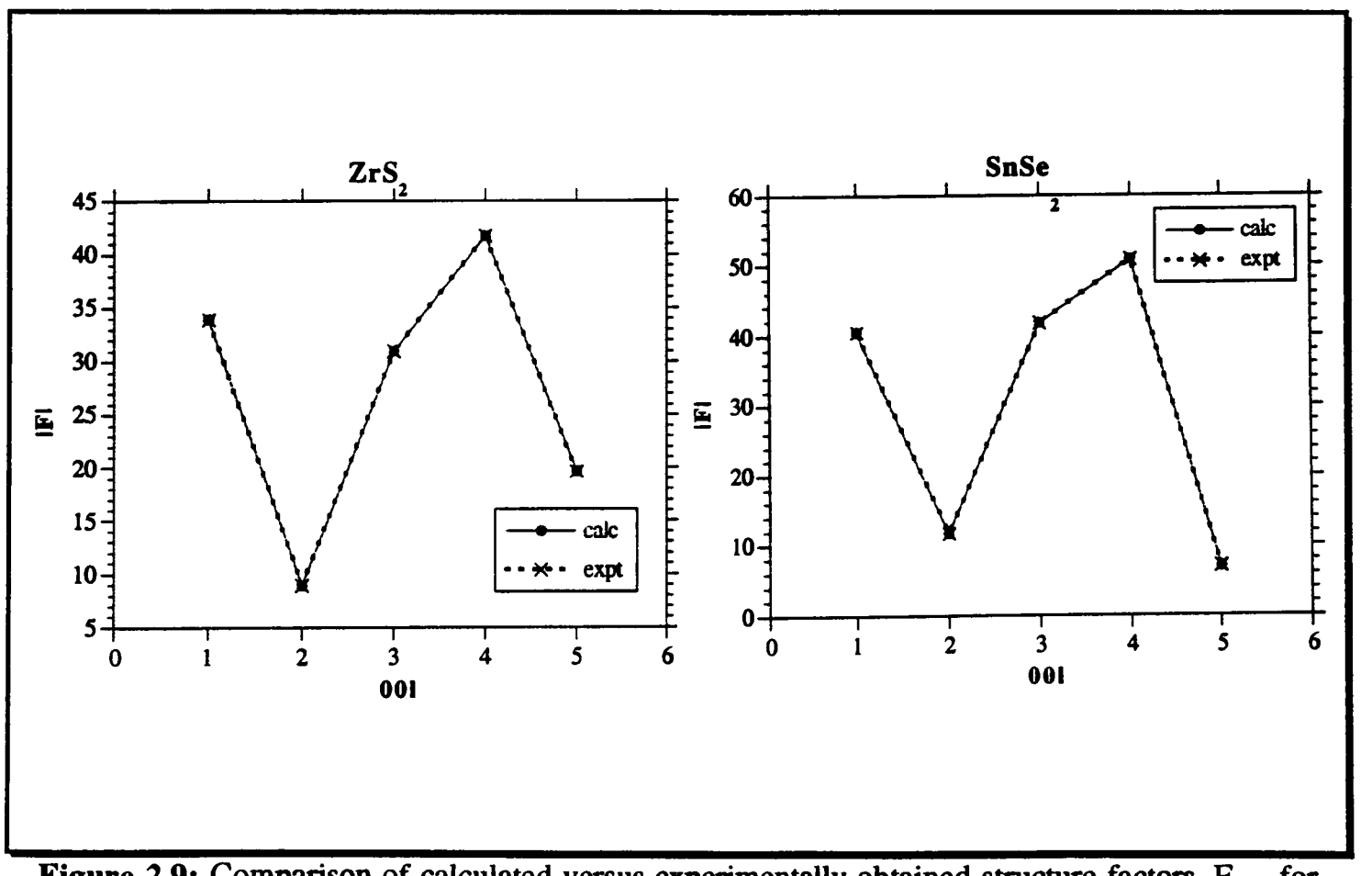

Figure 2.9: Comparison of calculated versus experimentally obtained structure factors, F_{00l} for unintercalated hosts, ZrS_2 and $SnSe_2$. Crosses and solid circles represent experimentally observed and calculated values of |F| respectively.

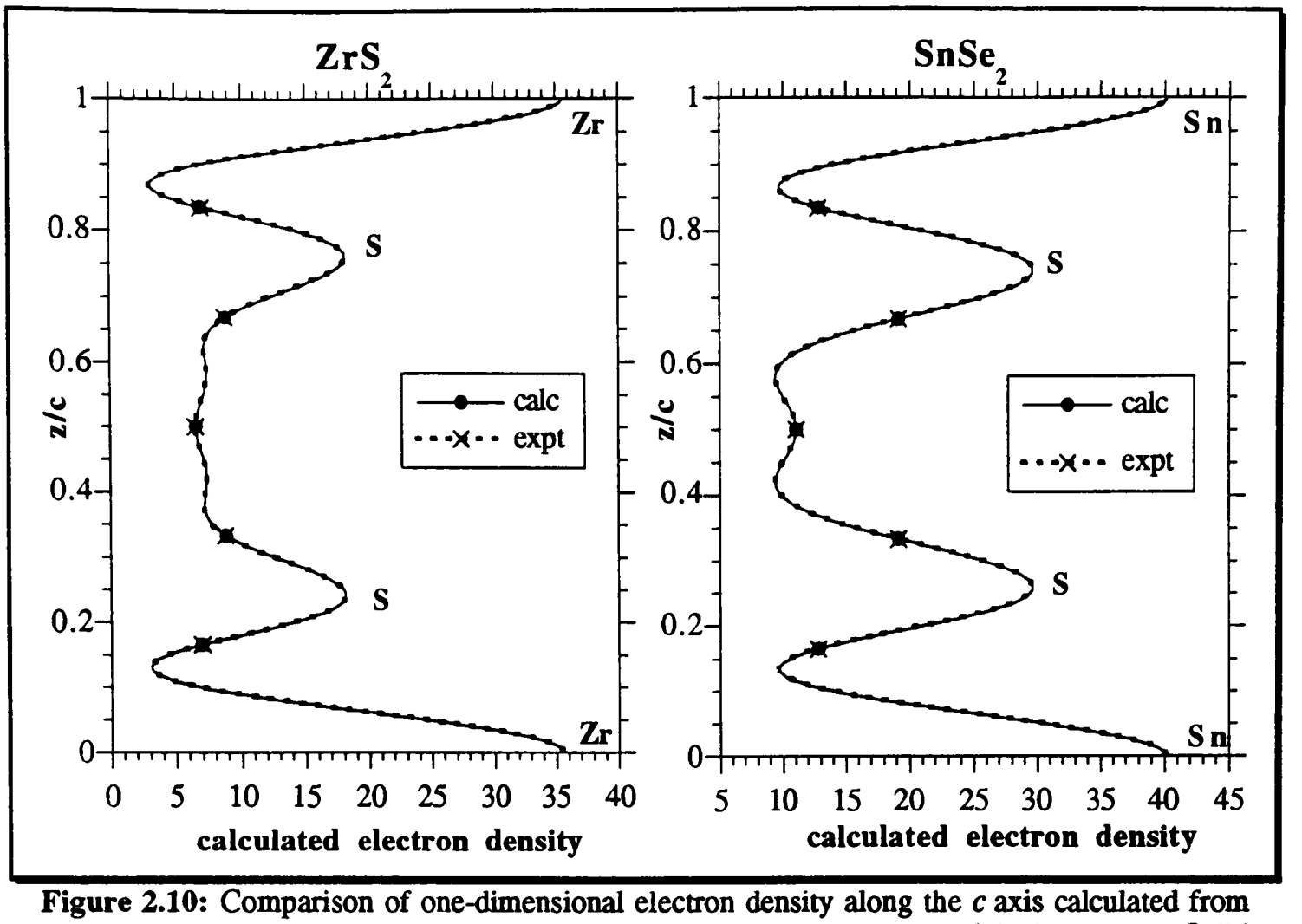

Figure 2.10: Comparison of one-dimensional electron density along the *c* axis calculated from experimental data versus that calculated from known atomic coordinates of the host atoms. Solid and dotted lines represent calculated and experimentally observed values respectively.

2.4.2. Results from the Intercalates

X-ray diffraction spectra of aligned intercalate crystals gave relatively sharp spectra (see Figure 2.11) from which integrated intensities for *00l* reflections up to $l = 10$ could be extracted. The *c* axis dimensions of the intercalates (obtained from least squares analyses of the X-ray data) are tabulated in Table 2.2 with the *c* axis expansion (Δc), stoichiometry and dimensions of the guest molecule. These figures compare favourably with those reported previously [8, 22-24].

Table 2.2: Comparison of lattice expansion along the *c* axis for $SnSe_2$ and ZrS_2 intercalates with the dimensions of guest species; length and width conventions are shown in Figure 2.12.

			Guest Dimensions[c]	
Compound	*c* spacing (Å)[a]	Δc (Å)[b]	length (Å)	width (Å)
$SnSe_2\{Co(\eta\text{-}C_5H_5)_2\}_{0.30}$	11.84(1)	5.70	6.96	6.76
$ZrS_2\{Co(\eta\text{-}C_5H_5)_2\}_{0.25}$	11.23(1)	5.41	6.96	6.76
$ZrS_2\{Cr(\eta\text{-}C_5H_5)_2\}_{0.20}$	11.26(1)	5.43	6.96[d]	6.76[d]
$ZrS_2\{Co(\eta\text{-}C_5H_4\text{-}CH_3)_2\}_{0.20}$	11.27(1)	5.44	6.96[d]	7.38
$ZrS_2\{W(\eta\text{-}C_7H_7)(\eta\text{-}C_5H_4\text{-}CH_3)\}_{0.20}$	11.86(3)	6.03	-	-
$ZrS_2\{Mo(\eta\text{-}C_6H_6)_2\}_{0.20}$	11.71(1)	5.88	7.08	7.23
$ZrS_2\{Ti(\eta\text{-}C_8H_8)(\eta\text{-}C_5H_5)\}_{0.20}$	12.20(1)	6.37	6.97	8.15

[a] obtained by least squares refinement of experimental data; [b] using $c(ZrS_2) = 5.83$ Å, $c(SnSe_2) = 6.14$Å; [c] dimensions of un-ionised guests (see Figure 2.12); [d] based on $Co(\eta\text{-}C_5H_5)_2$ dimensions

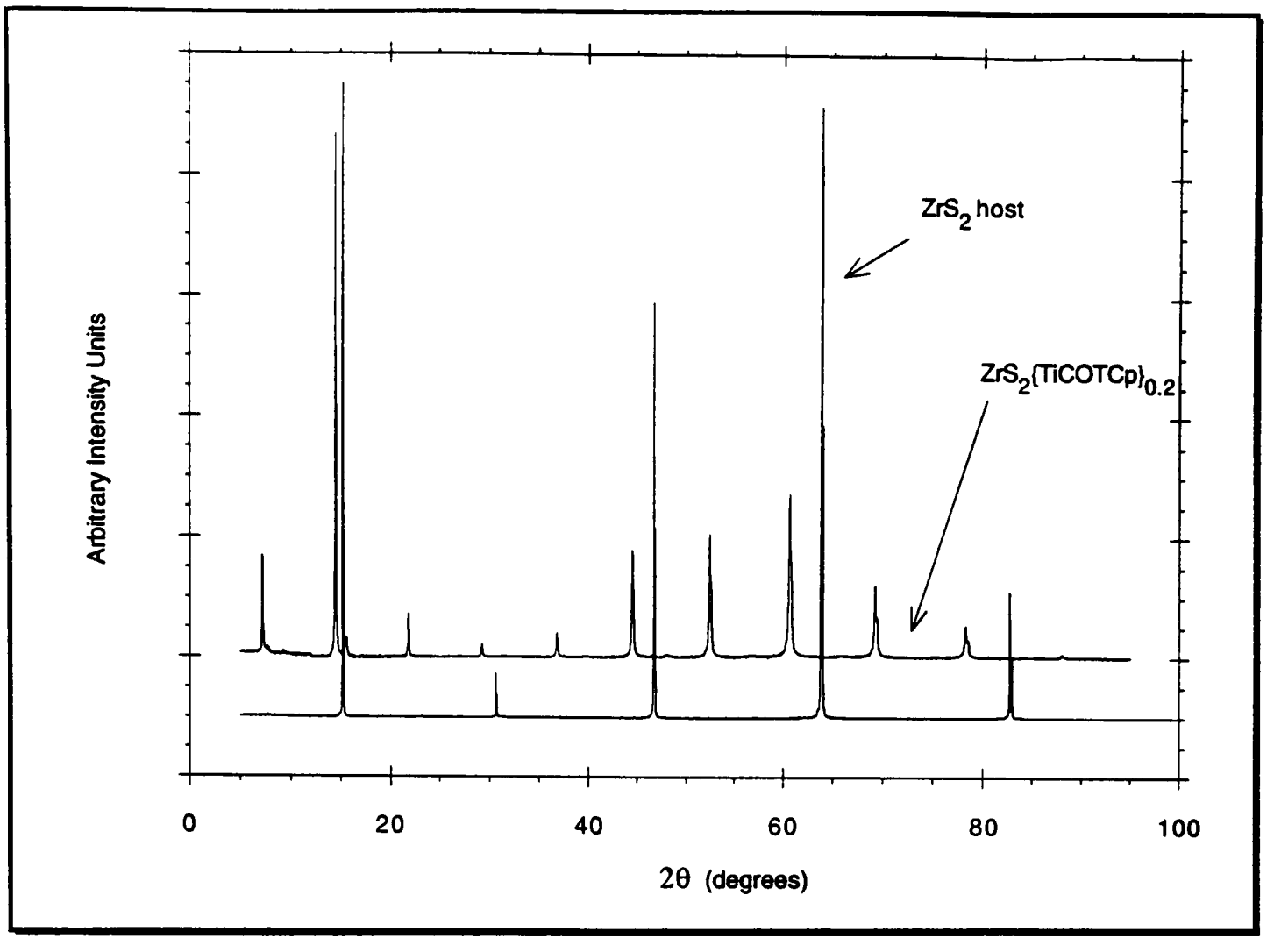

Figure 2.11: X-ray diffraction spectrum of pristine ZrS_2 and $ZrS_2\{TiCotCp\}_{0.2}$.

Neutron data was only obtained for the symmetric metallocene guests $Co(\eta\text{-}C_5D_5)_2$ and $Cr(\eta\text{-}C_5D_5)_2$, given the limited access to neutron beam time and difficulty in obtaining well-deuterated samples of the other organometallic guests. However, X-ray diffraction, which is more readily accessible, was used to study a series of intercalates with varying sizes and geometries, ranging from the almost spherically symmetric $Co(\eta\text{-}C_5H_5)_2$ to the larger and truncated cone-shaped $Ti(\eta\text{-}C_5H_5)(\eta\text{-}C_8H_8)$ (cf. Figure 2.12). The results of both neutron and X-ray refinements are shown in Table 2.3.

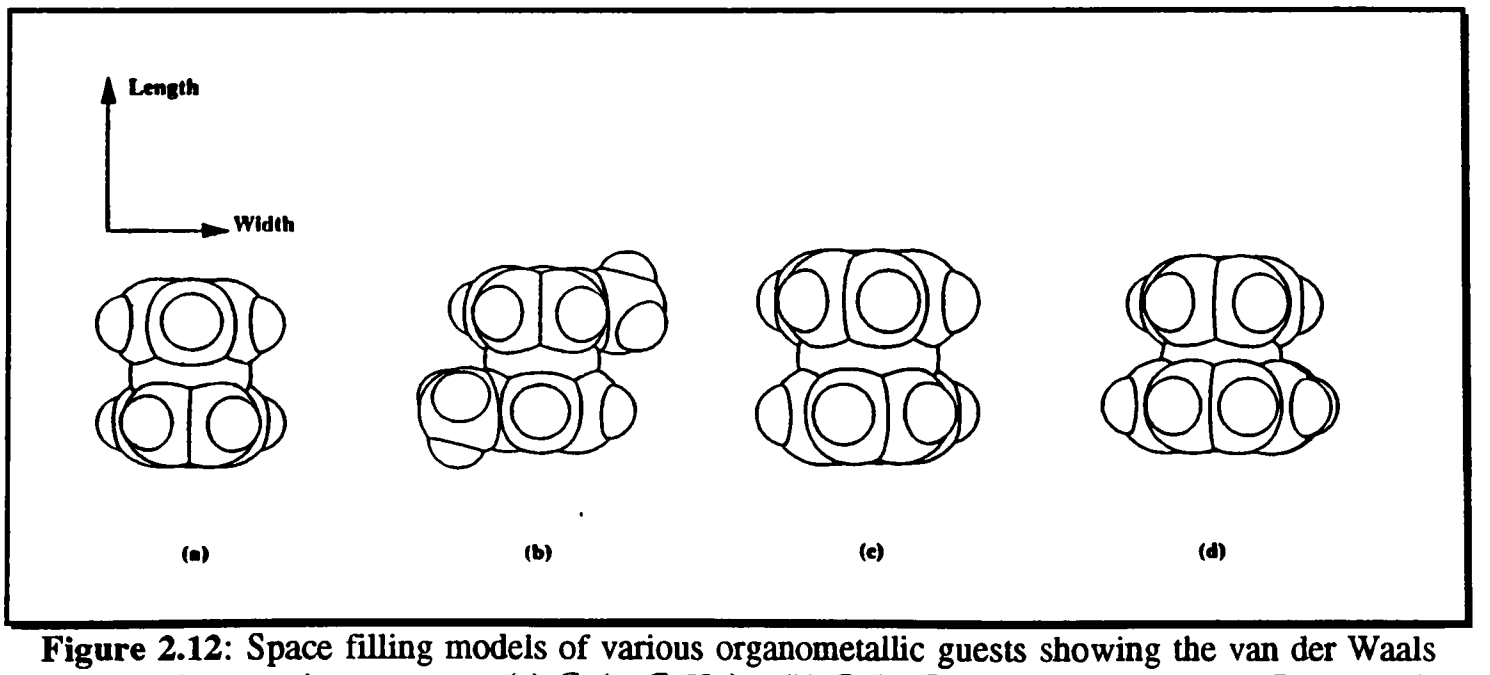

Figure 2.12: Space filling models of various organometallic guests showing the van der Waals radii of the constituent atoms. (a) $Co(\eta\text{-}C_5H_5)_2$, (b) $Co(\eta\text{-}C_5H_4CH_3)_2$, (c) $Mo(\eta\text{-}C_6H_6)_2$ (d) $Ti(\eta\text{-}C_5H_5)(\eta\text{-}C_8H_8)$.

Table 2.3: Summary of occupancy refinements for both X-ray and neutron diffraction data; the R-factor is defined $[\Sigma(I_{obs}- I_{calc})/(\Sigma I_{obs})] \times 100$, where I_{obs} and I_{calc} are the observed and calculated intensities respectively.

Compound	X-Ray					Neutrons				
	S1 coord (z/c)	parallel [a] occupancy	perpend.[a] occupancy	% parallel occupancy	R-factor(%)	S1 coord (z/c)	parallel [a] occupancy	perpend. [a] occupancy	% parallel occupancy	R-factor(%)
$SnSe_2\{Co(C_5H_5)_2\}_{0.30}$	0.134(1)	0.29(2)	0.01(2)	96.7	1.79	0.126(4)	0.291(7)	0.009(7)	97.0	8.15
$ZrS_2\{Co(C_5H_5)_2\}_{0.25}$	0.136(1)	0.24(1)	0.01(1)	96.0	1.42	0.126(4)	0.242(5)	0.008(5)	96.8	5.63
$ZrS_2\{Cr(C_5H_5)_2\}_{0.20}$	0.137(.4)	0.18(1)	0.02(1)	90.0	1.28	0.129(4)	0.202(8)	-0.002(8)	100.0	5.05
$ZrS_2\{Co(C_5H_4CH_3)_2\}_{0.20}$	0.135(1)	0.17(2)	0.03(2)	85.0	3.39					
$ZrS_2\{W(C_7H_7)(C_5H_4CH_3\}_{0.20}$	0.133(2)	0.16(5)	0.04(5)	80.0	3.51					
$SnS_2\{W(C_7H_7)(C_5H_4CH_3\}_{0.30}$	0.133(3)	0.21(3)	0.09(3)	70.0	5.20					
$ZrS_2\{Mo(C_6H_6)_2\}_{0.20}$	0.122(2)	0.19(2)	0.01(2)	95.0	2.70					
$ZrS_2\{Ti(C_8H_8)(C_5H_5\}_{0.20}$	0.122(.2)	0.19(1)	0.01(1)	95.0	1.06					

parallel and *perpendicular* refer to orientations in which the metal-ring centroid axis lies parallel or perpendicular to the layers respectively.

2.4.3. Discussion

Comparison of the observed and calculated scattering factors, as shown in Figure 2.13, demonstrates the excellent level of agreement between our experimental data and that determined from a model in which all the cobaltocene molecules were oriented with their C_5 axes parallel to the host layers (the "parallel" orientation).

The standard deviations on the refined X-ray and neutron data indicate that occupancy refinement tends to be more accurate using neutron data, while the relative S coordinates along the z-axis are more precisely determined by using X-ray data refinement. This difference can be rationalized by examining the relative contributions of the guest molecule toward the overall X-ray or neutron diffraction intensity in some ZrS_2 intercalates (see Table 2.4 and 2.5).

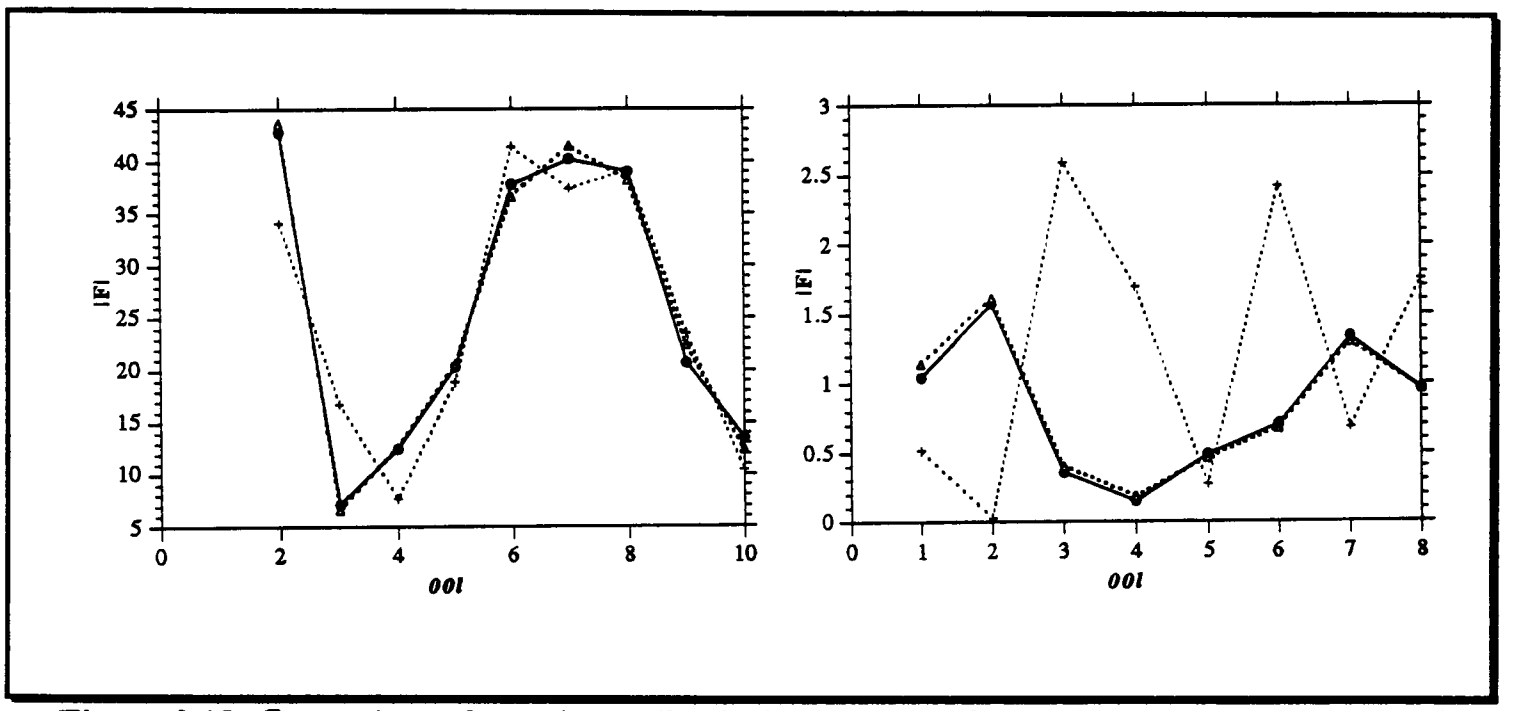

Figure 2.13: Comparison of experimentally obtained structure factors (•) versus those calculated from models in which the guests were assumed to be in one of two extreme orientations, that is, with the principal molecular axis parallel (Δ) and perpendicular (+) to the host layers. X-ray data (left) and neutron data (right) for $ZrS_2\{Cr(\eta\text{-}C_5H_5)_2\}_{0.2}$ and $ZrS_2\{Cr(\eta\text{-}C_5D_5)_2\}_{0.2}$ respectively.

Table 2.4: Relative contribution by guest molecule to overall diffraction in $ZrS_2\{G\}_x$ by X-rays.

Guest, G	Atomic No.	stoichiometry, x	% contribution
$Co(\eta\text{-}C_5H_5)_2$	97	0.25	25.2
$Cr(\eta\text{-}C_5H_5)_2$	94	0.20	20.7
$Co(\eta\text{-}C_5H_4\text{-}CH_3)_2$	113	0.20	23.9
$Mo(\eta\text{-}C_6H_6)_2$	126	0.30	34.4
$Ti(\eta\text{-}C_8H_8)(\eta\text{-}C_5H_5)$	113	0.25	28.2

Table 2.5: Relative contribution by guest molecule to overall diffraction in $ZrS_2\{G\}_x$ by neutrons.

Guest, G	Sum of Neutron Scattering Lengths (10^{-12} cm)	stoichiometry, x	% contribution
$Co(\eta\text{-}C_5D_5)_2$	13.575	0.25	72.5
$Cr(\eta\text{-}C_5D_5)_2$	13.6855	0.20	68.0
$Co(\eta\text{-}C_5D_4\text{-}CD_3)_2$	17.5742	0.20	73.2
$Mo(\eta\text{-}C_6D_6)_2$	16.681	0.30	79.6
$Ti(\eta\text{-}C_8D_8)(\eta\text{-}C_5D_5)$	16.9748	0.25	76.8

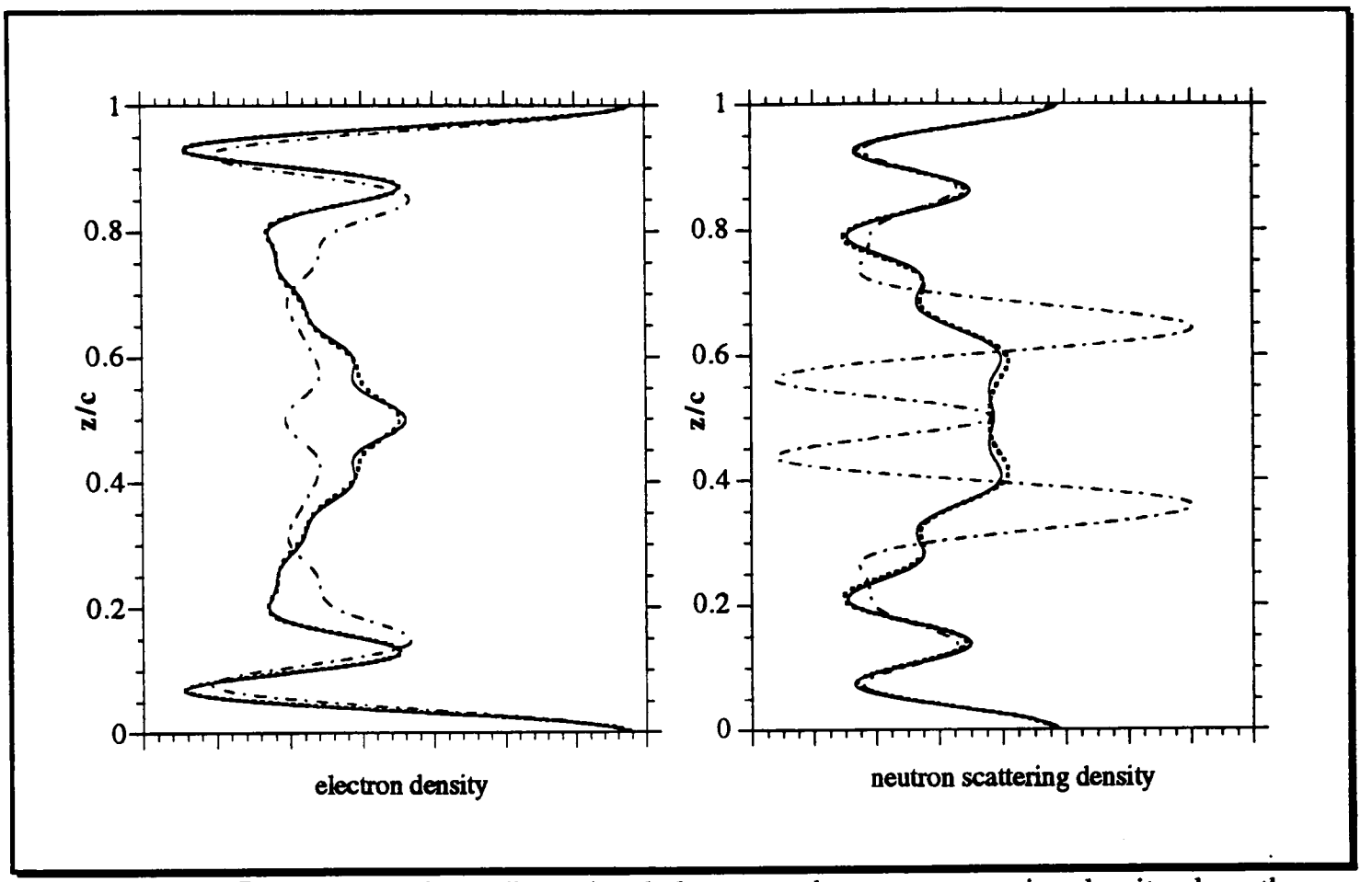

Figure 2.14: Comparison of one-dimensional electron and neutron scattering density along the *c* axis calculated from experimental data (——) versus those calculated from models in which the guests were assumed to be in one of two extreme orientations, that is, with the principal molecular axis parallel (- - - -) and perpendicular (– . – . –) .to the host layers. X-ray data (left) and neutron data (right) for $ZrS_2\{Cr(\eta\text{-}C_5H_5)_2\}_{0.2}$ and $ZrS_2\{Cr(\eta\text{-}C_5D_5)_2\}_{0.2}$ respectively.

In neutron diffraction, the deuterocarbon component of guest molecules dominate the overall scattering, making it a much more sensitive probe of guest orientation. In contrast, X-rays are predominantly scattered by the ZrS_2 or $SnSe_2$ host and are therefore a more sensitive indicator of the changes to the S coordinates. However, while X-ray diffraction is a less discriminating probe of guest structure than neutron diffraction, comparison of results for $Co(\eta\text{-}C_5H_5)_2$ and $Cr(\eta\text{-}C_5H_5)_2$ in Table 2.3 data shows it is still a *qualitatively* good indicator of guest orientation. Both methods indicate that the organometallic guests reside with their metal-ring centroid axis parallel to the host layers. This finding is supported by data in Table 2.2 which show that the *c* axis expansion

increases as a function of the width of the guest, while the length remains essentially constant.

Taken together, the data in Table 2.2 and Table 2.3 allow us to make several observations about the guest orientations and packing between the layers. The dimensions of $Co(\eta\text{-}C_5H_5)_2$ and $Ti(\eta\text{-}C_5H_5)(\eta\text{-}C_8H_8)$ from ring-centroid to ring-centroid are roughly the same, as are their stoichiometries in the intercalates. Hence the difference in *c* axis expansion can only be due to parallel orientation of guest within host layers. This is confirmed by one-dimensional refinement of the diffraction data in both cases. In contrast, $Co(\eta\text{-}C_5H_5)_2$ and $Cr(\eta\text{-}C_5H_5)_2$ intercalates of ZrS_2 show virtually the same inter-layer expansions. Since they have similar molecular dimensions, the difference in stoichiometry of the intercalates reflects the absence of close packing in $ZrS_2(CrCp_2)_{0.20}$. Since $Co(\eta\text{-}C_5H_4CH_3)_2$ is somewhat bigger than $Co(\eta\text{-}C_5H_5)_2$ perpendicular to the metal-to-ring centroid axis, it might be expected to induce a significantly larger interlayer expansion upon intercalation into ZrS_2. The absence of such a larger expansion and its lower guest stoichiometry in the intercalate suggest that the methyl substituents lie between the sulphur layers, making their effective "width" the same as $Co(\eta\text{-}C_5H_5)_2$ (see Figure 2.15).

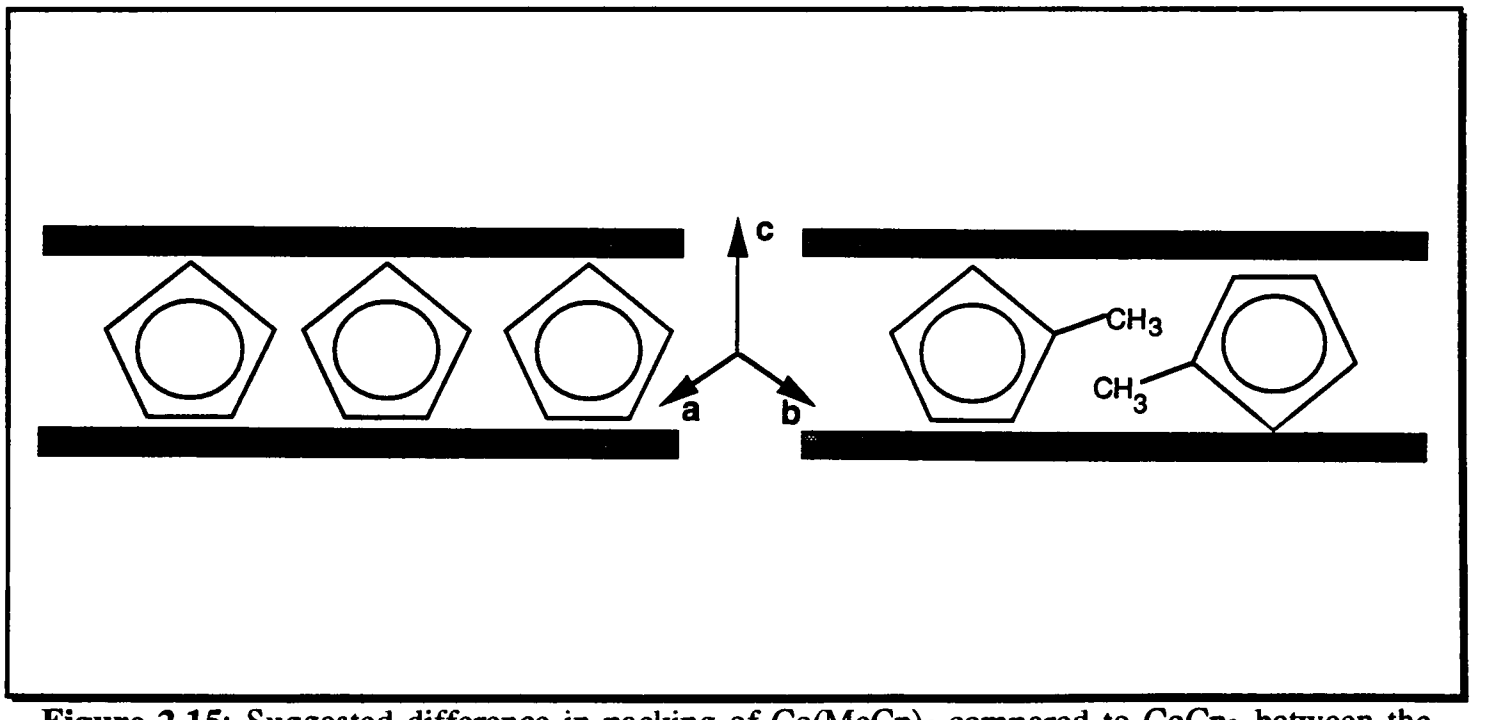

Figure 2.15: Suggested difference in packing of $Co(MeCp)_2$ compared to $CoCp_2$ between the layers.

An observation common to all the intercalates studied is that the lattice expansion is somewhat smaller than the van der Waals dimensions of the guest molecules (Table 2.2). The origin of this discrepancy can be ascribed to one of two reasons, or possibly a combination of both:

(a) since the organometallic guests are ionised upon intercalation into the lattice, there is a net positive charge on the metal centre which causes a contraction of the molecule and hence a reduction in its effective van der Waals dimensions.

(b) there may be some inter-penetration of the C-H or C-D bonds of the carbocylic rings into the chalcogen layers, so that the lattice need not expand by the full van der Waals width of the guest molecule.

The guest organometallic sandwich complexes in the intercalates examined were found, within the experimental uncertainty of the refinements, to adopt an orientation in which the principal molecular axis lies parallel to the *ab* plane of the host crystal. These findings corroborate those of O'Hare *et al.*[10] in $SnS_2(CoCp_2)_{0.3}$ as well as of Davies[24] for ZrS_2 intercalated with mixed ring chromium sandwich complexes. Although there exists an apparent discrepancy between our results and those of Clement *et al.*[25] for the substituted bis(arene) molybdenum intercalates of ZrS_2, Evans[26] has recently shown that this may be due to dynamical *re-orientation* of the guest species *after* intercalation. Moreover, the orientation in which the plane of the carbocyclic ring lies perpendicular to the host layers is similar to that adopted by pyridine when it is intercalated into 2H-TaS_2[27] and NbS_2[28].

The orientational preference of the amines in the interlayer space is thought to arise from intralayer guest-guest interactions of two types[29]:

(a) hydrogen bonding between pyridine and pyridinium species (the latter being formed by oxidation of pyridine to N_2 and H^+ upon intercalation).

(b) π-π interactions between adjacent aromatic rings.

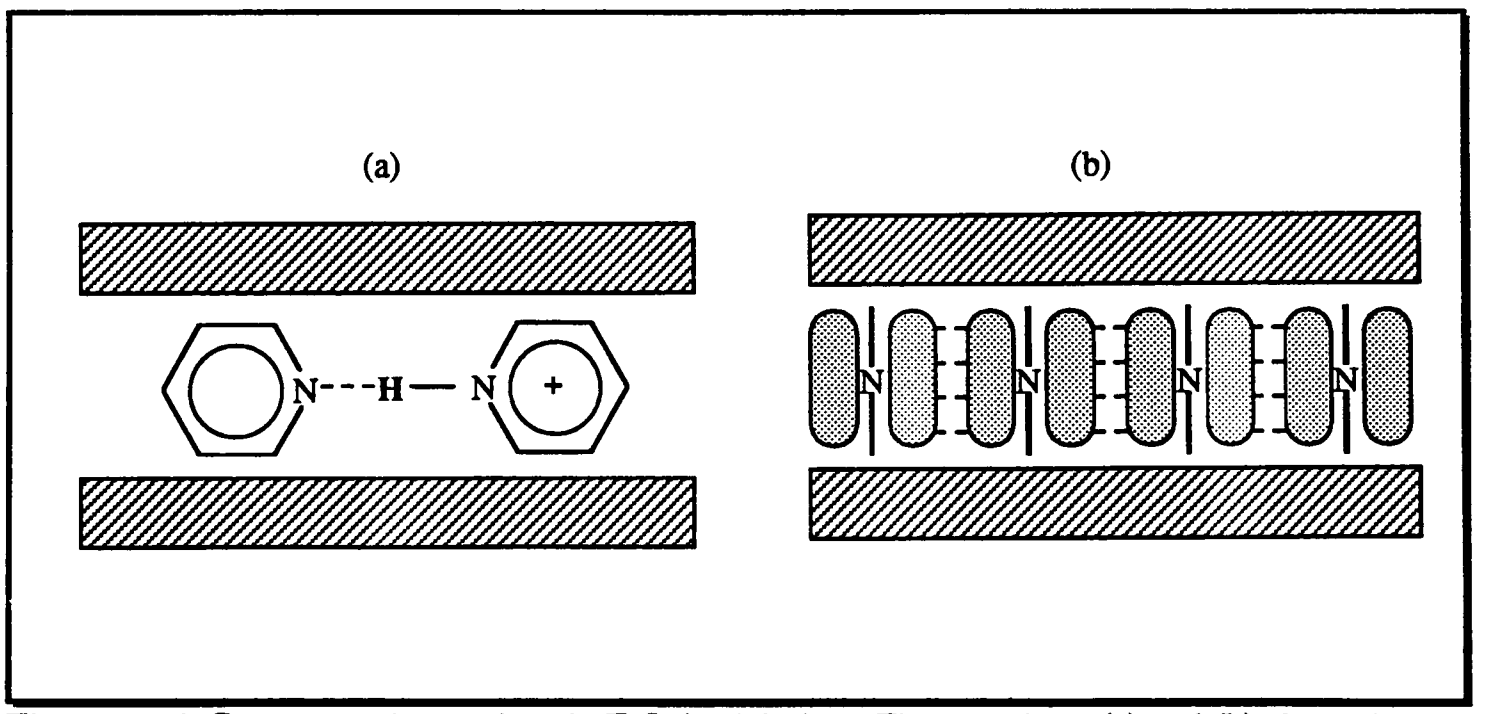

Figure 2.16: Guest-guest interactions in $TaS_2(pyridine)_{0.5}$. The two views (a) and (b) shown in the figure are related to each other by a 90° rotation along an axis perpendicular to the layers. The delocalised π orbitals above and below the pyridine rings are depicted as shaded ovals and the ring plane as a thick black line. Dotted lines show the suggested π–π interactions.

Although hydrogen bonding interactions of the type shown in Figure 2.16(a) are not present in the organometallic intercalates of the metal dichalcogenides, the extra stability conferred by the type of π–π interactions shown in Figure 2.16(b) may be an

important determinant of guest orientation in these systems. It is important, however, not to ignore other considerations which may affect this disposition of the guest, such as the interactions which exist between the guest molecules and the layers of chalcogen atoms. The original view which held that these guest-host interactions would principally determine the ultimate orientation of the guests has since been discredited by the contradictory evidence in pyridine, amine and organometallic intercalates. Nevertheless, the proximity of guest to host atoms, as well as the charge separation which exists between them, is likely to influence the guest orientation to some extent. The influence of guest-host relative to guest-guest interactions may serve to explain the small deviations from the parallel orientation observed in the intercalates of this chapter, as well as the few reports of organometallic sandwich complexes adopting the parallel orientation in ZrS_2[24] and TaS_2[12].

2.5 ^{2}H-NMR Spectroscopy Experiments

To confirm the orientation of $CoCp_2$ deduced by X-ray and neutron diffraction analysis, ^{2}H NMR spectra of $SnSe_2\{Co(\eta\text{-}C_5D_5)_2\}_{0.3}$ and $ZrS_2\{Co(\eta\text{-}C_5D_5)_2\}_{0.25}$ were recorded. The crystals were selected by examination under an optical microscope mounted within a glove box; only crystals with no visible physical defects (i.e., cracks, twinning, etc.) were mounted and sealed in NMR tubes under a nitrogen atmosphere. Spectra for both $SnSe_2\{Co(\eta\text{-}C_5D_5)_2\}_{0.3}$ and $ZrS_2\{Co(\eta\text{-}C_5D_5)_2\}_{0.25}$ were recorded at room temperature with the crystal layers (*ab* plane) oriented perpendicular to the magnetic field.

The ^{2}H NMR spectra for crystals oriented with their planes perpendicular to the applied magnetic field $\mathbf{B}_0$ are shown in figure 2.17. Both spectra show a single doublet with a splitting of 67 kHz. Previous work on polycrystalline samples of these compounds has established that rapid C_5 ring rotation occurs for the $CoCp_2$ molecules and results in the principal direction of the averaged axially symmetric tensor lying along the principal molecular axis[12, 13, 30]. Therefore, as discussed earlier, the doublet separation seen for a particular orientation of a $Co(\eta\text{-}C_5D_5)_2$ molecule will indicate the orientation of its principal axis. The observed splitting of *ca.* 67 kHz indicates this axis is perpendicular to the field $\mathbf{B}_0$. This means that for both intercalates examined, the principal molecular axis of the intercalated $Co(\eta\text{-}C_5D_5)_2$ molecules all lie parallel to the layers, as shown in figure 2.18.

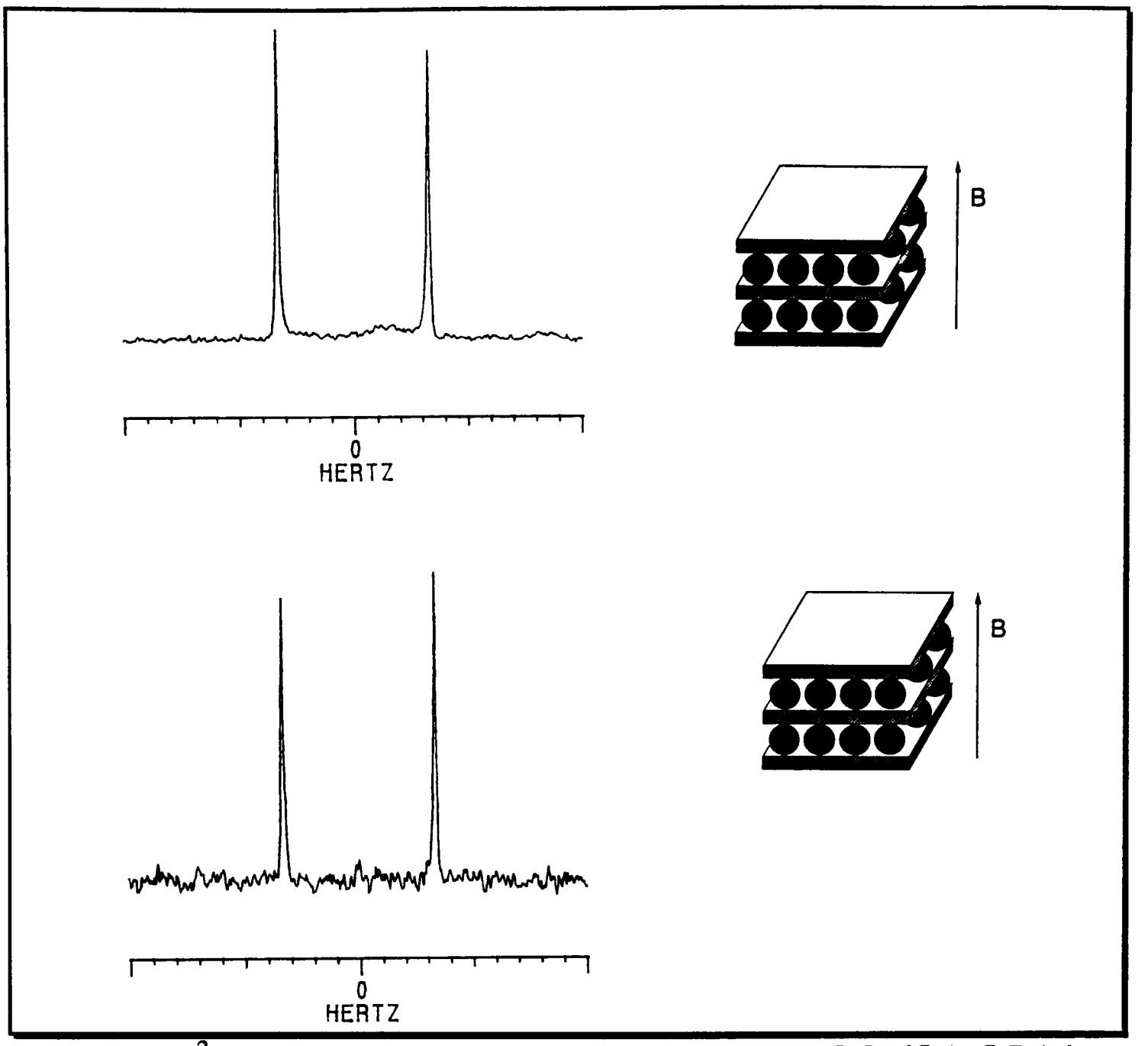

Figure 2.17: ^{2}H NMR spectra of $ZrS_2\{Co(\eta\text{-}C_5D_5)_2\}_{0.25}$ (top) and $SnSe_2\{Co(\eta\text{-}C_5D_5)_2\}_{0.3}$ (bottom) oriented with their layer planes perpendicular to the magnetic field.

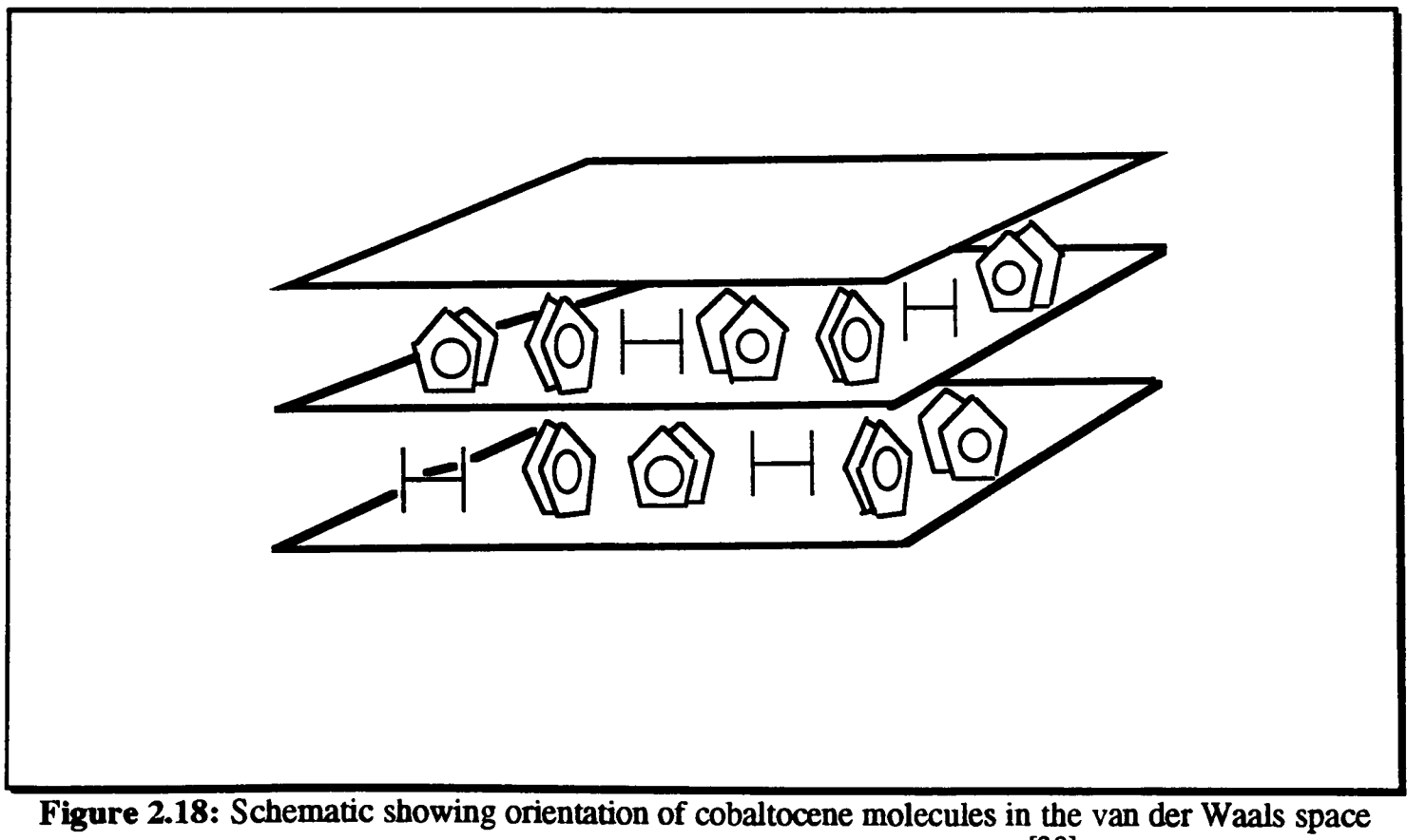

Figure 2.18: Schematic showing orientation of cobaltocene molecules in the van der Waals space that is consistent with the observed NMR spectra (courtesy of Sue Mason[30]).

Similar observations on the orientation of $CoCp_2$ in metal dichalcogenides have been made in the ^2H NMR studies of $SnS_2(CoCp_2)_{0.3}$[10, 13] and $TaS_2(CoCp_2)_{0.25}$,[12]. For $TaS_2(CoCp_2)_{0.25}$ however, a second orientation of $CoCp_2$ where the C_5 molecular axis is oriented perpendicular to the host layers was also observed.

More recently, further ^2H NMR spectroscopy investigations of crystals oriented with their layers parallel to the field have shown that there are six different orientations for d^{10}-$CoCp_2$ molecules between the layers[30]. The angular relationships of these have been explained by the possible presence of three domains. Within each of these domains, there are two orientations of cobaltocene, related to each other by a 85° rotation. Each domain is thought to be present throughout a layer, with different domains represented in different layers.

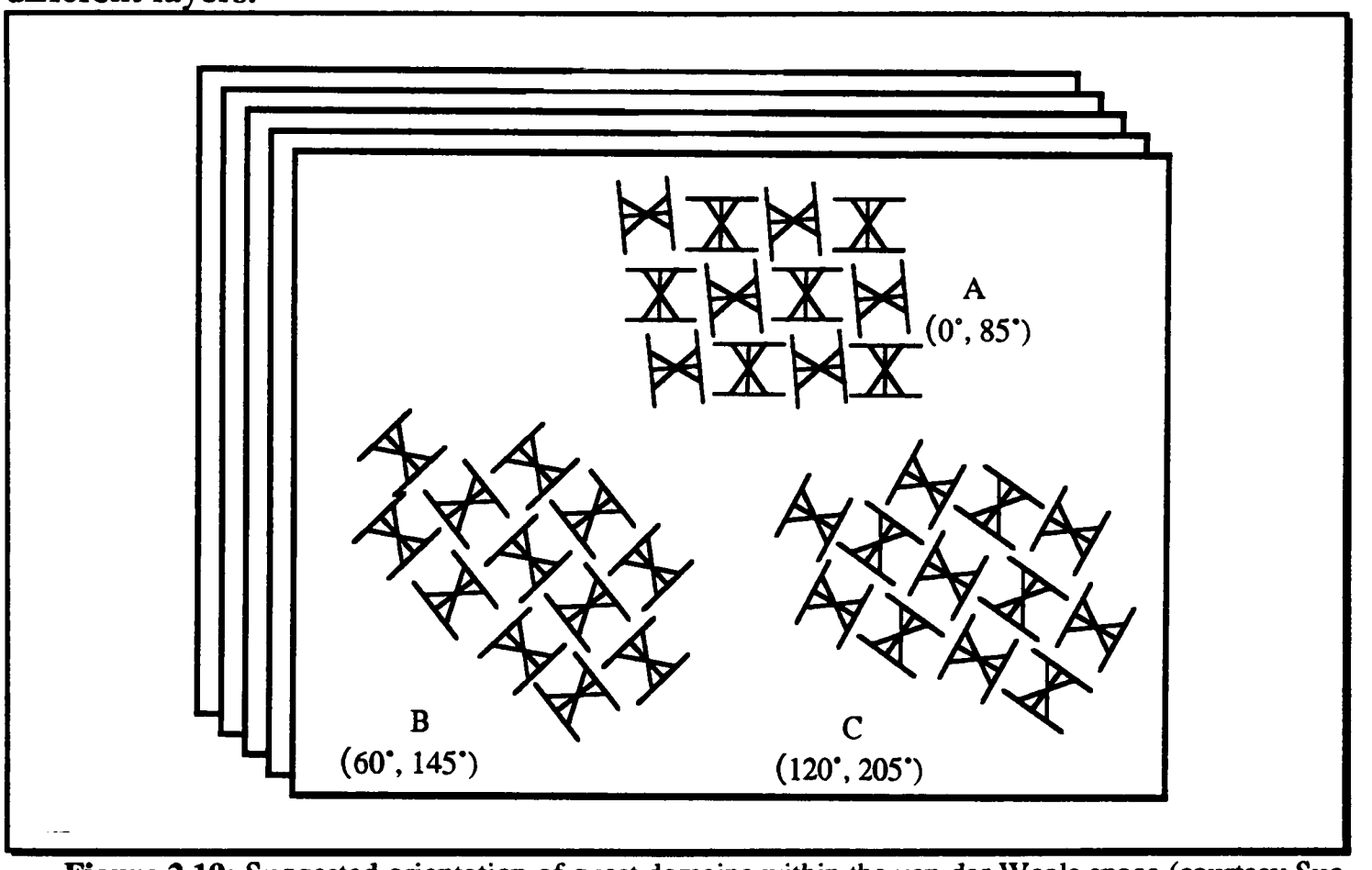

Figure 2.19: Suggested orientation of guest domains within the van der Waals space (courtesy Sue Mason[30]).

2.6 Conclusion

Both techniques (diffraction and ^2H NMR spectroscopy) employed to study the single crystal intercalates provide a means of discerning the guest orientation in the van der Waals space between the host layers. ^2H NMR spectroscopy probes all the nuclei in the sample, while X-ray and neutron diffraction data represents an average of all environments present.

Diffraction experiments using oriented crystals of the intercalate require smaller sample sizes than powder diffraction experiments, but the crystals must be of good quality. Neutron diffraction, because of the low flux of the neutron beam, requires significantly more sample than a X-ray experiment, but has the advantage that neutron scattering is dominated by the guest molecules, making it a more discriminating

technique for studying guest orientation. However, the need for highly deuterated samples in order to reduce the incoherent scattering from hydrogen atoms limits the use of neutron diffraction to samples in which deuteration can be carried out on a gram scale. Nonetheless, from the ease of data collection and reduction developed in this chapter, diffraction techniques should prove to be a versatile and powerful technique in studying layered intercalates.

Solid state ^2H NMR spectroscopy, while a more sensitive technique requiring only a *single* crystal, relies on dynamics of the guest molecules so that crystal defects such as twinning can affect the spectra and hence the interpretation of guest orientations present. As such, careful selection of crystals is required. ^2H NMR spectroscopy was employed in this work to corroborate the results of the diffraction experiments as well as to ascertain some of the dynamics present in these intercalates. However, as alluded to in the previous section, solid state deuterium NMR spectroscopy is an extremely powerful technique which can yield significantly more structural information than had previously been thought possible[30]. Thus, although it is a difficult technique since experimental set-up, data acquisition and analysis require specialist skills, its sensitivity allows the chemist to extract much more information about the guest, including dynamics as well as their disposition relative to the host layer atoms.

In conclusion, an array of organometallic guest molecules with varying sizes and geometry has been intercalated into single crystals of ZrS_2. These crystals, along with $SnSe_2\{Co(\eta\text{-}C_5H_5)_2\}_{0.3}$, have been examined by X-ray and neutron diffraction in order to extract information as to the nature of the guest orientation between the layers. While the neutron data conclusively demonstrate that both $Co(\eta\text{-}C_5H_5)_2$ and $Cr(\eta\text{-}C_5H_5)_2$ exist virtually exclusively in an orientation with their principal molecular axes parallel to the layers, we have shown that X-ray diffraction is a more convenient, albeit less discriminating, probe of the guest disposition between the dichalcogenide layers. The ease of employing one-dimensional X-ray diffraction analysis on non-deuterated crystal samples has been exploited to show that this parallel orientation is also the preferred one in several other intercalates of ZrS_2. The findings of one-dimensional X-ray and neutron diffraction analysis with regard to guest orientation have been confirmed by ^2H NMR spectroscopy on single crystals of deuterated cobaltocene intercalates of ZrS_2 and $SnSe_2$.

References:

1. F. J. DiSalvo, *J. Low Temp. Phys.* (1974), **3**, 417-427.

2. A. H. Thompson, F. R. Gamble and R. F. Koehler, *Phys. Rev. B* (1972), **5**, 2811-2816.

3. W. Biberacher and A. Lerf, *Mol. Cryst. Liq. Cryst.* (1985), **121**, 149-152.

4. T. H. Geballe, A. Menth, F. J. DiSalvo and F. R. Gamble, *Phys. Rev. Lett* (1971), **27**, 314-316.

5. G. R. Miller, *Colloids and Surfaces* (1990), **45**, 243-250.

6. J. M. Vandenberg-Voorhoeve, in *Optical and Electrical Properties*, ed. P. A. Lee, D. Reidel Publishing Company: Dordrecht-Holland, 1976, p. 423-457

7. D. C. Johnston, *Solid State Comms.* (1982), **43**, 533-536.

8. C. A. Formstone, M. Kurmoo, E. T. Fitzgerald, P. A. Cox and D. O'Hare, *J. Mater. Chem.* (1991), **1**, 51-57.

9. D. E. Prober, R. E. Schwall and M. R. Beasley, *Phys. Rev. B* (1980), **21**, 2717-2733.

10. D. O'Hare, J. S. O. Evans, P. J. Wiseman and C. K. Prout, *Angew. Chemie - Int. Ed. in English* (1991), **30**, 1156-1158.

11. L. F. Nazar and A. J. Jacobson, *J. Chem. Soc. - Chem. Comm.* (1986), 570-571.

12. S. J. Heyes, N. J. Clayden, C. M. Dobson, M. L. H. Green and P. J. Wiseman, *J. Chem. Soc., Chem. Comm.* (1987), 1560-1562.

13. C. Grey, J. S. O. Evans, D. O'Hare and S. Heyes, *J. Chem. Soc., Chem Comm.* (1991), 1380-1382.

14. D. O'Hare, H. V. Wong, S. Hazell and J. W. Hodby, *Adv. Mater.* (1992), **4**, 658-660.

15. G. E. Bacon, *Netron Diffraction*, Clarendon Press: Oxford, 1962.

16. P. J. Wiseman, *PJWB*, Oxford, 1987.

17. R. Berglund and J. Tegnefeld, *J. Magnetic Resonance* (1977), **27**, 315.

18. J. W. Emsley, S. K. Khoo and G. R. Luckhurst, *Mol. Phys.* (1979), **37**, 959.

19. H. W. Speiss, *Colloid Polym. Sci.* (1983), **261**, 193.

20. S. LaPlaca, *JCPDF Grant-in-Aid Report* (1959),

21. B. L. Evans and R. A. Hazelwood, *Brit. J. Appl. Physics* (1969), **2**, 1507-1516.

22. L. Benes, J. Votinsky, P. Lostak, J. Kalousova and J. Klikorka, *Phys. Stat. Sol. (A)* (1985), **89**, K1-K4.

23. J. Votinsky, L. Benes, J. Kalousova, P. Lostak and J. Klikorka, *Chem. Papers* (1988), **42**, 133-137.

24. W. B. Davies, *B. A. (Part II) Thesis*. Oxford University, 1976.

25. R. P. Clement, W. B. Davies, K. A. Ford, M. L. H. Green and A. J. Jacobson, *J. of Mol. Catalysis* (1977/78), **3**, 191-194.

26. J. S. O. Evans, *D. Phil. Thesis*. Oxford University, 1993.

27. C. Riekel, D. Hohlween and R. Schollhorn, *J. Chem. Soc., Chem. Comm.* (1976), 863-4.

28. C. Riekel and R. Schollhorn, *Mat. Res. Bull.* (1976), **11**, 369-376.

29. R. Schollhorn, H. D. Zagefka, T. Butz and A. Lerf, *Mat. Res. Bull.* (1979), **14**, 369-76.

30. S. J. Mason, *D. Phil. Thesis*. Oxford University, 1993.

CHAPTER THREE

ELECTRONIC PROPERTIES

CHAPTER THREE

ELECTRONIC PROPERTIES

3.1. Introduction

As discussed in Chapter One, the electronic properties of layered metal dichalcogenides are modified, often quite dramatically, upon intercalation. Many of these changes can be understood in the context of the Rigid Band Model[1]. Two such properties, electrical conductivity and magnetism, are described briefly in Sections **3.1.1** and **3.1.2**. In anticipation of work described on a superconducting intercalate later in the chapter, some basic principles of superconductivity are also laid out (Section **3.1.3**). Finally, a survey of the recent literature on the electronic properties of metal dichalcogenide intercalates (Section **3.1.4**) creates a contextual framework for the discussions in this chapter.

3.1.1. Conduction in crystalline and non-crystalline systems

Resistivity is a result of deviations from the perfect crystal lattice resulting either from thermal vibrations or from the presence of impurities. For metals, the Bloch-Gruneisen relationship applies[2, 3]:

$$\rho \approx 4\left(\frac{T}{\theta_D}\right)^5 \int_0^{\frac{\theta_D}{T}} \frac{e^x x^5}{\left(e^x - 1\right)^2} dx \qquad (1)$$

where θ_D is the Debye temperature, a measure of the vibrational stiffness of the crystal and $x = (\hbar\omega/k_B T)$. At high temperatures (that is, $T > \theta_D$), $\rho \propto k_B T$, while for $T \rightarrow 0$, $\rho \propto T^5$ and at intermediate temperatures, $\rho \propto T^\nu$, where $1 < \nu < 5$.

Empirically, it has been observed that most metals conform to Matthiesen's rule, whereby the measured resistivity is the sum of temperature independent (ρ_i) and temperature dependent (ρ_L) terms (see equation (2)). ρ_L is the resistivity caused by thermal phonons while ρ_i is the resistivity caused by scattering of the electron waves by static defects that disturb the periodicity of the lattice.

$$\rho = \rho_i + \rho_L \qquad (2)$$

For non-crystalline solids, the resistivity behaviour is more complicated and is treated in greater detail elsewhere[4]. The conductivity, σ (= $1/\rho$), in these solids is often described by the Kubo-Greenwood formula[5, 6]:

$$\sigma = \int \frac{2\pi e^2 \hbar^3}{m^2} |D_E|_{av}^{\ 2} \{N(E)\}^2 \frac{df}{dE} dE \qquad (3)$$

where D_E is the matrix element

$$D_E = \int \psi_{l'} \frac{\partial}{\partial x} \psi_l d^3x$$

for which $\psi_{l'}$ and ψ_l are wave functions of states with energy E and the suffix "av" means an average over all states l and l' with this energy.

The Kubo-Greenwood formulation reduces to that of the Boltzmann type conductivity obtained for metals when the electron mean free path is large in relation to the interatomic spacing ($l > a$). For $l \sim a$, Anderson localisation of the electrons occurs such that states become localised in the tails of the band. The energy separating the localised from the non-localised states is known as the mobility edge.

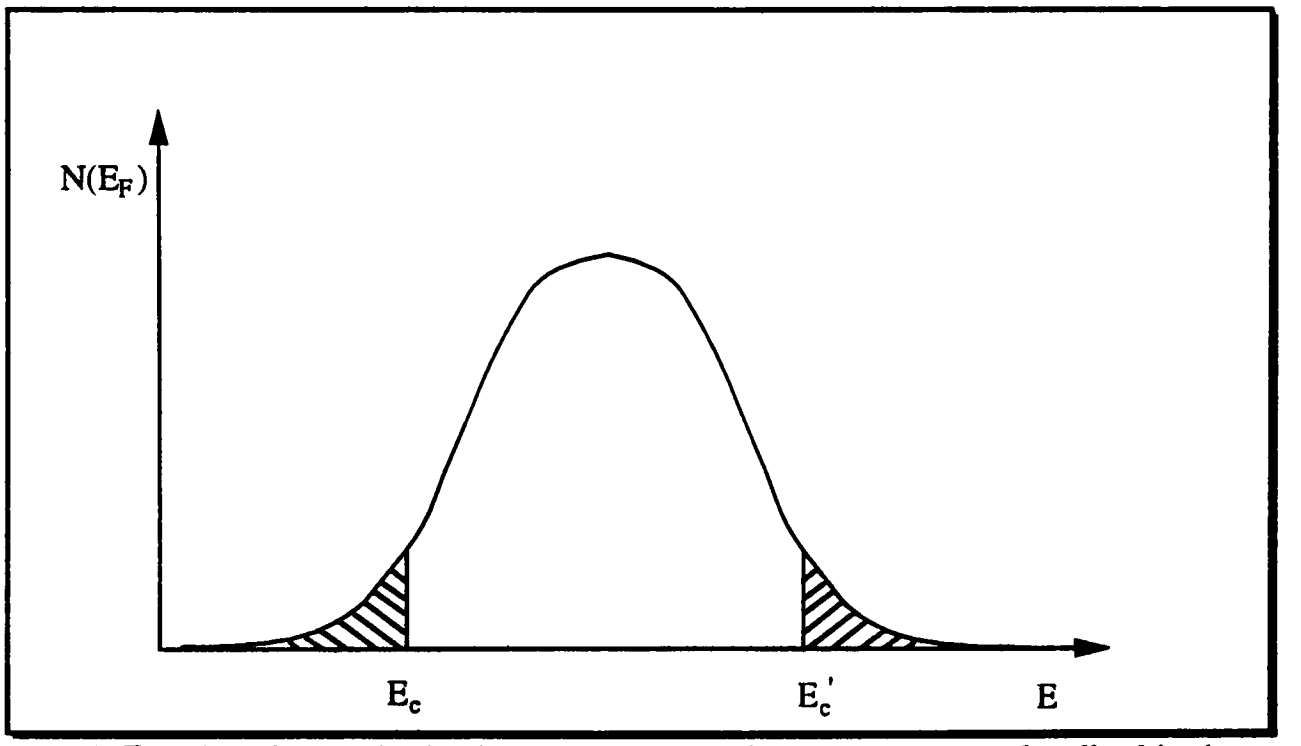

Figure 3.1: Density of states in the Anderson model, where states are non-localised in the centre of the band. Localised states are shaded. E_c and $E_{c'}$ separate localised from non-localised states.

When the electron states at the Fermi energy of an electron gas are localised, two conduction mechanisms are possible:

(a) Excitation of carriers to the mobility edge. Neglecting electron-phonon interactions, the conductivity is of the form:

$$\sigma = \sigma_0 exp\{-(E_C - E_F)/k_B T\} \qquad (4a)$$

(b) Thermally activated hopping mechanisms. The conductivity is of the form:

$$\sigma = A\ exp\{-(T_0/T)^{1/(1+v)}\} \qquad (4b)$$

where v is the dimensionality of the hopping process.

Measurement Considerations for Resistivity

(a) Contact Resistances

When 2 conductors are placed in electrical contact, charge flows between them until the Fermi levels are equalised and they are at the same chemical potential. For metals, this contact potential is concentrated at that point of contact and there is virtually no barrier to electron tunelling. In contrast, for a semiconductor-metal junction, the relatively small number of carriers means that the development of large potential gradients is not possible[7] since

$$\frac{\delta^2 V}{\delta x^2} = \frac{-\rho}{\varepsilon\varepsilon_0} \qquad (5)$$

where ε= relative permitivity of the semiconductor
ε_0 = permittivity of free space (8.854×10^{-12} Fm^{-1})
ρ = charge density
V = potential.

Instead, electrons from the surface region of the semiconductor flow into the metal, leaving a spatially extended "depletion region" through which electrons in the conduction band must tunnel across[8]. This then, gives rise to a large experimentally observed *contact resistance.*

The problem of forming a non-depleted *ohmic* contact with the semiconductor can be overcome by picking metals with the appropriate work function to match that of the semiconductor (high work-function, i.e. gold, for p-type material; low work-function, i.e. Ga-In eutectic for n-type) as the contacts. In reality, however, finding a suitable metal to obtain good ohmic contact is very much a trial and error process.

(b) Electrode Arrangements

If sample resistances are large relative to the contact resistances ($\geq 100\Omega$), then a simple 2-probe meaurement using a multimeter arrangement will suffice. If not, impedance of the leads, contact resistance and various other effects become significant, necessitating the use of a 4-probe technique.

The technique uses 4 electrical leads, 2 each for current and voltage measurements. One pair drive a known current through the sample and the voltage drop induced across the sample is measured between the other 2 leads. The simplest experimental set-up is a linear 4-probe arrangement, illustrated in Figure 3.2.

While simple, this experimental set-up requires that the sample be of a regular shape from which cross-sectional areas and distance between leads can be easily measured. Since this is not always possible, van der Pauw developed an arrangement whereby the conductivity of irregularly shaped crystals of uniform thickness can be measured[9]. Fortuitously, all the samples in this study were flat platelets which could be cut into regular quadrilateral shapes and the simple linear 4-probe electrode arrangement was thus exclusively employed throughout.

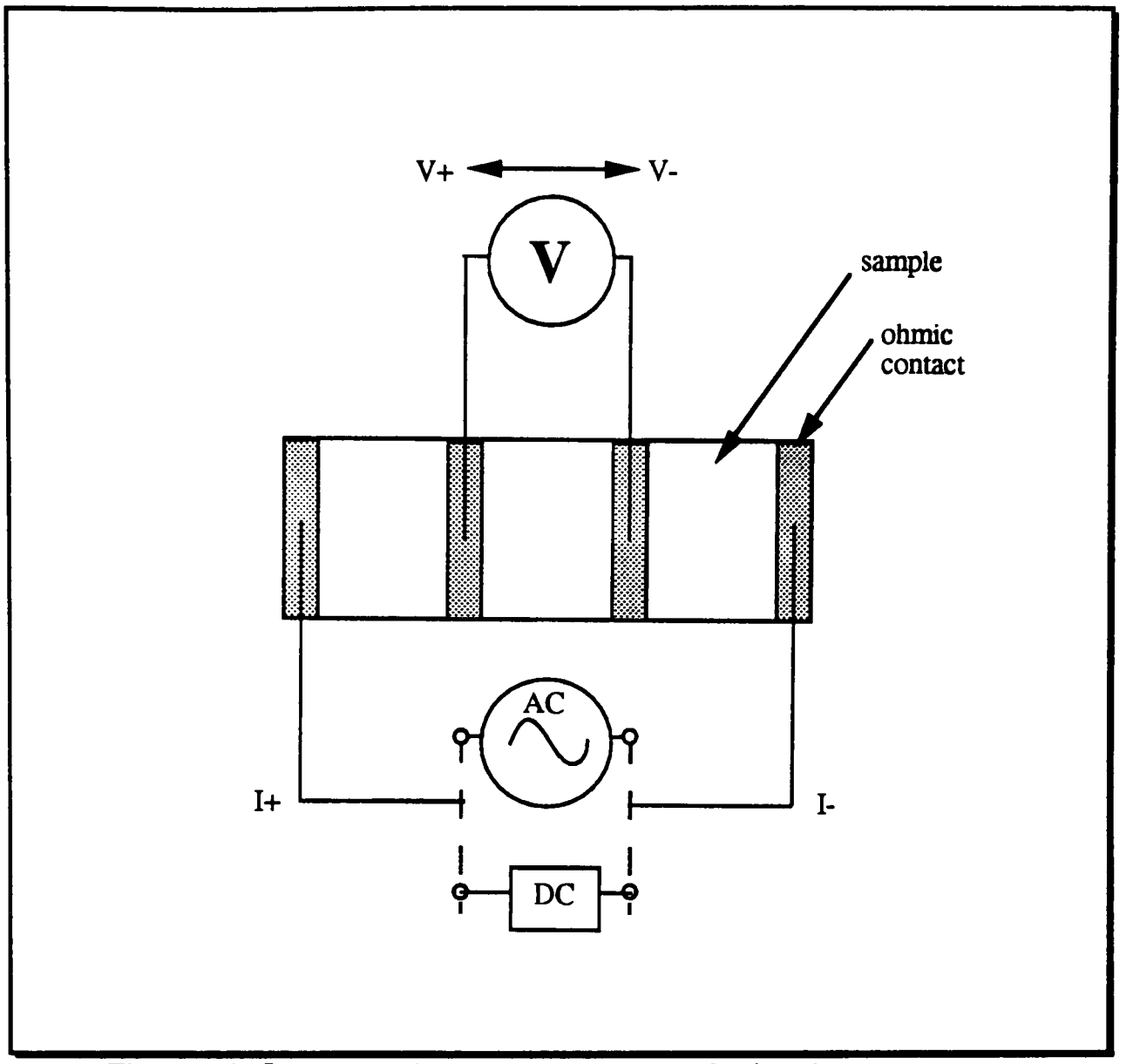

Figure 3.2: Schematic of electrode arrangement for 4-probe measurement.

3.1.2. Magnetism

The magnetic moment of a free atom comes from 3 principal sources: the electron spin, the orbital angular momentum about the nucleus; and the change in the orbital moment induced by an applied magnetic field. The first two effects give paramagnetic contributions to the magnetisation and the third gives a diamagnetic contribution.

The magnetisation is defined as the magnetic moment per unit volume while the magnetic susceptibility per unit volume is defined as:

$$\chi = \frac{M}{B} \tag{6}$$

Substances with a *negative* susceptibility are called *diamagnetic* and those with *positive* susceptibilities are *paramagnetic*. In some cases, it is more convenient to define the magnetic susceptibility with respect to unit mass (χ_m) or a mole of substance (χ_{molar}). In this chapter, molar magnetic susceptibility (χ_{molar}) will be used throughout, unless otherwise stated.

Diamagnetism is associated with the tendency of the electronic charges to shield the interior of a body from an applied magnetic field. In superconductors, this tendency is strong and can under appropriate conditions perfectly shield the sample so that no

magnetic flux lines penetrate the sample. For materials in the normal state, the shielding, albeit weak, is still present, giving rise to measurable diamagnetic contributions on the order of ~10^{-7} emu per mole of atom.

Electronic paramagnetism is found in:

(a) atoms, molecules and lattice defects possessing an odd number of electrons (as here the total spin of the system cannot be zero).

(b) free atoms and ions with partially filled inner shells, e.g., transition elements, ions isoelectronic with transition elements, rare earths and actinide elements.

(c) a few compounds with even number of electrons but which possess non-singlet ground states, e.g., molecular oxygen, organic biradicals.

(d) metals

Most paramagnetic materials obey the Curie law:

$$\chi = \frac{C}{T} \tag{7}$$

where χ = magnetic susceptibility
C = Curie constant
T = temperature in Kelvin.

The law derives from summing the individual moments of each energy level characterised by the quantum numbers, m_J, m_{J-1}, m_{J-2}, ... m_{-J}, weighted by a statistical Boltzmann factor (P_i):

$$M = \sum_{i=m_{-J}}^{i=m_J} \mu_i P_i \tag{8}$$

where M = Total magnetic moment
$\mu_i = m_s g \mu_B$ = magnetic moment of an ion in level i

$$P_i = \frac{(\Delta E_i / kT)}{\sum_{i=m_{-J}}^{i=m_J} \exp(-\Delta E_i / kT)}$$

For most cases, $g\mu_B B_0 << 2kT$, so that the expression can be simplified:

$$M = \frac{N\mu_B^2 B_0}{3kT} g^2 J(J+1) \tag{9}$$

In the spin only case (i.e., angular momentum, L = 0), J = S such that

$$M = \frac{N\mu_B^2 B_0}{3kT} g^2 s(s+1) \tag{10}$$

Since susceptibility is the rate of change of magnetisation with field,

$$\chi = \frac{M}{B_0} = \frac{N\mu_{eff}^2}{3kT} \tag{11}$$

(where $\mu_{eff} = g\sqrt{s(s+1)}\,\mu_B$ is defined as the effective magnetic moment in units of Bohr magnetons.)

Comparison of this expression for χ with the Curie law reveals the relation:

$$C = \frac{N\mu_{eff}^2}{3k} \tag{12}$$

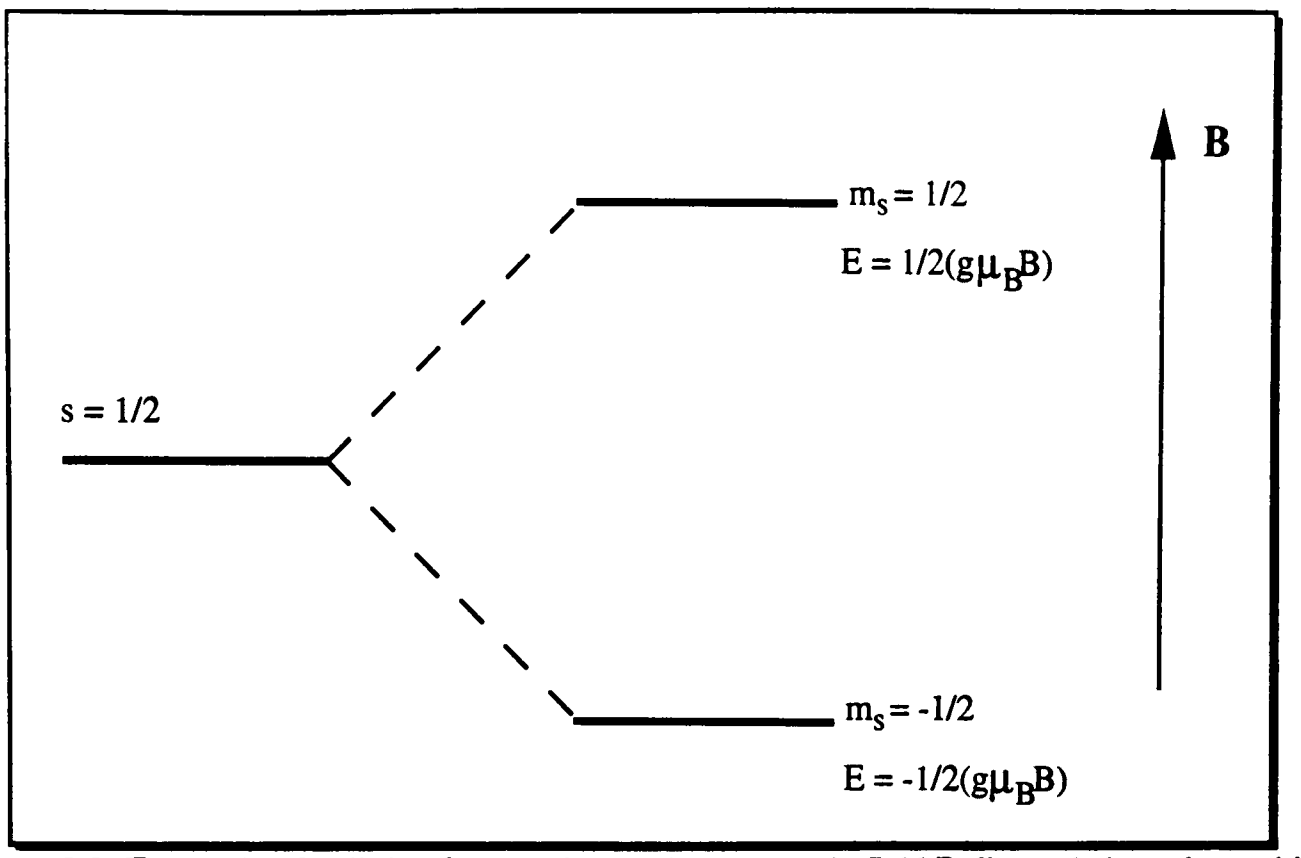

Figure 3.3: Energy level splitting for one electron in a magnetic field B directed along the positive z axis. For an electron the magnetic moment is opposite in sign to the spin s, so that $\mu = -g\mu_B s$. Thus, in the low energy state, the magnetic moment is parallel to the magnetic field.

Working in CGS units and substituting the appropriate values for Avogadro's number and Boltzmann's constant yields a simple expression for evaluating μ_{eff} for Curie paramagnets[10]:

$$\mu_{eff} = \sqrt{8C} \qquad (13)$$

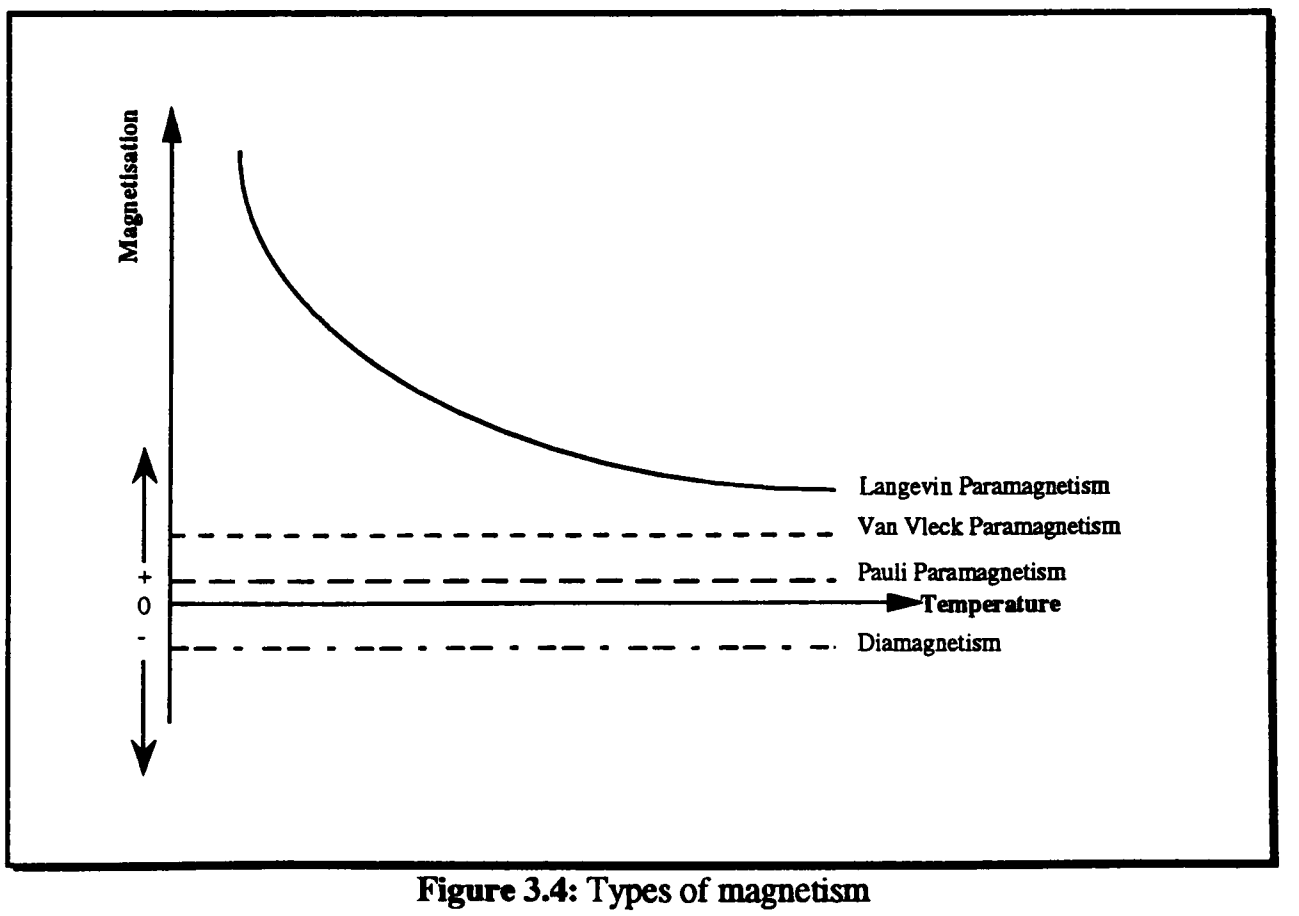

Figure 3.4: Types of magnetism

Some materials exhibit paramagnetism which is independent of temperature. These may be metals with conduction electrons (Pauli paramagnetism) or systems with spin singlet ground states whose wave functions mix with those of the excited states (Van

Vleck paramagnetism). By application of Fermi-Dirac distributions on the electrons, the Pauli spin magnetisation of the conduction electrons can be expressed as

$$M_{Pauli} = \mu_B^2 N(E_F) B \qquad (14)$$

where $N(E_F)$ = density of states at Fermi level
B= applied magnetic field
μ_B = Bohr magneton = $9.274 \times 10^{-24} JT^{-1} = 5.77 \times 10^{-3}$ eV $^{1/2} cm^{3/2}$

A summary of the different types of magnetism is presented in Figure 3.4.

3.1.3. Superconductivity and the Meissner Effect

Superconductivity in a material is characterised by the loss of electrical resistivity. However, superconductivity also confers dramatic magnetic properties on the sample, whereby a bulk superconductor in a weak magnetic field behaves as a perfect diamagnet, with zero magnetic induction in its interior. Thus, when the specimen is placed in a magnetic field and cooled through the transition temperature for superconductivity, the magnetic flux originally present is expelled from the sample. This flux expulsion is called the *Meissner effect.*

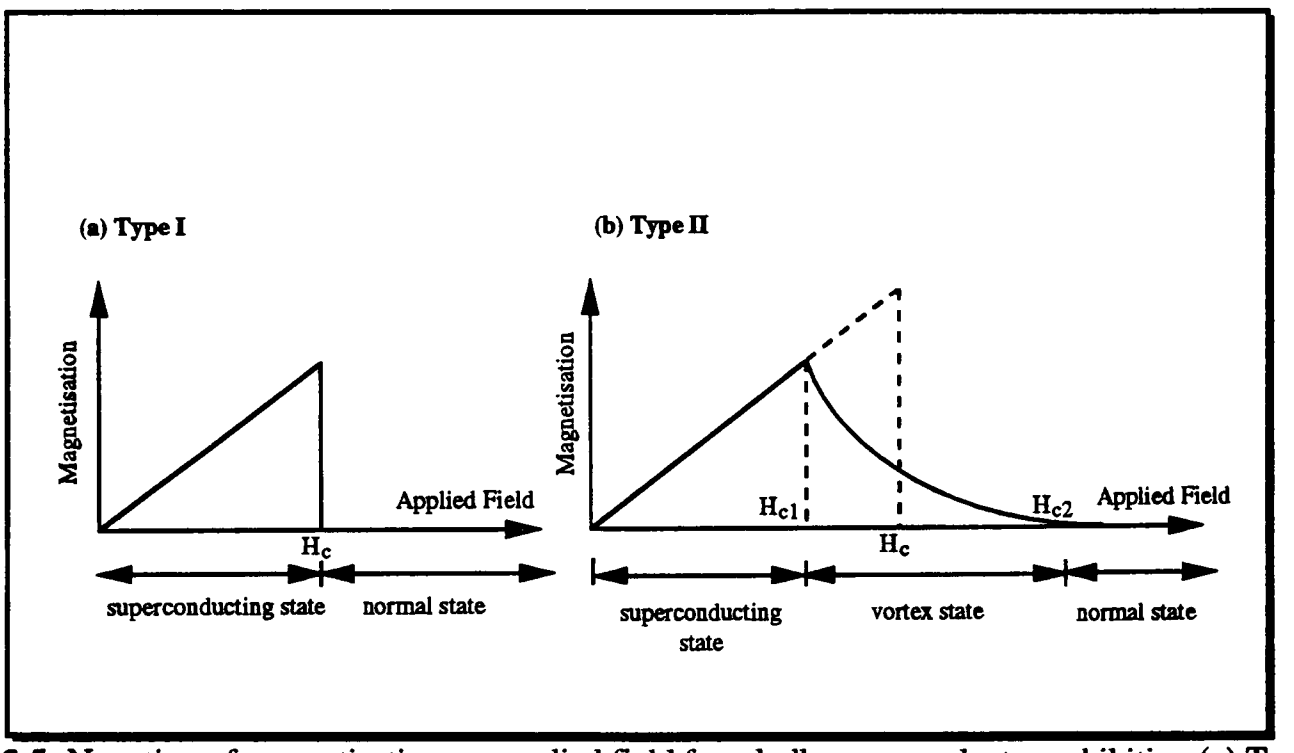

Figure 3.5: Negative of magnetisation vs. applied field for a bulk superconductor exhibiting (a) Type I (b) Type II behaviour. For (b), the horizontal scale between H_{c1} and H_{c2} have been greatly compressed for clarity of presentation.

Superconductors can be classed in one of two categories, *Type I* or *Type II* superconductors. The former, also known as *soft* superconductors, exhibit magnetisations which are linear with respect to the applied field until a critical field H_{c2} beyond which complete flux penetration occurs. The values of H_{c2} for Type I superconductors are usually too low for any useful technical applications. In contrast, Type II superconductors, which tend to be alloys or transition metals with high electrical resistivities in the normal state, have two critical fields H_{c1} and H_{c2}. Up to H_{c1}, Type II

superconductors behave just as Type I superconductors but between H_{c1} and H_{c2}, there is partial flux penetration (the Meissner effect is incomplete) and the sample is said to be in a *vortex state*. The value of H_{c2} may be two or more orders of magnitude greater than the value of the thermodynamic critical field, H_C.

Although the quantum theory of superconductivity by Bardeen, Cooper and Schrieffer[11] has successfully described superconductivity, the phenomenological equations of London and Ginzburg-Landau provide useful physical insights into the superconducting state. Two useful parameters which arise from these are the London penetration depth, λ_L, and the Pippard coherence length, ξ_0.

$$\lambda_L = \sqrt{\frac{mc^2}{4\pi q^2}} \tag{14}$$

$$\xi_0 = \frac{\hbar v_F}{2E_g} \tag{15}$$

where q = Particle charge
m = Particle mass
E_g = energy gap of superconductor.
v_F = electron velocity at the Fermi surface.

The London penetration depth is a fundamental length that characterises a superconductor and is a measure of the depth of penetration of the magnetic field. It is not, however, a precise measure of the actual penetration depth, as the London equation is an oversimplification of the true situation. Nonetheless, it serves as a useful parameter with which to describe and characterise these materials.

An independent length is the coherence length, ξ, which is a measure of the distance within which the superconducting electron concentration cannot change drastically in a spatially varying magnetic field. It is also a measure of the minimum spatial extent between the normal and superconducting areas of the sample. In practice, for impure materials and alloys, the empirically determined coherence length, ξ, is shorter than ξ_0. This forms the basis of quality comparisons between superconductors, where the ratio $\kappa = \lambda_L/\xi$ is a measure of the purity of a sample (that is, the degree of sample in the superconducting state).

3.1.4. Survey of Electronic Properties in Layered Intercalates

The intercalation reaction of metal dichalcogenides is in all known cases, accompanied by electron transfer from the intercalants to the layered host material, where the electron occupies the lowest lying *d* conduction band. Thus the Group IV dichalcogenides MX_2 (M=Ti, Zr, Hf; X=S, Se) are transformed from semiconductors to *d*-band metals. Furthermore, since the conduction bands formed from *d* orbitals on the metal atoms reside in the centre of the three-layered MX_2 sandwich, changes in the local bonding are small. This is the basis for the rigid band model (see Chapter 1 and references therein).

There is a considerable body of experimental information (*vide infra*) on the electronic properties of the alkali metal and amine intercalates of transition metal dichalcogenides and they are found to show the metallic properties expected from the filling of the transition metal *d* band with increasing charge donation from the guest. While there is little controversy that metallic behaviour is conferred to metal dichalcogenides upon intercalation, the mechanism of the electron scattering as well as the conduction behaviour at low temperatures is a matter of some debate.

Early work by Benda[12]and Thompson[13] on the transport properties of TiS_2 indicated a T^2 dependence of resistivity (T = temperature), which Thompson proposed was due to electron-electron scattering being the dominant mechanism. Electron-electron scattering that results in loss of current requires collisions between electrons with different effective masses, as in the *s-d* scattering considered by Baber[14] for transition metals or electron-hole scattering[15]. However, such a mechanism cannot explain the strong pressure dependence of the room temperature resistivity, ρ, ($d\ln\rho/dP$ = -2.5%/kbar)[16] exhibited by TiS_2, since only small changes in resistivity should be expected from pressure induced modifications of the band structure.

Subsequently, Klipstein *et al.* [17] showed that fitting the resistivity to $\rho = \rho_0 + AT^v$ gives a value of v between 1.6 and 2.3, the exact value being dependent on the stoichiometry of the excess Ti atoms which are known to occur in this dichalcogenide[18, 19]. They proposed a phonon scattering mechanism which is consistent with these results involving both optical and acoustic phonons. Below the Debye temperature, a simple model involving intra and inter-valley scattering by acoustic phonons accounts for the observed magnitude and variation of resistivity. They note that a T^2 dependence for resistivity is observed in samples of $Ti_{1+x}S_2$ where the stoichiometric excess of Ti is minimal. Further support for this phonon scattering model was provided in single crystal transport studies of the hydrazine intercalates of TiS_2, $TiSe_2$ and ZrS_2[20] as well as $LiZrS_2$[21].

Despite the metallic behaviour of metal dichalcogenide intercalates, some of them, as well as the pristine hosts, show a discontinous increase of resistivity at low temperatures. The resistivity of 1T-TaS_2 increases rapidly below 4K, following a dependence of the form $\rho \sim exp(T_0/T)^n$ where the value of n has been reported by DiSalvo and Graebner[22] to be 1/3 and more recently by Onuki *et al.*[23, 24] to be 1/2. In $TaS_2(N_2H_4)_{2/3}$ and $TaS_2(N_2H_4)_{4/3}$, Sarma *et al.* [25]have shown the value of n to be 1/3. Both DiSalvo and Graebner as well as Sarma and co-workers[22, 25]suggest that electron localisation takes place as a result of impurities or crystal defects, and the $T^{1/3}$ law is a result of two-dimensional variable range hopping. Such a hypothesis is strengthened by reports of anistropic conductivities in similar systems such as 2H-TaS_2(pyridine)$_{1/2}$ (where the intraplanar to interplanar conduction ratio, $\sigma_{//}/\sigma_{\perp} = 10^4$) as well as in pristine 1T-TaS_2 ($\sigma_{//}/\sigma_{\perp} = 500$). The resistivity phenomenon has been described by Fukuyama

and Yosida[26, 27] in terms of an Anderson localisation model[28] while Fazekas and Tosatti[29] propose that the loss of carriers results from a Mott metal-insulator transition[4].

In addition to affecting the resistivity of the host, the electron transfer that occurs upon intercalation also manifests itself in the magnetic susceptibility of the intercalated material, usually giving rise to a measurable temperature independent Pauli susceptibility. In some cases, the temperature independent susceptibility of these materials is increased significantly. Murphy *et al.* [30] have shown that in various lithium intercalates of metal dichalcogenides, temperature independent susceptibilities ranging from 10^{-3} to 10^{-5} emu/mole were observed. Similar measurements by Guy *et al.*[31, 32] for $TiSe_2(N_2H_4)_{0.6}$ yielded a Pauli susceptibility of 74 x 10^{-6} emu/mole while Ahmad[21] found an increase of 78 x 10^{-6} emu/mole for the lithium intercalate of ZrS_2 relative to the pristine host. In contrast, Trichet *et al.* [33] reported very high Pauli susceptibilities of 400 x 10^{-6} emu/mole for $Li_{0.35}ZrS_2$.

Table 3.1: Magnetic susceptibility and density of states at the Fermi level, $N(E_F)$ for several group IV intercalation complexes. χ_{Pauli} is obtained from χ_{total} by subtraction of χ_{dia} estimated from Pascal's constants and $N(E_F)$ is determined from $\chi_{Pauli.}$(adapted from Ahmad, 1987[21])

Compound	χ_{total} (10^{-6} emu mol^{-1})	χ_{Pauli} (10^{-6} emu mol^{-1})	$N(E_F)$ (states eV^{-1} formula unit $^{-1}$)	Ref
1T-VSe_2	247	346	10.4	[34]
$LiVSe_2$	815	914	27.4	[30]
$TiSe_2(N_2H_4)_{0.6}$	61	185	5.6	[31]
$LiTiSe_2$	250	351	10.5	[30]
$Ag_{0.33}TiS_2$	9	98	3.0	[35]
$Li_{0.33}TiS_2$	63	144	4.3	[36]
$LiTiS_2$	177	258	7.7	[30]
"	141	222	6.7	[36]
$LiZrS_2$	16	106	3.2	[30]
"	-12	78	2.4	[21]

The high Pauli susceptibilities reported by Trichet as well as that for $LiVSe_2$ [30] are reminiscent of exchanged enhanced metals like Pd where the electron-electron correlation near the Fermi level is very high. Models for such highly correlated electron gases have been proposed by Brinkmann and Rice[37] and such compounds have the following properties[38]:

(a) they must be metallic.

(b) the Pauli susceptibility *and* the electronic specific heat are both greatly enhanced.

(c) measurements of the Hall coefficient will give the total number of electrons.

Since the Pauli susceptibility is proportional to the density of states, the enhancement of the latter may be responsible for the superconducting transitions observed in some of the metal dichalcogenide intercalates[39-42].

3.1.5. Overview of Chapter

This chapter describes a study of electronic properties in the organometallic intercalates of zirconium and tin dichalcogenides. In Section **3.2**, measurements of electrical resistivity for the ZrS_2 intercalates are described and discussed. The temperature independent magnetic behaviour of these intercalates is explored in Section **3.3** and attempts to measure the extent of guest ionisation from the size of the Curie paramagnetic term in the overall magnetic susceptibility of these compounds are also described. Section **3.4** examines the superconducting anisotropy in an organometallic intercalate, $SnSe_2(CoCp_2)_{0.3}$, by means of critical field measurements on single crystal samples oriented parallel and perpendicular to the applied magnetic field in a SQUID magnetometer.

3.2. Conductivity Studies on ZrS_2 Intercalates

This section describes electrical resistivity measurements performed on some organometallic intercalates of ZrS_2, namely, $ZrS_2(CoCp_2)_{0.25}$, $ZrS_2(CrCp_2)_{0.2}$ and $ZrS_2(TiCotCp)_{0.2}$. The syntheses of these compounds, as well as details of the apparatus constructed for these measurements are described in Chapter Five.

3.2.1. Resistivity measurements

All air sensitive crystal samples were mounted onto 8 pin dual-in-line (DIL) headers in a glove box fitted with a stereo zoom microscope. The crystals were mounted using the linear 4-probe arrangement (Figure 3.2). Details of sample mounting are given in Chapter 5.

The purpose-built apparatus for resistivity measurements was based on modules so that existing commercially available electronics components could be easily interfaced into the system. The rig consists of 3 modules; the *temperature control*, the *data measurement* and the *acquisition* systems. These modules are described in Chapter Five. A schematic of the software design is set out in Figure 3.6.

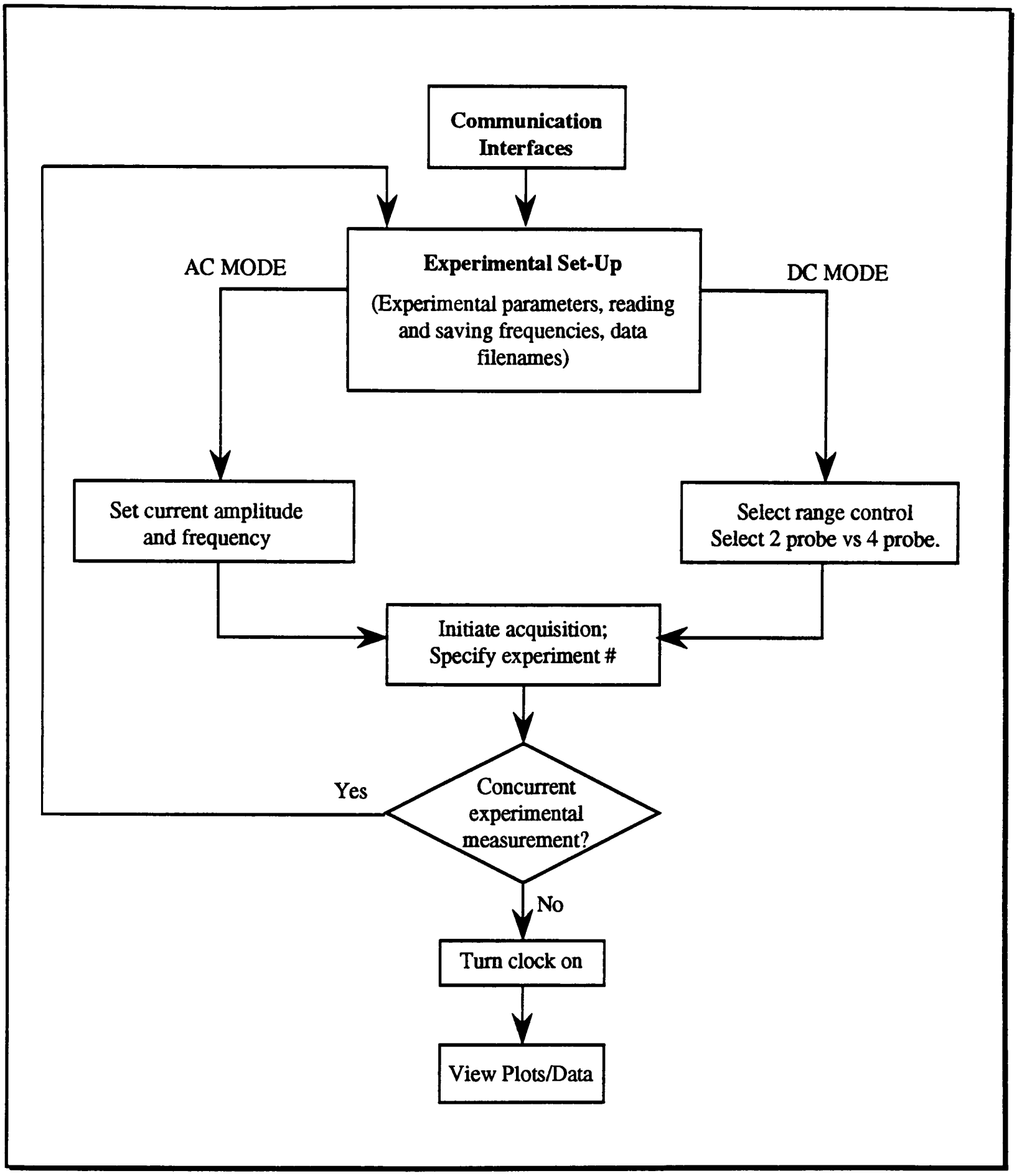

Figure 3.6: Flow diagram showing modular design of data acquisition software.

Resistivities were measured using either AC or DC mode. All electrical leads were grounded to reduce electrical noise. Typically, for AC measurements, currents of 25μA or 100μA and frequencies of 10 or 33Hz were passed through the sample, across which the potential drop was measured by a Princeton Lock-In Amplifier Model 5210 interfaced to a Viglen microcomputer running Microsoft Windows® compatible software developed in the Inorganic Chemistry Laboratory (Oxford) by Dr Peter Trevellick. Temperature changes of ±1 K/min were employed between 4K and 300K for both

warming and cooling cycles to allow complete temperature equilibration of the sample within the cryostat. For DC measurements, a Hewlett-Packard HP 3478 multimeter, operating in the manual entry mode and IEEE-interfaced to a Viglen microcomputer, was used to obtain 4-probe resistance measurements directly.

All the resistance data obtained were converted to resistivity units (ohm-cm) by measuring the crystal dimensions immediately after the experiment. For a crystal configured in the 4-probe mode with the dimensions shown in Figure 3.7, the resistance, R, is related to resistivity, ρ, by the following equation, where p, q and r are the linear dimensions defined in Figure 3.7.

$$\rho = \frac{R(q.r)}{p} \qquad (17)$$

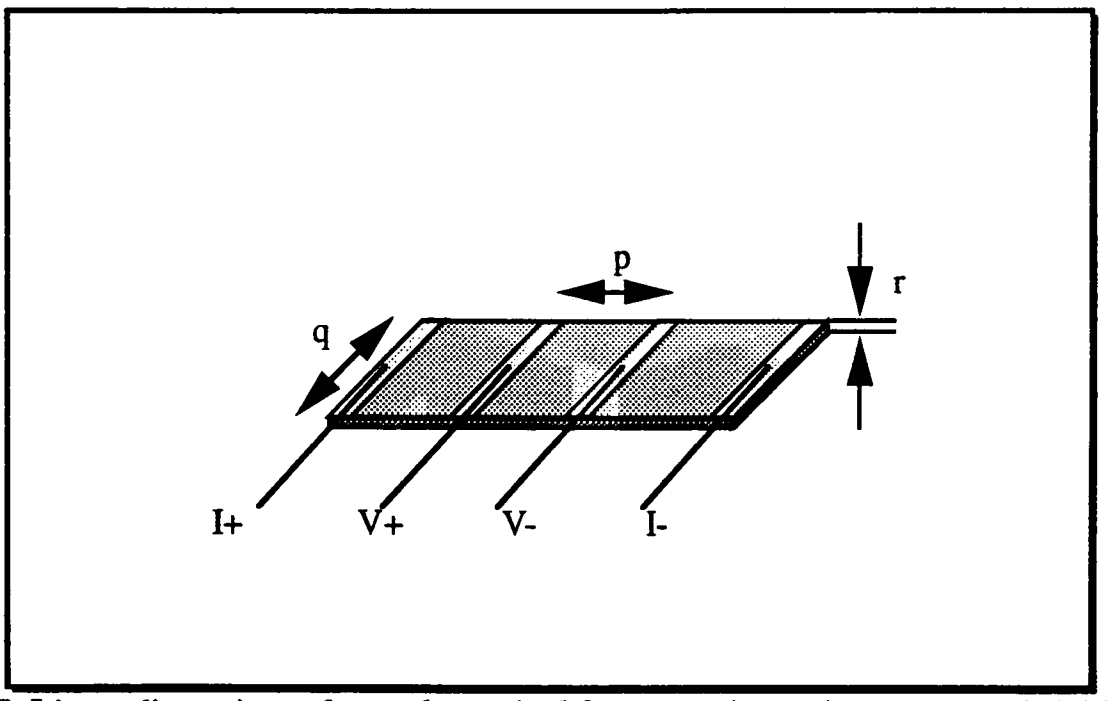

Figure 3.7: Linear dimensions of crystals required for converting resistances to resistivities.

Some of the earlier experimental data was collected on a similar apparatus built by Dr M. Kurmoo, in which a RML 380Z microcomputer was used for data acquisition and an Oxford Instruments Temperature Controller 3120 replaced the ITC-4[43].

3.2.2. Results/Discussion

A summary of the resistivity data obtained for the host ZrS_2 and the $ZrS_2(G)_x$ intercalates {G = $CoCp_2$, $CrCp_2$, TiCOTCp; $0.20<x<0.25$} for the temperature range 4.2K to 300K is shown in Figures 3.8 and 3.9.

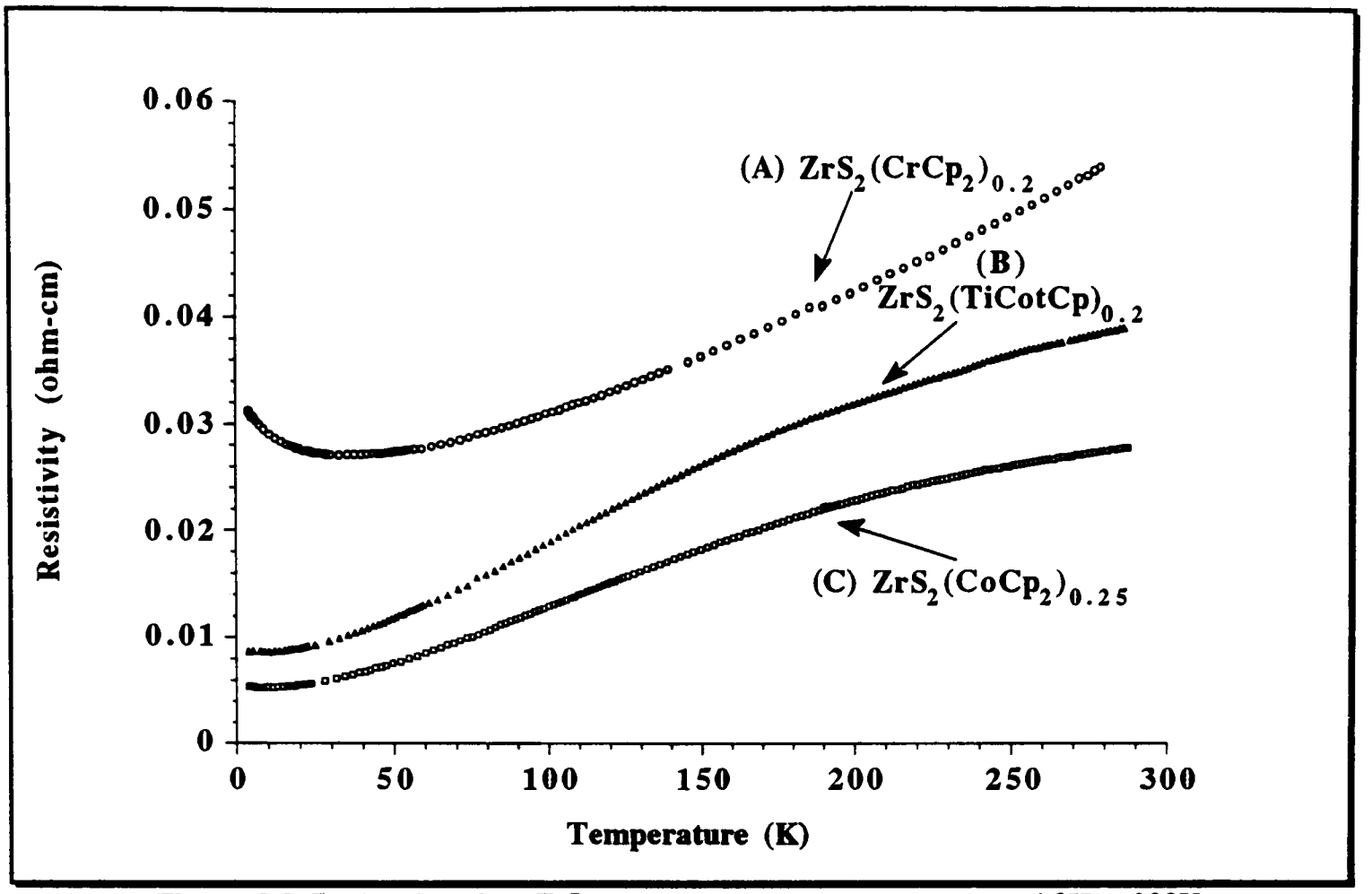

Figure 3.8: Resistivity of the ZrS_2 intercalates for temperature range 4.2K to 300K.

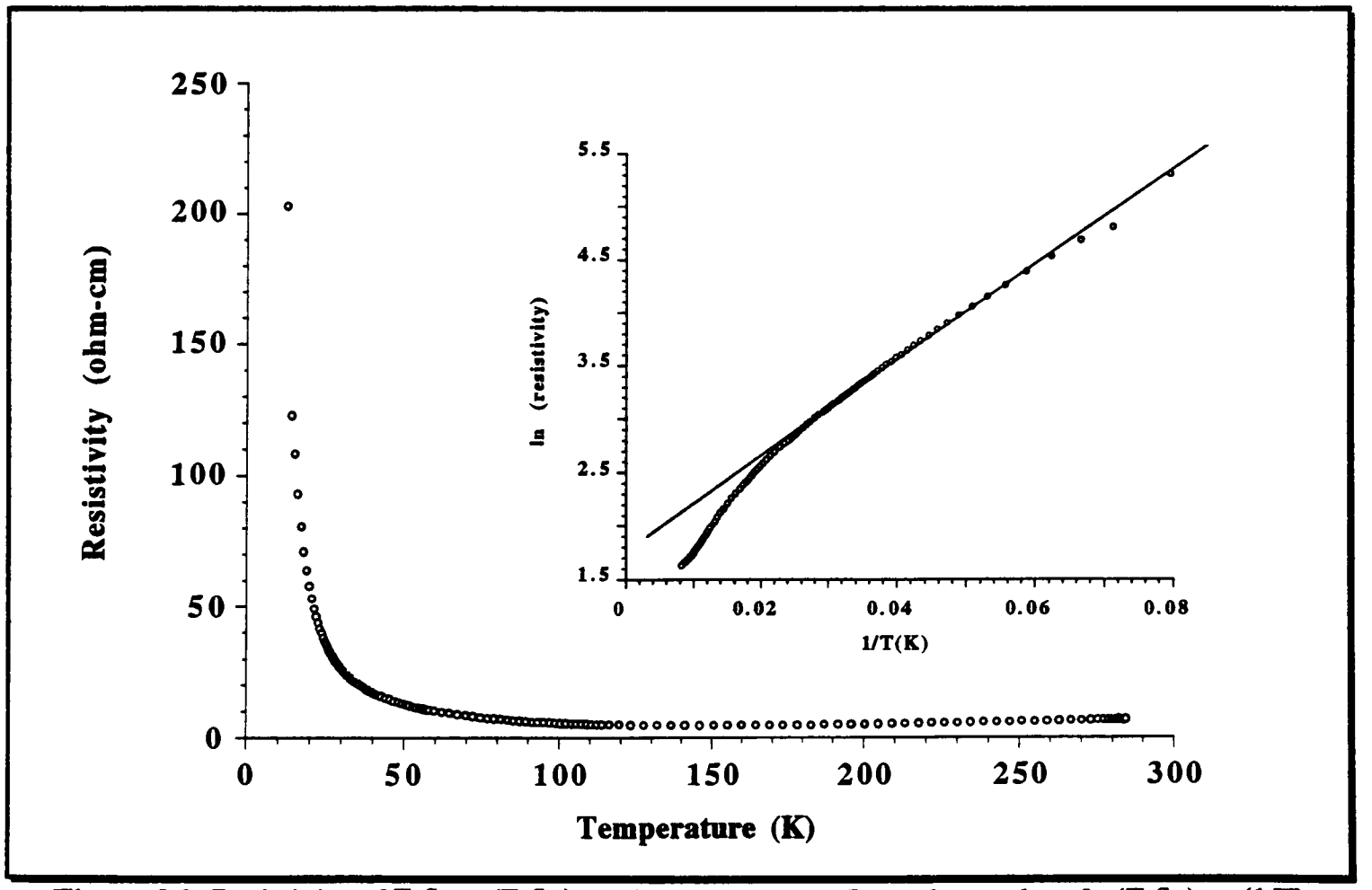

Figure 3.9: Resistivity of ZrS_2, $\rho(ZrS_2)$, against temperature. Inset shows plot of $\rho(ZrS_2)$ vs (1/T).

The resistivity of the host ZrS_2 rises dramatically at low temperatures, as expected for a semiconductor with a band gap of 1.7eV[44, 45]. However, a non-linear plot of $ln\rho$ *vs* $1/T$ was obtained, indicating that the use of iodine during the vapour phase growth of these crystals had introduced impurities into the band. A plot of $ln\rho$ *vs* $(1/T)^{1/3}$ for data below 200K yielded a straight line characteristic of conduction by two-dimensional

variable range hopping[4] while above 200K, metallic conduction was observed and resistivity was found to be proportional to T.

In contrast, the resistivity associated with the layered intercalates was more complicated, typically assuming a sigmoidal profile with two points of inflection over the temperature range examined. As such, the resistivity profile can be qualitatively described if three temperature regimes are considered, namely: *high* (*ca.* 300 to *ca.* 150K), *medium* (*ca.*150 to 50K) and *low* (<30K) regions. In the first two regions, metallic behaviour was observed for all three intercalates although the dominant electron scattering mechanism differs, while in the low temperature region, $ZrS_2(CrCp_2)_{0.2}$ exhibits a different behaviour from the other two intercalates. $ZrS_2(CoCp_2)_{0.25}$ and $ZrS_2(TiCotCp_2)_{0.2}$ behave in accordance with Matthiesen's Rule and approach a residual resistivity, ρ_i, at low temperature. For $ZrS_2(CrCp_2)_{0.2}$, on the other hand, localisation of electrons occurs, suggesting a metal to non-metal transition. Each of the three temperature regions are described for the three intercalates below.

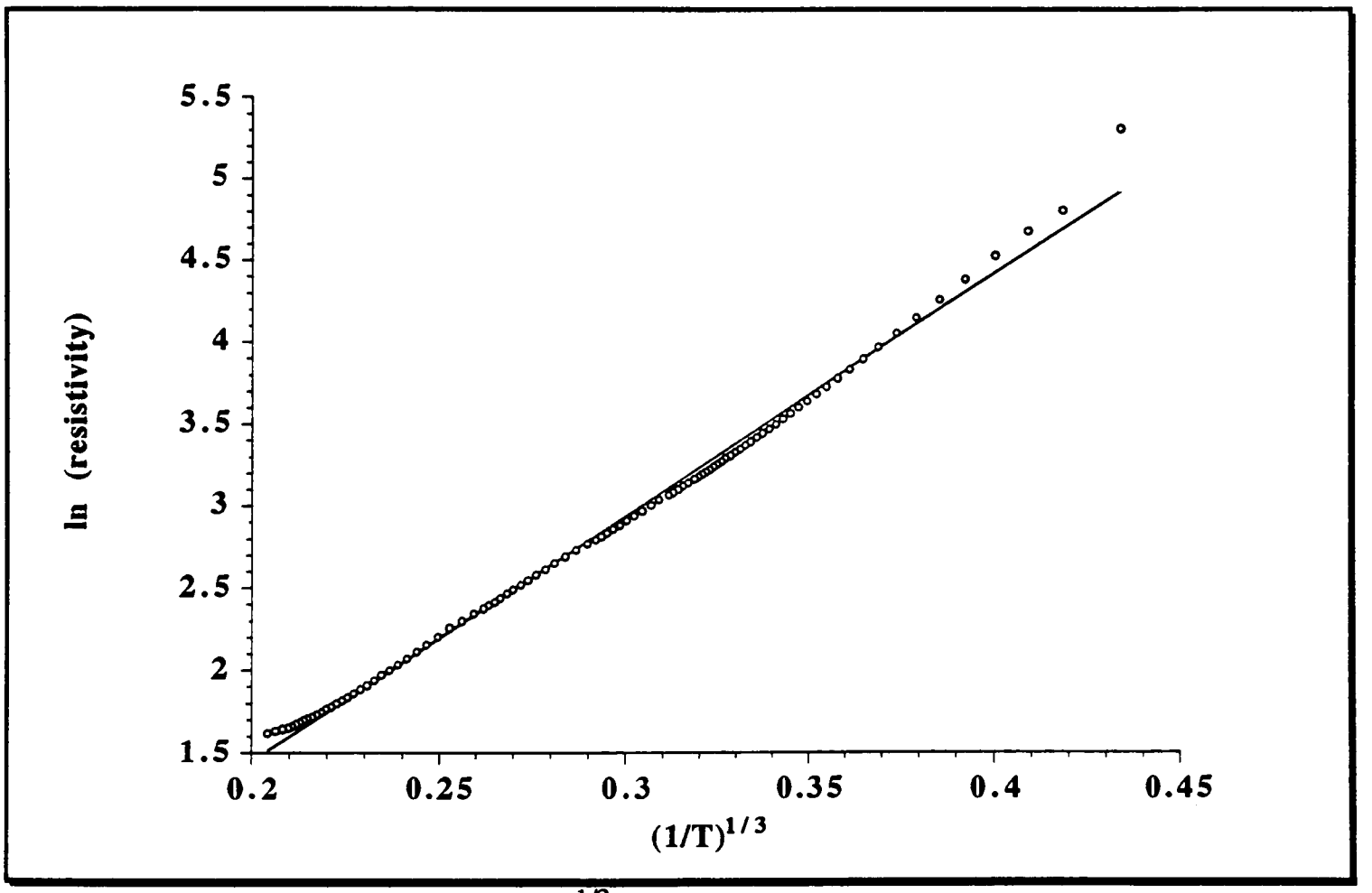

Figure 3.10: $\rho(ZrS_2)$ against $(1/T)^{1/3}$ to emphasise the variable range hopping regime.

(a) High Temperature Regime

In the first of these regions, all the intercalates show a linear dependence of resistivity on temperature (Figure 3.11). A linear dependence of the resistivity on temperature occurs in metals above their Debye temperatures since electron-phonon scattering dominates the conduction mechanism. The linear metallic conductivity displayed by the intercalate suggests a similar mechanism is operative at these temperatures. The temperatures where deviation from linearity occurs for the three

intercalates are marked in Figure 3.11. From the resistivity data, the Debye temperatures for the three intercalates (θ_D(Intercalate), decrease in the order: $\theta_D(ZrS_2(CoCp_2)_{0.25}) > \theta_D(ZrS_2(TiCotCp)_{0.2}) > \theta_D(ZrS_2(CrCp_2)_{0.2})$. Since the Debye temperature is a measure of the vibrational stiffness of the crystal, the data suggests that the $ZrS_2(CoCp_2)_{0.25}$ is the most rigid lattice. $ZrS_2(TiCotCp)_{0.2}$, which has weaker interlayer attractions as a result of the larger lattice expansion upon intercalation (see Chapter Two) thus has less rigidity in its structure, while in $ZrS_2(CrCp_2)_{0.2}$, the lattice permits significant electron phonon-coupling (see section **3.3**).

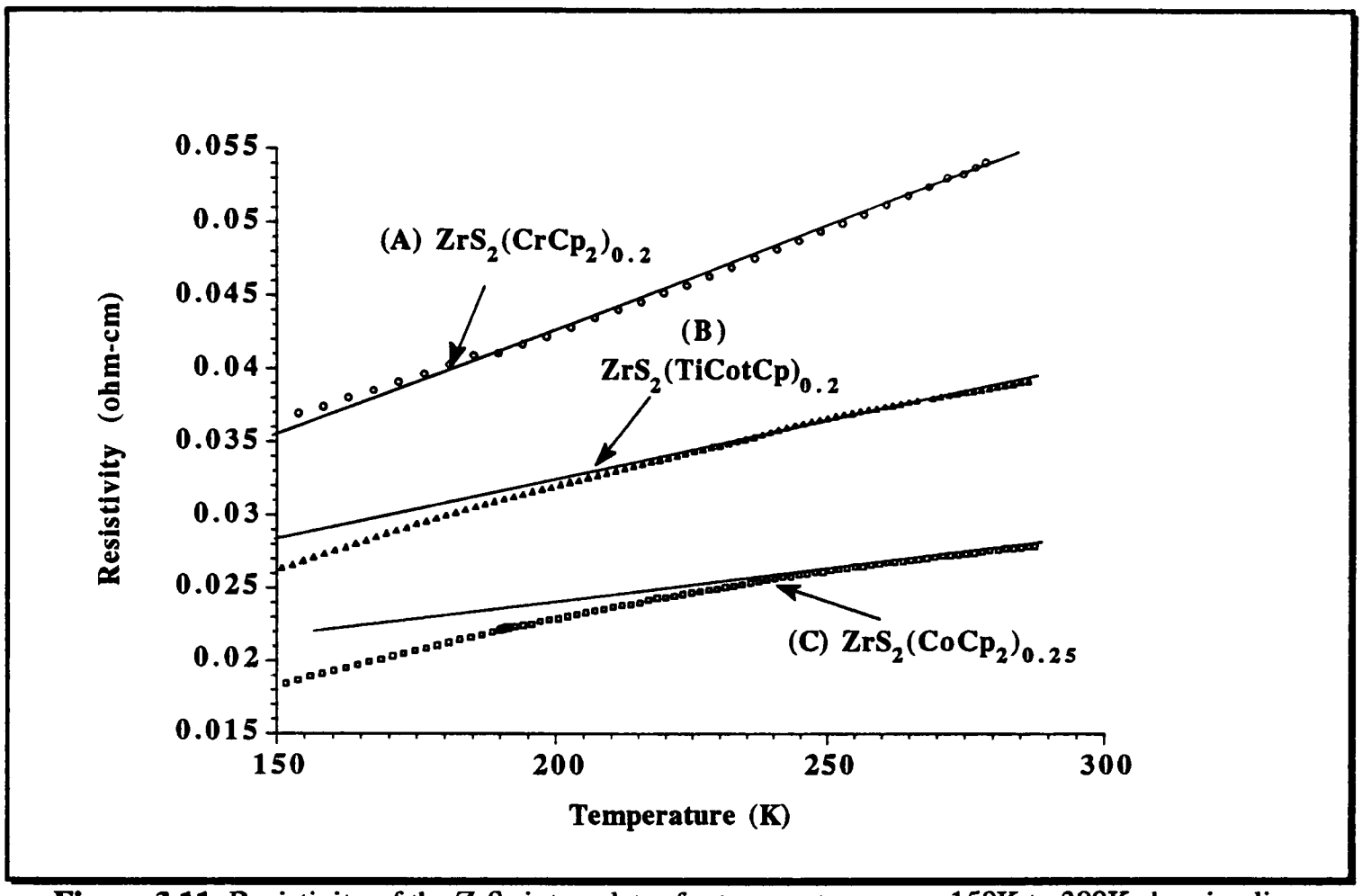

Figure 3.11: Resistivity of the ZrS_2 intercalates for temperature range 150K to 300K showing linear dependence on temperature down to the Debye temperature (arrowed).

(b) Medium Temperature Regime

For the temperatures from 50K to 150K, the resistivity of $ZrS_2(CrCp_2)_{0.2}$ varies as T^2, as shown by the linearity of the resistivity versus T^2 plot (see Figure 3.12). This is the temperature dependence predicted for the Landau-Baber electron-electron scattering mechanism which is also likely to be dominant here. In contrast, the resistivity of the $CoCp_2$ and TiCotCp intercalates do not show such a clear T^2 dependence, which suggests that the electron scattering mechanism arises from a combination of mechanisms, with no single one dominating. Although the conduction mechanism in $ZrS_2(CrCp_2)_{0.2}$ can be ascribed to Landau-Baber scattering at these temperatures, another possibility has been raised by Klipstein to explain the observed behaviour.

As pointed out in **3.1.4**, Klipstein and others[17, 20, 21, 46, 47] have observed such T^2 dependences on resistivity which are also consistent with, and which they ascribe to, a

mechanism involving a combination of longitudinal acoustic phonons and optical phonons scattering the conduction electrons. Without a clearer idea of the density of states at the Fermi level to assess the likelihood of strong electron-phonon scattering at these temperatures nor other measurements to determine the extent of optical and acoustic phonon scattering present, it is not possible to unequivocally distinguish between the two mechanisms.

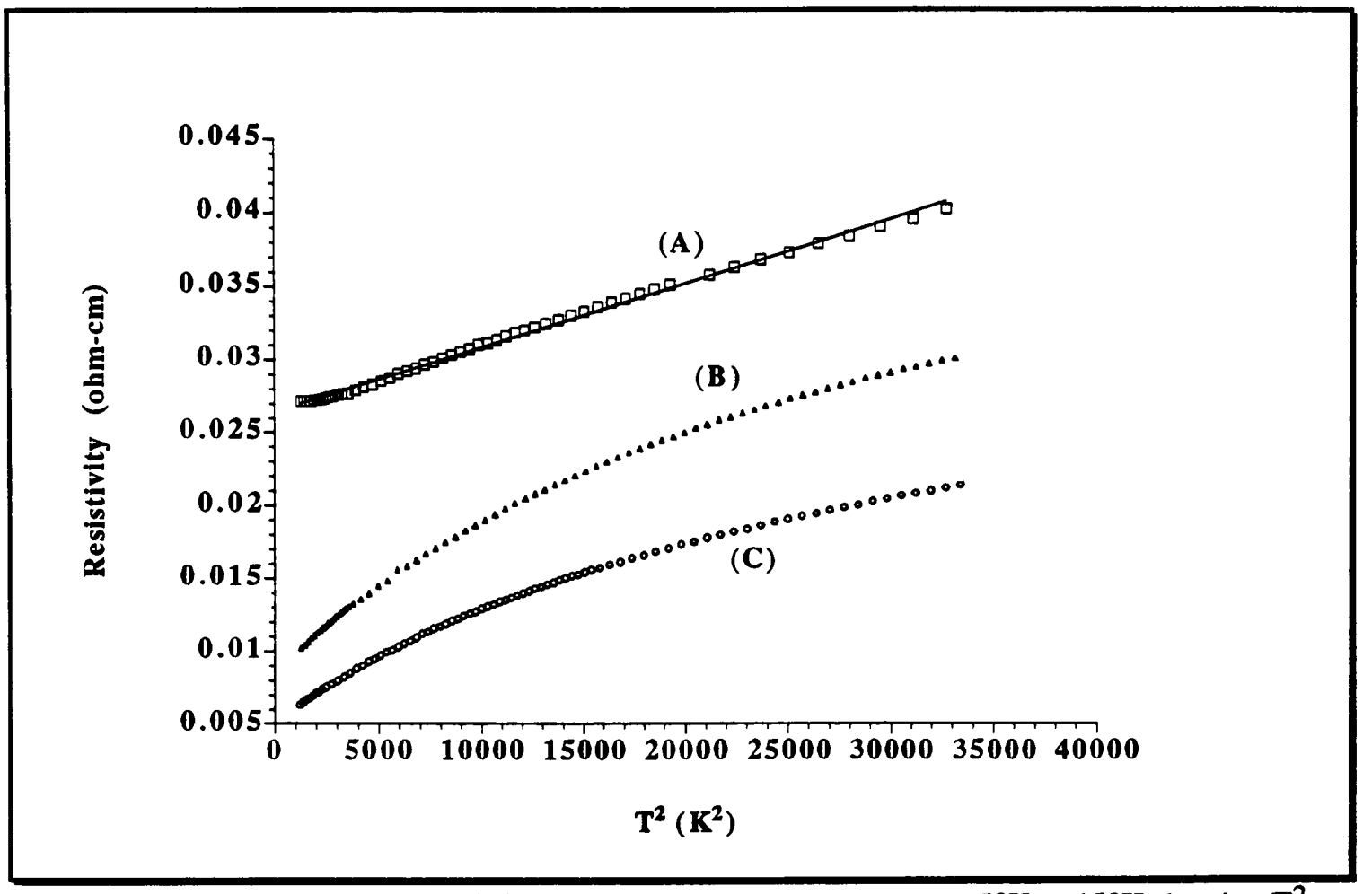

Figure 3.12: Resistivity of the ZrS_2 intercalates for temperature range 50K to 150K showing T^2 dependence on temperature.

(c) Low Temperature Regime

Finally, at low temperatures (4.2K < T < 30K), the resistivity rises sharply for the $CrCp_2$ intercalate (Figure 3.8) but levels off to a residual value, ρ_i, in the $CoCp_2$ and TiCotCp intercalates (Figure 3.13). For $ZrS_2(CoCp_2)_{0.25}$, $\rho_i = 5.4 \times 10^{-3}$ Ω-cm and for $ZrS_2(CrCp_2)_{0.2}$, $\rho_i = 8.5 \times 10^{-3}$ Ω-cm. The resistivity of $ZrS_2(CrCp_2)_{0.2}$ both as a function of $T^{-1/3}$ and $T^{-1/4}$ is plotted in Figure 3.14. Both plots give reasonably good fits to a straight line but the fit is marginally better for the latter. The correspondence of resistivity to a $T^{1/n}$ law ($3 < n < 4$) is good evidence for variable range hopping in this intercalate. Based on the slightly better agreement with the $T^{1/4}$ law, the hopping is tentatively assigned as a three-dimensional process. The dimensionality of the hopping observed here contrasts with that reported by Sarma for the hydrazine intercalates of 1T-TaS_2 (where $ln\rho \propto T^{-1/3}$) but is consistent with that in organometallic intercalates such as $SnSe_xS_{2-x}(CoCp_2)_{0.3}$ $\{0 \leq x \leq 2\}$ where three-dimensional variable range hopping was observed[48].

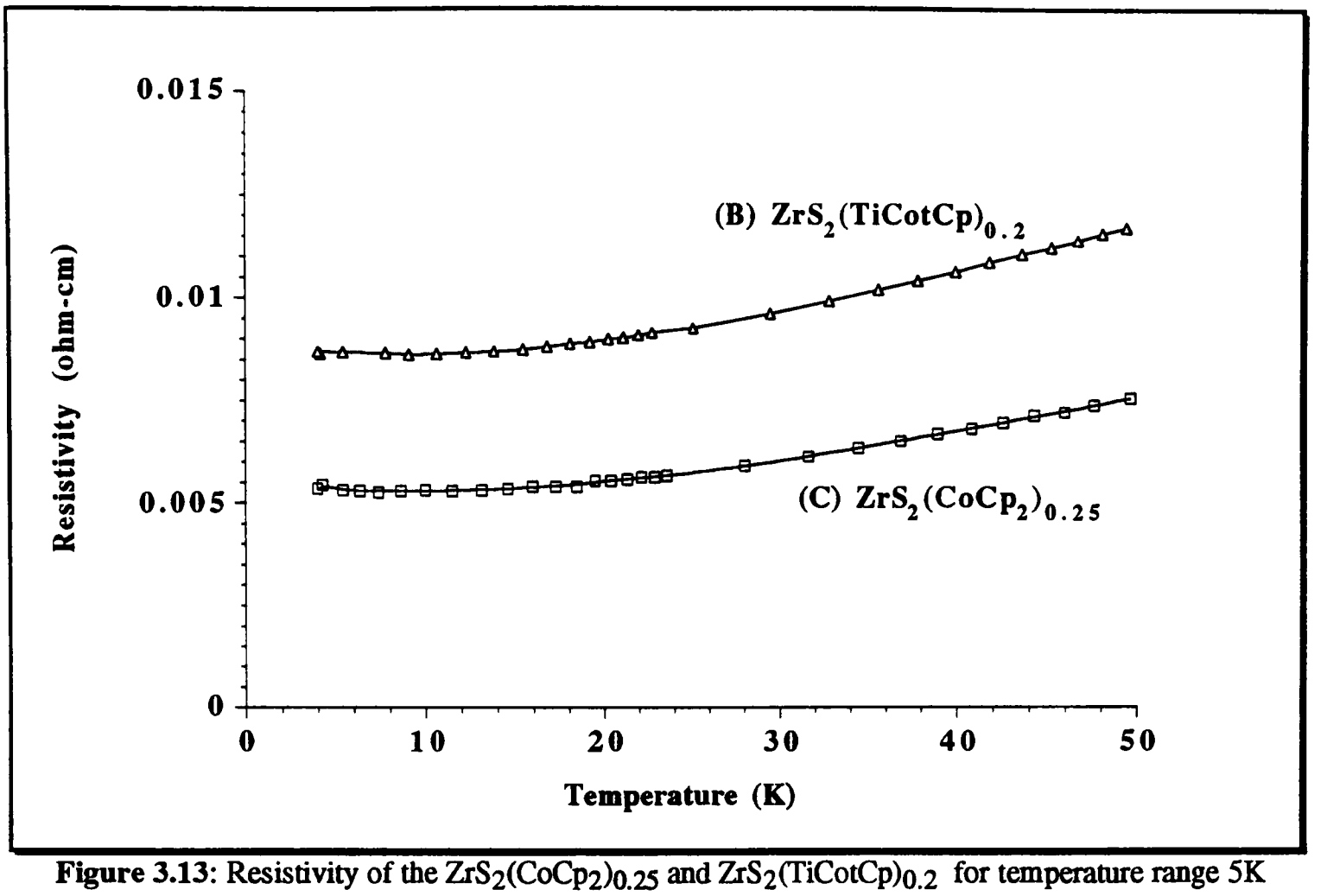

Figure 3.13: Resistivity of the $ZrS_2(CoCp_2)_{0.25}$ and $ZrS_2(TiCotCp)_{0.2}$ for temperature range 5K to 50K

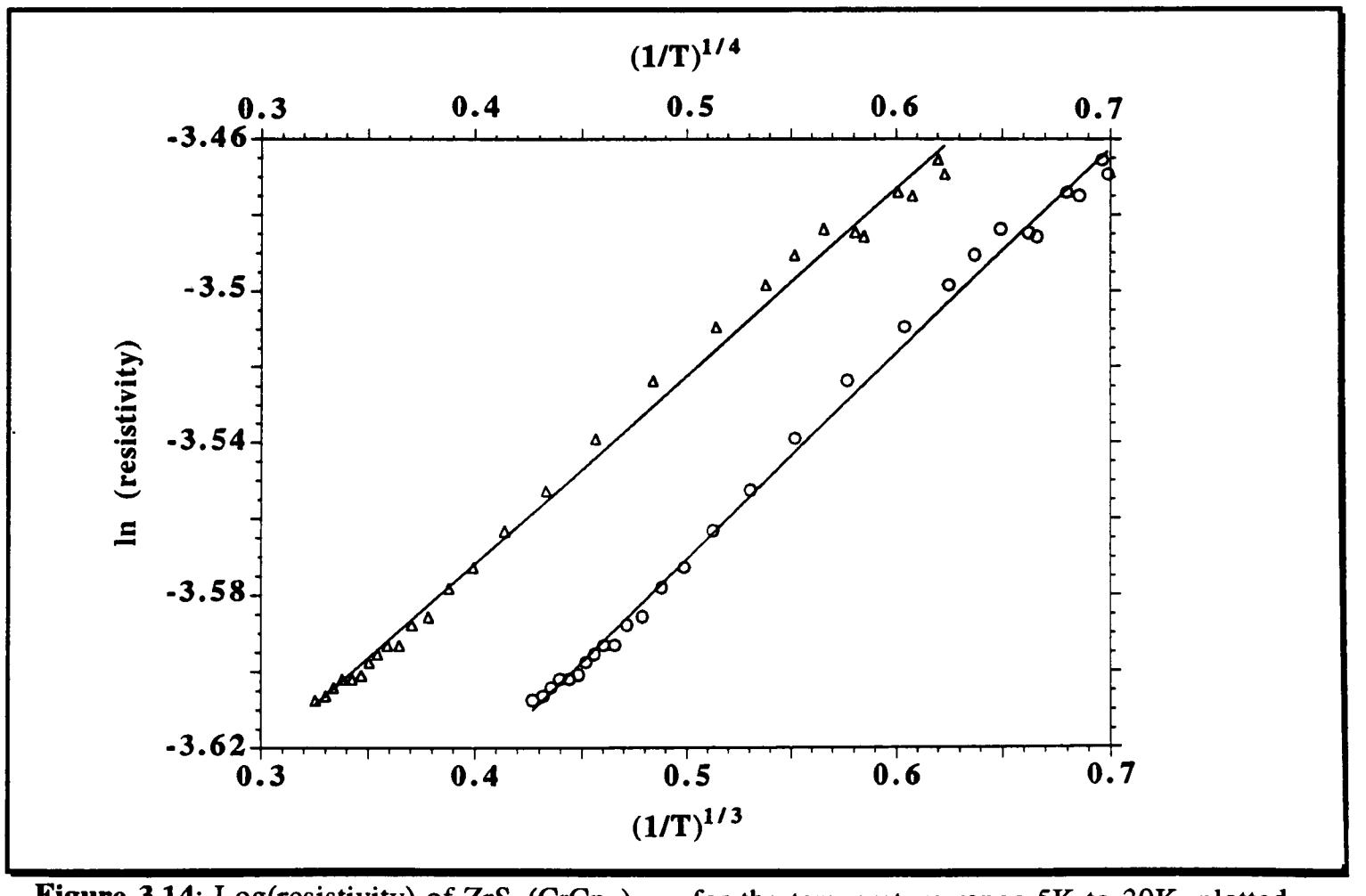

Figure 3.14: Log(resistivity) of $ZrS_2(CrCp_2)_{0.2}$ for the temperature range 5K to 30K, plotted against $(1/T)^{1/3}$ (Δ) and $(1/T)^{1/4}$ (o). Least squares fits to the data give coefficients of fits, R=0.997 and R=0.998 respectively.

3.3. Magnetic Studies on Tin and Zirconium Dichalcogenides

3.3.1. Data acquisition

Magnetic data were obtained between 6K and 300K on a Cryogenics Consultants SCU 500 SQUID Magnetometer in conjunction with a Lakeshore DRC-91C Temperature Controller. For measurements of diamagnetic susceptibility in superconducting samples, pumping of the liquid helium cavity permitted measurements down to 1.6K. Both microcrystalline and single crystal samples were loaded under nitrogen into silica holders and stoppered with a rubber seal before transferring to the cryostat. The silica holders for single crystals were specially modified to allow the samples to be oriented either parallel or perpendicular to the applied field (see Chapter 5). All magnetisation data were corrected for intrinsic diamagnetic susceptibility of the sample holders and the electronic cores of the constituent atoms. The corrected data was converted into molar susceptibility, χ_m, in units of emu per mole, by the relation:

$$\chi_m = \frac{M_{raw}}{10B.n} \qquad (18)$$

where M_{raw} = Raw moment (Am^2)
B = Field (Tesla)
n = number of moles

3.3.2. Results

All of the samples, were measured in at least two fields between temperatures of 6K to 300K. They all exhibit temperature dependent magnetic susceptibility for the temperature range examined. The magnetic behaviour was analysed as the superposition of 3 terms; *Curie paramagnetism, temperature independent diamagnetism* and *temperature independent Pauli paramagnetism.*

$$\chi_{total} = \chi_d + \chi_p + \chi_c \qquad (19)$$

where χ_d= Landau diamagnetism
χ_p = Pauli paramagnetism
χ_c = Curie paramagnetism = C/T

The diamagnetic susceptibilities of the intercalates were estimated by summing the contributions for each of the atoms present, weighted by their stoichiometric abundance {i.e., for $ZrS_2(CoCp_2)_{0.25}$, $\chi_d = \chi_d(ZrS_2) + 0.25*\chi_d(CoCp_2)$}. In performing these calculations, the diamagnetic susceptibilities for the metal dichalcogenides hosts {$\chi_d(ZrS_2)$, $\chi_d(SnS_2)$, $\chi_d(SnSe_2)$} were obtained from Pascal's constants[49] while for the organometallic sandwich complexes, values reported by Konig *et al.* were used[50].

To obtain the temperature independent Pauli paramagnetic component in each intercalate, the Curie tail was subtracted from the value of ($\chi_{total} - \chi_d$). The extent of Curie magnetism was computed using the low temperature data (≤50K), where the Curie contribution greatly exceeds that of the temperature independent terms. An example of the data, before and after correcting for χ_d and χ_c is shown in figure 3.15.

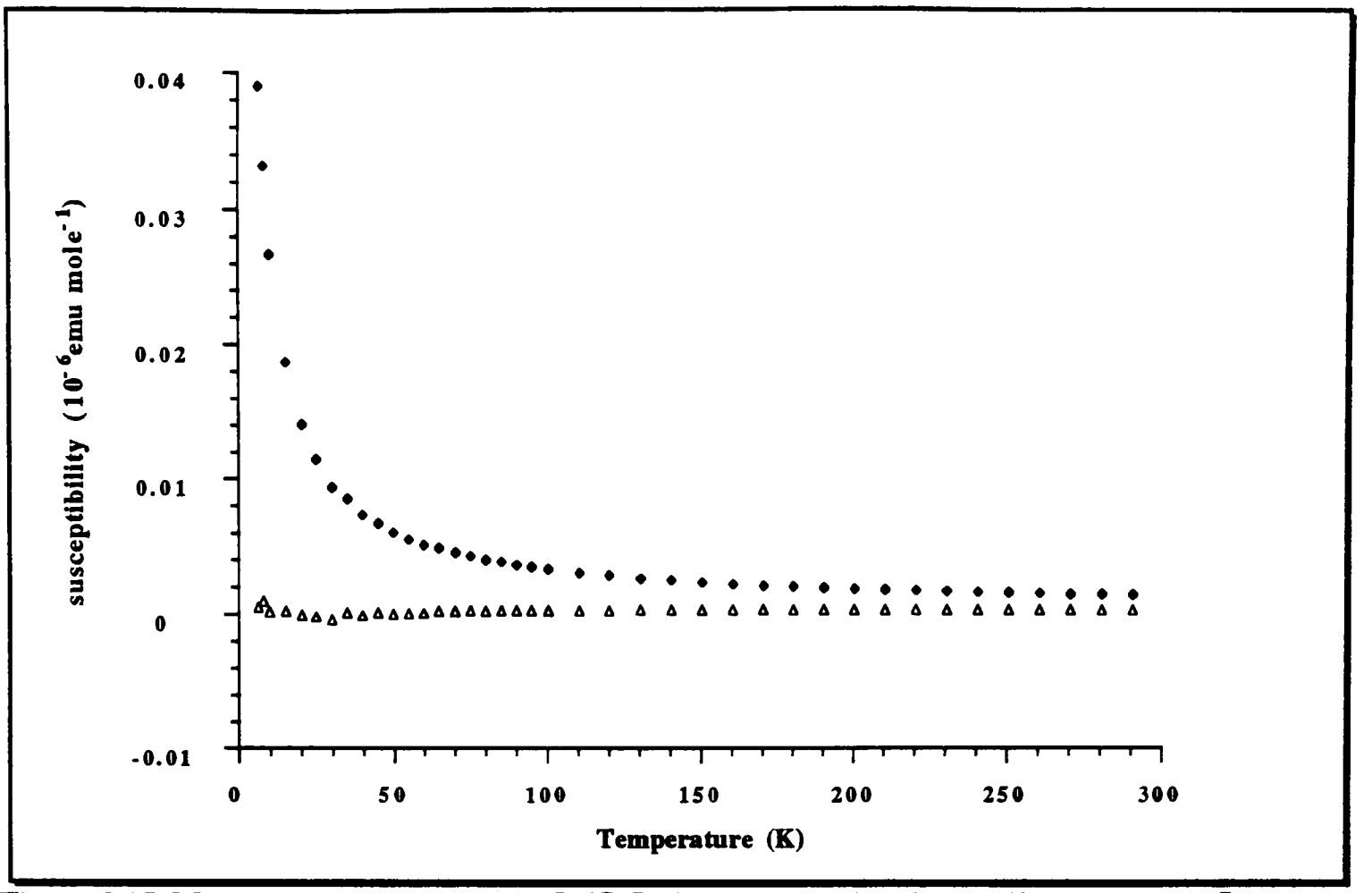

Figure 3.15: Magnetic susceptibility for $ZrS_2(CrCp_2)_{0.2}$, before (♦) and after (Δ)correcting for Curie paramagnetism (χ_p) and temperature independent diamagnetism (χ_d).

Similar analyses were performed for several intercalates of ZrS_2 and tin dichalcogenides and yielded the temperature independent data in Table 3.2.

Table 3.2: Magnetic susceptibilities, χ_d and χ_p, and density of states at the Fermi level, $N(E_F)$,, for the intercalates studied.

Compound	χ_d (10^{-6} emumol^{-1})	χ_p (10^{-6} emumol^{-1})	$N(E_F)$ (states eV^{-1} formula unit $^{-1}$)
$ZrS_2(CoCp_2)_{0.25}$	-123	195	5.9
$ZrS_2(CrCp_2)_{0.2}$	-91	370	11.1
$ZrS_2(TiCotCp)_{0.2}$	-94	20	0.6
$ZrS_2(WChtCp')_{0.2}$	-99	75	2.3
$ZrS_2(MoChtCp')_{0.2}$	-97	175	5.3
$SnSe_2(CoCp_2)_{0.3}$	-156	112	3.4
$SnS_2(CoCp_2)_{0.3}$	-156	75	2.3
$SnS_2(CoCp'_2)_{0.2}$	-136	66	2.0

Charge transfer from guest to host during intercalation into metal dichalcogenides is a well documented phenomenon[51]. The ionisation of the guest can be complete, as in Li_xTiS_2[30, 36], or partial, as in $SnS_2(CoCp_2)_{0.3}$[52]. From the temperature independent

Curie tails obtained from the magnetic data, an attempt was made to estimate the extent of guest ionisation.

Since the hosts (ZrS_2, SnS_2 and $SnSe_2$) are diamagnetic, any localised spins present in the intercalate must be contributed by the organometallic guest or valence trapped electrons in the host. Thus,

$$\mu_{eff}^2(Intercalate) = (z-x)\mu_{eff}^2(Guest) + x\mu_{eff}^2(Guest^+) + x\mu_{eff}^2(Host) \qquad (20)$$

where $\mu_{eff}^2 = zg^2s(s+1)$
Guest $^+$ = ionised organometallic guest
z = stoichiometry of the guest
x = amount of ionised guest.

Measurements by Ahmad on $LiZrS_2$ have shown that it exhibits temperature independent Pauli paramagnetism after correcting for the small amounts of paramagnetic and ferromagnetic impurities present. They also report that the lithium is fully ionised so that the electron donated to the ZrS_2 must be delocalised over the host lattice. Moreover, our resistivity measurements on the ZrS_2 described above show that the host undergoes a non-metal to metal transition after intercalation of the organometallic guests, further strengthening the case that the donated electron is not localised (except at very low temperatures in the case of $(ZrS_2(CrCp_2)_{0.2})$. By assuming a similar fate for the electron donated by the organometallic complexes, then μ_{eff}^2(Reduced host) can be assumed to be 0. Thus,

$$\mu_{eff}^2(Intercalate) = (z-x)\mu_{eff}^2(Guest) + x\mu_{eff}^2(Guest^+) \qquad (20a)$$

In the systems examined, only chromocene contains unpaired spins in both the neutral and cationic forms ($CrCp_2$: $e_{2g}^3a_{1g}^1 \rightarrow CrCp_2^{+1}$: $e_{2g}^2a_{1g}^1$)[53] so that for all the other cases, equation (20) simplifies to:

$$\mu_{eff}^2(Intercalate) = (z-x)\mu_{eff}^2(Guest) \qquad (20b)$$

or
$$\mu_{eff}^2(Intercalate) = x\mu_{eff}^2(Guest^+) \qquad (20c)$$

Solution of equation 20 or one of its simplified forms gives an estimate of x, from which the extent of ionisation of the organometallic guest can be obtained. These are tabulated as percentage ionisations in Table 3.3 and compared with two conventional measures of the ease of ionisation of these organometallics, the gas phase ionisation potential (I.P.) and the electrochemical reduction potential (E^+/E^0).

Table 3.3: Magnetic moments of some organometallic intercalates and the estimated extents of ionisation of the intercalated species.

Compound	μ_{eff} (B. M.)	%ionised†	I.P.(eV)	E^+/E^0(V) #
$ZrS_2(CoCp_2)_{0.25}$	0.38	81	5.56	-0.91‡
$ZrS_2(CrCp_2)_{0.2}$	1.58	64	-	-0.55§
$ZrS_2(TiCotCp)_{0.2}$	0.17	95	5.67*	-
$ZrS_2(WChtCp')_{0.2}$	0.68	90	-	-0.79¶
$ZrS_2(MoChtCp')_{0.2}$	0.68	90	-	-0.63¶
$SnSe_2(CoCp_2)_{0.3}$	0.24	94	5.56	-0.91‡
$SnS_2(CoCp_2)_{0.3}$	0.36	86		
$SnS_2(CoCp'_2)_{0.2}$	0.30	88	-	-

† percentage of fully ionised organometallic guest
‡ from J. L. Robbins *et al.*, J. Amer. Chem. Soc., (1982), **104**, 1882-1893.
§ from U. Koelle and F. Khouzani, Angew. Chem. Int. Ed. Engl., (1980), **19**, 640-641.
* from S. Evans *et al.*, J. Chem. Soc. - Dalton Trans., (1974), 304-311.
¶ from D. P. K. Ng, D. Phil. Thesis, Oxford (1992).
# versus Standard Calomel Electrode (SCE)

3.3.3. Discussion

From the size of the Curie tails, estimates could be made of the extent of ionisation of the organometallic guests. The results indicate within experimental error that virtually complete ionisation occurs for all of the organometallic species except for $ZrS_2(CrCp_2)_{0.2}$, which has the smallest reduction potential (see Table 3.3). The significantly greater proportion of un-ionised, neutral $CrCp_2$ reduces the electrostatic interaction between guest and host layers and may thus be responsible for the more extensive electron-phonon coupling in $ZrS_2(CrCp_2)_{0.2}$ (see Figure 3.22b).

Amongst the other intercalates, the apparent lack of correlation between ease of ionisation in the organometallic guests (as measured by I.P. or electrochemical reduction potentials) and the calculated extents of ionisation is likely to be due to the large experimental uncertainties for these measurements.

The small stoichiometries of the organometallic guests (0.2 to 0.3 per formula unit of host) result in small magnetic moments, a problem that is often accentuated by the ionisation of a paramagnetic guest upon intercalation. To avoid the effects of the temperature independent Pauli susceptibility (which was usually significant relative to the small magnetic moments being measured), a restricted and therefore rather less statistically significant data set (temperature < 50K) was used to fit the Curie expression. Moreover, the calculation of the extent of ionisation is very sensitive to the stoichiometry of the guest, which could not be determined to an accuracy greater than ±10% by C/H/N

elemental analysis, because of the air sensitive nature as well as the low stoichiometric presence of the organometallic. As such, the confidence level for the extents of ionisation are at best 10 to 15%, so that it is difficult to make comparisons amongst the intercalates where greater than 80% of the guest is ionised. Nonetheless, the results show that ionisation of the guest does occur in all the organometallic intercalates, and in particular, that the chromocene guest is the least ionised upon intercalation. This observation of significant electron donation from guest to host is consistent with the conductivity results of the previous section and is similar to that found in simpler lithium and amine intercalates of metal dichalcogenides.

The Pauli paramagnetism in metal dichalcogenide intercalates has been extensively studied and in several cases, it is shown to be higher than expected from that based on band structure calculations assuming free electron behaviour[30, 31]. Such enhancement of the Pauli susceptibility has been demonstrated in various lithium intercalates of the metal dichalcogenides, charge transfer salts[54] and C_{60} intercalates[55] and is thought to arise from greater electron correlation due to the narrowing of the band width near the Fermi level[56].

The enhanced values of Pauli susceptibility reported by Murphy [30] for $LiTiSe_2$ and $LiTiS_2$ (1.77×10^{-4} emu mol^{-1} and 2.46×10^{-4} emu mol^{-1} respectively) are very similar to the values for Pauli susceptibility measured in the $CrCp_2$, $CoCp_2$ and MoChtCp intercalates of ZrS_2. In the absence of detailed information on the band structure of these latter intercalates, it is difficult to infer the extent, if any, of Pauli enhancement in these organometallic intercalates. However, the previously reported value of the Pauli susceptibility in $LiZrS_2$[21] can provide the following useful comparisons. Unlike $LiZrS_2$, an average of less than one electron per Zr atom is donated by the organometallic guests (since stoichiometry of guest:host is *ca,* 1:5). If we assume that the band structure of the organometallic intercalates is similar to that for the lithium intercalate of ZrS_2 (i.e., the rigid band model applies in both cases); then the $N(E_F)$ of 2.4 states eV^{-1} formula $unit^{-1}$ obtained by Ahmad for $LiZrS_2$[21] represents an upper limit in the absence of exchange enhancement in these organometallic intercalates. Under such an assumption, it would appear that the $CrCp_2$, $CoCp_2$ and MoChtCp' intercalates of ZrS_2 exhibit enhanced Pauli susceptibilities.

However, like the extents of guest ionisation calculated above, the Pauli susceptibilities estimated are subject to large experimental uncertainties. As alluded to above, the relatively large values of Curie susceptibility in these organometallic intercalates makes accurate estimates of the underlying contribution from Pauli susceptibility difficult. Frequently, the magnitude of the Curie term even at 300K is a significant percentage (20-30%) of the total susceptibility so that the uncertainty in calculated χ_p's are high. A more definitive test of whether there is significant exchange enhancement in these systems would be specific heat measurements since they would not

be as significantly affected by the presence of the organometallic species. Alternatively, Hall, Seebeck or infra-red reflectivity measurements could be used to probe the carrier density in these systems.

Nonetheless, in $ZrS_2(CrCp_2)_{0.2}$ at least, the magnitude of the Pauli susceptibility is larger than can be accounted for by experimental uncertainty. Moreover, the resistivity data, which shows electron localisation at low temperatures, is consistent with a narrow band gap at the Fermi level. The electron correlation in the band is likely to be significant, thus giving rise to an enhanced Pauli susceptibility, in accordance with the susceptibility measurements.

3.4. Superconductivity in $SnSe_2(CoCp_2)_{0.3}$

Unlike the organometallic intercalates of ZrS_2 discussed previously, $SnSe_2(CoCp_2)_{0.3}$ is a Type II superconductor which exhibits semi-metallic resistivities in the normal state[48]. Measurements on the variable temperature resistivity and critical field anisotropy of this superconducting intercalate are described in the following section.

3.4.1. Electrical Resistivity

The sample studied in this chapter differed from that obtained by Formstone *et al.*[48] in two main respects: (a) non-metallic conductivity was observed from *ca.* 70K to 300K and (b) the superconducting temperature of the crystal was 8.3K, about 36% higher than the value reported by Formstone *et al.*

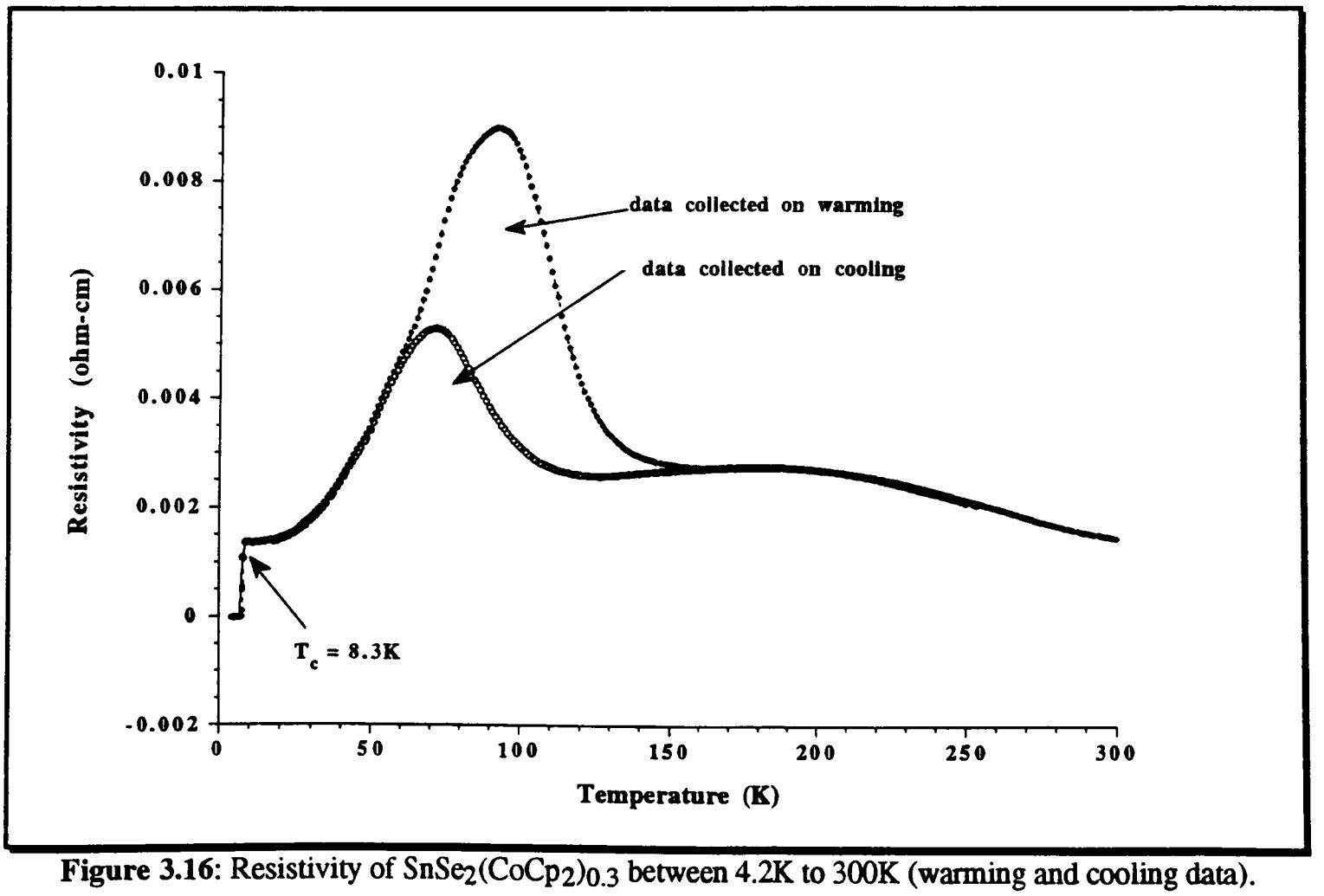

Figure 3.16: Resistivity of $SnSe_2(CoCp_2)_{0.3}$ between 4.2K to 300K (warming and cooling data).

The intercalate shows gradually increasing resistivity as the sample is cooled but at *ca.* 125K, a large increase in resistivity is observed. This increase in resistivity is ascribed to the onset of a charge density wave, similar to that observed in some low-dimensional metals (2H-TaS_2, 2H-$TaSe_2$, κ-(BEDT-TTF)$_2$Cu(NCS)$_2$) where periodic lattice distortions occur because of strong electron-phonon coupling interactions[54, 57]. The resistivity increases to its maximum value at *ca.* 95K before decreasing till 8.3K where a sudden transition (ΔT_c = 0.3K) to the superconducting state occurs. The resistance anomaly shows hysteresis, with the peak of resistance occuring at *ca.* 90K for warmed samples.

3.4.2 Critical field measurements

One estimate of the anisotropy of a superconductor can be obtained by measurement of the of the critical field H_{c2} parallel ($H_{c2\parallel}$) and perpendicular ($H_{c2\perp}$) to the host layers. The values of $H_{c2\parallel}$ and $H_{c2\perp}$ for $SnSe_2(CoCp_2)_{0.3}$, a type II superconductor[41], were measured on oriented single crystals in a SQUID magnetometer with either the host *ab*–plane parallel or perpendicular respectively to the applied magnetic field. $H_{c2\parallel}$ and $H_{c2\perp}$ were defined as the magnetic fields at which the diamagnetic shielding was zero and complete flux penetration had occurred. Figure 3.17 shows typical magnetisation *versus* field plots between 2.0 and 5.7K for a single crystal of $SnSe_2(CoCp_2)_{0.3}$ oriented with the basal planes of the host perpendicular to the magnetic field. Above 6.1K, a Meissner effect was still observable but the data was not of a sufficiently good quality to extract critical field values.

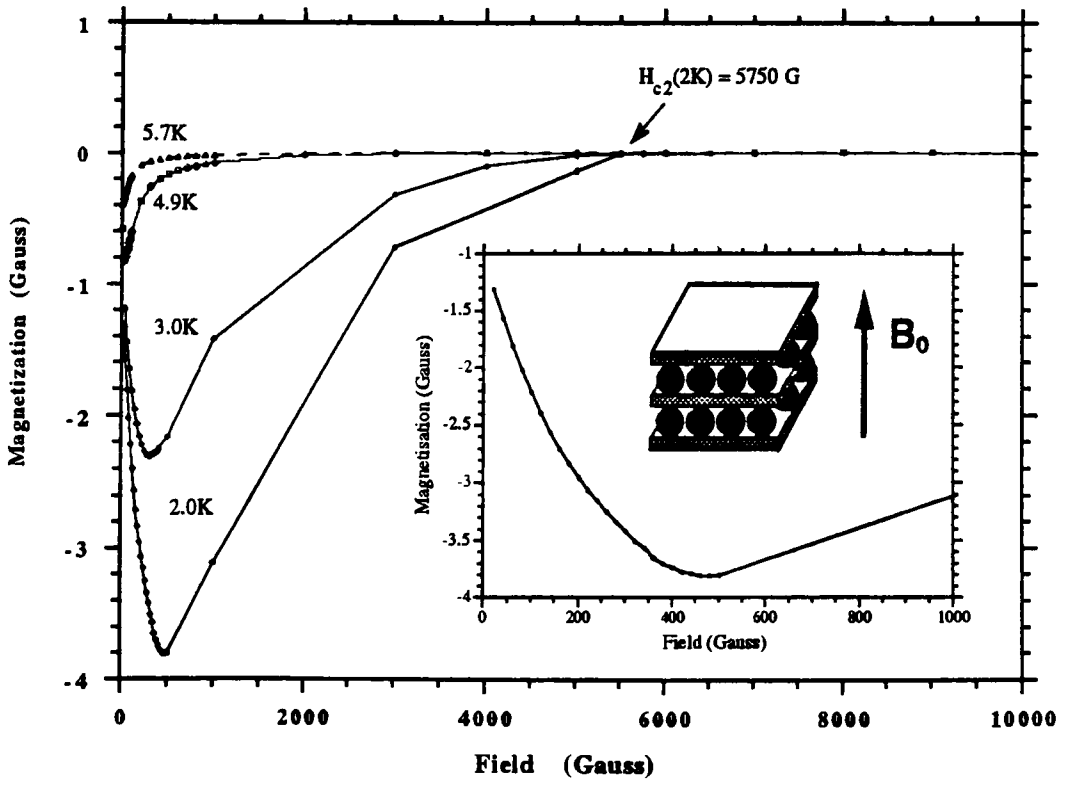

Figure 3.17: Typical magnetisation vesus field between 2.0 and 5.7K for $SnSe_2(CoCp_2)_{0.3}$ oriented with the basal planes of the crystal perpendicular to the magnetic field.

3.4.3. Discussion

As with previous studies on superconductivity in layered transition metal chalcogenides[58, 59], we have applied the Ginzburg-Landau description for anisotropic superconductivity.

$$H_{c2\theta}(T) = \frac{\Phi_0}{2\pi\xi^2(T)\sqrt{\left\{\cos^2\theta + \frac{m}{M}\sin^2\theta\right\}}} \qquad (20)$$

such that

$$\left(\frac{M}{m}\right) = \left(\frac{H_{c2\parallel}}{H_{c2\perp}}\right)^2 \qquad (21)$$

where m and M are the pair masses of propagation within the layers and in the z-direction respectively, Φ_0 the flux quantum, ξ the coherence length in the layer plane and θ the angle between the layers and the applied field. Furthermore, the coherence length in the z-direction, ξ_z, is related to ξ by:

$$\xi_z^2(T) = \frac{m}{M}\xi^2(T) \qquad (22)$$

where ξ_z =coherence length in the z–direction

The thermodynamic critical field, H_c, is related to the upper and lower critical fields (H_{c2} and H_{c1}) through the Ginzburg-Landau parameters as shown in the equations below.

$$\kappa = \frac{1}{\sqrt{2}}\frac{H_{c2}}{H_c} \qquad (23)$$

$$\kappa = \frac{1}{\sqrt{2}}\frac{H_c}{H_{c1}}(\ln\kappa + 0.497) \qquad (24)$$

The temperature dependence of H_{c2} for both crystal orientations is shown in Figure 3.18. The superconducting temperature, T_c, extrapolated to zero field is 8.3K, in good agreement with the resistivity data presented in Section **3.4.1**. The critical properties and anisotropy of the superconducting state have been modelled using Ginzburg-Landau theory and a model proposed by Klemm, Beasley and Luther [60, 61]. The calculated data have been tabulated in Table 3.4, along with critical field data reported by previous workers[42, 59]. The dimensionless parameters, α, and r are as defined by Klemm, Beasley and Luther. The former, α, characterizes the strength of pair breaking due to Pauli paramagnetism (assuming no spin-orbit scattering) relative to that due to orbital effects while r characterizes the relative two-dimensionality of the material (smaller r values imply a greater degree of two-dimensionality).

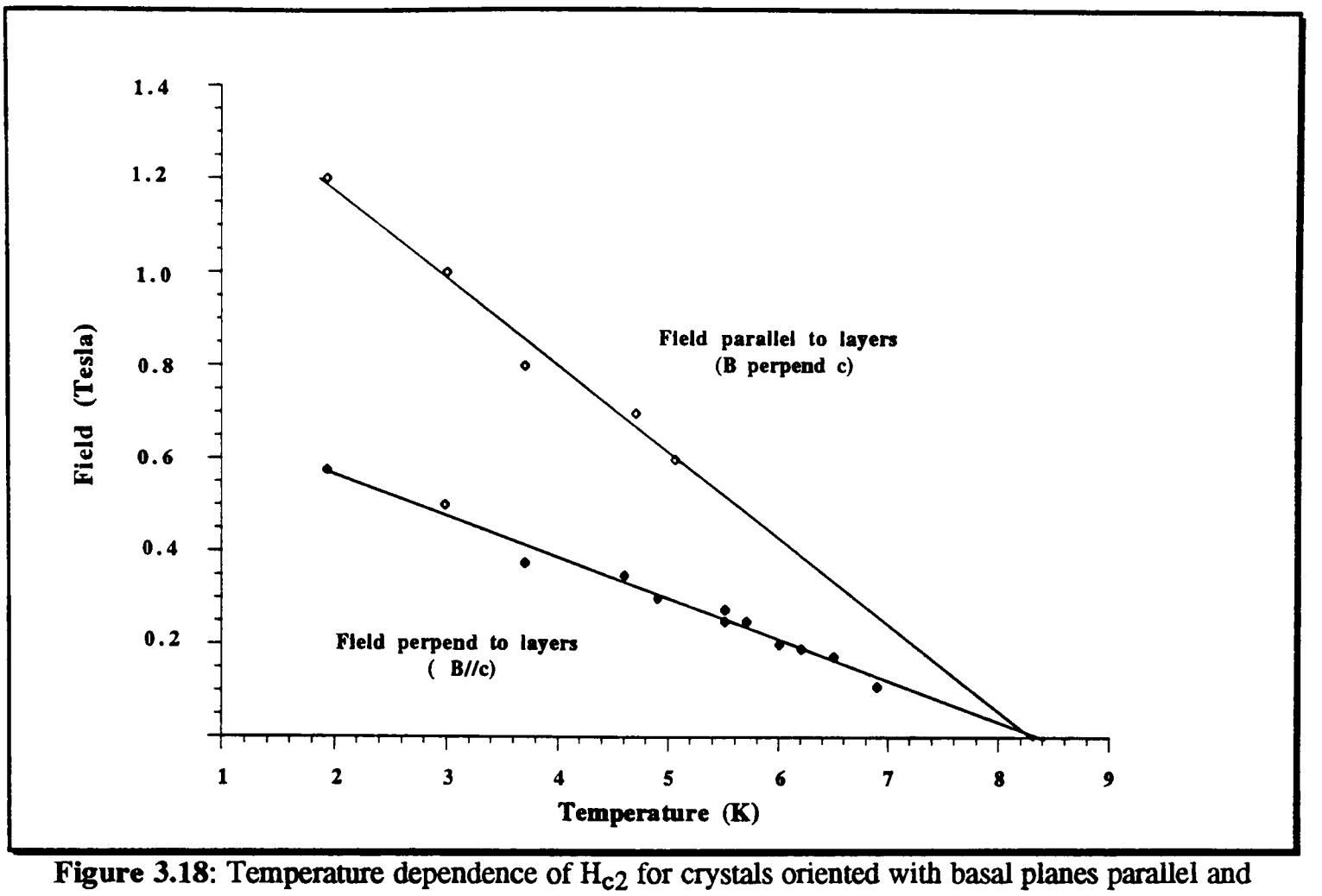

Figure 3.18: Temperature dependence of H_{c2} for crystals oriented with basal planes parallel and perpendicular to the applied field.

The Ginzburg-Landau coherence lengths derived from the critical field data suggests that $SnSe_2(CoCp_2)_{0.3}$ exhibits almost *isotropic superconductivity* with an anisotropy ratio, $\xi(0)/\xi_z(0)$, of 2. This observation is in sharp contrast to the superconducting intercalates of TaS_2 where the anisotropy ratios are at least one order of magnitude greater ($\xi(0)/\xi_z(0)$ = 20 to 40). The anisotropy ratio of $SnSe_2(CoCp_2)_{0.3}$ is more comparable to that of the superconducting metal diselenides and their intercalates[42, 62-64], suggesting that the reduced anisotropy is due to the greater polarisability of selenium relative to sulfur atoms. However, the difference in anisotropies cannot be accounted for wholly by the polarisability of selenium versus sulfur; $SnSe_2(CoCp_2)_{0.3}$ has an anisotropy ratio *half* that of metal diselenides and their intercalates but an interlayer spacing that is *twice* as large. This suggests that the presence of the organometallic guest also contributes to the reduced anisotropy of $SnSe_2(CoCp_2)_{0.3}$ relative to similar metal dichalcogenide systems. Such a hypothesis is consistent with single crystal conductivity studies on $SnSe_xS_{2-x}(CoCp_2)_{0.3}$ $\{0 \leq x \leq 1.3\}$ which show these intercalates exhibit three-dimensional variable range hopping in the normal state[48]. The existence of a three-dimensional hopping mechanism provides evidence that, at least in the normal state, the conduction mechanism in this organometallic intercalate is not confined to the layer planes.

Table 3.4: Comparison of superconducting parameters in some layered metal dichalcogeneide systems.

Compound	δ†	T_c (K)	$-dH_{c2\perp}/dT$ (kG/K)	$-dH_{c2//}/dT$ (kG/K)	$[M/m]^{1/2}$	ξ(0) (Å)	ξz(0) (Å)	r‡	α§
$SnSe_2(CoCp_2)_{0.3}$	*11.5*	*8.3*	*0.9*	*1.88*	*2*	*210*	*105*	*422*	*0.1*
$TaS_2(collidine)_{0.17}$	9.7	3.2	3.3	100	30	180	6.0	1.95	5.3
$TaS_2(pyridine)_{0.5}$	12.0	3.47	2.8	70	25	183	7.3	1.90	3.7
$TaS_2(aniline)_{0.75}$	18.1	2.9	2.6	96	37	209	5.6	0.50	5.1
$TaS_{1.6}Se_{0.4}$	6.1	4.1	8.0	44	5.5	100	18.2	4.53	2.3
$NbSe_2$	6.3	7.1	7.7	27.5	-	-	26	>100	1.5
$Nb_{0.8}Ta_{0.2}Se_2$	-	-	8.2	59.0	-	-	13	20	3.1
$Li_{0.49}ZrSe_2$	6.6	1.70	0.759	2.54	3.10	510	150	2600	0.1
$Na_{0.52}ZrSe_2$	7.5	2.00	1.74	6.72	2.80	310	80	570	3.1
$Na_{0.32}ZrSe_2$	7.0	2.08	2.33	7.56	2.95	260	80	660	0.1
$K_{0.71}ZrSe_2$	8.5	2.02	2.64	11.4	5.85	250	58	260	0.6
$K_{0.78}ZrSe_2$	8.1	2.19	2.10	11.6	5.70	400	72	360	0.6
$Rb_{1.0}ZrSe_2$	8.3	1.52	2.13	14.6	6.20	390	58	250	0.8
$Rb_{1.0}ZrSe_2$	8.3	1.85	2.00	7.88	4.77	300	110	940	0.4
$Cs_{0.76}ZrSe_2$	9.2	1.39	-	-	-	-	-	-	-
$Cs_{0.84}ZrSe_2$	9.2	1.38	3.54	17.3	3.00	260	73	320	0.9

† δ = interlayer spacing in Å.
‡ $r = (4/\pi)[\xi_z(0)/(s/2)]^2$
§ $\alpha = [dH_{c2//}/dT]/[18.95kG/K]$

Moreover, in an earlier photoelectron study of these materials. Formstone *et al.*[65] reported that the X-ray photoelectron spectra (PES) of $SnSe_2(CoCp_2)_{0.3}$ showed the presence of both neutral and oxidised cobaltocene intercalated within the host layer planes[65] in a 3:1 ratio. It has been hypothesised that this mixed valence situation would facilitate inter–layer electronic conduction and thus reduce the electronic anisotropy[48, 66]. However, Cleary *et al.* have suggested that the mixed valency of the cobalt observed in PES measurements of these intercalates is due to reduction of cobaltocenium *during* the experiment and that the metallocene actually exists in the intercalate as the *fully* ionised cation $CoCp_2^+$.[74] The magnetic susceptibility measurements of the previous section also support Cleary's assertion that the cobaltocene in $SnSe_2(CoCp_2)_{0.3}$ is virtually completely ionised. Nonetheless, the existence or absence of neutral $CoCp_2$ notwithstanding, interlayer conduction does occur. Electron hopping within and across the layers of cobaltocene requires only that molecules are redox active. Two indicators of the redox activity of $CoCp_2$ are its low ionisation potential (5.56 eV)and its highly negative electrochemical reduction potential (-0.91V vs SCE) Since the large interlamellar spacings (*ca.* 11Å) mean that Se-Se interactions are unlikely to be significant, the molecules of the cobaltocene intercalant must somehow mediate the interlayer conduction process.

From our low temperature (<4K) magnetisation data (see Figure 3.17), we can estimate the fields at which the observed magnetisation deviates from linearity. For example, at 2K, when the applied field is perpendicular to the layer planes, deviation occurs at *ca.* 125 G while parallel to the layer planes, this occurs at *ca.* 100 G. This should ostensibly allow us to extract $H_{c1\perp}$and $H_{c1||}$ and hence calculate the thermodynamic critical field, H_c (using relations 23 and 24). However, in reality, shape-dependent demagnetisation effects need to be taken into account if realistic estimates of $H_{c1||}$ and $H_{c1\perp}$ are to be obtained. While previous workers[67, 68] have studied these effects for rectangular slabs, they do not address the situation for thin, plate-like samples such as ours. Moreover, without a good idea of the critical currents of the sample in both orientations, it is impossible to tell if the deviation from linearity is from critical field or critical current effects.

As an alternative means of evaluating H_c, we assumed a BCS-like gap of $\Delta = 1.76 k_B T_c$, so that we could evaluate $H_c(0)$ from the density of states at the Fermi level $N(E_F)$ by the equation,

$$H_c^2(0) = \mu_0 \Delta^2(0) N(E_F) \qquad (26)$$

where μ_0 is the permeability of free space. For a T_c of 8.3K, $\Delta(0) = 2.01 \times 10^{-22}$ J . Above 8.3 K $SnSe_2(CoCoCp_2)_{0.3}$ exhibits nearly temperature independent paramagnetism (see previous section). From the magnitude of this Pauli paramagnetism, $N(E_F)$ of $SnSe_2\{Co(\eta\text{-}C_5H_5)_2\}_{0.3}$ in the normal state was estimated to be 2.26×10^{22}

states/eVcm^3, so that $H_c(0)$ = 602 G. The empirical relation known as Tuyn's law[69] allows $H_c(T)$ to be calculated from the thermodynamic critical field, $H_c(0)$, and the superconducting temperature, T_c:

$$H_c(T) = H_c(0)\{1-(T/T_c)^2\} \qquad (27)$$

Assuming Tuyn's law to be applicable in $SnSe_2(CoCoCp_2)_{0.3}$, $H_c(2K)$ = 457 G.

3.5. Conclusion

The electrical resistivities and magnetic susceptibilities of several organometallic intercalates of zirconium and tin dichalcogenides have been measured between 4.2 and 300K. The donation of electrons from the organometallic species to the host material causes these compounds to exhibit metallic behaviour down to very low temperatures. The extent of ionisation of all the organometallic guests except $CrCp_2$ parallels that of alkali metals in analogous metal dichalcogenide intercalates, where complete charge transfer occurs. Both the resistivity and magnetic data indicate that $ZrS_2(CrCp_2)_{0.2}$ is electronically quite different from $ZrS_2(CoCp_2)_{0.25}$ and $ZrS_2(TiCotCp)_{0.2}$. At low temperatures, localisation of electrons occurs within the former but not the latter two compounds. Moreover, the Pauli susceptibility in the chromocene intercalate is also significantly higher than that for the cobaltocene and TiCotCp intercalates. The resistivity and magnetic data are therefore consistent with a narrower band width for $ZrS_2(CrCp_2)_{0.2}$ than the $CoCp_2$ and TiCotCp intercalates.

The anisotropy of superconductivity in the cobaltocene intercalate of $SnSe_2$ has also been examined. Measurement of the critical field anisotropy shows that the superconductivity in this superconducting intercalate is almost three dimensional. This contrasts with earlier reports on the layered superconducting transition metal disulfides[70] and their intercalates[71, 72] such as the long chain organic amine intercalates of 2H-TaS_2, where the large interlayer separation is so large that superconductivity is thought to be confined to the layer planes[73]. The large discrepancy in anisotropy ratios may be ascribed to the difference in polarisability between sulfur and selenium atoms in the layers (which would facilitate inter-layer interactions) but in view of the three-dimensional variable range hopping conduction for $SnSe_xS_{2-x}(CoCp_2)_{0.3}$ intercalates in the normal state[48], the superconducting mechanism in $SnSe_2(CoCp_2)_{0.3}$ is likely to also include inter-layer interactions which are mediated by the organometallic intercalant.

References

1. W. Y. Liang, in *Intercalation in Layered Materials*, ed. M. S. Dresselhaus, Plenum Press: New York and London, 1986, p. 31

2. *The Electron-Phonon Interaction in Metals.*, ed. G. Grimvall, N. Holland Publ. Co.: Amsterdam, 1981.

3. G. T. Meaden, *Electrical Resistivity of Metals*, Heywood Books: London, 1966.

4. N. F. Mott and E. A. Davis, *Electronic Processes in non-crystalline materials*, Clarendon Press: Oxford, 1971.

5. D. A. Greenwood, *Proc. Phys. Soc.* (1958), **71**, 585.

6. R. Kubo, *Can. J. Phys.* (1956), **34**, 1274.

7. *Solid State Chemistry Techniques.*, ed. A. K. Cheetham and P. Day, Clarendon: Oxford, 1988.

8. A. Many, Y. Goldstein and N. B. Grover, *Semiconductor Surfaces*, N. Holland, Amsterdam, 1965.

9. L. J. van der Pauw, *Philips Res. Reports* (1954), **13**, 1-9.

10. R. L. Carlin, *Magnetochemistry*, Springer-Verlag: Berlin, 1986.

11. J. Bardeen, L. N. Cooper and J. R. Schrieffer, *Phys. Rev.* (1957), **108**, 1175.

12. J. A. Benda, *Phys. Rev. B.* (1974), **10**, 1409-20.

13. A. H. Thompson, *Phys. Rev. Lett.* (1975), **35**, 1786-9.

14. W. G. Baber, *Proc. R. Soc.* (1937), **158A**, 383-96.

15. C. A. Kukkonen and P. F. Maldague, *Phys. Rev. Lett.* (1976), **37**, 782-5.

16. R. H. Friend, D. Jerome, W. Y. Liang, J. C. Mikkelsen and A. D. Yoffe, *J. Phys. C.* (1977), **10**, L705-8.

17. P. C. Klipstein, A. G. Bagnall, W. Y. Liang, E. A. Marseglia and R. H. Friend, *J. Phys. C.* (1981), **14**, 4067-81.

18. S. Takeuchi and H. Katsuta, *J. Jap. Inst. Metals* (1970), **34**, 758-63.

19. A. H. Thompson, F. R. Gamble and C. R. Symon, *Mater. Res. Bull.* (1975), **10**, 915-20.

20. A. M. Ghorayeb and R. H. Friend, *J. Phys. C* (1987), **20**, 4181-4200.

21. N. Ahmad, P. C. Klipstein, S. D. Obertelli, E. A. Marseglia and R. H. Friend, *J. Phys. C: Solid State Physics* (1987), **20**, 4105-4114.

22. F. J. DiSalvo and J. E. Graebner, *Solid State Comm.* (1977), **23**, 825.

23. Y. Onuki, R. Inada and S. Tanuma, *Physica B* (1980), **99**, 177.

24. R. Inada, Y. Onuki and S. Tanuma, *J. Phys. Soc. Japan* (1983), **52**, 3536-43.

25. M. Sarma, A. R. Beal, S. Nulsen and R. H. Friend, *J. Phys. C.* (1982), **15**, 4367-78.

26. H. Fukuyama and K. Yosida, *J. Phys. Soc. Japan* (1979), **46**, 1522.

27. H. Fukuyama and K. Yosida, *J. Phys. Soc. Japan* (1979), **46**, 102.

28. P. W. Anderson, *Phys. Rev.* (1958), **109**, 1492.

29. P. Fazekas and E. Tosatti, *Phil. Mag. B.* (1979), **39**, 229.

30. D. W. Murphy, F. J. DiSalvo, G. W. Hull and J. W. Wasczczak, *Inorg. Chem.* (1976), **15**, 17.

31. D. R. P. Guy, R. H. Friend, D. C. Johnson and M. J. Sienko, *J. Phys. C.* (1982), **15**, 1251-5.

32. D. R. P. Guy, R. H. Friend, M. R. Harrison, D. C. Johnson and M. J. Sienko, *J. Phys. C.* (1982), **15**,

1245-9.

33. L. Trichet, A. O. Ghaloun, J. Rouxel, Y. Chabre and C. Berthier, *Studies in Inorganic Chemistry*, Elsevier: New York, 1983.

34. R. H. Friend, D. Jerome, D. Schleich and P. Molinie, *Solid State Comms.* (1978), **27**, 169-173.

35. J. I. Meakin, P. C. Klipstein and R. H. Friend, *J. Phys. C.* (1986), **19**, 4953.

36. L. Bernard, W. Glausinger and P. Colombet, *Solid State Ionics* (1985), **17**, 81-9.

37. W. F. Brinkman and T. M. Rice, *Phys. Rev. B.* (1970), **2**, 4302.

38. N. F. Mott, *Metal-Insulator Transitions*, Taylor and Francis: London, 1990.

39. F. R. Gamble and A. H. Thompson, *Solid State Comms* (1978), **27**, 379-382.

40. F. R. Gamble, E. J. DiSalvo, R. A. Klemm and T. H. Geballe, *Science* (1970), **168**, 568-571.

41. C. A. Formstone, E. T. Fitzgerald, D. O'Hare, P. A. Cox, M. Kurmoo, J. W. Hodby, D. Lillicrap and M. Goss-Custard, *Chem. Comm.* (1990), 501-503.

42. Y. Onuki, S. Yamananka, R. Inada, M. Kido and S. Tanuma, *Syn. Met.* (1983), **5**, 245-55.

43. C. A. Formstone, *D. Phil Thesis*. Oxford University, 1991.

44. D. L. Greenaway and R. Nitsche, *J. Phys. Chem. Solids* (1965), **26**, 1445-1458.

45. A. A. Balchin, in *Crystallography and Crystal Chemistry of Materials with Layered Structures*, ed. F. Levy, D. Reidel Publishing Company: Dordrecht-Holland, 1976, p. 1-50

46. M. Sarma, A. R. Beal, S. Nulsen and R. H. Friend, *J. Phys. C* (1982), **15**, 477-93.

47. P. C. Klipstein and R. H. Friend, *J. Phys. C.* (1987), **20**, 4169-79.

48. C. A. Formstone, M. Kurmoo, E. T. Fitzgerald, P. A. Cox and D. O'Hare, *J. Mater. Chem.* (1991), **1**, 51-57.

49. P. W. Selwood, *Magnetochemistry*, Interscience: New York, 1956.

50. E. Konig, R. Schnakig, S. Kremer, B. Kanellakopulos and R. Klenze, *Chemical Physics* (1978), **27**, 331-344.

51. R. H. Friend and A. D. Yoffe, *Adv. Phys.* (1987), **36**, 1-94.

52. D. O'Hare, W. Jaegermann, D. L. Williamson, F. S. Ohuchi and B. A. Parkinson, *Inorg. Chem.* (1988), **27**, 1537-1542.

53. C. Elschenbroich and A. Salzer, *Organometallics: A Concise Introduction*, VCH: Weinheim, 1991.

54. I. D. Parker, R. H. Friend, M. Kurmoo, P. Day, C. Lenoir and P. Batail, *J. Phys. C.* (1989), **1**, 4479.

55. A. P. Ramirez, M. J. Rosseinsky, D. W. Murphy and R. C. Haddon, *Phys. Rev. Lett.* (1992), **69**, 1687-90.

56. H. P. Hughes, C. Webb and P. M. Williams, *J. Phys. C.* (1980), **13**, 1125.

57. P. C. Klipstein, R. H. Friend and A. D. Yoffe, *Philos. Mag. B* (1985), **52**, 611.

58. R. C. Morris and R. V. Coleman, *Phys. Rev. B* (1973), **7**, 991.

59. D. E. Prober, R. E. Schwall and M. R. Beasley, *Phys. Rev. B* (1980), **21**, 2717-2733.

60. R. A. Klemm, M. R. Beasely and A. Luther, *J. Low Temp. Phys.* (1974), **16**, 607-613.

61. R. A. Klemm, A. Luther and M. R. Beasley, *Phys. Rev. B* (1975), **12**, 877.

62. M. Ikebe, K. Katagiri, K. Noto and Y. Muto, *Physica B* (1980), **99**, 209-214.

63. Y. Onuki, R. Inada, S. Tanuma, S. Yamanaka and H. Kamimura, *Physica B* (1981), **108**, 1037-8.

64. Y. Onuki, R. Inada, S. Tanuma, S. Yamanaka and H. Kamimura, *J. Phys. Soc. Japan* (1982), **51**, 880.

65. C. A. Formstone, E. T. Fitzgerald, P. A. Cox and D. O'Hare, *Inorg. Chem.* (1990), **29**, 3860-3866.

66. D. O'Hare, H. V. Wong, S. Hazell and J. W. Hodby, *Adv. Mater.* (1992), **4**, 658-660.

67. F. M. Sauerzopf, H. P. Wiesinger and H. W. Weber, *Cryogenics* (1990), **30**, 650-655.

68. M. Soinski, *IEEE Transactions on Instrumentation and Measurement* (1990), **39**, 704-710.

69. J. S. Blakemore, in *Solid State Physics*, ed. Cambridge University Press: Cambridge, 1985, p. 271

70. R. F. Frindt, *Phys. Rev. Lett.* (1972), **28**, 299-301.

71. M. Ikebe, K. Katagiri and Y. Muto, *Physica B + C* (1981), **105**, 453-7.

72. F. R. Gamble, J. H. Osiecki, M. Cais, R. Pisharody, F. J. DiSalvo and T. H. Geballe, *Science* (1971), **174**, 493-497.

73. F. J. DiSalvo, R. Schwall, T. H. Geballe, F. R. Gamble and J. H. Osiecki, *Phys. Rev. Lett.* (1971), **27**, 310-313.

74. D. A. Cleary, D. R. Baer, *Chem. Mat.*, (1992), **4**, 112-116.

CHAPTER FOUR

INTERCALATION KINETICS

CHAPTER FOUR

INTERCALATION KINETICS

4.1. Introduction

A survey of the literature and of our current understanding of intercalation kinetics has been presented in Chapter One. This section provides the background information necessary for a study on the kinetics of intercalation in metal dichalcogenides. These include the physical characteristics of guest and host species, the techniques which can be applied to study them during the course of intercalation reactions as well as a brief introduction to the technique employed in this study, energy-dispersive diffraction at a synchrotron radiation facility.

4.1.1. Characteristics of Guest Species

The guest species in intercalation reactions can exist in either the solid, liquid or gaseous phase. Most commonly, however, they react with the host either as a liquid (solvated or molten) or as a vapour. Examples of the former are electrochemical[1] or alkali metal hydroxide intercalations[2] while the latter include ammonia[3], hydrazine[4], pyridine[5, 6] and alkali metal vapour[7-9] reactions with layered hosts.

While intercalation of solvated guest provides flexibility and generality to the reaction scheme, it is often complicated by solvent co-intercalation, giving products with poorly-defined stoichiometries. Solvent co-intercalation can be reduced by use of bulky solvents; however these solvents tend not to have the favourable dielectric constants necessary to support the redox processes that occur during the intercalation and/or are less readily available. Although vapour phase intercalation does not suffer the disadvantage of solvent co-intercalation, it is limited to guest reactants with appreciable vapour pressure at moderate temperatures.

4.1.2. Characteristics of Host Species

The most ubiquitous examples of layered intercalates are graphite and metal dichalcogenide intercalation compounds. Although the hosts tend to be well-ordered crystalline lattices, despite the relatively weak van der Waals forces between their layers in the *ab* plane, intercalation of guest species reduces the interlayer communication to the extent that individual layers are often out of registry with the planes above or below, giving rise to diffuse diffraction peaks for all but the *00l* reflections (see Chapter One,

1.5.1). Fortunately, for the purpose of accurately measuring the extent of intercalation in kinetic experiments, sharp *00l* reflections are not only necessary but also sufficient. As such, it is often preferable to work with large, oriented single crystal samples, in order that non-*00l* reflections, which complicate the diffraction profile, can be avoided. Moreover, oriented crystal samples benefit from large coherent scattering from *00l* planes which can be aligned directly towards the detector, thus markedly improving the quality of spectra compared to that obtained from powdered samples.

For this reason, the pioneering experiments on kinetics of intercalation in layered materials were done on graphite intercalates since oriented samples in the form of highly-oriented pyrolytic graphite are readily available commercially. As such, the following section will review kinetic phenomena not only in metal dichalcogenide but also graphite intercalates as observations on this latter class have many parallels in metal dichalcogenide intercalation kinetics.

4.1.3. Techniques for studying intercalation kinetics

Although extensive studies have been made on the kinetics of intercalation into graphite[10], much less attention has been focused on the transition metal chalcogenide intercalates. This disparity is attributable to the difficulty of performing structural studies on powdered samples of the intercalates which, unlike graphite intercalation compounds, have to be grown as single crystals by vapour phase transport or Bridgman methods and are thus not so readily available as large oriented single crystals. Without the coherent scattering from planes of oriented crystal samples, the quality of diffraction spectra that can be obtained on time scales feasible for extracting kinetic data is usually too poor to be of any conceivable use.

As such, researchers have turned to indirect methods for tracking the extent of intercalation in order to obtain kinetic data on layered metal chalcogenides[2, 4]. Acrivos measured the weight gain of 2H-TaS_2 upon exposure to N_2H_4 vapour while Subba-Rao and Shafer[2] monitored the rate of disappearance of alkali metal hydroxide from the reaction system 2H-TaS_2 + MOH (M= K, Na) by the laborious process of titrating aliquots extracted at periodic intervals. Clearly this latter method suffers from at least two disadvantages; (a) the aliquots removed from the reaction reduce the volume of alkali solution, so that unless a large excess of solution is used initially, the reaction conditions will vary gradually with time, and (b) the rate of disappearance of the alkali metal hydroxide is not necessarily the same as the rate of intercalation, since side reactions such as hydrolysis of the host lattice by the alkali hydroxide are known to occur.

An alternative approach is to track the intercalation electrochemically, and because this technique can be applied more generally to both solvated and gas phase guest intercalants, it has been the method of choice for several studies[1, 11, 12]. However, interpretation of the results from electrochemical experiments is not straightforward, thus

offsetting the advantage of this method's generality.

Several kinetic studies on metal chalcogenide intercalates to date have monitored the progress of the reaction by structural means[13-15, 47-49]. Chianelli *et al.* performed some elegant *in situ* X-ray diffraction on Li intercalating into TiS_2 while Riekel and Schollhorn's neutron diffraction study on the 2H-TaS_2-ammonia system yielded a qualitative understanding into the intercalation process as well as to the orientation of the guest species, but the available levels of beam flux, whilst high by neutron standards, necessitated either very large sample sizes (~15g) or long acquisition times, making a thorough, quantitative study under varying reaction conditions of temperature, concentration and particle size unfeasible. Moreover, because of the large incoherent scattering from hydrogen atoms by neutrons, the samples studied had to be highly deuterated, an expensive and not always achievable prerequisite in other systems.

Concomitant with subsequent increases in intensity of X-ray sources, *in situ* X-ray experiments for monitoring metal chalcogenides intercalates were developed. The first such study[15] examined the intercalation of solvated Cs^+ into NbS_2 single crystals and pressed powder electrodes. While the small quantitites required for such experiments were a significant advance over neutron diffraction techniques, the cell design and geometry limited the application of this technique to electrochemical intercalation at moderate rates (diffraction scan rate ~30 minutes).

In recent years, the technological and experimental advances in energy-dispersive powder diffraction using synchrotron X-ray sources ha , provided new possibilities for the solid state kineticist. The markedly higher intensity (several orders of magnitude) over conventional laboratory X-ray sources means that good quality spectra can be obtained from relatively small samples (tenths of a gram) on a time scale of seconds, making kinetic studies on fast intercalation reactions a realizable goal. The high intensity of the X-rays is not significantly attenuated by a variety of materials suitable for cell windows, facilitating the construction of sealed sample holders. Moreover, the fixed geometry of this technique greatly simplifies the design of any sample environment. The less stringent space constraints in synchrotron X-ray diffractometers also allow construction of more elaborate sample cells which can accomodate a wider variety of reactants, such as single crystal or microcrystalline hosts, reacting with solvated or gas phase guests, all within a sealed, dry, nitrogen atmosphere.

4.1.4. Synchrotron Radiation at Daresbury Laboratory

Synchrotron radiation is the electromagnetic radiation emitted by electrons or positrons moving at relativistic velocities along a curved trajectory with a large radius of curvature[16]. The radiation is emitted over a continuum whose energy range depends on the energy of the particle beam, and on the field strength of the bending magnets. In addition the radiation is highly collimated, linearly polarised and many times more

intense than that from conventional sources.

The radiation is emitted tangentially as the electrons are accelerated around the ring by bending magnets. The radiation is then chanelled along *beam lines* to various experimental stations. The energy ranges of the emitted radiation can be modified by the use of magnetic insertion devices which modify the local gyration radius of the circulating electrons. The station used for the work described in this thesis, Station 9.7, utilizes white radiation emitted directly from a 5 Tesla wiggler magnet.

For the energy dispersive technique used on Station 9.7, the diffraction angle from the powder specimen is kept fixed and the energy distribution of the scattered white beam is measured using a solid state detector. A detailed description of the technique as well as the diffractometer on Station 9.7 is included in Chapter Five. The main advantages of the energy dispersive technique are the fixed detector angle (useful for sample environments with small windows), the simultaneous measurement of the whole pattern and the rapid data collection times possible.

4.1.5. Overview of Chapter

This chapter will consist of 3 main sections. Section **4.2** describes the *commissioning experiments* conducted to verify the utility of the apparatus constructed for use on Station 9.7. The results are presented in Sections **4.3** and **4.4**, each with a discussion immediately following it. Section **4.3** contains *quantitative analyses* of the kinetic data obtained for the intercalation of tin disulfide and tin diselenide in a dimethoxyethane solution of cobaltocene. Section **4.4** documents *qualitative observations* made during the intercalation of the tin dichalcogenides using a different solvent (toluene) and their implications on the intercalation mechanism. Section **4.5** concludes the chapter with a brief summary of the results herein.

4.2. Commissioning experiments

The design and construction of the apparatus used on Station 9.7 to perform the *in situ* kinetic studies in this chapter, as well as its alignment in the diffractometer are described in Chapter 5. A drawing of the apparatus is shown in the figure below. It consists of an upper and lower reservoir containing the pre-warmed and equilibrated solutions respectively, an electronic-timer based injection system, and the reaction-cum-diffraction cell.

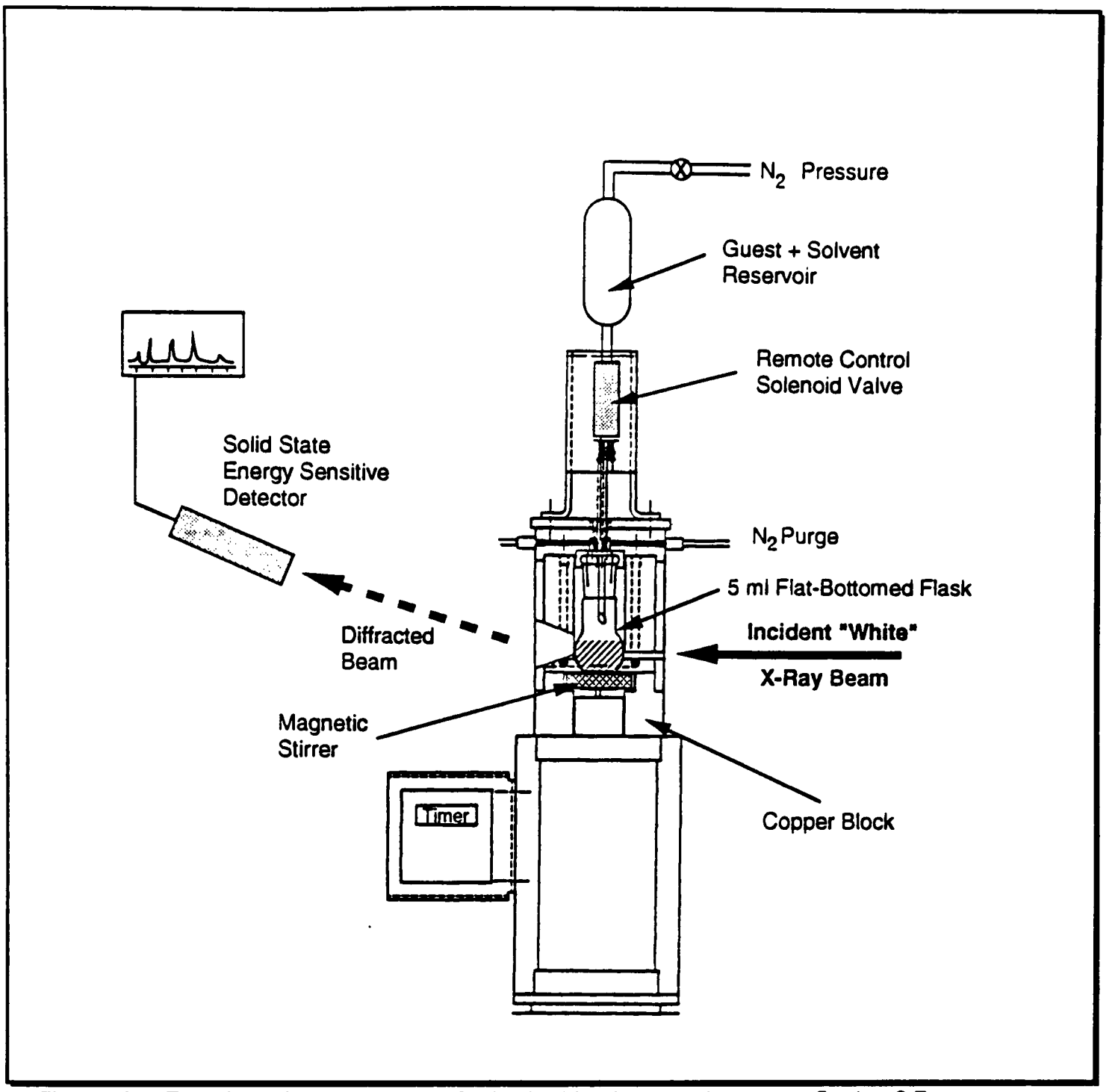

Figure 4.1: Drawing of apparatus used for in situ kinetics experiments on Station 9.7.

Commissioning experiments were performed to test the temperature stability of the system, to calibrate the volumes injected, the efficacy of the diffraction cell and the extent of damage to the sample due to the stirring required to bring the sample into suspension. The temperature stability of the reaction vessel fluctuated by less than 0.5°C for temperatures above 25°C and by about 1°C for temperatures below room temperature. Volumes dispensed were calibrated as a function of the time the valve was opened as well as of the over-pressure of nitrogen applied to the upper reservoir.

To determine the experimental parameters necessary for obtaining good quality spectra for quantitative kinetics measurements, suspensions of both the microcrystalline host and the final intercalate were loaded into the cell and energy-dispersive powder diffraction spectra collected while the contents of the flask were stirred vigorously. Examples of the spectra obtained from two of these trials using SnS_2 host and its cobaltocene intercalate, $SnS_2(CoCp_2)_{0.3}$ are shown in Figure 4.2. The diffraction spectrum of the intercalate has been "stacked" above that of the host to emphasize the

differences in peak positions for the two samples. The *00l* peaks of both the host and the intercalate in the energy window examined are well resolved and are indicated in the figure. The Sn absorption K edge is visible at about 28 keV, as are the K_α and K_β resonance peaks. The curved appearance of the baseline between 30 keV and 65 keV is due to amorphous scattering from the Pyrex glass in the reaction vessel while the small feature at *ca.* 54 keV is a Bragg peak from the lead in the diffractometer shielding. From these commissioning trials, it was determined that reasonable spectra (for qualitative comparisons) could be acquired in as little as 10 seconds when 200mg of sample was used although for quantitative data analysis, spectral acquisition times of 20 seconds or more were employed.

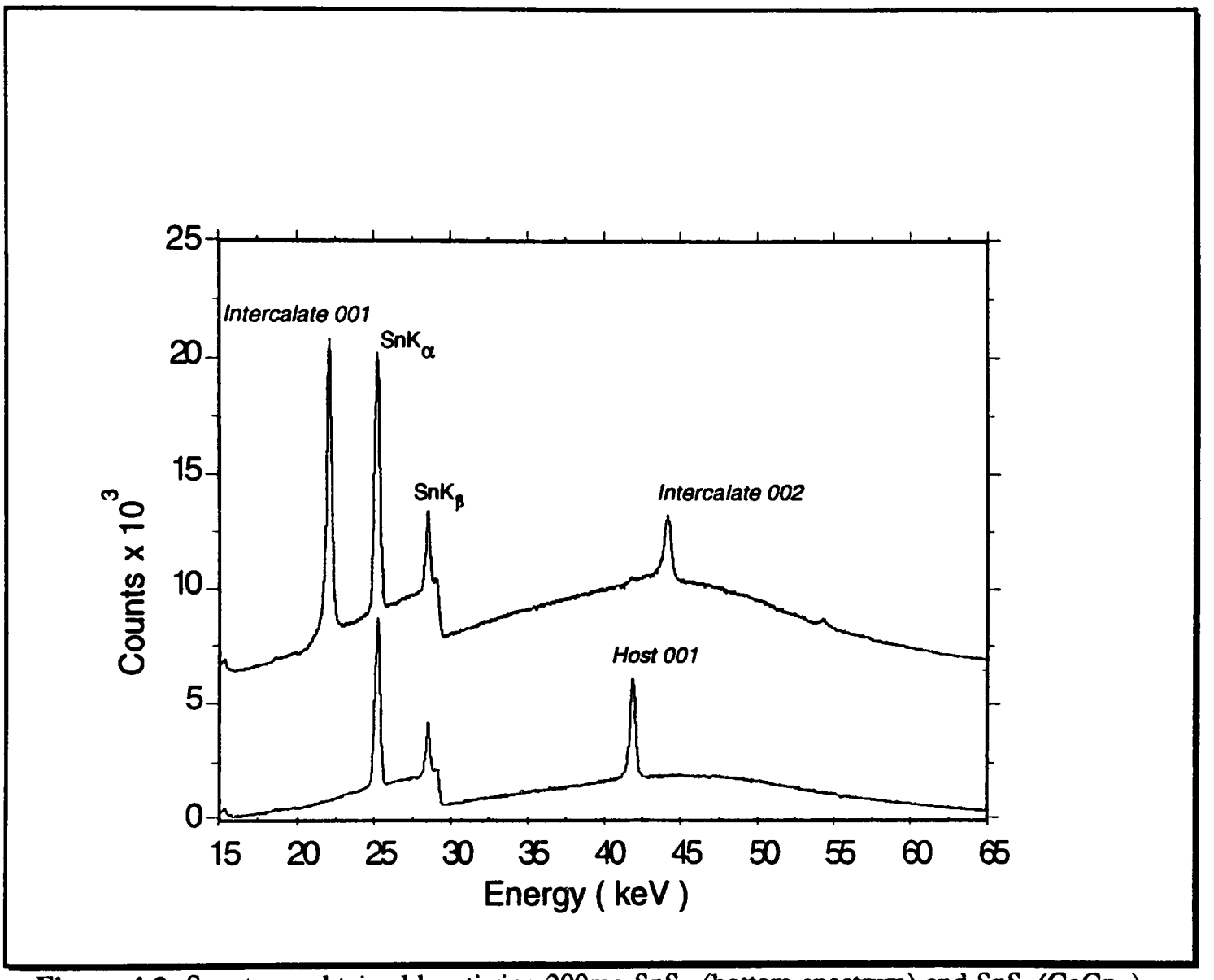

Figure 4.2: Spectrum obtained by stirring 200mg SnS_2 (bottom spectrum) and $SnS_2(CoCp_2)_{0.3}$ (top spectrum) in 4ml dimethoxyethane within the reaction cell. Particle size: 90→250μm. Acquisition time per spectrum: 30 seconds. Detector angle : 2.89°

Given the very vigorous stirring rates needed to lift the sample into suspension, it was necessary to confirm that there is not significant damage to the crystals during the course of the reaction. To this end, SnS_2 was stirred for 75 minutes in DME, a duration many half-lives longer than the slowest reactions examined. Aliquots of the SnS_2 suspension were examined before and after stirring under a microscope. Photos taken of the particles before and after stirring in DME show some disintegration of the original particles but the crystallites remain largely intact (see Figure 4.3).

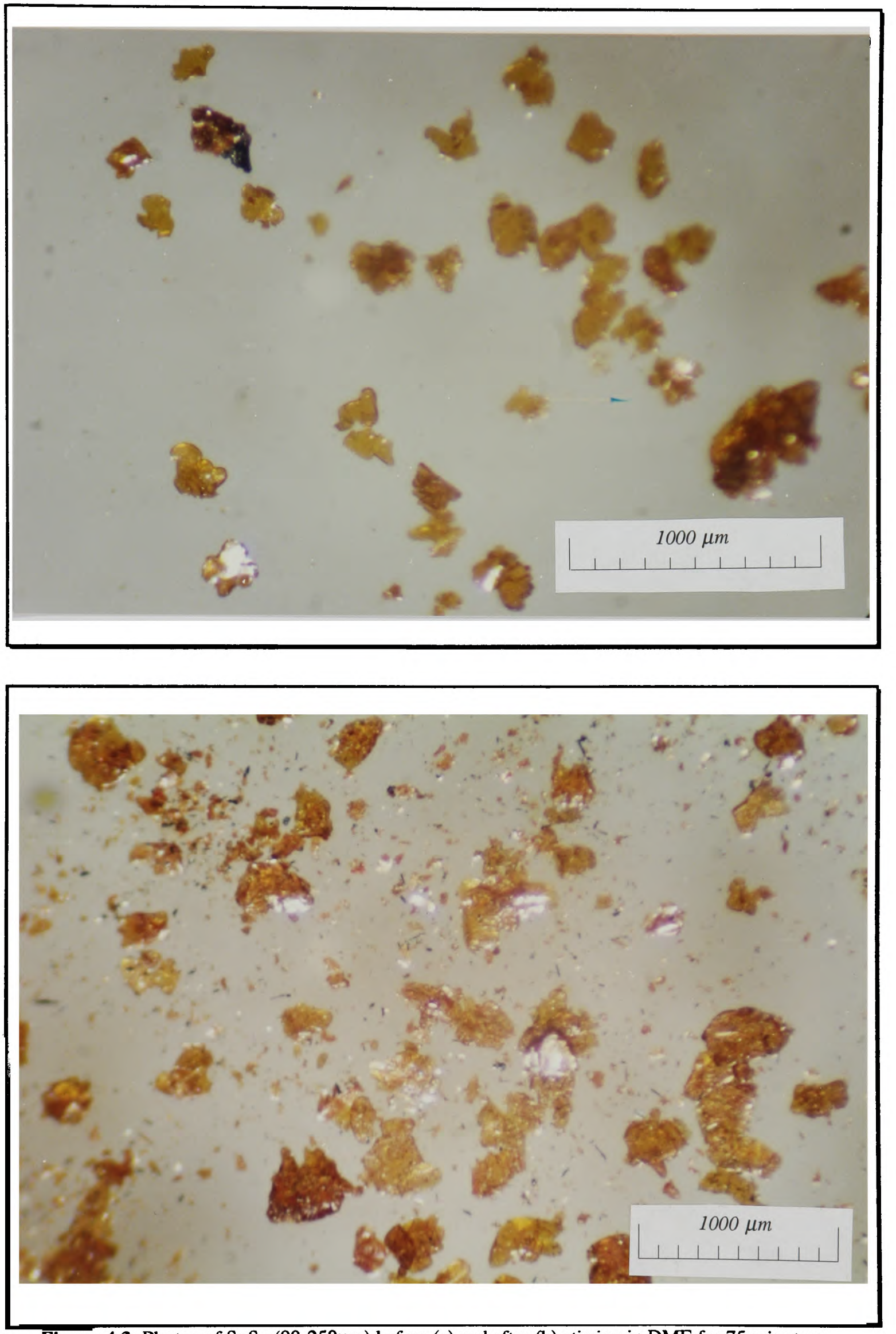

Figure 4.3: Photos of SnS_2 (90-250μm) before (a) and after (b) stirring in DME for 75 minutes.

4.3. Quantitative Analysis - Rates and mechanisms

4.3.1. Results

In situ energy-dispersive diffraction spectra were obtained for the intercalation of SnS_2 and SnS_2 in a dimethoxyethane (DME) solution of $CoCp_2$ for the temperature range 10→70°C using acquisition times ranging from 60 seconds to as little as 10 seconds for the very fast reactions at high temperatures. The resulting kinetic data obtained for SnS_2 and $SnSe_2$ are described in turn below, with details of the analyses and discussion postponed to Section **4.3.2.**

4.3.1.1. $SnS_2/CoCp_2$ kinetics

A typical data set obtained for the reaction using microcrystalline SnS_2 powder of particle size between 90 and 250μm is shown in Figure 4.4 as a series of *stacked* spectra, where the energy window depicted corresponds to a d-spacing from 12.3 to 5.5Å. The spectra represent snapshots of the diffraction pattern at different times during the course of the reaction, with each sucessive spectrum "stacked" on top of the previous one, so that a profile showing the evolution of peaks as a function of time is obtained. Thus, the peak at 42 keV, which represents the 001 reflection of the host SnS_2, disappears as the peaks at 22 and 43 keV, corresponding to the 001 and 002 reflections of the intercalate, grow in, until eventually, at time = 2310 seconds, only the intercalate peaks are present.

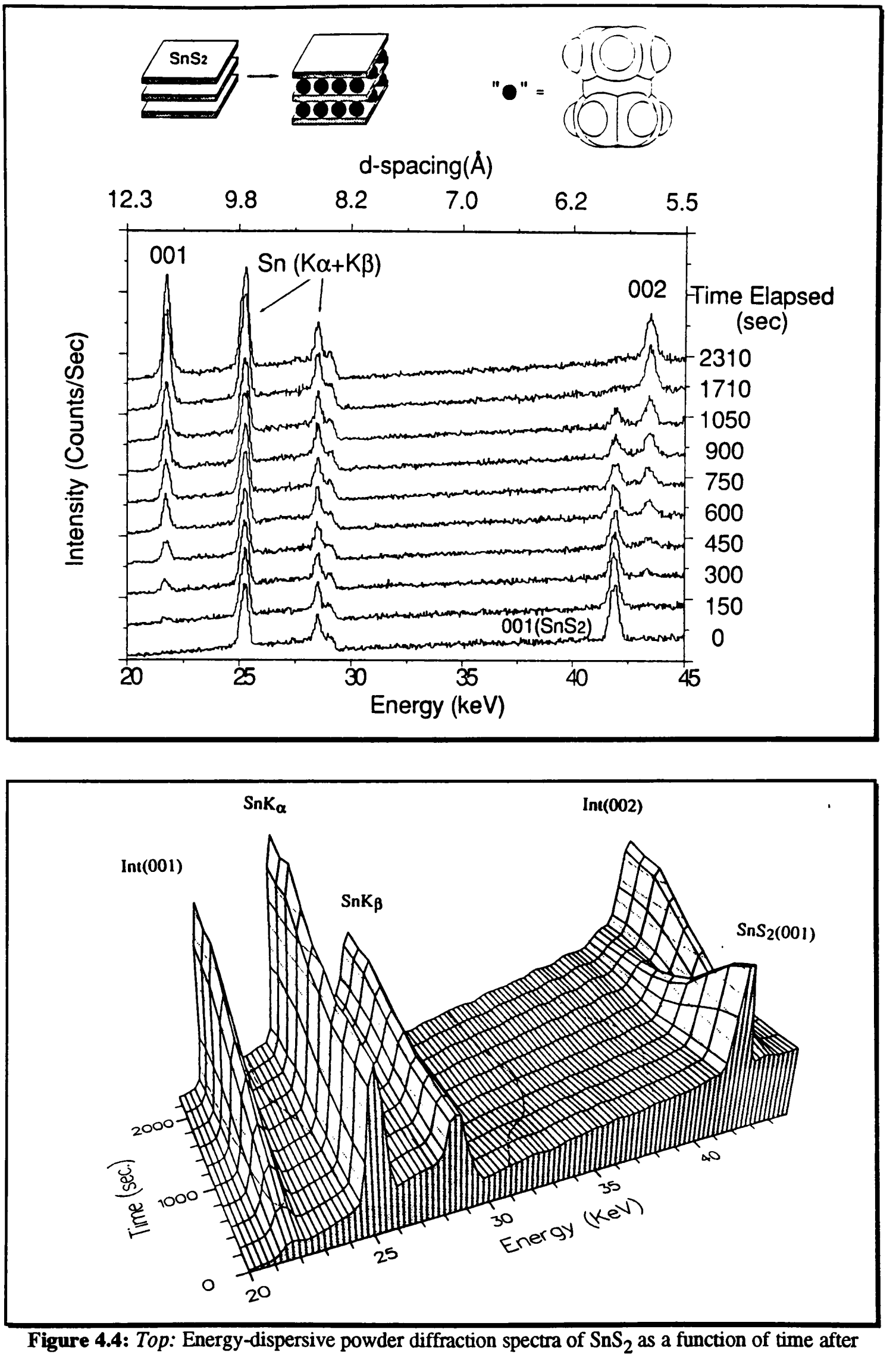

Figure 4.4: *Top:* Energy-dispersive powder diffraction spectra of SnS_2 as a function of time after exposure to $CoCp_2$ in dimethoxyethane. SnS_2 host *001*, $SnS_2\{CoCp_2\}_{0.3}$ intercalate *001* and *002* peaks correspond to 5.8Å, 11.2Å & 5.6Å respectively. Particle size of SnS_2: 90-250μm. Acquisition time per spectrum was 30 seconds. Detector angle : 2.89°. *Bottom:* the spectra arranged as a 3-D time-resolved plot.

By integrating the area under the Bragg peaks for the *00l* reflections of host (reactant) and intercalate (product), measures of the amount of reactant and product as a function of time could be obtained. In order to account for small differences in the quantity of particles in suspension that diffract the incoming X-ray beam, the intercalate data was normalised with respect to the SnK_α resonance intensity, which is proportional to the total amount of sample in the beam. Thus,

$$m_{int00l}(t) = \frac{I_{00l}(t)}{I_{SnK\alpha}(t)} \qquad (1)$$

where $m_{int00l}(t)$ = amount of intercalate, based on *00l* intensity at time t.
$I(t)$ = Intensity of *00l* reflection at time t
$I_{SnK\alpha}(t)$ = Intensity of SnK_α resonance at time t.

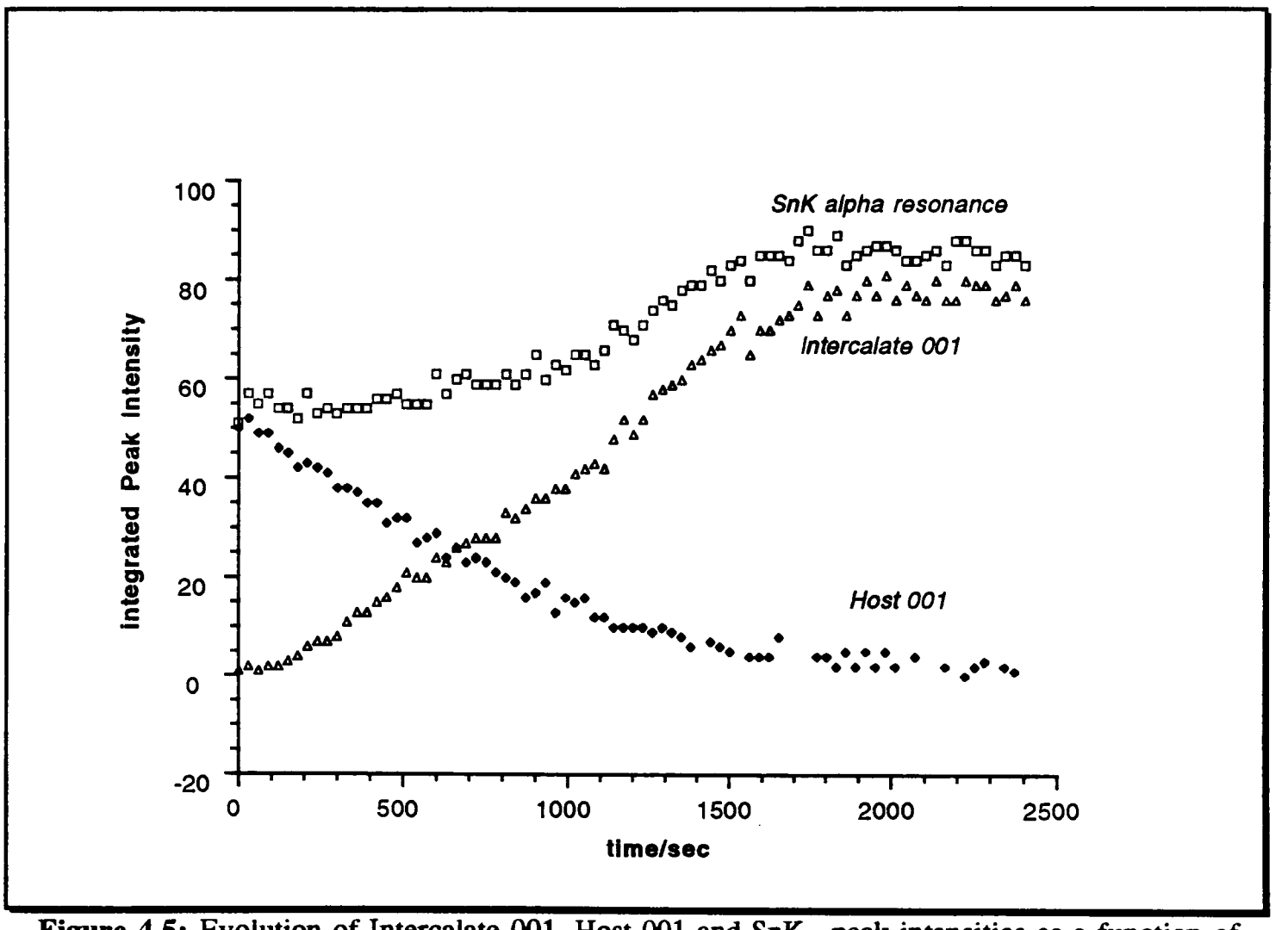

Figure 4.5: Evolution of Intercalate 001, Host 001 and SnK_α peak intensities as a function of time.

From Figure 4.5, it can be shown that the rate of disappearance of host is equal to the rate of appearance of intercalate so that the extent of the reaction, α, can be measured by monitoring either the evolution of the host or intercalate peak. That is,

$$\alpha(t) = \frac{I_{int00l}(t)}{I_{int00l}(t\to\infty)} \qquad (2)$$

For the purpose of our data analysis, the intensity of the 001 peak of the intercalate was used to represent $\alpha(t)$ as this had better signal-to-noise characteristics than the other host or intercalate peaks. Intensities were obtained by integration of the area under the peaks using INTPEAK, a modification of a peak fitting program developed at

Daresbury by Simon Clark (see Appendix C). The modification allows the user to integrate peaks in a single spectrum or in sums of consecutive spectra, the latter option being useful in improving the signal-to-noise ratios for spectra which were acquired faster than was necessary for the rate of the reaction studied. A sample of the data obtained after applying INTPEAK, then normalising with the SnK_α intensity, is shown in Figure 4.6. The data is plotted on a *reduced-time* scale, $t/t_{1/2}$, which allows the data from reactions with very different rates to be represented on the same horizontal scale.

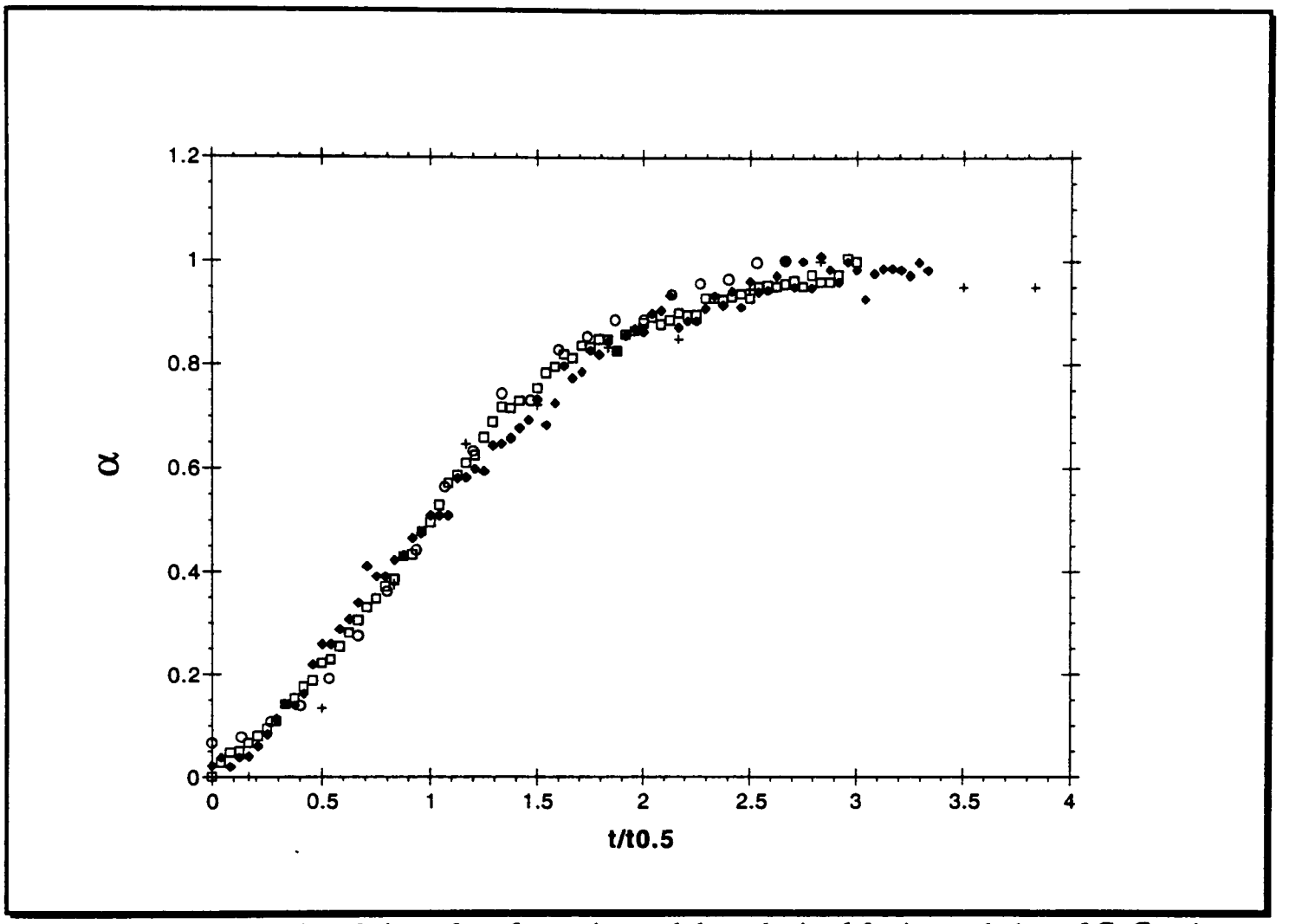

Figure 4.6: α vs. reduced-time plot of experimental data obtained for intercalation of $CoCp_2$ into SnS_2 (particle size: 90-250μm) at several temperatures: (❑)10°C, (♦)20°C, (o)40°C, (Δ) 50°C, (+) 60°C.

4.3.1.2. $SnSe_2/CoCp_2$ kinetics

Similar experiments for the intercalation of $CoCp_2$ into $SnSe_2$ were performed. The experiments were performed over a smaller temperature range, 50→80°C, the upper temperature boundary being the boiling point of the solvent, while temperatures less than 50°C were unfeasible because of the appreciably slower kinetics. The slower rate of this reaction permitted longer spectral acquistion times of 60 seconds to be employed, as evidenced by the better spectral resolution (see Figure 4.7).

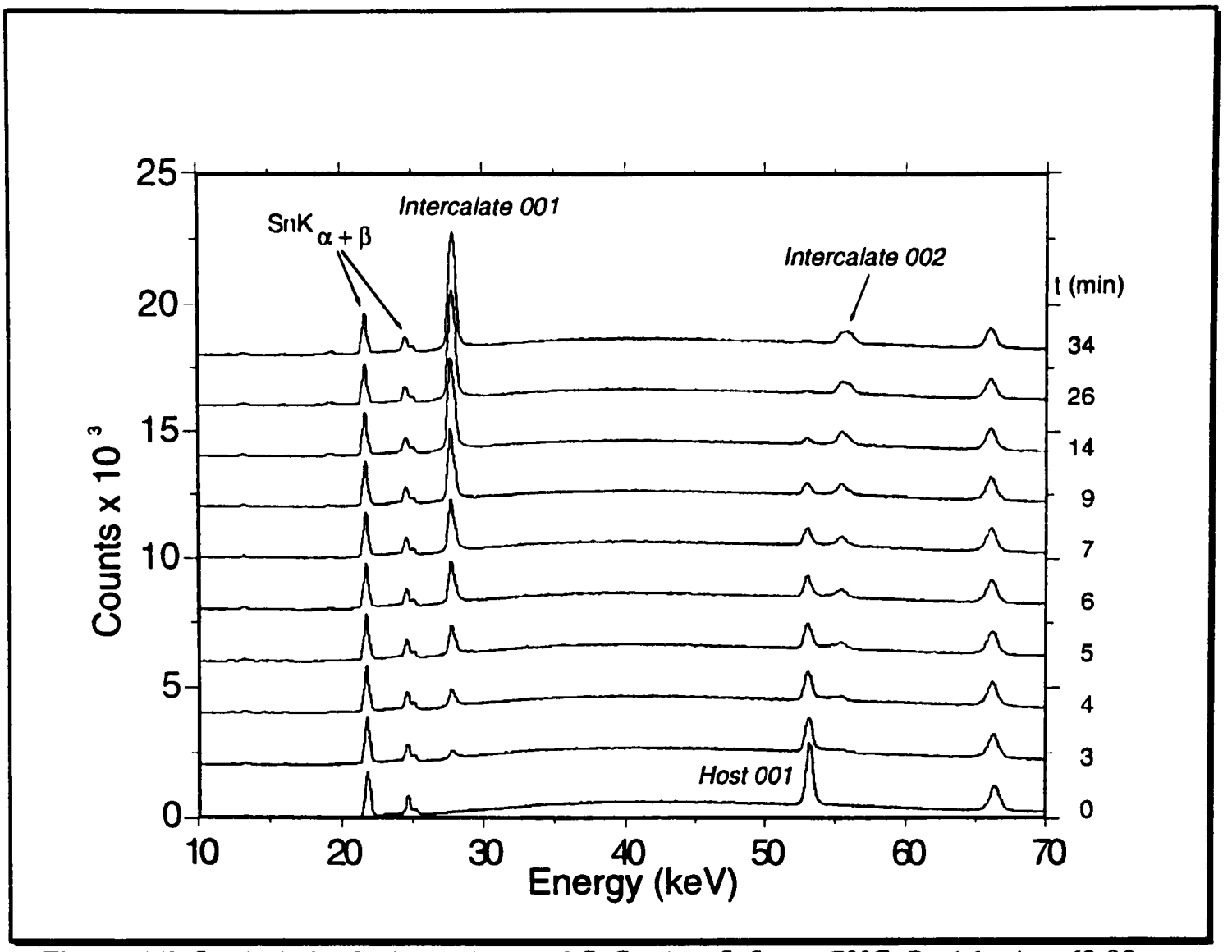

Figure 4.7: Stacked plot for intercalation of $CoCp_2$ into $SnSe_2$ at 73°C Particle size: 60-90μm. Acquisition time per spectrum: 60 seconds. Detector Angle: 2°.

4.3.2. Discussion

4.3.2.1. Reaction Mechanism

Preliminary screening of the data was performed using the method developed by Sharp and Hancock[17], which allows the experimentalist to distinguish between broad classes of solid state reaction types such as first order, Avrami and contracting volume kinetics. Essentially, $ln(-ln(1-\alpha))$ values are plotted against $ln(time)$, with the slope, m, of these straight line plots indicative of the kinetic mechanism that is operative. For example, for $m = 1$, the rate expression is first order and for $m = 2$ or 3, Avrami-Erofe'ev kinetics apply. Table 4.1 summarises the m values which characterise each of these reaction types.

In practice, however, the poor quality of solid state kinetic data (relative to data quality for solution kinetics) often renders this test useful only in narrowing the rate mechanism down to a handful of options without unequivocally singling out any of them.

Table 4.1: Values of *m* from Sharp-Hancock plots for solid state reaction rate equations.

Function[¶]	Equation	m[§]
$D_1(\alpha)$	$\alpha^2=kt$	0.62
$D_2(\alpha)$	$(1-\alpha)\ln(1-\alpha)+\alpha=kt$	0.57
$D_3(\alpha)$	$\{1-(1-\alpha)^{1/3}\}^2=kt$	0.54
$D_4(\alpha)$	$(1-2\alpha/3)-(1-\alpha)^{2/3}=kt$	0.57
$F_1(\alpha)$	$-\ln(1-\alpha)=kt$	1.00
$R_2(\alpha)$	$1-(1-\alpha)^{1/2}=kt$	1.11
$R_3(\alpha)$	$1-(1-\alpha)^{1/3}=kt$	1.07
Zero order	$\alpha=kt$	1.24
$A_2(\alpha)$	$\{-\ln(1-\alpha)\}^{1/2}=kt$	2.00
$A_3(\alpha)$	$\{-\ln(1-\alpha)\}^{1/3}=kt$	3.00

[§](from $\ln(-\ln(1-\alpha)=\ln B+m\ln t$)

[¶] D_1, D_2, D_3 = diffusion controlled reactions
R_1, R_2, R_3 = phase boundary controlled reactions
A_2, A_3 = Avrami-Erofe'ev reactions
F_1 = first order reactions

(a) $SnS_2/CoCp_2$ kinetics

For the data collected on the $SnS_2/CoCp_2$ system using the protocol summarised above, the Sharp-Hancock analysis suggested that the models most likely to fit the data were either first order or Avrami second order kinetics.

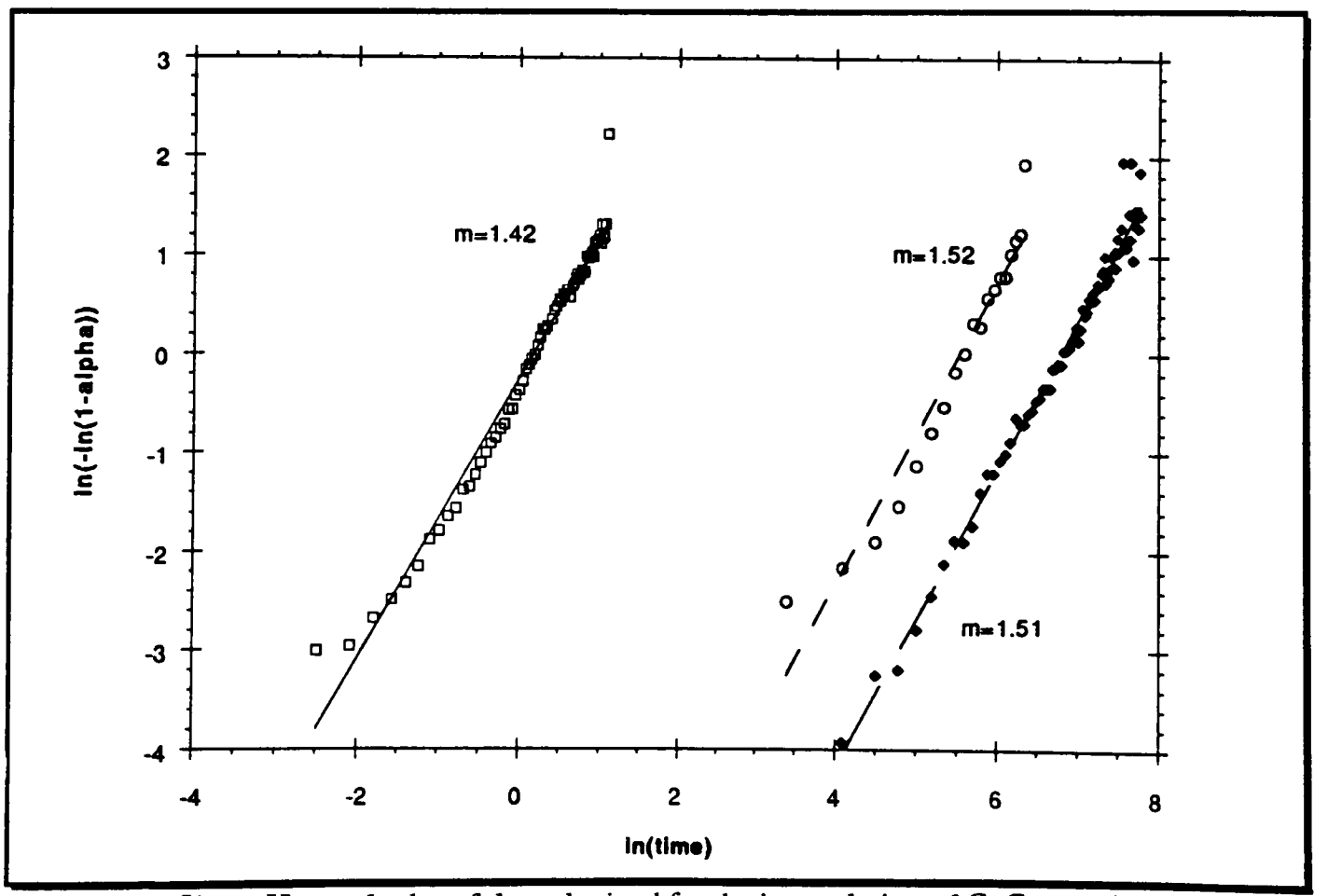

Figure 4.8: Sharp-Hancock plot of data obtained for the intercalation of $CoCp_2$ by SnS_2 at various temperatures. (❑)10°C, (♦)20°C, (o)40°C. The slopes, m, of the lines obtained by least squares fit to the data are indicated.

Since the best-fit straight line through the experimental data yields a slope of approximately 1.5, the rate equation assumes a form with non-integral order, m:

$$(kt)^m = -ln(1-\alpha) \qquad (3)$$

Hulbert has developed a Nuclei Growth Model which treats rate expressions such as that shown above with non-integral order[18]. Unlike the diffusion controlled models where only rate expressions of integral order make physical sense, models based on nuclei growth can be more broadly interpreted. For the latter model, the volume of product at a given time t, V(t), is given by the expression below:

$$V(t) = \int_0^t V(t,t_j)\left(\frac{dN}{dt}\right)dt \qquad (4)$$

This expression can be viewed as the superposition of two terms; the nucleation term, $\frac{dN}{dt}$, and the growth term, $V(t, t_j)$, which is the volume occupied by nuclei formed at time = t_j. $V(t, t_j)$ depends on the type of growth law applied, F(t), the shape factor, σ, and the dimensionality of the nucleation, λ:

$$V(t, t_j) = \sigma\{r(t,t_j)\}^\lambda = \sigma\left(\int_{t_j}^{t} F(t)dt\right)^\lambda \qquad (5)$$

Different rate expressions but with the generalised form: $(kt)^m = -ln(1-\alpha)$ can be derived from various combinations of these terms, applied in 1, 2 or 3 dimensional nucleation models. The order *m* can assume values between 0 and 3 with the values being dependent on (a) reaction mechanism (b) nucleation rate & (c) geometry of the nuclei. Table 4.2 summarises the relationship between various *m* values and the categories of nuclei growth models for which they apply. It is evident from Table 4.2 that a kinetic investigation which is limited to the establishment of the value of *m* most appropriate to the assumed growth law, does not provide sufficient information for the reaction mechanism to be deduced.

Table 4.2: Various reaction mechanisms with differing dimensionality within the Nuclei Growth Model and their corresponding values of m in the rate expression, $(kt)^m = -ln(1-\alpha)$. (adapted from Hulbert, 1969[18])

Growth Model	*m*	
	Phase Boundary Controlled	**Diffusion Controlled**
Three Dimensional Growth (i.e. spheres)		
Case A: Constant Nucleation Rate	4.0	2.5
Case B: Zero Nucleation Rate (saturation of point sites)	3.0	1.5
Case C: Decreasing Nucleation Rate	3.0-4.0	1.5-2.5
Two Dimensional Growth (i.e. plates)		
Case A: Constant Nucleation Rate	3.0	2.0
Case B: Zero Nucleation Rate (saturation of point sites)	2.0	1.0
Case C: Decreasing Nucleation Rate	2.0-3.0	1.0-2.0
One Dimensional Growth (i.e. rods)		
Case A: Constant Nucleation Rate	2..0	1.5
Case B: Zero Nucleation Rate (saturation of point sites)	1.0	0.5
Case C: Decreasing Nucleation Rate	1.0-2.0	0.5-1.5

An order of $m = 1.5$ for the rate expression can be satisfied by several classes of reactions within the Nuclei Growth Model. In our particular case however, if we assume the nucleation and growth of the intercalate in layered systems is a two-dimensional process, then only one of the listed mechanism gives a rate order of $m = 1.5$: a decelatory rate of nucleation followed by a diffusion controlled growth of the product phase (Table 4.2). That is, if we take nucleation to be the arrival of the guests at the crystal edge and its initial "prying" open of the layers, then the simplest model which describes the intercalation process is illlustrated in Figure 4.9 below. The intercalant spreads apart the layers, then proceeds to diffuse towards the crystal centre. Since the number of nucleation sites on the crystal edge is finite, the nucleation rate must slow down as the availability of pristine crystal edge is depleted. While nucleation is a relatively quick process, the rate of intercalation is limited by the speed with which the product phase can permeate through the crystal, that is the rate determining step after the initial stages of the intercalation is the diffusion of guests toward the crystal centre. A comparison of the experimental data with the theoretical curves calculated for Avrami second order, phase boundary controlled and deceleratory nucleation kinetics is shown in Figure 4.10. The deceleratory nuclei growth model under diffusion control constrasts with that proposed for Li intercalation into TaS_2[19, 20]. In this latter case, the physically smaller lithium ion diffuses significantly faster than the cobaltocene molecule so that the intercalation rate is limited by the reaction at the phase boundary between reactant and product, rather than diffusion of the intercalant.

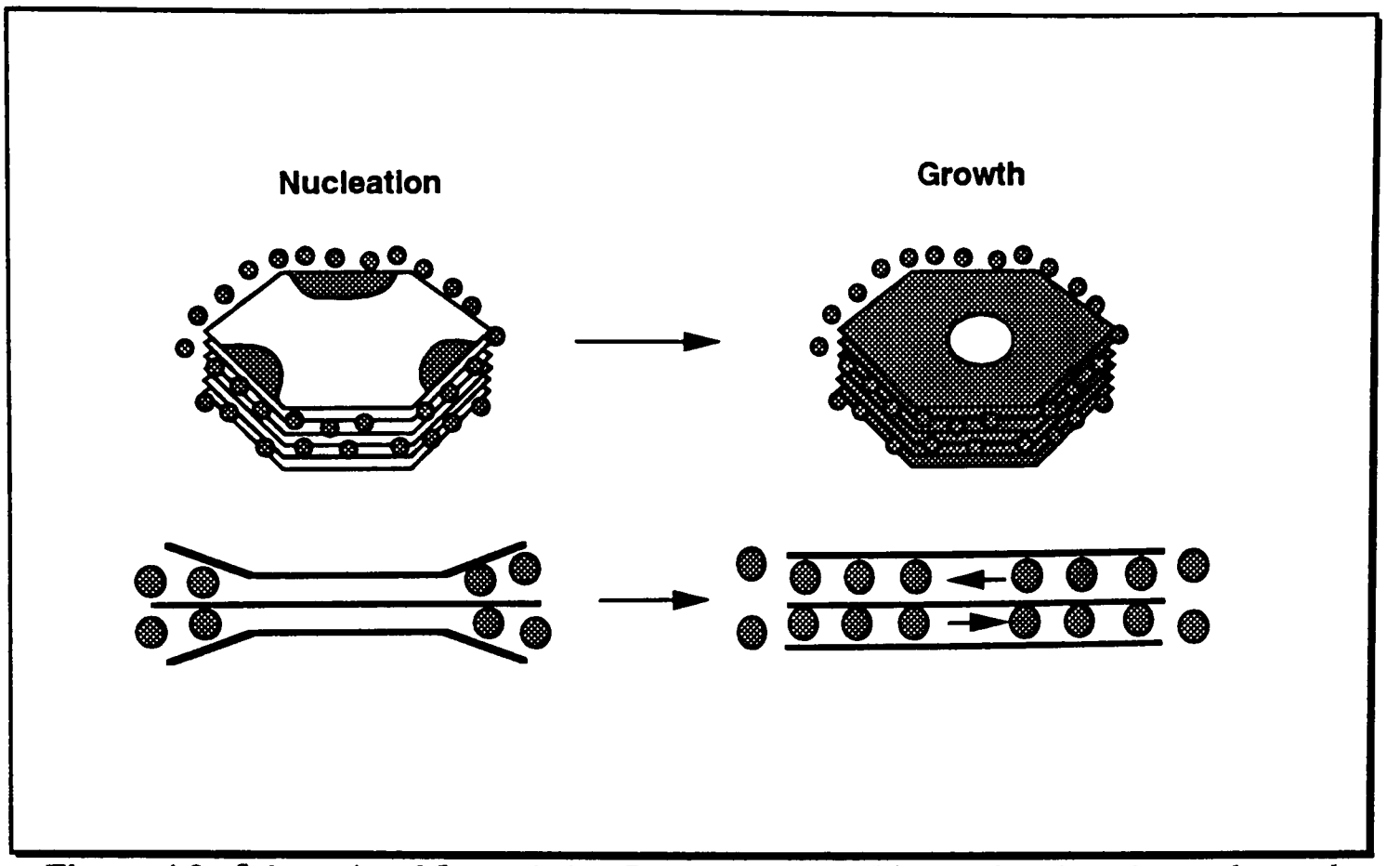

Figure 4.9: Schematic of Intercalation Process showing (a) initial activated complex and spreading apart of the host layers (b) growth of product phase by gradual diffusion of the intralayer guests towards the crystal centre.

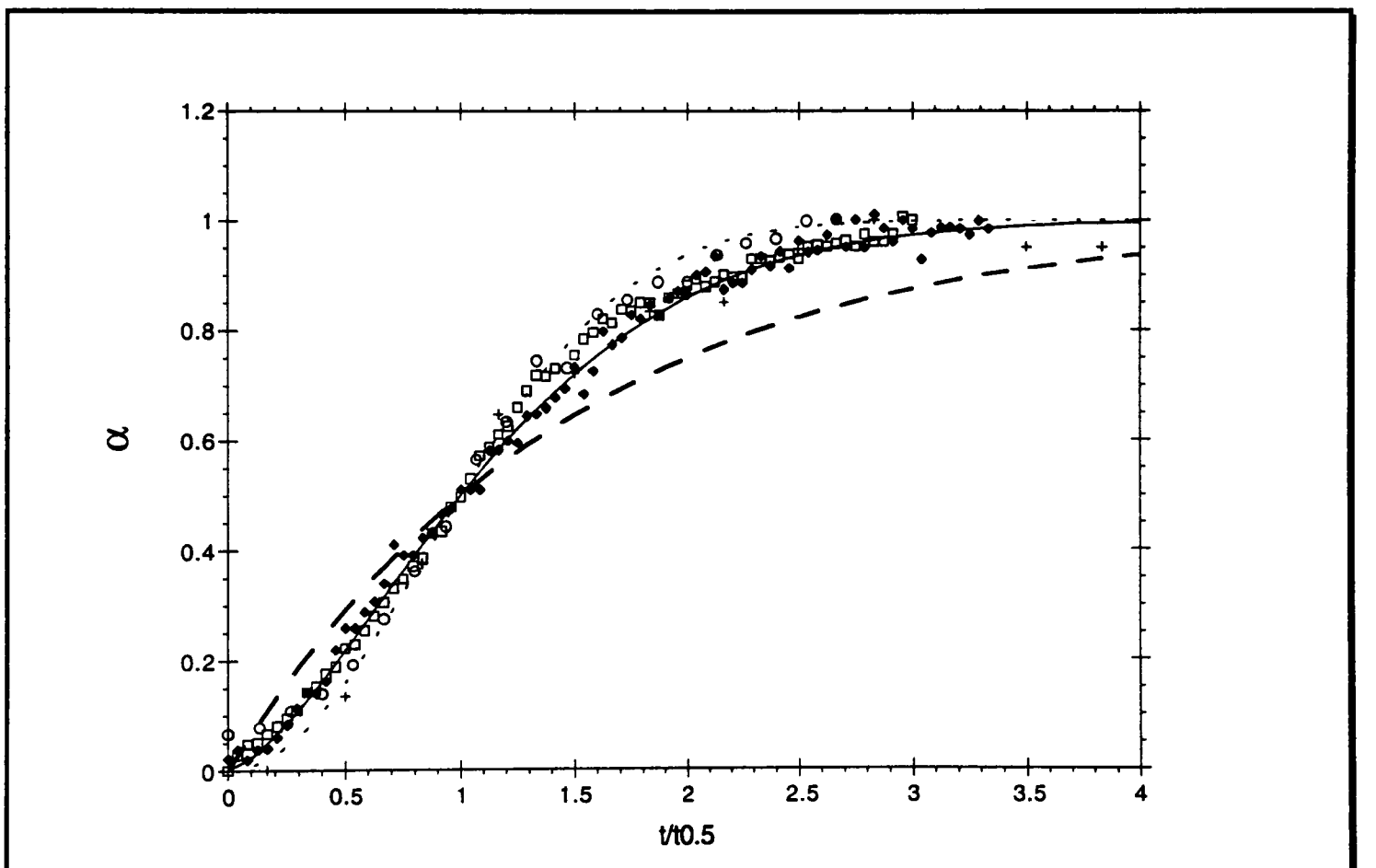

Figure 4.10: Comparison of experimental data obtained for intercalation of $CoCp_2$ into SnS_2 (particle size: 90-250μm) at several temperatures {(❑)10°C, (♦)20°C, (o)40°C, (Δ) 50°C, (+) 60°C}with some theoretically determined curves. (·····) Avrami 2nd order: $\alpha = 1- \exp(-kt)^2$; (– – –); First order: $\alpha = 1-\exp(-kt)$; (———); Deceleratory nuclei-growth: $\alpha = 1- \exp(-kt)^{1.5}$). The data is plotted on a reduced-time scale, $t/t_{0.5}$, in order to incorporate the data collected at temperatures from 10→70°C.

The kinetic rate constants obtained by fitting the data to the rate expression for the deceleratory nuclei growth model, $\alpha(t) = \exp\{-(kt)^{1.5}\}$, for several particle sizes are shown in Table 4.3. From the rate constant, k, half-lives ($t_{1/2}$) for the intercalation were computed for various particle sizes examined at 30°C. These half-lives correspond to the value of t when $\alpha = 1/2$, that is, when the reaction is halfway to completion. Since diffusion is the rate limiting step and if we assume that the intercalants diffuse in from the edge of a disc-shaped crystallite (of average radius, r) at a constant rate, then $t_{1/2}$ corresponds to the time when the cobaltocene "front" has intercalated half the volume of the crystal (see Figure 4.11). This simplifying assumption (which ignores the effect of nucleation on the reaction rate) allows the diffusion coefficient of the cobaltocene intercalant at various temperatures to be estimated using Fick's First Law of Diffusion,

$$J = -D\frac{\delta c}{\delta r} \qquad (6)$$

where J = Flux (moles cm^{-2} s^{-1})
D = diffusion coefficient (cm^2 s^{-1})
$\delta c/\delta r$ = concentration gradient (mol cm^{-4})

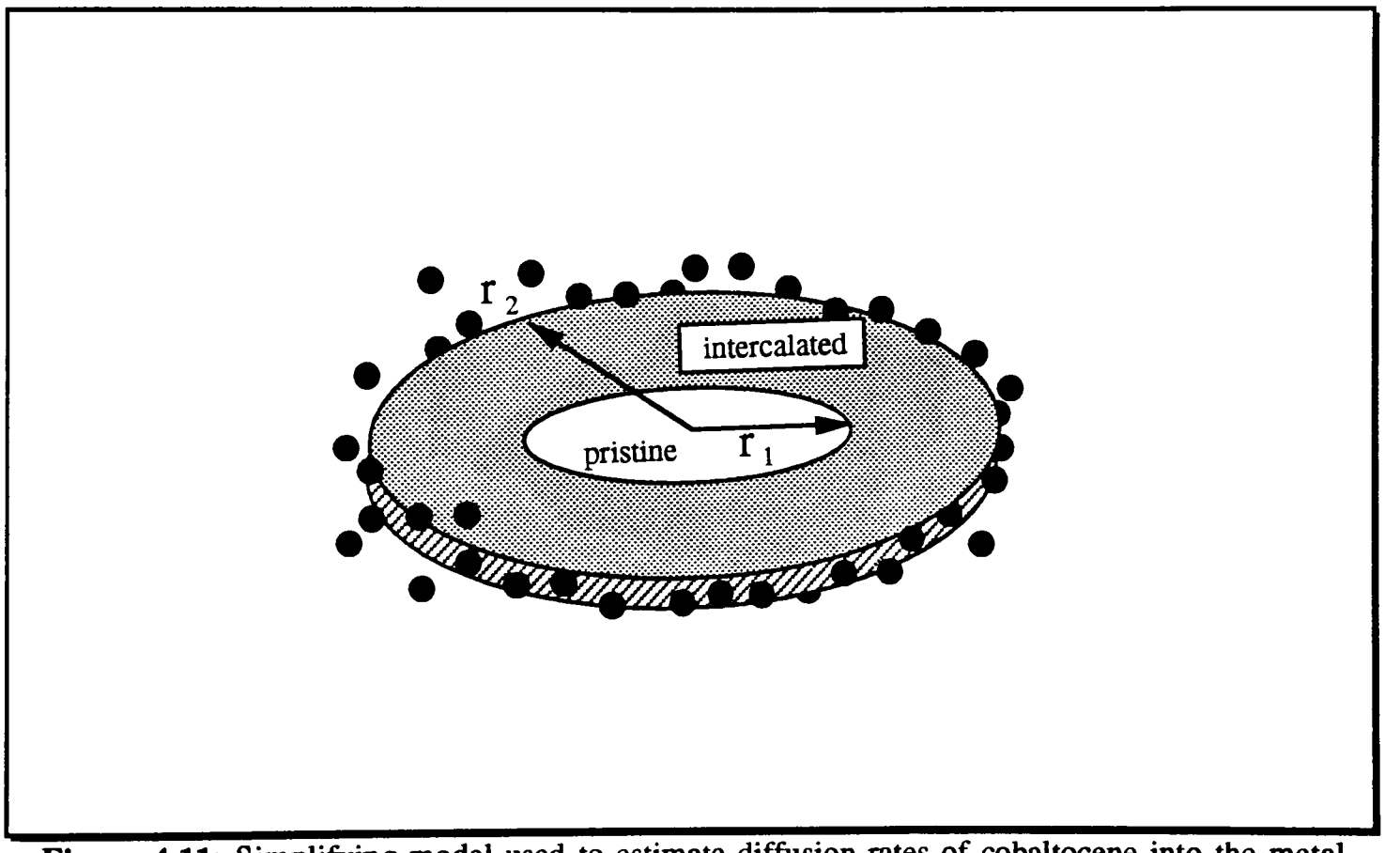

Figure 4.11: Simplifying model used to estimate diffusion rates of cobaltocene into the metal dichalcogenide host lattice. Situation depicted corresponds to $\alpha(t = t_{1/2})$, that is when the reaction is half complete ($r_1 = r_2/\sqrt{2}$).

Assuming both a linear rate of diffusion and distribution of intercalant within the crystal for the period $t = 0 \rightarrow t_{1/2}$, the concentration gradient, $\delta c/\delta r$ and the flux, J, can be calculated:

$$\frac{\delta c}{\delta r} = - \frac{c}{(1-1/\sqrt{2})r}$$

$$J = \frac{(c/2).V(t_{1/2})}{t_{1/2}.A_{av}}$$

where c = maximum concentration of intercalant within crystal
r = radius of crystal
$r(t_{1/2})$ = radius of crystal intercalated at $t = t_{1/2}$
$V(t_{1/2})$ = volume of crystal intercalated at $t = t_{1/2}$
A_{av} = Average surface area over which diffusion is occuring
$= 2\pi(\sqrt{3}/2)r.h$ {where h = crystal thickness}

Substitution of the relevant parameters of the above model and evaluating the constants,

$$D = - \frac{J}{\delta c/\delta r} = \frac{(1-1/\sqrt{2})^3}{2\sqrt{3}} \frac{r^2}{t_{1/2}} \approx 0.007 \frac{r^2}{t_{1/2}} \qquad (7)$$

The values for the diffusion coefficient of $CoCp_2$ in SnS_2 obtained using Equation (7) are shown in Table 4.3. The calculated values seem to display a dependence on particle size. This is unlikely to be correct since the $CoCp_2$ is diffusing through chemically identical lattices albeit of different crystal sizes. The apparent size dependence of the diffusion coefficient can be explained if defects in the crystals are considered. Since larger crystals might be expected to have more defects than smaller crystals, the values of D calculated for large crystals using the model above (which assumes perfect crystallinity) will be correspondingly greater overestimates of the true D in these systems than the values calculated for small crystals.

Table 4.3: Kinetic rate constants (k), half-lives ($t_{1/2}$) and estimated diffusion coefficients, D(30°C), as a function of particle size for the intercalation of $CoCp_2$ into SnS_2 at 30°C.

Diameter range (μm)	Average radius (μm)	k ($sec^{-1.5}$)	$t_{1/2}$ (sec)	D(30°C) ($10^{-9}cm^2/sec$)
~ 60	30	0.011745	66.7	1.35
60-90	37.5	0.009548	82.0	1.71
90-250	85	0.005103	153.4	4.68
250-350	150	0.002970	263.6	8.51

(b) $SnSe_2/CoCp_2$ kinetics

The intercalation of $CoCp_2$ by $SnSe_2$ differs from that into SnS_2 in two main respects.

(1) the reaction kinetics are significantly slower ($t_{1/2}(50°C)$ ~ 10 minutes for $SnSe_2$ versus $t_{1/2}(50°C)$ ~ 30 seconds for SnS_2).

(2) the rate of disappearance of host is approximately twice as fast as the rate of appearance of the stage 1 intercalate.

As a means of illustrating the latter observation, the quantities of host and intercalates have been normalised to a dimensionless quantity, α, so that α_{host} and $\alpha_{intercalate}$ are both equal to zero at time t = 0 and approach a value of 1.0 as $t \rightarrow \infty$. The evolution of the intercalate 001 peak, $\alpha_{host}(t)$ is a sigmoidal function while in contrast, the host 001 peak disappears as a first order function so that $\alpha_{intercalate}(t) = 1 - \exp(-kt)$ (see Figure 4.12). Both $\alpha_{host}(t)$ and $\alpha_{intercalate}(t)$ can be fitted to a generalised rate expression of variable order, m, as in the kinetics analysis for SnS_2 intercalation:

$$\alpha(t) = 1 - \exp\{-(kt)^m\}$$

The values of k and m obtained from least squares fitting of the experimental data collected between 50 and 80°C are shown in Table 4.4.

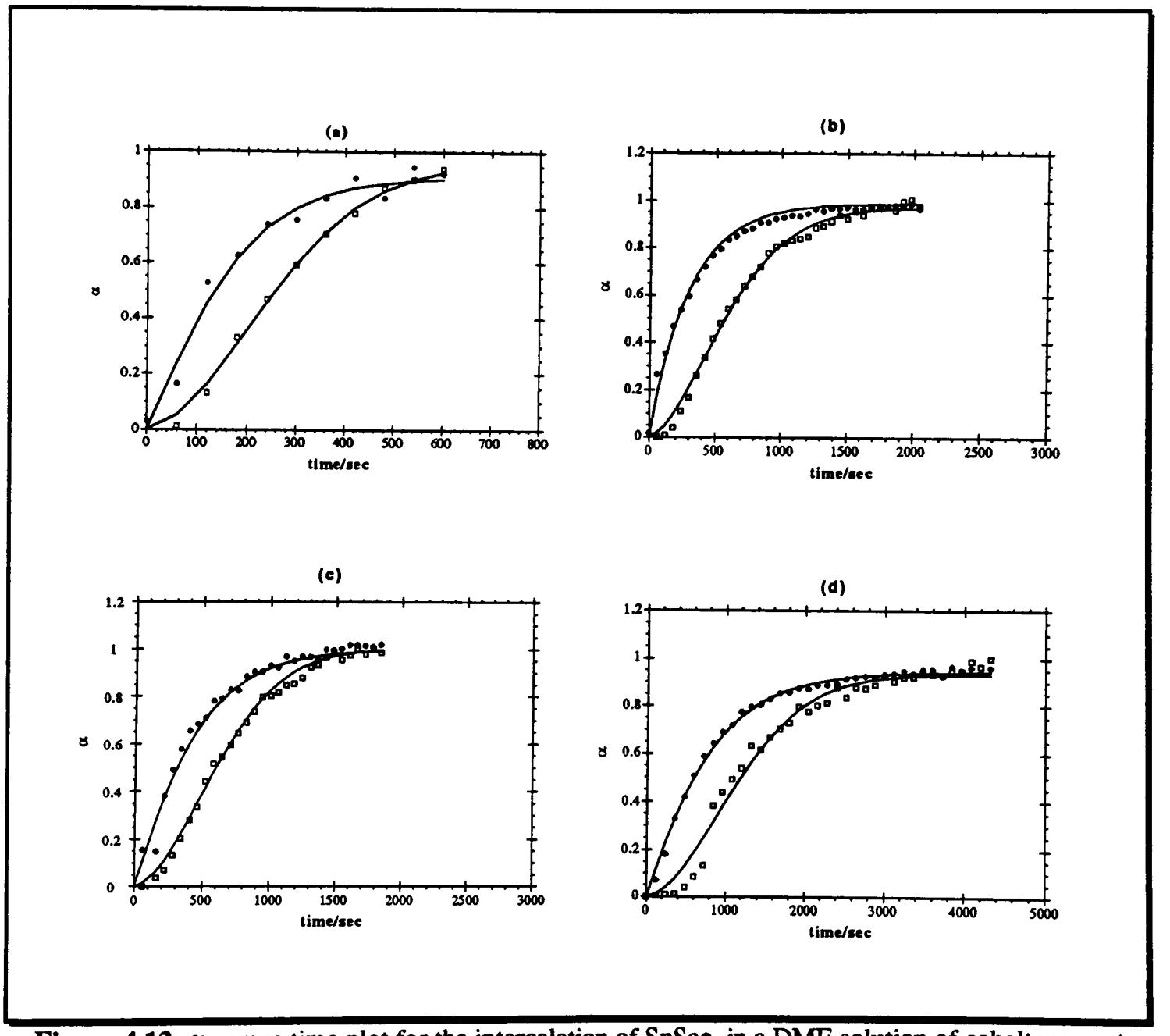

Figure 4.12: α versus time plot for the intercalation of $SnSe_2$ in a DME solution of cobaltocene at various temperatures. (a) 80°C (b) 73°C (c) 64°C (d) 48°C. Solid and open symbols represent data points for $\alpha_{host}(t)$ and $\alpha_{intercalate}(t)$ respectively. Solid lines correspond to curve fits of the data for $\alpha_{host}(t)$ and $\alpha_{intercalate}(t)$ to the generalised expression $\alpha(t) = 1 - \exp\{-(kt)^m\}$, where m = 1.0 and 1.8 respectively.

Table 4.4: Kinetic rate constant, k, and reaction order, m, for the intercalation of temperatures between 50 and 80°C.

	Intercalate 001		Host 001	
Temp (°C)	k ($10^3 sec^{-1}$)	m	k ($10^3 sec^{-1}$)	m
48	0.717	1.8	1.28	1.1
64	1.35	1.8	2.31	1.1
73	1.42	1.8	3.26	0.8
80	3.26	1.8	6.17	1.2

The disparity in the kinetic rate constants between the evolution of $\alpha_{host}(t)$ and $\alpha_{intercalate}(t)$ constrasts sharply with those obtained for SnS_2 intercalation with $CoCp_2$, where $\alpha_{host}(t)$ and $\alpha_{intercalate}(t)$ are approximately the same. The difference in rate constants for $\alpha_{host}(t)$ and $\alpha_{intercalate}(t)$ implies that the host phase does not evolve directly into the intercalate phase. However, no evidence of staging is seen in these intercalates. An alternative explanation is that depicted in Figure 4.13.

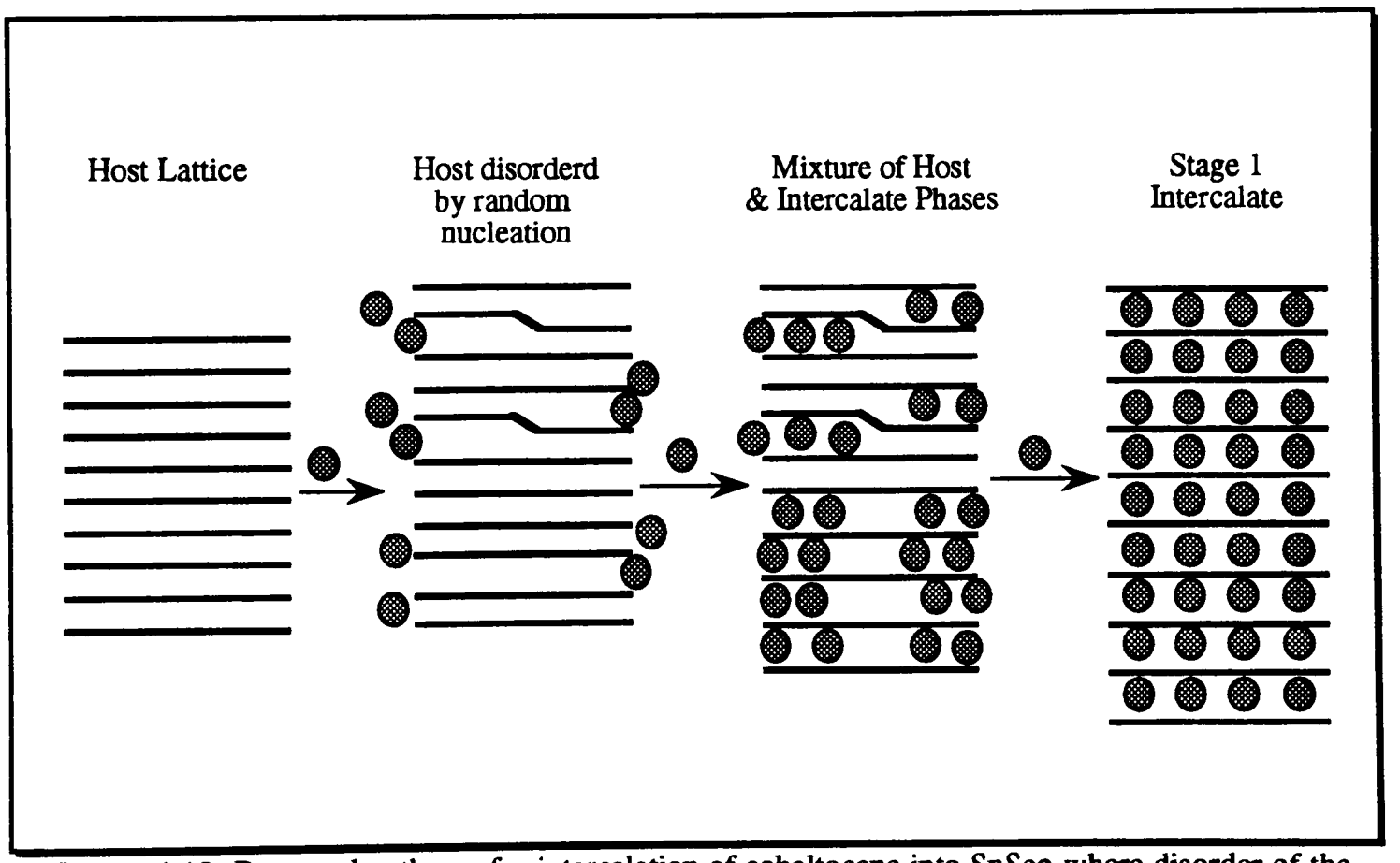

Figure 4.13: Proposed pathway for intercalation of cobaltocene into $SnSe_2$ where disorder of the host phase precedes the ordering of the intercalate phase.

In the initial stages of the reaction, only a few random layers are intercalated with cobaltocene (that is, random nucleation occurs). As a consequence, the repeat order of the host phase is lost, but there is insufficient ordering of the intercalate phase to be detected by X-ray diffraction of the bulk sample. However, as the reaction proceeds, the number of nucleated sites gradually increases (that is, less unintercalated layers remain),and the intercalate phase attains sufficient dimensions to give coherent X-ray scatter. As the

intercalant diffuses into the crystal, the intercalate phase grows rapidly (as evidenced by the steeply rising portion of the sigmoidal growth function, $\alpha_{intercalate}(t)$) while in contrast, the rate at which the host phase disappears is slowing down. Although there is no independent proof for this model, it adequately explains the difference in kinetic rate constants as well as the discrepancies between $\alpha_{host}(t)$ and $\alpha_{intercalate}(t)$ profiles. Moreover, similar observations have been made in recent experiments on ZrS_2[21].

The model for $SnSe_2$ intercalation is thus similar to that for SnS_2, involving two main steps, nucleation and growth. The two intercalation reactions differ in the relative rates of the two steps. For SnS_2, diffusion is rapid compared to nucleation, while diffusion of $CoCp_2$ into $SnSe_2$ is slow relative to nucleation. As a result, the rate of appearance of the intercalate is roughly equal to the rate of disappearance of host in the former case while loss of the host phase precedes growth of the intercalate in the latter.

4.3.2.2. Activation Energy

From the kinetic rate constants extracted for the various temperatures between 10° and 70°C, an Arrhenius-type activation energy can be calculated from the expression:

$$k = A\exp\left(-\frac{E_a}{RT}\right) \qquad (6)$$

where A = pre-exponential factor
E_a = activation energy in J/mole
R = Molar Gas constant = 8.314 J/mole
T = temperature in Kelvin

A plot of ln k vs 1/T is shown in Figure 4.14 for two particle size fractions of SnS_2 (90→250μm and 250→350μm), from which an average activation energy of 40±5 kJ/mole was calculated.

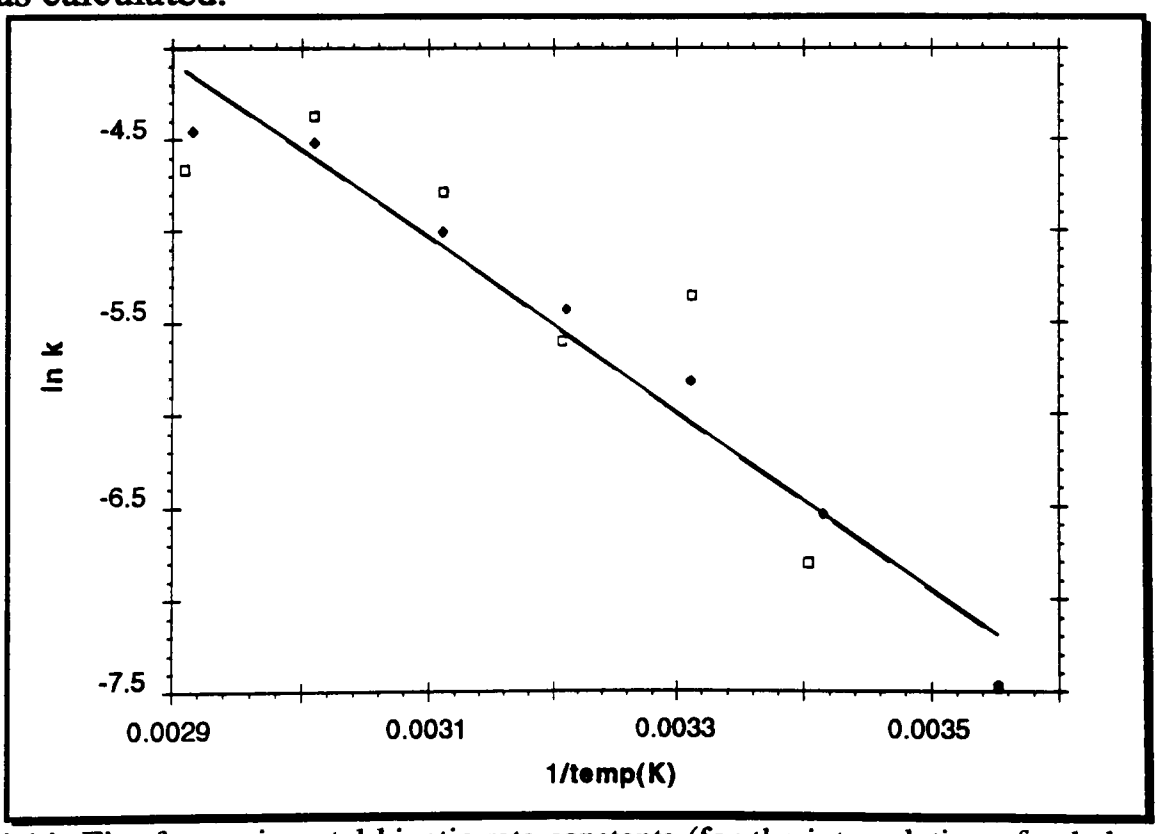

Figure 4.14: Fit of experimental kinetic rate constants (for the intercalation of cobaltocene into SnS_2) to an Arrhenius-type expression of the form: $k = A\exp(-E_a/RT)$ by plotting ln k vs 1/T (where k = kinetic rate constant, A=pre-exponential factor, E_a = activation energy, R=molar gas constant, T=temperature). Data for two different particle sizes are shown: (♦) 90-250μm, (❑)250-355μm.

In analogy with the kinetic analysis for the intercalation of $CoCp_2$ into SnS_2, an Arrhenius plot was also attempted for the $SnSe_2$ system (Figure 4.15). Fitting the data to a straight line yielded activation energies of 43 and 39 kJ/mole for rate constants extracted from $\alpha_{host}(t)$ and $\alpha_{intercalate}(t)$ respectively.

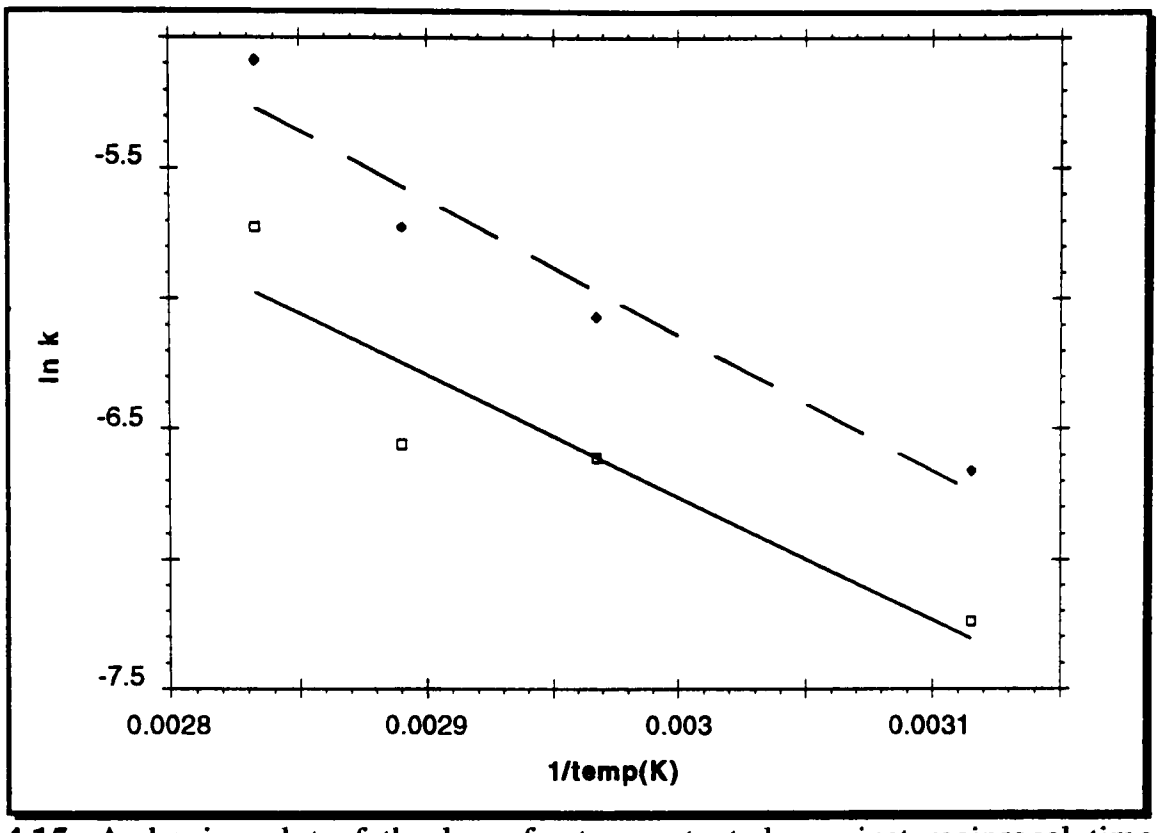

Figure 4.15: Arrhenius plot of the log of rate constant, k, against reciprocal time for the intercalation of cobaltocene into $SnSe_2$.

However, significant deviations from linearity were observed for both data sets, so that the activation energies calculated suffer from large experimental uncertainty. Indeed, their similarity to the activation energies for the analogous intercalation into SnS_2 despite the order of magnitude decrease in reaction rate strongly suggests that these Arrhenius values are not good measures of the energy barrier of the intercalation reaction. In view of this, a more accurate, convenient and easily interpretable measure of the ease of intercalation is to compare the half-lives of the reactions. A comparison between the half-lives for the intercalation of cobaltocene into SnS_2 and $SnSe_2$, shown in Table 4.5, reflects this difference in ease of intercalation between these two host lattices.

Table 4.5: Comparison between the half-lives for the intercalation of cobaltocene into SnS_2 and $SnSe_2$ at various temperatures. Particle size of $SnSe_2$ used was 60-90μm while data for two particle sizes of SnS_2 (A = 60-90μm, B = 250-350μm) are shown since the smaller particle size of SnS_2 reacted too quickly at temperatures > 60°C.

Approx. Temp (±4°C)	$t_{1/2}(SnSe_2$, host) (sec)	$t_{1/2}(SnSe_2$, Int) (sec)	$t_{1/2}(SnS_2$, A) (sec)	$t_{1/2}(SnS_2$, B) (sec)
50	560	1140	90	120
60	310	610	50	70
70	220	580	-	70
80	116	250	-	-

The values of half-lives depend not only on the characteristics of guest and host but also on the particle size. For diffusion limited reactions, we can define a size-independent parameter, $\varpi(T)$, which characterises the *susceptibility* of a lattice to intercalation by a given guest at a given temperature, T. The *kinetic intercalation susceptibility*, $\varpi(T)$, will be proportional to the diffusion coefficient, D(T). Choosing the proportionality constant to be 10^{10} s cm^{-2}, $\varpi(T)$ becomes a dimensionless quantity.

$$\varpi = 10^{10} \text{ s cm}^{-2} D(T)$$

Under such a definition, the intercalation susceptibility of SnS_2 to $CoCp_2$ at 50°C, $\varpi(50°C)$ is *ca.* 10^2 while for $SnSe_2$, $\varpi(50°C)$ is *ca.* 1.

4.3.2.3. Comparison with previous work

The intercalation of Lewis bases into layered host lattices is thought to consist of 4 basic steps[2, 22]: (a) diffusion of the intercalant to the surface of the host material (b) adsorption of the intercalate on the surface (c) formation of an activated complex with the host surface atoms and concomitant opening of the layers & (d) diffusion of the intercalants into the lattice to give a stable intercalation compound. Steps (a) and (b) are generally quick processes and are not expected to be rate limiting.

Subba-Rao and Shafer[2] report that while step (c) is likely to be the rate determining step for the intercalation of potassium hydroxide into TaS_2, its effect on the reaction rate is likely to be fairly small since the deintercalation of hydroxide intercalates is easily achieved (i.e., the reaction is thermodynamically reversible). However, they note that step (d) may also be rate limiting, especially in cases where intercalation has proceeded to a considerable extent. By then, all the surface sites of the host will have reacted with the metal hydroxides and the inherent slowness of intercalant diffusion into the bulk of the lattice prevents further activated complex formation.

Such an interplay between activated complex formation (nucleation) and diffusion of the intercalant as the rate determining step is observed by Kikkawa in the intercalation of pyridine into the layered host FeOCl[22]. From Sharp-Hancock analyses, initially nucleation is the rate-determining step, but in the latter half of the reaction, diffusion of pyridine molecules into the inner regions of the lattice becomes rate limiting. Moreover, they report a difference in the dimensionality of nucleation, with Avrami-Erofe'ev second order kinetics pre-dominating at high temperatures (70→128°C) while at low temperatures (14→55°C), first order kinetics are operative. For both steps (c) and (d), in the high and low temperature regime, they report activation energies ranging from 25 to 63 kJ/mole.

Similarly, for the intercalation of NH_3 and N_2H_4 into TaS_2, Acrivos *et al.* find that the kinetic data fits a model in which formation of an activated complex and a mobile species on top of TaS_2 lamella of the reactant phase is assumed to be rate limiting, rather than separation of layers and the subsequent diffusion of guest species[4].

In contrast, the electrochemical intercalation of Li into TiS_2 is perceived by Bruce and Saidi[1] to be a simpler two-step process: (1) partial desolvation of an ion in the solution adjacent to the electrode and adsorption of the ion on the electrode surface (adion formation); (2) rapid diffusion of the ion across the surface, loss of the remaining solvent and incorporation of the ion in the lattice[1]. Moreover, for both cubic and layered TiS_2 (TiS_2-C and TiS_2-L respectively), the incorporation of the ions in the lattice is rate limiting. The activation energies for these processes are calculated to be largely the same (Table 4.6) while the energies for adion formation in the case of the cubic polymorph is double that for TiS_2-L. From the similarity of the activation energies for incorporation into the lattice of both polymorphs, the authors deduce that the cations enter the lattice in their unsolvated form.

Table 4.6: Comparison of activation energies for the intercalation of Lewis bases into layered hosts.

Compound	E_a (kJ/mole)	Reference
$Li_{0.2}TiS_2$-L	13(1), 33(2)[a]	[1]
$Li_{0.2}TiS_2$-C	26(2), 27(1)[a]	[1]
$FeOCl(py)_x$ {14-55°C}	25, 48[b]	[22]
{70-128°C}	38, 63[b]	[22]
$TaS_2(N_2H_4)_x$	70	[4]
$TaS_2(M)_x(H_2O)_y$	3	[2]

[a] Values refer to activation energies for adion formation, E_{ct}, and lattice incorporation, E_{latt}, respectively. Estimated standard deviations are give in parentheses.
[b] Postulated as a two-step process; the first number refers to activation energy of nucleation while the second number is the activation energy for subsequent diffusion of intercalant into the host layers.

Although the Arrhenius activation energy has been used as a yardstick for comparison of energy barriers to intercalation by previous workers, it is unclear what this energy corresponds to along the reaction coordinate for intercalation[23]. The results of the previous section have demonstrated that while the Arrhenius activation energy gives a temperature independent comparison across different systems, it may not accurately reflect the propensity of a particular lattice towards intercalation. A more informative measure would be intercalation half-lives, or in the case of diffusion limited intercalations, intercalation susceptibilities (see previous section). The latter parameter has the advantage over half-life values that it is independent of host particle size and convenient comparisons can be made across different lattices intercalated with the same guest.

The diffusion coefficients for $CoCp_2$ in SnS_2 estimated in the previous section can be compared to the values reported in the literature. Although attempts have been made to estimate the diffusion coefficients of ions in various intercalation systems, they

have been derived using very different methodologies and on different host lattices so that a wide range of values have been reported.

Calculations of diffusion coefficients from line-broadening in NMR experiments yield values for H in H_xMoO_3[24] and H_xWO_3[25] of D(300K) ranging from 10^{-8} to 10^{-11} cm^2 s^{-1}. In contrast, measurements on the diffusion coefficients of Cu in $Cu_xMo_6S_8$ within a solid state cell at 441K[26] give much higher values of 7×10^{-7} to 4.8×10^{-5} cm^2 s^{-1} for $1.5 < x < 3.27$ while diffusion coefficients for Li and Na may vary from 10^{-6} to 10^{-10} cm^2 s^{-1} in $Ti_{1+x}S_2$, depending on the stoichiometry of the host[27-29]. From TDPAC spectroscopic measurements, Butz *et al.*[30] have estimated that D(300K) for lithium in tantalum and titanium disulfides is between 10^{-8} to 10^{-9} cm^2 s^{-1}.

Clearly, the diffusivity of guests through a host lattice varies a great deal from one intercalate to another. It is thus difficult to know if the values calculated for the diffusion coefficient in SnS_2 are reliable unless we can compare it with the diffusion coefficient of another guest species in SnX_2 or similar metal dichalcogenide. However, as noted in the previous section, the simplistic model used to estimate diffusion coefficients in this chapter assumes that the particles are *perfect* circular crystals so that the intercalation proceeds inwards from the edge only. Realistically, the crystals will have defects which means intercalation can also proceed from these sites; the diffusion coefficients of cobaltocene in tin disulfide estimated and shown in Table 4.3 therefore represent lower limits for these values.

4.4. Qualitative Considerations on Reaction Intermediates

4.4.1. Observations

In order to examine if the choice of solvent affects the intercalation process, both SnS_2 and $SnSe_2$ were additionally intercalated in a toluene solution of $CoCp_2$. The rates of intercalation were significantly slower with toluene as the solvent, than when DME was used. As a consequence, the experiments with toluene-$CoCp_2$ were conducted at significantly higher temperatures (70→120°C) in order that the reaction occurred on a time scale convenient for data collection. Representative data sets are shown in Figures 4.16 and 4.17 for SnS_2 and $SnSe_2$ intercalation respectively. The stacked spectra show the time course of the reaction as a series of energy-dispersive diffraction spectra taken at fixed time intervals.

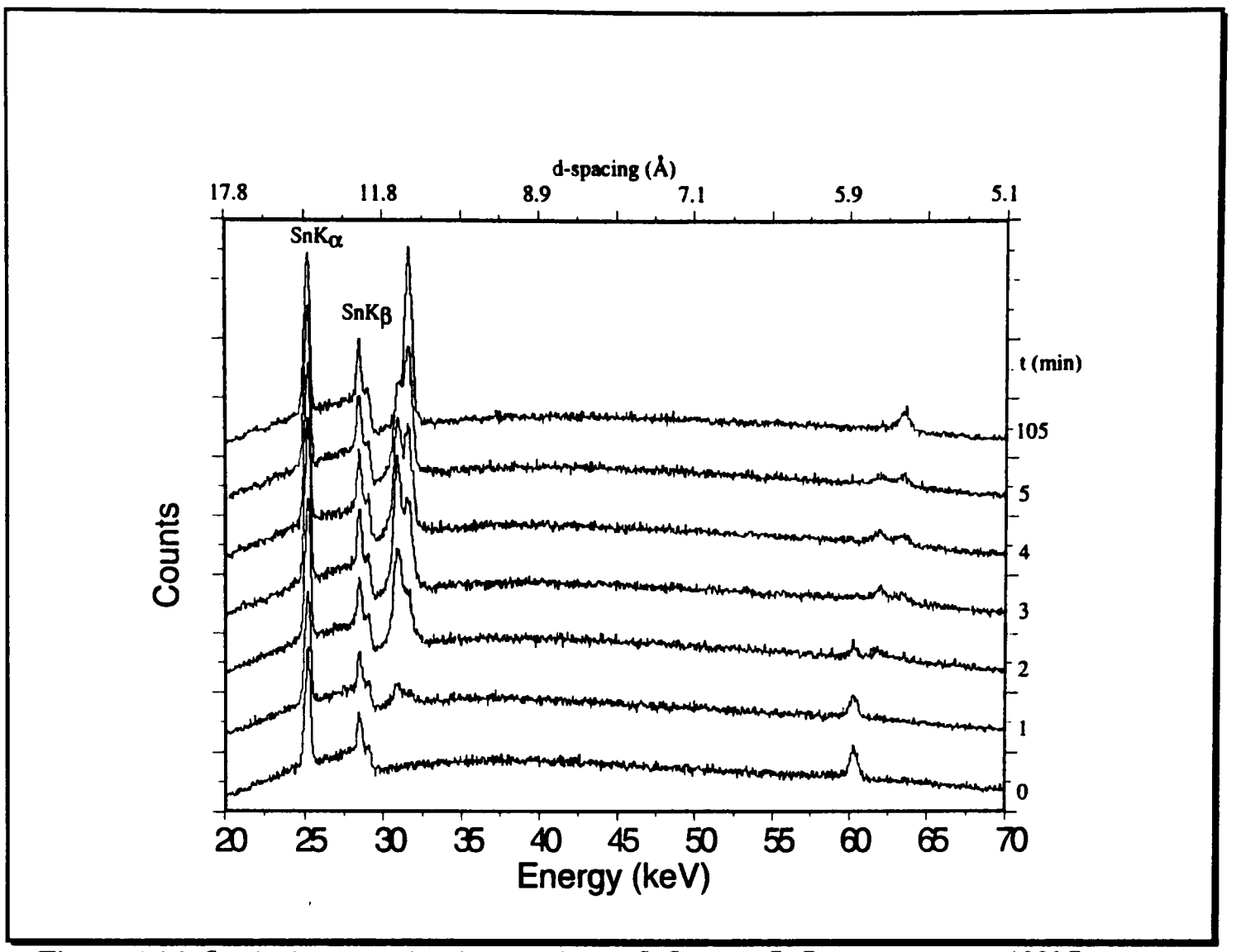

Figure 4.16: Stacked spectra showing reaction of SnS_2 with $CoCp_2$ in toluene at 120°C. Particle size: 60→90μm. Detector angle : 2.0°. Acquisition time per spectrum: 60 sec.

The main difference between using toluene and DME as solvent is the appearance of intermediate peaks during the course of the reaction for the former. The most significant feature is the peak on the high energy side of the *001* reflection for the intercalate; in $SnSe_2$ it overlaps with the main 001 peak (peak positions being 11.8Å & 11.5Å respectively) and can only be deconvoluted by Gaussian peak fitting (see Figure 4.19) while in SnS_2 the peaks are actually resolvable (see Figure 4.18). In addition, for $SnSe_2$ intercalates, broad features are also observed at 14.90Å, 9.95Å and 5.95Å during the early stages of the reaction (see Figure 4.17a).

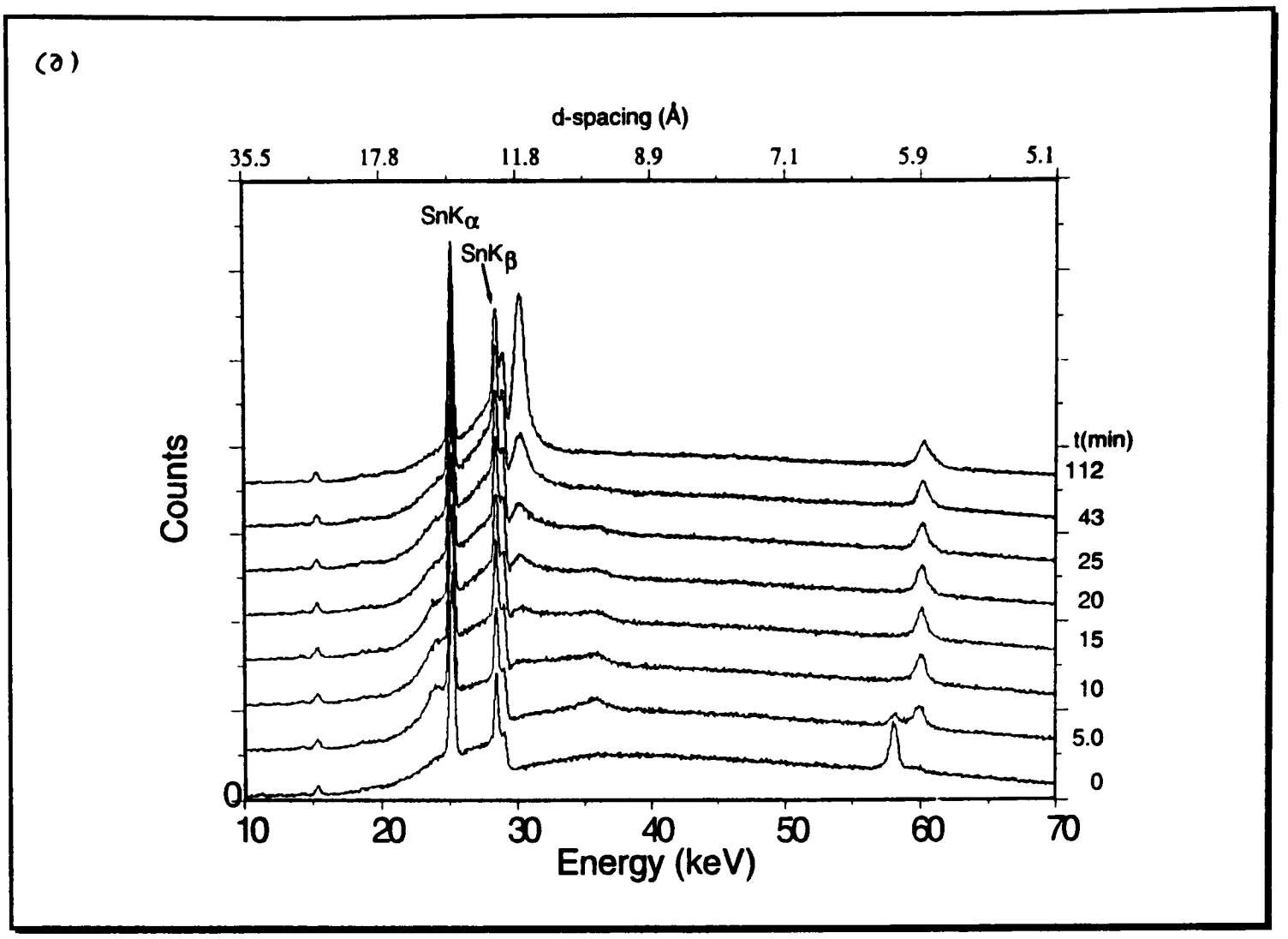

Figure 4.17: Stacked EDPD spectra showing reaction of $SnSe_2$ with $CoCp_2$ in toluene at 95° (*top*) and 120°C (*botttom*). Particle size: 60→90μm. Detector angle : 2.0°. Acquistion time per spectrum: 300 sec.

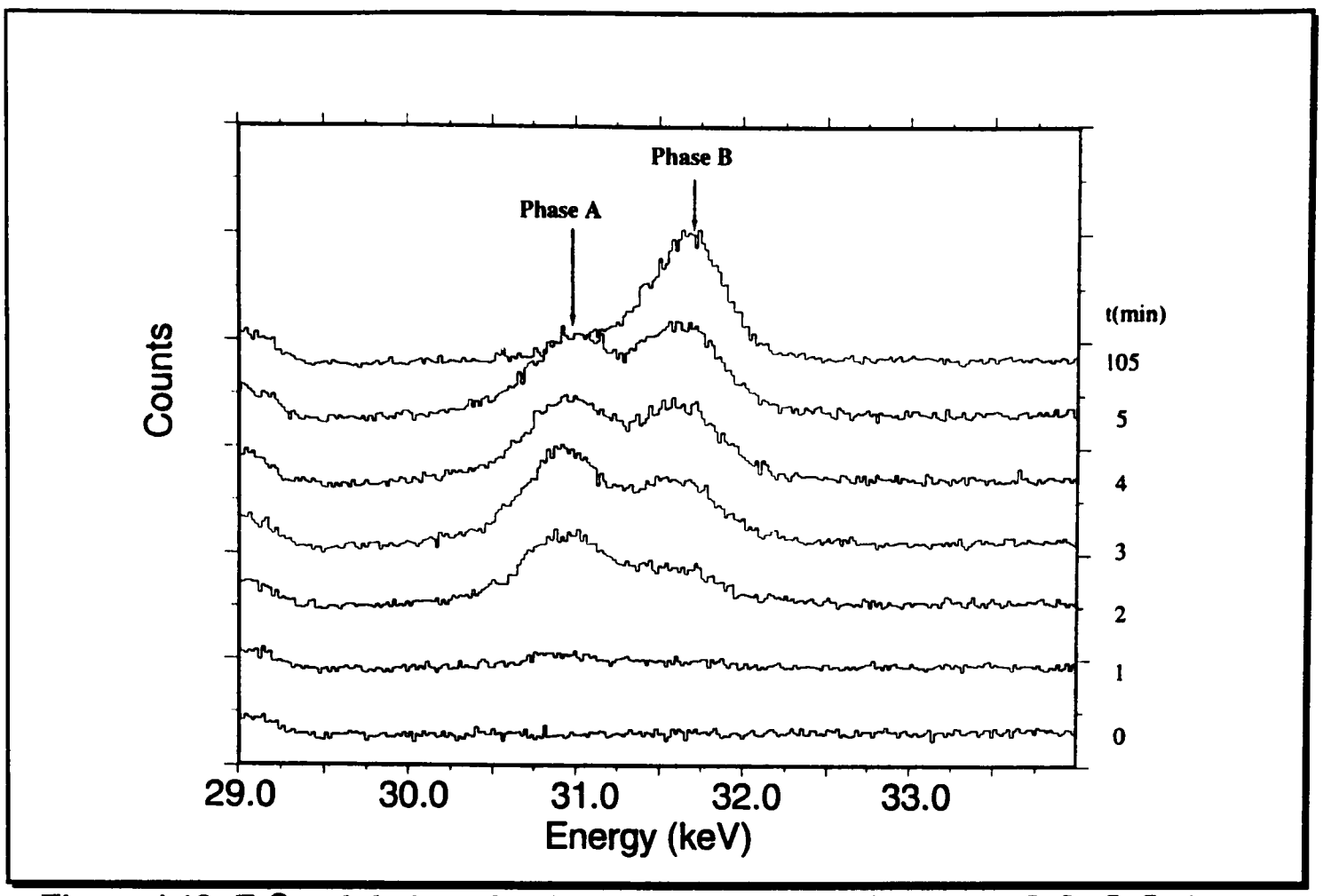

Figure 4.18: Expanded view of region around Intercalate 001 peak of $SnS_2(CoCp_2)_{0.3}$ to emphasise the two overlapping peaks with d-spacings 11.5 and 11.2Å.

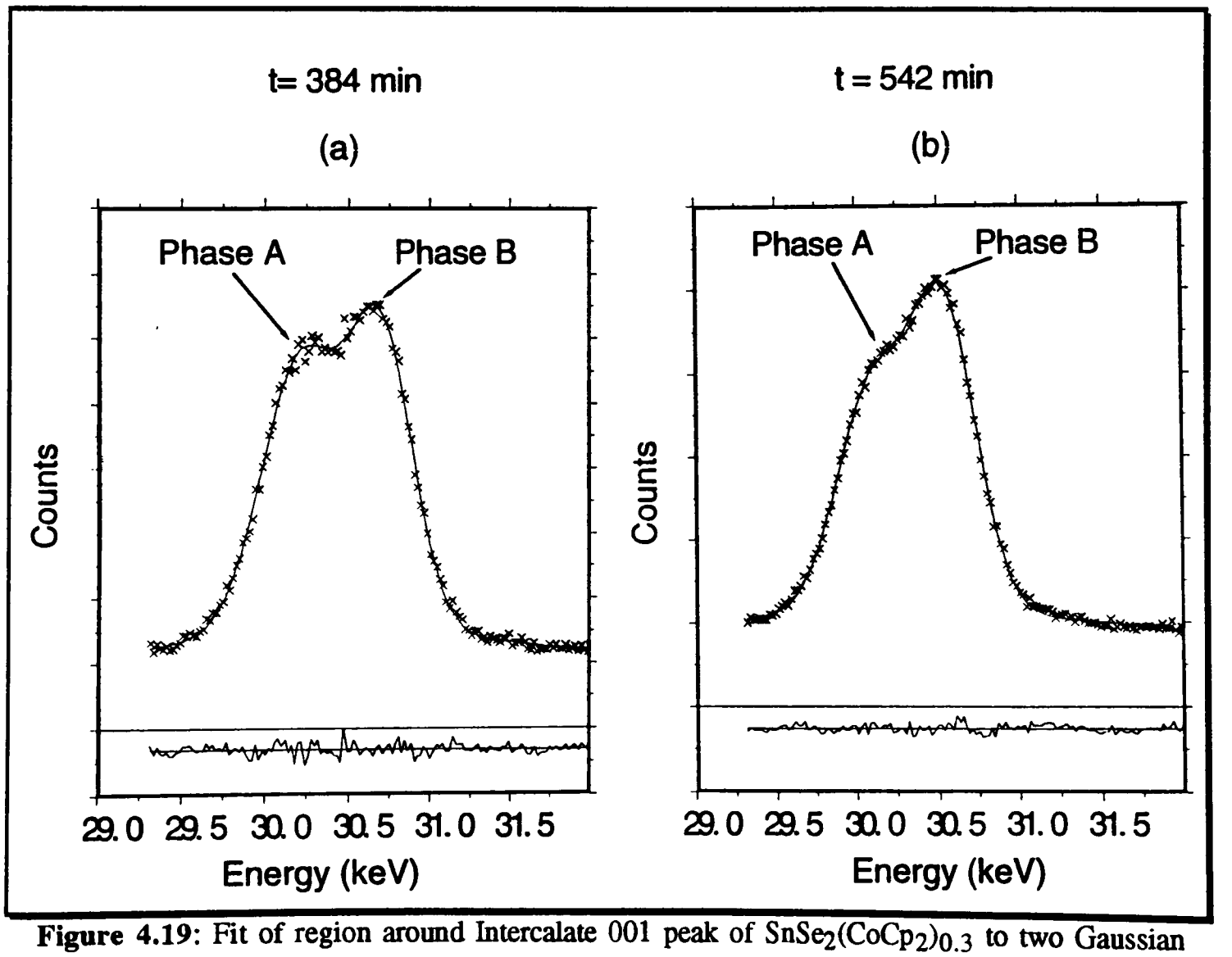

Figure 4.19: Fit of region around Intercalate 001 peak of $SnSe_2(CoCp_2)_{0.3}$ to two Gaussian profiles.

4.4.2. Discussion

The intermediate peaks which appear transiently during the intercalation process give d-spacings which can be indexed as *00l*'s of one of 3 apparent phases present, nominally assigned A, B and C. These are tabulated below (Tables 4.7 and 4.8):

Table 4.7: d-spacings of some intermediate Bragg peaks and their tentative assignments for SnS_2 intercalates.

Temp	Phase A[a]		Phase B[b]	
(°C)	*002*	*004*	*001*	*002*
70	11.47	5.70	11.23	5.60
80	11.48	5.74	11.22	5.60
95	11.48	5.73	11.22	5.59
120	11.48	5.77	11.23	5.59

[a] corresponds to unit cell with *c* axis dimensions of 22.9±0.2 Å
[b] corresponds to unit cell with *c* axis dimensions of 11.2±0.1 Å (Stage 1 Intercalate)

Table 4.8: d-spacings of some intermediate Bragg peaks and their tentative assignments for $SnSe_2$ intercalates.

Temp	Phase A[a]		Phase B[b]		Phase C[c]			
(°C)	*002*	*004*	*001*	*002*	*002*	*003*	*004*	*005*
70‡	11.83	5.88	-	-	14.90	-	-	5.98
80‡	-	-	-	-	14.92	9.93	-	5.93
95	11.76	5.89	11.56	5.78	14.90	9.95	-	5.95
120	11.80	5.89	11.60	5.80	-	-	-	-

‡ These reactions were not run to completion.
[a] corresponds to unit cell with *c* axis dimensions of 23.7±0.2 Å
[b] corresponds to unit cell with *c* axis dimensions of 11.5±0.1 Å (Stage 1 Intercalate)
[c] corresponds to unit cell with *c* axis dimensions of 29.8±0.2 Å

Phase B, with a d-spacing identical to that observed for $SnS_2(CoCp_2)_{0.3}$ synthesised in DME, corresponds to the stage 1 intercalate. However, the identity of Phase A and C cannot be unambiguously determined. One possibility, reflected in the tables above, is that Phases A and C represent stage 3 and 4 intermediates respectively (see Figure 4.20). Staging has been observed in graphite and transition metal dichalcogenide intercalates previously[12, 14, 15, 31-41] but was not observed in tin dichalcogenide intercalates formed in DME (see section 4.6.).

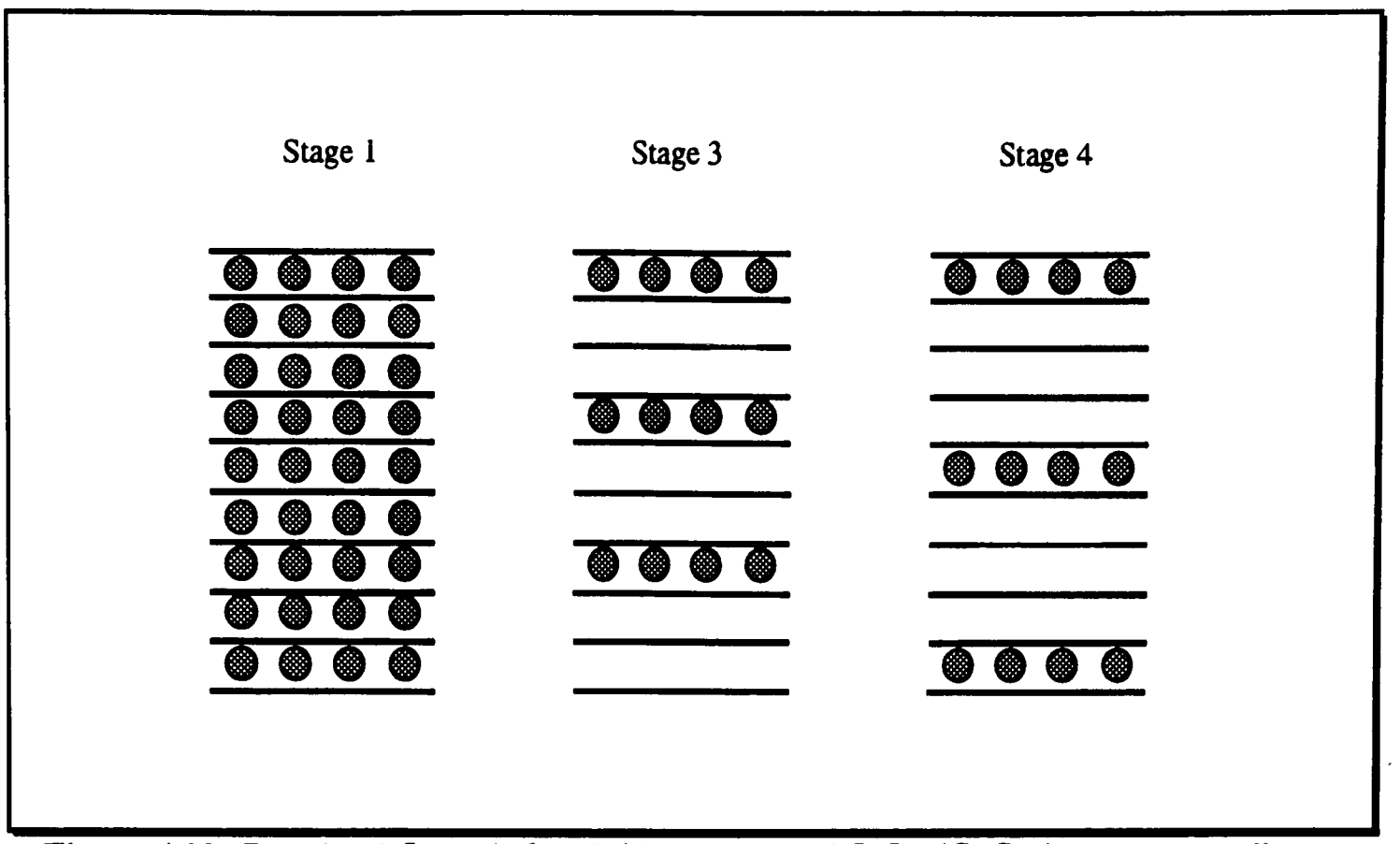

Figure 4.20: Postulated Stage 1, 3 and 4 intercalates of $SnSe_2(CoCp_2)_{0.3}$ corresponding to Phases B, A and C respectively.

However, there are two alternative interpretations which can explain the observed results. These two alternatives are listed below:

Alternative I: Phases C represents stage 1 products with co-intercalated solvent molecules while Phase A is due to $CoCp_2$ molecules intercalated in a different orientation that gives a larger lattice expansion. There have been precedents for both these possibilities; co-intercalation of solvent molecules, albeit of smaller sizes than toluene, has been reported previously[8, 9, 42] while two different orientations of cobaltocene have been observed by Heyes in TaS_2 using ^2H NMR[43].

Alternative II: Phase A represents a kinetic phase of the intercalate in which the intercalated layers are expanded relative to their thermodynamically stable position (Phase B). The kinetic phase is present only during the intercalation process, with the slightly larger interlayer spacing allowing cobaltocene molecules to "slide" into the van der Waals gap more readily (see Figure 4.21).

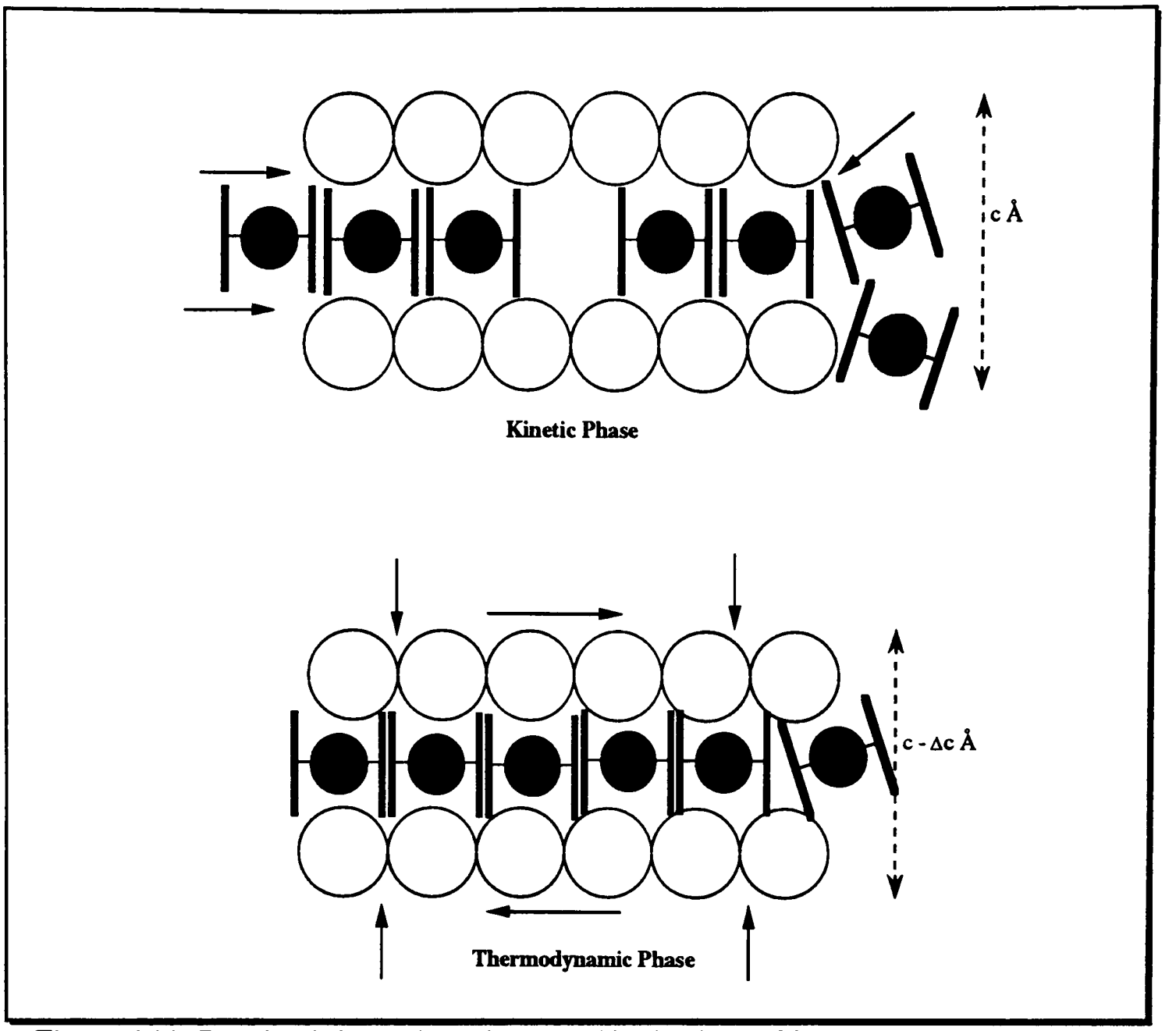

Figure 4.21: Postulated thermodynamic versus kinetic phase of intercalate, where the larger interlayer spacing of the latter allows cobaltocene molecules to diffuse into interlayer space more readily.

(a) Alternative I

The first alternative interpretation was examined using ^2H NMR spectroscopy of partially intercalated crystals. ^2H NMR spectroscopy is a sensitive probe of cobaltocene orientation (see Chapter 2) and could therefore be employed to test the hypothesis that the larger lattice expansion of Phase A relative to Phase B is attributable to a different orientation of cobaltocene.

Single crystals of SnS_2 (size: *ca.* 2mm x 2mm x 0.1mm) were partially intercalated by immersion in a toluene solution of $Co(\eta\text{-}C_5D_5)_2$ for 30 minutes at 100°C. The crystal were rinsed with toluene and mounted immediately into a sample tube in order to acquire a ^2H NMR spectrum before the kinetic phase, if present, could relax back to the low d-spacing phase. The crystal thus examined was checked by X-ray diffraction after the NMR experiment (see Figure 4.22) to verify the existence of Phases A and B.

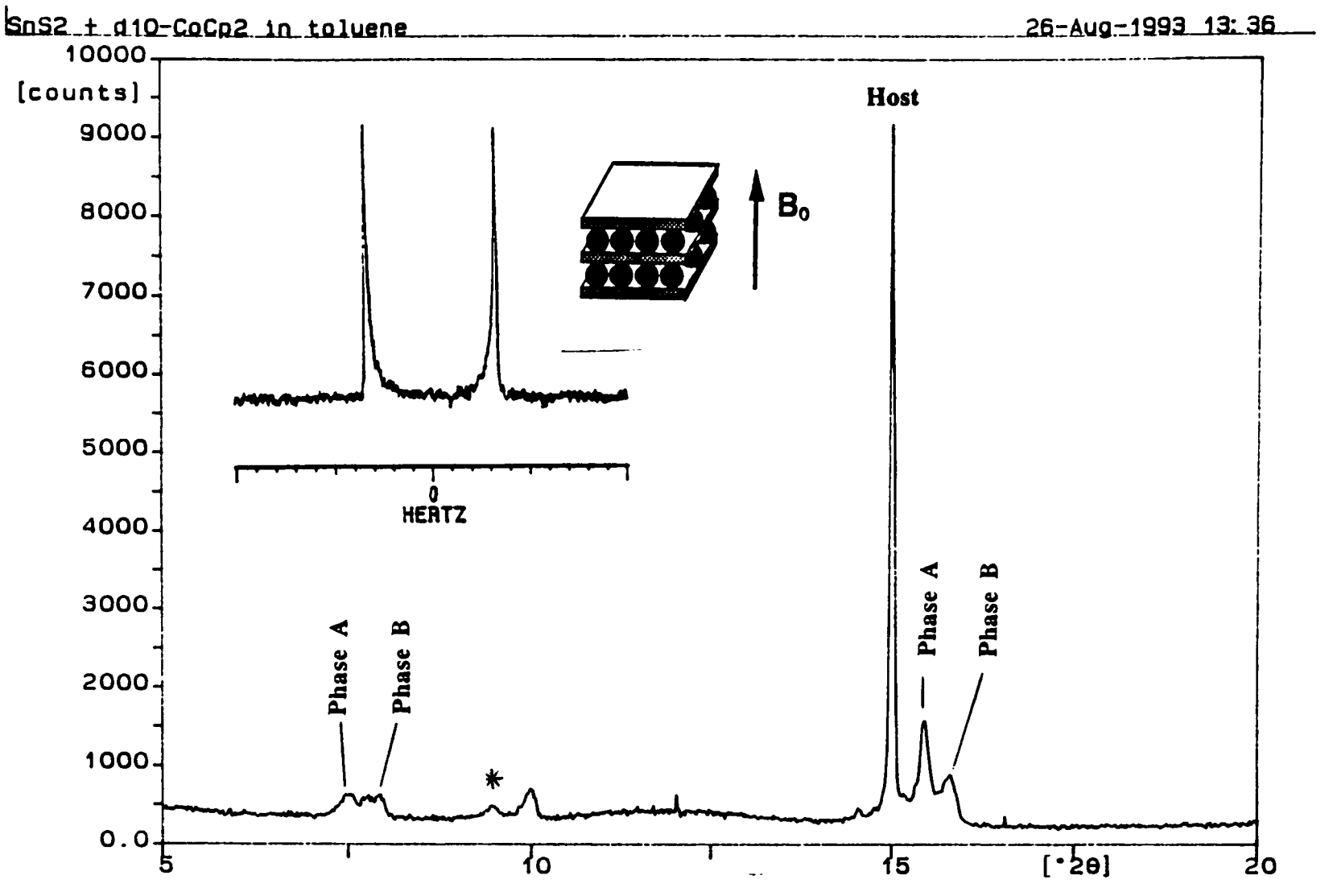

Figure 4.22: X-ray diffraction spectrum of SnS_2 crystal partially intercalated in toluene solution of deuterated cobaltocene. Inset shows the ^2H NMR spectrum obtained for the same crystal oriented with its layers perpendicular to the magnetic field. The splitting of the doublet in this spectrum is 67 kHz. The peak labelled with an asterisk (*) is due to the sample holder.

For crystals oriented with the layers perpendicular to the magnetic field, the ^2H-NMR spectrum showed the existence of only one doublet (see figure 4.22), with a splitting of 67 kHz, suggesting that only one orientation of $CoCp_2$ molecules is present; that is, an orientation in which they are undergoing rapid C_5 rotation with the principal moleular axis oriented perpendicular to the field (i.e., C_5 axis parallel to the crystal layers). There is no evidence of the 134kHz splitting that is associated with $CoCp_2$ in the other extreme orientation (i.e., C_5 axis parallel to the field or perpendicular to the layers) which could explain the existence of phase A.

^2H NMR spectroscopy was also used to test if Phases A and C were attributable to phases with different amounts of co-intercalated solvent molecules. Crystals were prepared as above except that a d^8-toluene solution of $CoCp_2$ was used instead. The crystals were rinsed with non-deuterated toluene after partial intercalation to remove surface amounts of deuterated toluene before the ^2H NMR experiment.

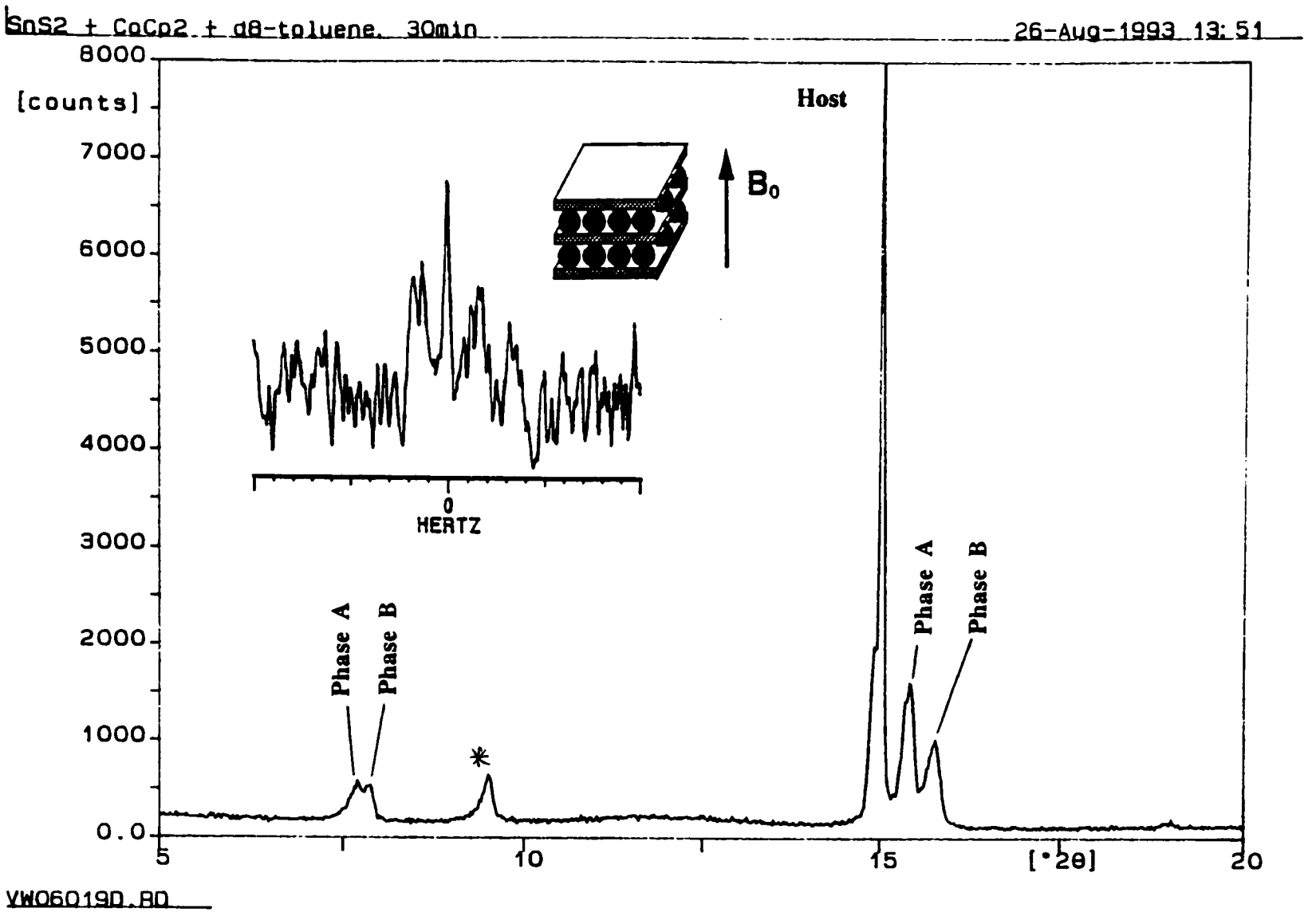

Figure 4.23: X-ray diffraction spectrum of SnS_2 crystal partially intercalated in deuterated toluene solution of cobaltocene. Inset shows the ^2H NMR spectrum obtained for the same crystal oriented with its layers perpendicular to the magnetic field. The peak labelled with an asterisk (*) is due to the sample holder.

If d^8-toluene molecules co-intercalate into the host lattice to a significant extent, the ^2H-NMR spectrum should show evidence of associated with the toluene deuterons. The ^2H NMR spectra obtained from the crystal examined is shown in Figure 4.23. The partially intercalated crystal shows only a few non-symmetrical peaks of very weak intensity, barely distinguishable above the baseline. They may be attributable to traces of d^8-toluene in the intercalate. However, the amount of d^8-toluene is very small, as shown by comparison with the ^2H NMR spectrum obtained for a similarly intercalated crystal, except that both deuterated toluene and cobaltocene were used in the synthesis (Figure 4.24).

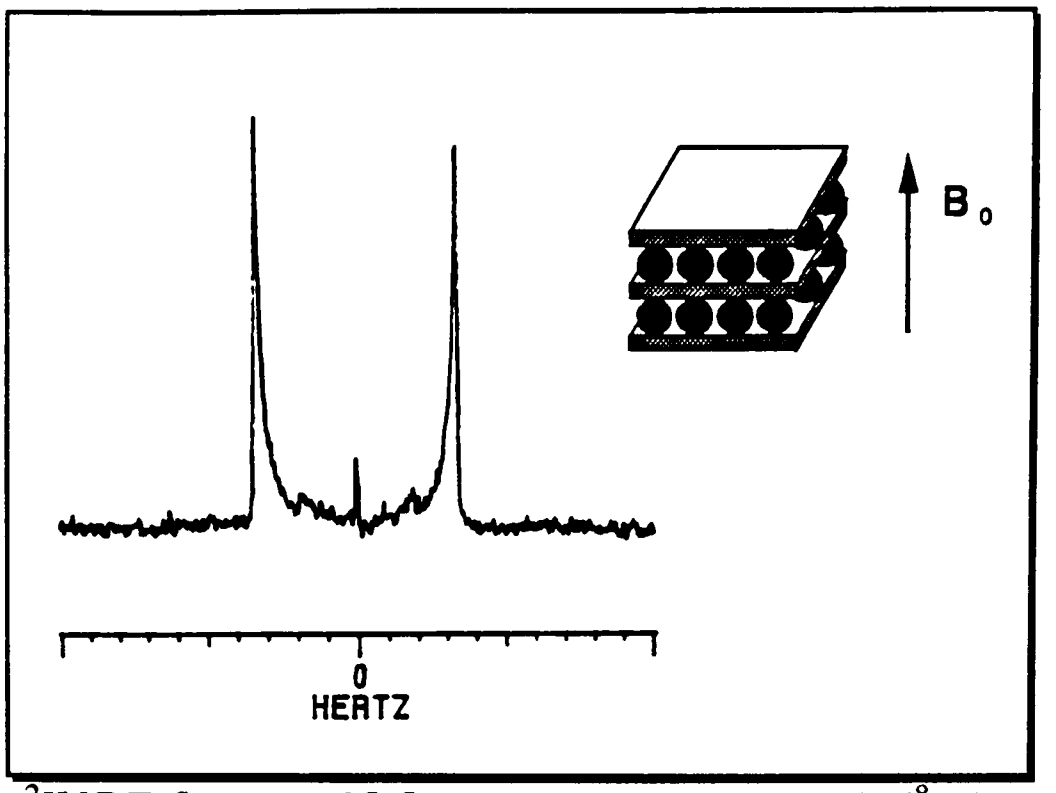

Figure 4.24: ^{2}H-NMR Spectrum of SnS_2 crystal partially intercalated in d^8-toluene solution of d^{10}-cobaltocene.

(b) Alternative II

There is no good method for distinguishing the existence of a kinetic phase with a large interlayer spacing from higher stage intermediates. Although the absence of certain *00l* peaks in Phases B and C might suggest that the indexed peaks present may not have been assigned correctly (Tables 4.7 and 4.8), it may also be due to systematic absences or small structure factors $|F_{00l}|$ in these staged intermediates, or in the case of high d-spacing peaks, limited by the resolution of the detector at low energies. The detector resolution $\Delta E/E$ is a sensitive function of E and θ and any phases with a d-spacing greater than 12Å would be not visible within the constraints of the present experiment. Moreover, although there exists experimental evidence for staging in these metal dichalcogenide intercalates[12, 14, 44, 45], there is no precedent for a kinetic phase with a larger interlayer spacing than that observed in the final product. Thus, on balance, it seems reasonable to suppose that Phases B and C correspond to Stage 3 and 4 intercalates of the tin dichalcogenides respectively when the reaction is carried out in toluene solution of cobaltocene.

(c) Reflections on Staging Model

It is curious that Stage 1,3 and 4 intermediates of $SnX_2(CoCp_2)_z$ {X=S, Se, $0<z<0.3$} are observed during the intercalation process, but not Stage 2 or other stages greater than Stage 4. Moreover, the presence of the Stage 4 intercalate seems to be very transient and exists in relatively small quantities, as evidenced by the diffuse *00l* reflections. The absence of Stage 2 intercalates is curious since the Daumas-Herold

Model predicts that stage transformations of the type n→n-1→n-2...2→1 should occur with relative ease by migration of stage islands (see Chapter 1). The domain island model was invoked to circumvent the difficulty of explaining odd→even (e.g Stage 3→2) or even→odd (Stage 4→3) stage transformations since such transitions would otherwise require depopulation of entire planes of guest molecules if staging were to be maintained uniformly throughout the crystal (see Figure 4.25).

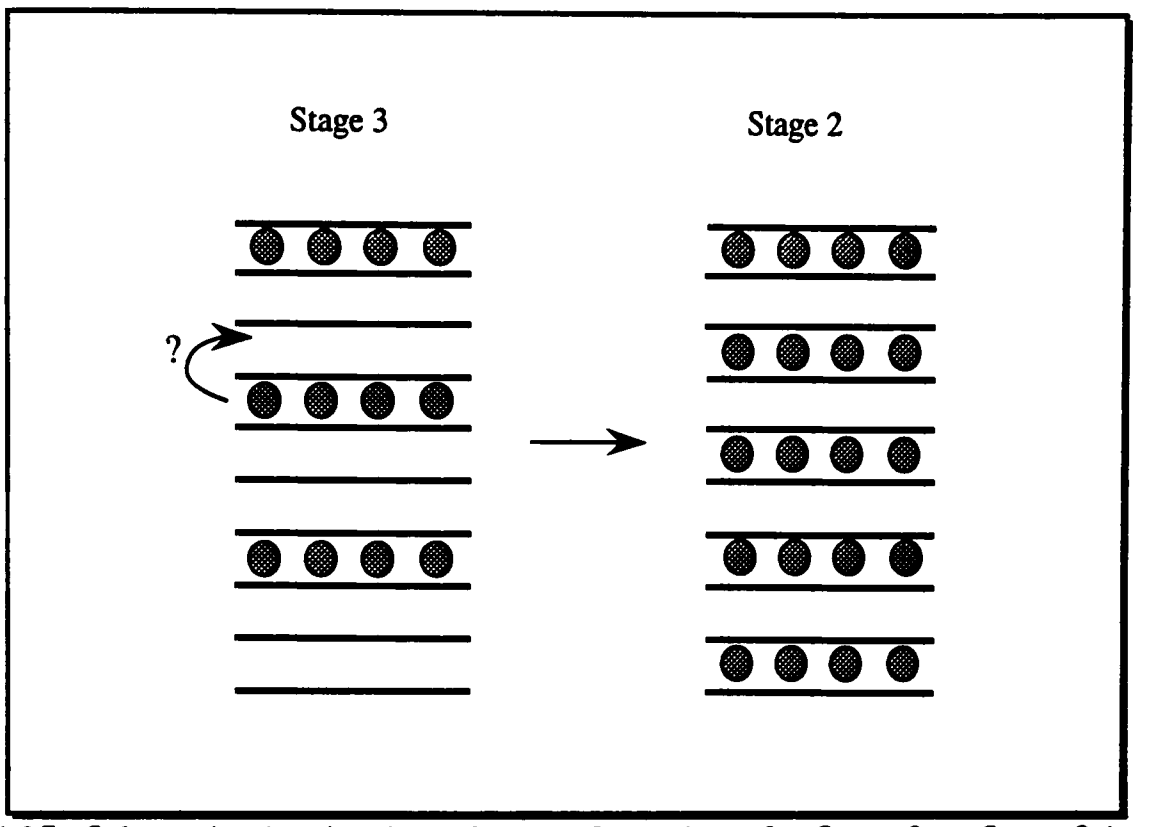

Figure 4.25: Schematic showing how the transformation of a Stage 3 to Stage 2 intercalate requires depopulation of exisiting intercalated layers.

However, in view of the absence of Stage 2 intercalates and the relative paucity of Stage 4 species, it is possible that the Daumas-Herold Domain model does not hold in the case of $CoCp_2$ intercalation into tin dichalcogenides. If complete intercalation of layers occurs in preference to formation of islands of domains (as is perhaps more likely for the rigid metal dichalcogenide layers than for the more flexible graphite layers), then odd→even and even→odd stage transformations cannot occur easily, which would explain the absence or relative dearth of even numbered stages. The small amounts of Stage 4 intermediates need not transform to Stage 1 intercalates via a Stage 3 intermediate; one possiblity is via a fractional stage such as Stage 4/3, where 3 out of every 4 layers contains guest species (see Figure 4.26). Such fractional stages have been observed in potassium-graphite intercalation compounds by Marcus *et al.*[46].

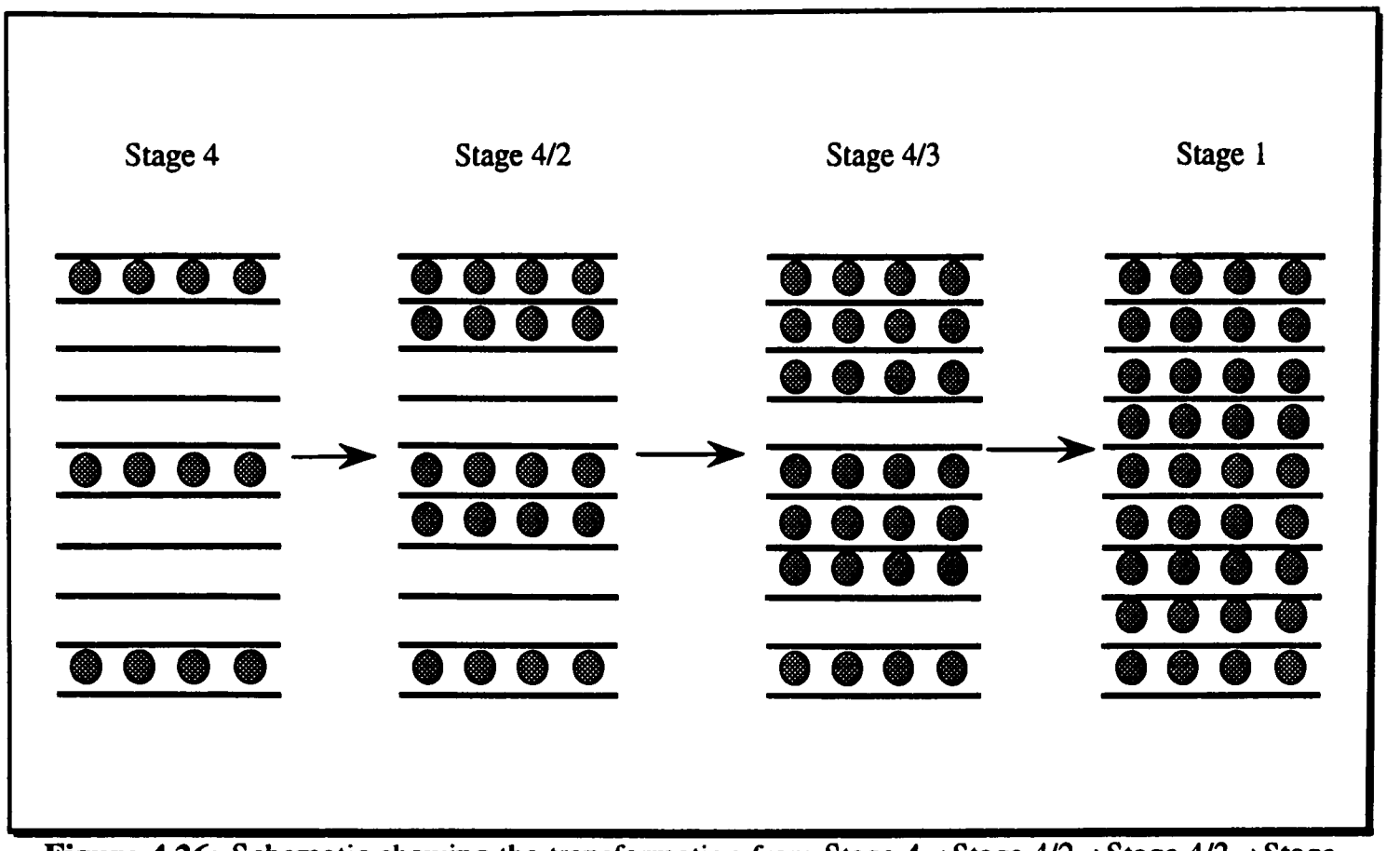

Figure 4.26: Schematic showing the transformation from Stage 4→Stage 4/2→Stage 4/3→Stage 1, without going through a Stage 3 or 2 intermediate.

4.5. Conclusions

An apparatus has been developed to study the kinetics of intercalation of air-sensitive guests into microcrystalline samples. The use of energy dispersive powder diffraction techniques enables reactions with half-lives of a minute or less to be examined while the modular design of the experiment allows a wide variety of solid-liquid reactions to be studied with minimal turn-around time.

From the *in situ* kinetics experiments for the intercalation of $CoCp_2$ into SnS_2 with dimethoxyethane as solvent, the rate expression which best fits the data is based on a Nuclei Growth Model[18], in which two-dimensional diffusion of the intercalant towards the crystal centre is the rate-determining step. The intercalation of $CoCp_2$ into $SnSe_2$ differs from that into SnS_2 in two main respects: (a) the speed of intercalation & (b) the relative rates of disppearance of host and appearance of intercalate. A model of intercalation which involves different rates of nucleation relative to intercalant diffusion is proposed to account for these differences.

From the variable temperature kinetic data, the activation energy calculated for the intercalation of $CoCp_2$ into SnS_2 is 40±5 kJ/mole while the corresponding value for $SnSe_2/CoCp_2$ intercalation is 41 ± 10 kJ/mole. Since the rates of these two reactions differ by at least an order of magnitude, it is proposed that a better parameter for comparing the ease of intercalation is the intercalation susceptibility. On such a scale, SnS_2 would have an intercalation susceptibility to $CoCp_2$ at 50°C of ~100 while $SnSe_2$ would have a value of ~1.

The choice of solvent can markedly influence the course of the reaction, albeit not the final product. Both the reaction rate, as well as the reaction pathway are sensitive to the solvent used. Intercalation is observed to occur much more quickly in a DME solution of $CoCp_2$ than a toluene solution under similar conditions of temperature, pressure, concentration and particle size of reactants. The latter solvent also leads to the formation of intermediates which are not observed with DME solutions of $CoCp_2$. The identity of these intermediates has not been unequivocally determined but is likely to be due to higher stage intercalates. The absence, or relative absence, of even numbered stages suggests that the Daumas-Herold Domain model is not operative, and an alternative pathway in which complete layers are intercalated instead is suggested.

References:

1. P. G. Bruce and M. Y. Saidi, *Solid State Ionics* (1992), **51**, 187-190.

2. G. V. Subba-Rao and M. W. Shafer, *J. Phys. Chem.* (1975), **79**, 557-560.

3. M. B. Dines and R. B. Levy, *J. Phys. Chem.* (1975), **79**, 1979.

4. J. V. Acrivos, C. Dellos, N. Y. Topsoe and J. R. Salem, *J. Phys. Chem.* (1975), **79**, 3003-10.

5. F. R. Gamble, F. J. DiSalvo, R. A. Klemm and T. H. Geballe, *Science* (1970), **168**, 568-571.

6. F. R. Gamble, J. H. Osiecki, M. Cais, R. Pisharody, F. J. DiSalvo and T. H. Geballe, *Science* (1971), **174**, 493-497.

7. F. J. DiSalvo, G. W. Hull, L. H. Schwartz, J. M. Voorhoeve and J. V. Waszczak, *J. Chem. Phys.* (1973), **59**, 1922-1929.

8. D. W. Murphy, S. A. Sunshine and S. M. Zahurak, in *Chemical Physics of Intercalation*, ed. S. Flandrois, A. P. Legrand, Plenum Press: New York, 1987, p. 173

9. J. Rouxel, L. Trichet, P. Chevalier, P. Colombet and O. Abou-Ghaloun, *J. Solid State Chem* (1979), **29**, 311-21.

10. X. W. Qian, D. R. Stump and S. A. Solin, *Phys. Rev. B.* (1986), **33**, 5756-69.

11. D. Deroo, D. Pedone and F. Daland, *J. of Applied Electrochemistry* (1990), **20**, 835-840.

12. C. Riekel, H. Reznik and R. Schollhorn, *J. Solid State Chem.* (1980), **34**, 253-262.

13. C. Riekel and R. Schollhorn, *Mat. Res. Bull.* (1976), **11**, 369-376.

14. C. Riekel and C. O. Fischer, *J. Solid State Chem.* (1979), **29**, 181-90.

15. W. Paulus, H. Katzke and R. Schollhorn, *J. Solid State Chem.* (1992), **96**, 162-168.

16. G. Margaritondo, *Introduction to Synchrotron Radiation*, Oxford University Press: New York, 1988.

17. J. D. Hancock and J. H. Sharp, *J. Am. Ceramic Soc.* (1972), **55**, 74-77.

18. S. F. Hulbert, *J. Br. Ceram. Soc.* (1969), **6**, 11-20.

19. P. Ganal, T. Butz and A. Lerf, *Syn. Met.* (1989), **34**, 641-5.

20. R. Muehlberger, T. Butz and A. Lerf, *Physica B* (1981), **105**, 218-22.

21. J. S. O. Evans, *D. Phil. Thesis*. Oxford University, 1993.

22. S. Kikkawa, *J. Solid State Chem* (1980), **31**, 249-255.

23. *Reactions in the Solid State.*, ed. C. H. Bamford and C. H. P. Tipper, Elsevier Scientific Publ. Co.: New York, 1980.

24. R. C. T. Slade, T. K. Halstead and P. G. Dickens, *J. Solid State Chem.* (1980), **34**, 183.

25. C. J. Wright, *J. Solid State Chem.* (1977), **20**, 89.

26. G. J. Dudley, K. Y. Cheung and B. C. H. Steele, *J. Solid State Chem.* (1980), **32**, 259-267.

27. R. Schollhorn, in *Inclusion Compounds*, ed. Academic Press: London, 1984, p. 249-334

28. B. G. Silbernagel, *Solid State Comm.* (1975), 361.

29. D. A. Winn, J. M. Shemilt and B. C. H. Steele, *Mat. Res. Bull.* (1976), **11**, 559-566.

30. T. Butz, A. Lerf and J. O. Besenthal, *Rev. Chim. Min.* (1984), **21**, 556-587.

31. D. C. Dahn and R. R. Haering, *Solid State Comm.* (1982), **44**, 29-32.

32. H. Fernandez-Moran, M. Ohstuki, A. Hibino and C. Hough, *Science* (1971), **74**, 498-500.

33. J. Morales, C. Perez-Vincente and J. L. Tirado, *Solid State Ionics* (1992), **51**, 133-138.

34. R. Nishitani, Y. Uno and H. Suematsu, *Phys. Rev. B.* (1983), **27**, 6572-75.

35. R. Nishitani, Y. Uno and H. Suematsu, *Syn. Met.* (1983), **7**, 13-22.

36. R. Nishitani, Y. Sasaki and Y. Nishina, *J. Phys. Soc. Japan* (1987), **56**, 1051-1057.

37. R. Nishitani, Y. Sasaki and Y. Nishina, *Syn. Met.* (1989), **34**, 315-21.

38. W. Paulus, H. Katzke and R. Schollhorn, *J. Solid State Chem.* (1992), **96**, 162-168.

39. C. Riekel, H. G. Reznik and R. Schollhorn, *J. Solid State Chem.* (1979), **34**, 253-62.

40. R. Schollhorn, in *NATO ASI Series B: Applied Sciences*, ed. A. P. Legrand S. Flandrois, 1987, p. 149-171

41. H. Suematsu, *Annales de Physique, colloque no. 2, supplement #2* (1986), **11**, 75-83.

42. R. Schollhorn, W. Roer and K. Wagner, *Monatshefte fur Chemie* (1972), **110**, 1147-1152.

43. S. J. Heyes, N. J. Clayden, C. M. Dobson, M. L. H. Green and P. J. Wiseman, *J. Chem. Soc., Chem. Comm.* (1987), 1560-1562.

44. A. H. Thompson, *Phys. Rev. Lett.* (1978), **65**, 146.

45. T. Butz, H. Saitovitch and A. Lerf, *Chem. Phys. Lett.* (1979), **65**, 146-149.

46. B. Marcus, J. L. Soubeyroux and P. Tauzin, in *Chemical Physics of Intercalation*, ed. A. P. Legrand and S. Flandrois, Plenum Press: New York, 1987, p. 375

47. R. Chianelli, J. C. Scanlon, B. M. L. Rao, *J. Solid State Chem.*, (1979), **29**, 323-337

48. R. Chianelli, J. C. Scanlon, B. M. L. Rao, *J. Electrochem. Soc.*, (1979), **125**, 1563.

49. P. G. Bruce, personal communication.

CHAPTER FIVE

EXPERIMENTAL

CHAPTER FIVE

EXPERIMENTAL

Experimental syntheses and instrumental details for Chapters Two through Four are included here. Section **5.1** describes the syntheses of host crystals, organometallic guests and the intercalates. Sections **5.2** through **5.5** provide instrumental details of established techniques used in this thesis, namely, X-ray diffraction, neutron diffraction, ^2H NMR spectroscopy and magnetic susceptibility measurements. Finally, the construction of specialised equipment such as the conductivity apparatus and the *in situ* kinetics cell of Chapters Three and Four constitutes the bases for Sections **5.6** and **5.7** respectively.

5.1. Synthesis

The syntheses of metal dichalcogenide hosts, organometallic guests and the intercalates are described in Sections **5.1.1**, **5.1.2**, **5.1.3** respectively.

5.1.1. Host

(a) ZrS_2[1] :

(i) Microcrystalline powder

Stoichiometric quantities of elemental Zr and S, with 1% molar excess S, were heated to 900°C for 1 week in evacuated, sealed silica quartz ampoules. Typically 3.864g finely divided Zr wire (99.9%, Aldrich) and 2.774g S (99.9%, Aldrich) were used for a 10cm (length) x 1.5cm (i.d.) ampoule. The purple ZrS_2 had a reddish tinge (ZrS_3) and therefore was ground under nitrogen atmosphere and re-annealed at 900°C for another week to give a free flowing, purple-black powder. The purity of the ZrS_2 was checked by powder X-ray diffraction. Small quantities of ZrS_3 impurities, if present, were removed by sublimation at 900°C in an evacuated silica ampoule.

(ii) Single crystals

Single-phase ZrS_2 powder (*ca.* 1g) was sealed, with iodine as a transport agent, (4mg/ml) in an evacuated silica ampoule (25cm x 1.5cm i.d., 10^{-3} Torr) and heated in a three-zone furnace. A linear temperature gradient between 900 and 800°C was established in the furnace with the ZrS_2 charge sitting in the hot end. The sample was left to transport for a week, after which the ampoule was cracked open to yield large plate-

like crystals of ZrS_2 (*ca.* 4mm x 3mm x 0.2mm). The crystals, which hydrolyze slowly in moist air, were handled and stored under dry nitrogen.

(b) $SnSe_2$, SnS_2

The syntheses of SnX_2 (X=S,Se) were based on procedures established by Al-Alamy and Balchin[2]. Stoichiometric quantities of Sn powder (99.9%, Aldrich) and Se pellets or S powder (99.9%, Aldrich) were weighed out into silica glass tubes, evacuated to 10^{-3} Torr and sealed. The mixture was heated at the reaction temperature (see Table 5.1 below) for a week, ground with mortar and pestle, and annealed for another week. The powder X-ray diffraction patterns of the products corresponded closely with those available from the JCPDS-ICDD (International Centre for Diffraction Data, Swarthmore, PA 19081, U.S.A.) database.

Table 5.1: Growth conditions for single crystals of MX_2 (M=Zr, Sn; X=S, Se) hosts.

Compound	Reaction Temp(°C)	Growth Temp(°C)	Transport Agent
ZrS_2	900	800	Iodine
$SnSe_2$	560	510	Iodine
SnS_2	600	530	Bromine

Single crystals were grown by halogen vapour transport (Br_2 for SnS_2, I_2 for $SnSe_2$) whereby an evacuated sealed ampoule(25cm x 1.5cm i.d., 10^{-3} torr), containing a stoichiometric mixture of the elements and 200mg of transport agent, was heated in a temperature gradient appropriate for crystal growth (see table 5.1).

5.1.2. Organometallic Guests

All solvents used were pre-dried over anhydrous 5Å zeolite molecular sieves, before distillation (under an atmosphere of dinitrogen) from K (THF), Na (toluene), Na-K alloy (petroleum ether, b.p 40-60 °C). The solvents were stored under N_2 in Young's ampoules containing activated zeolite molecular sieves and were thoroughly degassed before use.

(a) $Co(\eta\text{-}C_5H_5)_2$[3]

15g Na sand was prepared by shaking molten Na in vigorously refluxing toluene. The toluene was decanted by cannula and replaced with *ca.* 40ml THF. 40ml of cyclopentadiene monomer was added dropwise (under N_2 and stirring) while the reaction vessel was cooled in an ice bath. The solvent was removed *in vacuo* to yield *ca.* 60g of the THF adduct of sodium cyclopentadienyl (NaCp).

To a one-liter round-bottomed flask, 20g (0.0778 moles) freshly sublimed (400°C, 10^{-5} torr) anhydrous cobalt (II) bis(acetylacetonate) (99%, Janssen Chimica), 17g (0.193 moles) NaCp and a Teflon-coated stirring bar were added. 500ml of THF was added by cannula and the purplish sludge stirred vigorously at 60° C for 8 hours, yielding a fine purple suspension. The suspension was filtered through a celite bed and the dark purple filtrate pumped to dryness. The purple-black solid was extracted with 40/60 petroleum ether and purified by sublimation (40°C, 10^{-2} Torr). Yield = 11.1g (75%).

(b) $Co(\eta\text{-}C_5D_5)_2$

The same procedure as that used to synthesise $Co(\eta\text{-}C_5H_5)_2$ employed except that C_5D_6 was used instead of C_5H_6. The synthesis of C_5D_6 is described below.

Cyclopentadiene monomer was obtained (35-40°C) by cracking the dicyclopentadiene (Aldrich) over a Vigreux column. 27.3g sodium pellets were added in small quantities to 250ml of D_2O (99.8%) under a N_2 atmosphere, at 0°C, to give 250ml 20% w/w NaOD in D_2O solution. 50ml of this solution were added, together with 50ml of DMSO (Aldrich), to 50ml of cyclopentadiene monomer. The mixture was stirred vigourously for one hour in an ice bath. The top phase containing the monomer was decanted (by cannula) into a second schlenk containing a fresh NaOD-DMSO mixture. Again, it was vigorously stirred for 1 hour in an ice bath. After a total of 5 such exchanges, the cyclopentadienyl monomer was distilled (35°C), and stored under nitrogen at -80°C. The extent of deuteration was >99.9%, as shown by mass spectrometry of deuterocobaltocene.

(c) $Cr(\eta\text{-}C_5H_5)_2$

This was synthesised by a modification of a procedure reported by Kohler[4, 5]. 20g $CrCl_3.6H_2O$ (BDH Chemicals) was reduced over granulated Zn in HCl solution (98ml conc. HCl, 24ml deionized H_2O) till the green Cr(III) solution was reduced to a bright blue. The $CrCl_2$ solution was filtered through a frit and into a saturated solution of sodium ethanoate (54g NaOEt in 72ml H_2O). The red precipitate that formed was filtered, washed twice each with H_2O, EtOH and 40/60 petroleum ether before prolonged pumping (60°C, 10^{-2} torr) to yield 13g of anhydrous, orange $Cr(OEt)_2$, which was stored under dry N_2.

4.5g $Cr(OEt)_2$ and 4.5g NaCp were stirred together in THF, under N_2 and at 50° C for 5 hours. The red suspension was filtered, pumped to dryness, extracted with 40/60 petroleum ether and sublimed to yield 2.3g of a very air-sensitive red solid which was stored in the dry N_2 box at -30° C.

(d) $Co(\eta\text{-}C_5H_4\text{-}CH_3)_2$

This synthesis was analogous to that for $Co(\eta\text{-}C_5H_5)_2$ except that Cp was replaced by $C_5H_4\text{-}CH_3$ (MeCp). The $Co(\eta\text{-}C_5H_4\text{-}CH_3)_2$ when purified by sublimation, yielded a black solid which was much less crystalline than $Co(\eta\text{-}C_5H_5)_2$, and sublimed at lower temperatures (*ca.* 30° C, 10^{-2} torr). Elemental analysis: C = 64.20% (theor.= 66.0%), H = 6.79% (6.42%)

(e) $Mo(\eta\text{-}C_6H_6)_2$

This was a gift from the M. L. H. Green group, and was prepared by the Fischer-Hafner synthesis[6, 7].

(f) $Ti(\eta\text{-}C_8H_8)(\eta\text{-}C_5H_5)$

This was synthesized according to a procedure reported by Van Oven *et al.*[8]. To 1.5g (0.0385 moles) K sand in THF (made by shaking molten K pellets in refluxing toluene), 1.124ml (0.010 mole) cyclo-octatetraene (Aldrich) was added. Pumping off the solvent yielded *ca.* 2g of K_2Cot {Cot = $(\eta\text{-}C_8H_8)$}, an off-white, highly pyrophoric powder.

2g K_2Cot and 0.65g NaCp were stirred in THF in a round-bottomed flask and 1.2ml of $TiCl_4$ added dropwise by cannula. The green cloudy solution turned purple after stirring for 2 hours at 60° C. Filtration through a glass frit yielded a bright green solution which was pumped to dryness; the resulting solid was purified by sublimation The bright green solid was verified by IR spectroscopy to show the Cp vibrations reported for $Ti(\eta\text{-}C_8H_8)(\eta\text{-}C_5H_5)$[8]. Yield = 1.2g (55%).

(g) $W(C_7H_7)(C_5H_4CH_3)$

This was a kind gift from Dennis P.K. Ng. The synthesis is described elsewhere[9].

(h) $Mo(C_7H_7)(C_5H_4CH_3)$

This was also a gift from Dennis P.K. Ng[10].

5.1.3. Intercalates

(a) Microcrystalline samples

Equimolar quantities of metal dichalcogenide powder (typically, 200mg powder in *ca.* 2ml of solution) and the organometallic guest species were stirred under N_2 in a toluene solution at 120° C for 3 days. The powder darkened considerably upon intercalation (ZrS_2: purple→ black, SnS_2: orange→ blue-black, $SnSe_2$:

metallic→black)and were washed with several aliquots of dry toluene before drying *in vacuo* and storing in the dry box.

Complete intercalation of the host was verified by X-ray powder diffraction of the sample in an air-tight Aluminium cell. The stoichiometry of the intercalates was determined by C/H/N analyses performed by the Oxford Inorganic Chemistry Laboratory Analytical Services.

(b) Large crystals

Large single crystals of host were trimmed using a sharp scalpel to *ca.* 2mm x 2mm x 0.2mm pieces and added to a toluene solution of the desired organometallic species. The reactants were heated to 120° C, without stirring, for 1 week before washing with several aliquots of toluene and drying *in vacuo*. The intercalates all showed significant visible expansion along the *c* axis in addition to the blackening of the crystals observed for the microcrystalline samples. The stoichiometries of the intercalates were determined by C/H/N elemental analyses performed by the Oxford Inorganic Chemistry Laboratory Analytical Services.

5.2. X-ray Diffraction

X-ray diffraction patterns of both microcrystalline powder and oriented crystal samples were recorded in Bragg-Brentano geometry on a Phillips PW1729 Diffractometer, driven by a PW1710 controller interfaced to a microcomputer running Phillips APDv3.5 software. CuKα radiation (λ = 1.5418Å) was used at 40kV, 30mA throughout.

Powder samples were checked for purity and the presence of complete intercalation using a fast scan mode, i.e, 0.05 deg/sec between $2\theta=5\rightarrow80°$, while overnight step scans (0.002 deg/s) between $2\theta = 4.3°\rightarrow90°$ were used for oriented crystal samples in order to collect accurate relative intensities for *00l* reflections.

Air sensitive powder samples were run in sealed aluminium cells with a non-crystalline window such as Mylar® or Scotch 3M® magic tape. For oriented samples, crystals of the intercalates were fixed, using silicon grease and under N_2, into a specially designed air-tight X-ray cell (see figure 5.1) consisting of Capoten® film supported within an aluminium frame. Peak intensities were corrected for the broad baseline due to the Capoten film and to small quantities of silicone grease present.

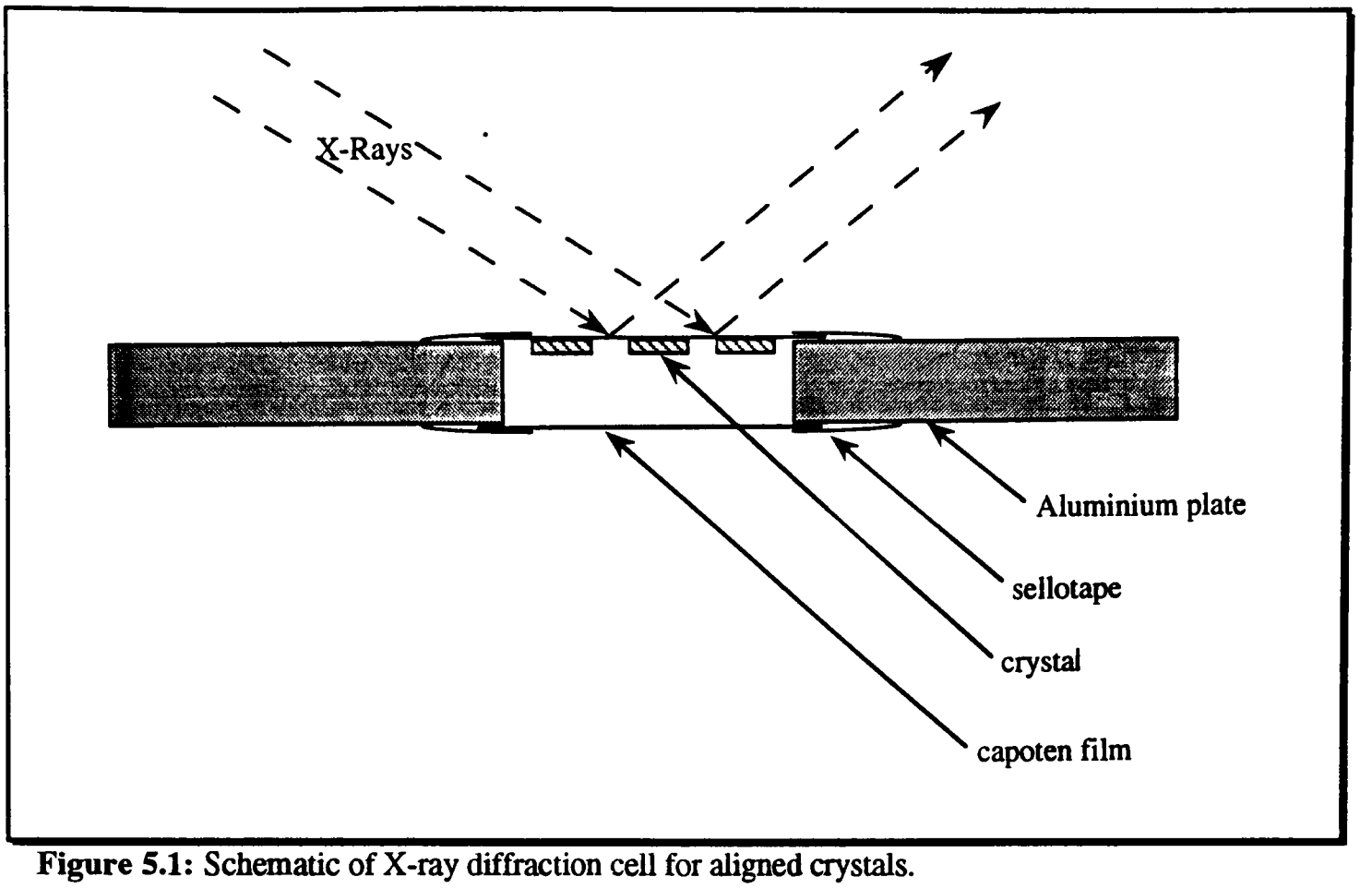

Figure 5.1: Schematic of X-ray diffraction cell for aligned crystals.

5.3. Neutron Diffraction

ISIS, a neutron diffraction and muon facility at the Rutherford Appleton Laboratory (RAL), provided the pulsed spallation source for the neutron diffraction experiments in this thesis. The source is based on an 800 MeV high intensity proton synchrotron which is designed to pulse at 2.5 x 10^{13} protons per pulse, with a pulse rate of 50Hz (mean current ~ 200μA). The protons are directed to a uranium target, where the collisions produce ~4 x 10^{16} fast neutrons/second. Four moderators close to the target (2 containing water, one with liquid methane at 100K and the fourth with liquid H_2 at 25K) slow the fast neutrons down to epithermal and thermal velocities, yielding pulse lengths in the range 1-100μs. The moderated neutrons then pass through one of 18 holes in the shield surrounding the target assembly, directly to the instruments or through neutron collimators.

Neutron diffraction spectra of aligned crystal samples of the intercalates were collected on the Liquid and Amorphous Diffractometer (LAD) of the RAL. LAD is a total diffraction instrument optimised for the study of amorphous solids and liquids. The detector banks are positioned in the horizontal plane at seven different scattering angles between 5° and 150° as listed in the Table 5.2.

Table 5.2: LAD detector bank parameters. Incident flight path = 10.0m

Bank No.	Average 2θ (°)	Total flight path (m)	Resolution ΔQ/Q (%)	Max. d-spacing (Å)
1	4.937	11.047	14	~80
2	9.704	11.033	7	~40
3	20.562	11.040	3.5	~17
4	35.183	11.043	1.8	~11
5	58.103	11.046	1.2	~7
6	90.131	11.039	0.8	~4.8
7	148.164	11.128	0.6	~3.7

The detector arrangement on the 2 sides of the instrument is bilaterally symmetric, so that the orthogonally related detector banks allow the structure factors F_{hkl} for a planar sample mounted at 45° to the incident beam to be determined simultaneously for the scattering vectors parallel and perpendicular to the plane of the sample. For the work in this thesis, since the reflections of interest were those from the layer planes (i.e, only the scattering vectors perpendicular to the layers), only half of the full circle of detector banks were employed to collect the diffraction data. The data refinement described in Chapter 2 required the accurate *relative* intensities of only *00l* reflections. In order to obtain spectral profiles of the peaks in the d-spacing range 12Å → 3Å with the maximum possible resolution for accurate counting statistics, the planar crystal sample was rotated manually, with the aid of a calibrated goniometer, to successively collect data from detector banks 3 through 7. The peaks in overlapping regions for each spectra obtained from adjacent detector banks allowed normalisation of intensities in order to obtain relative intensities for the *001* to *008* reflections.

The crystals were fixed in position by gluing them onto vanadium foil strips using epoxy resin (Araldite®), then fixing the foil in place within the vanadium cannister using tailor-made vanadium spacers. The cannisters were then sealed before removal from the dry N_2 box. On LAD, the vanadium cannisters were aligned with a calibrated goniometer so that the *001* to *008* reflections were successively collected in detector banks 3 to 7.

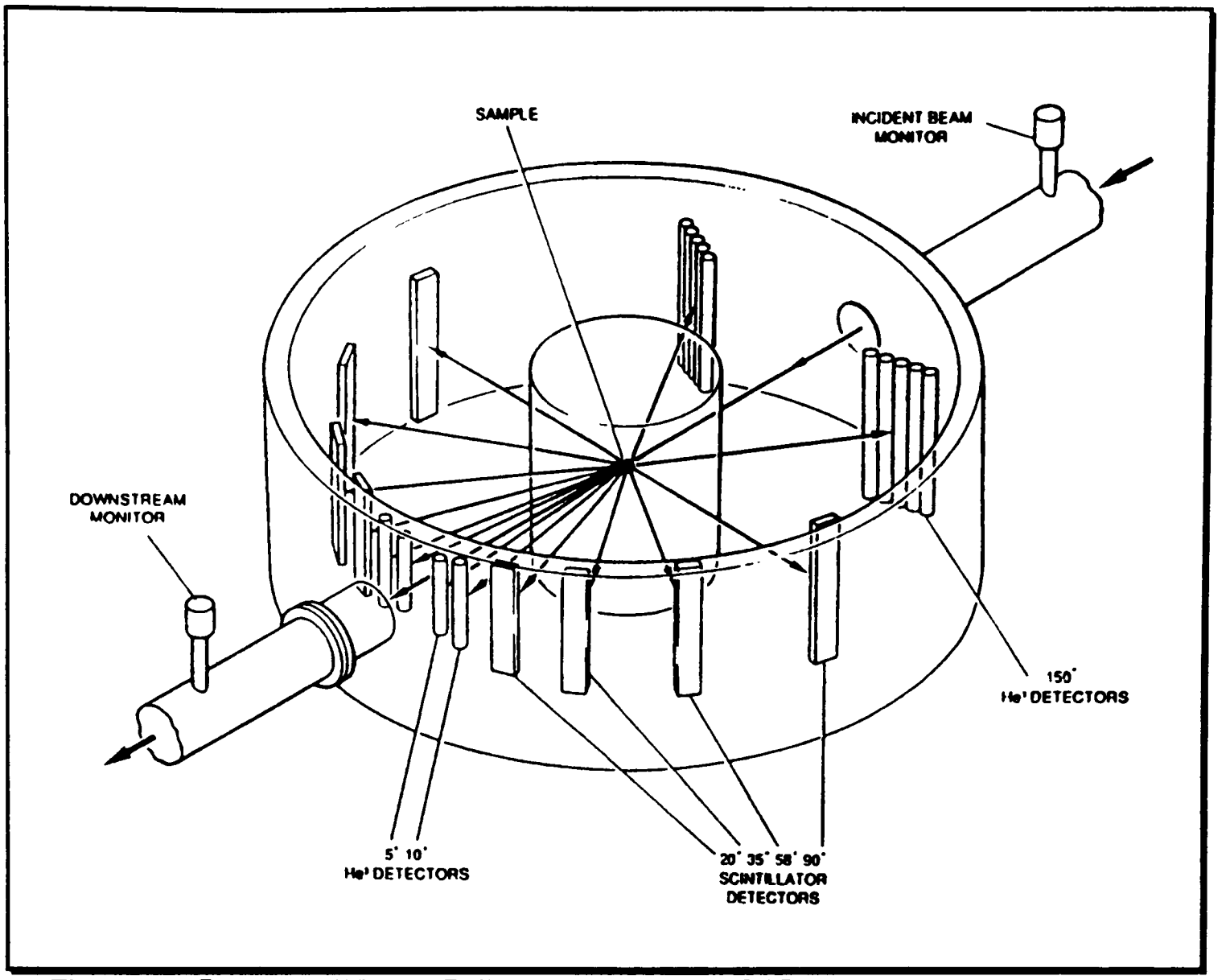

Figure 5.2: Geometry of Neutron Diffraction experiment on LAD.

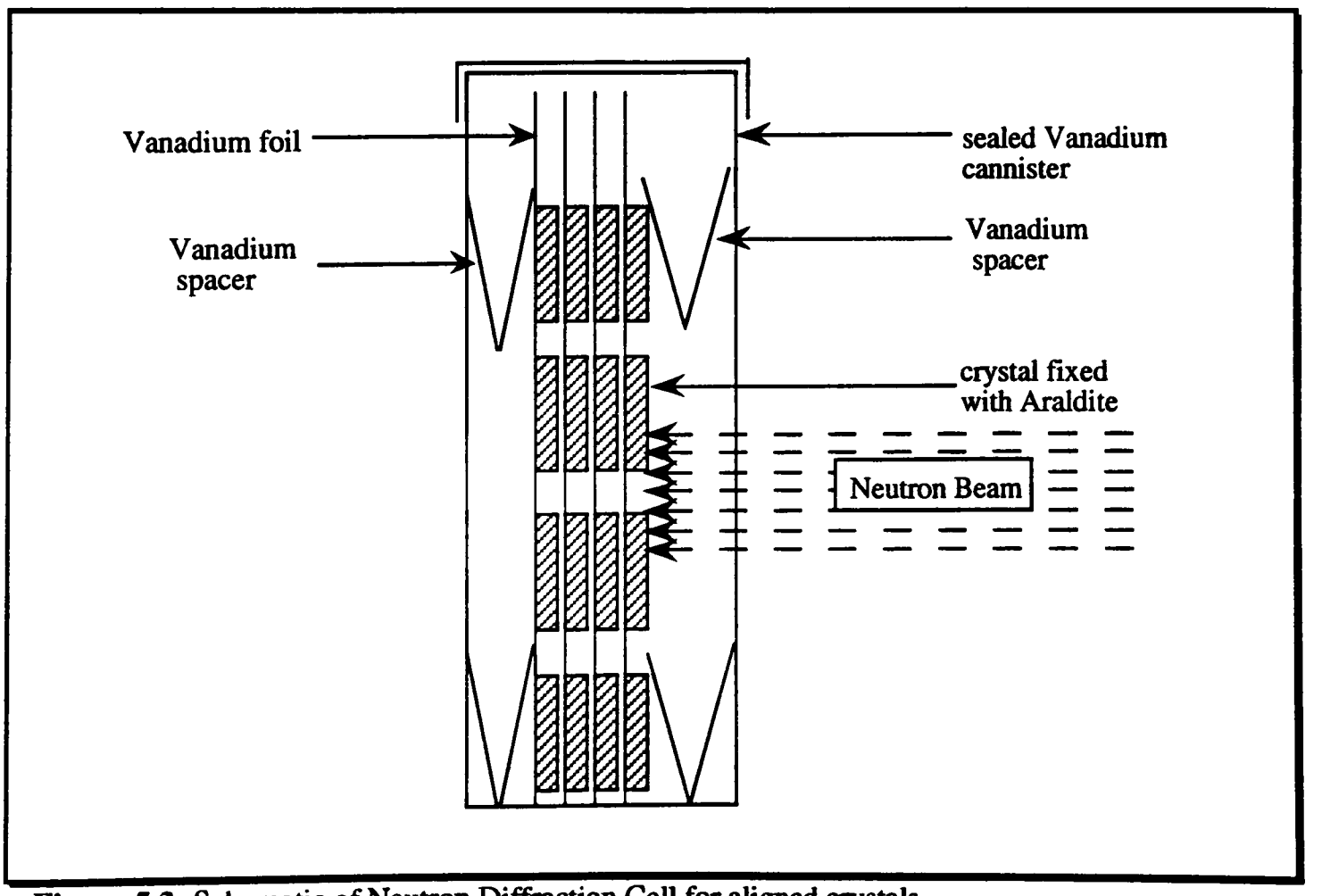

Figure 5.3: Schematic of Neutron Diffraction Cell for aligned crystals.

5.4. Magnetic Measurements

Variable temperature magnetic moments of intercalates were measured between 6K and 300K in a Cryogenics Consultants SCU500 SQUID Magnetometer in conjunction with a Lakeshore DRC-91C Temperature Controller, typically using fields of 1 to 3 Tesla. For measurements of diamagnetic susceptibility in superconducting samples, pumping of the liquid helium cavity permitted measurements down to 1.6K.

Both microcrystalline and single crystal samples were loaded under nitrogen into silica holders and stoppered with a rubber seal before transferring to the cryostat. The silica holders for single crystals were specially modified to allow the samples to be oriented either parallel or perpendicular to the applied field (Figure 5.4). All magnetisation data were corrected for intrinsic diamagnetic susceptibility of the sample holders and the electronic cores of the constituent atoms.

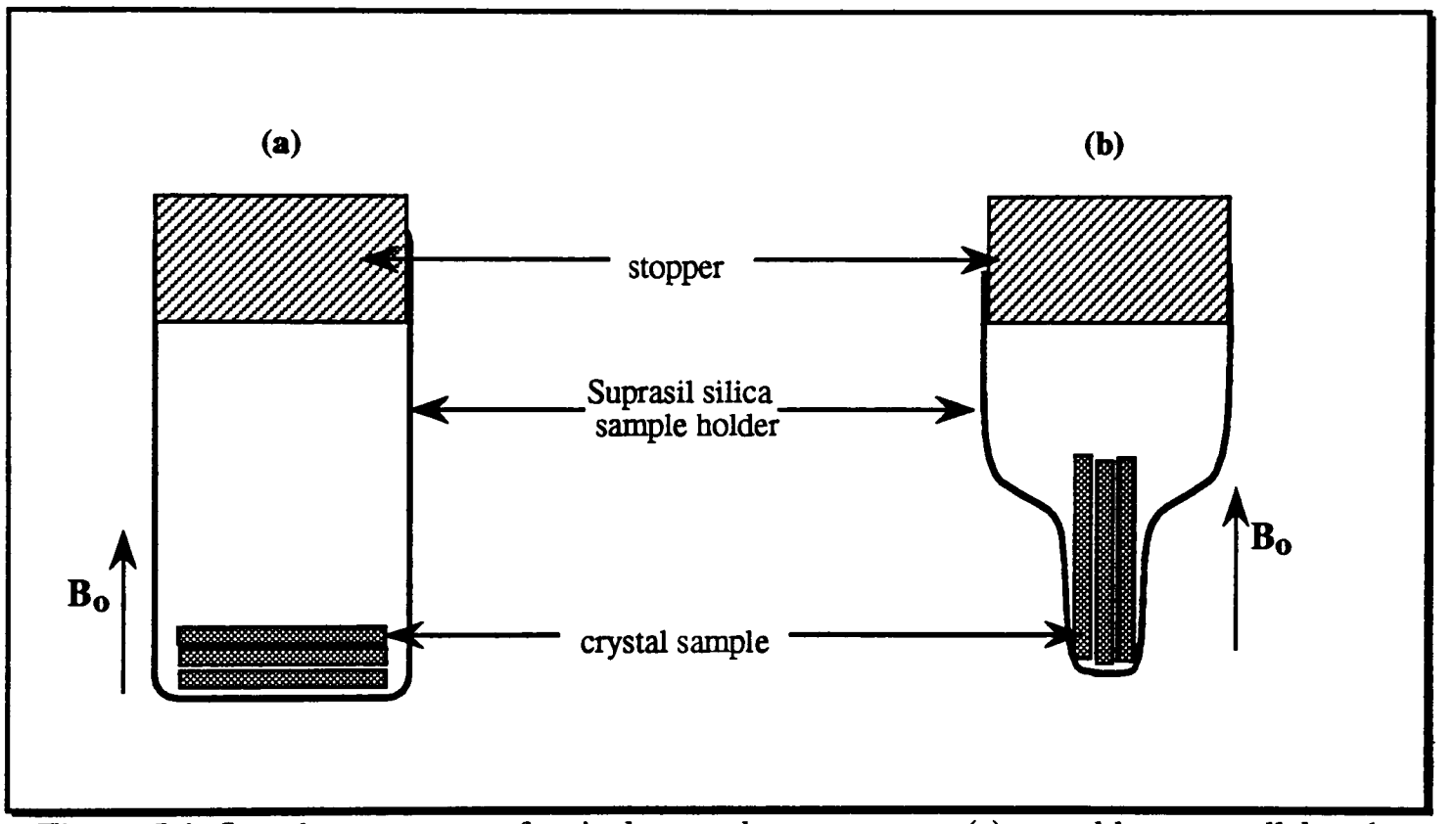

Figure 5.4: Sample arrangement for single crystal measurements (a) crystal layers parallel to the external field (b) perpendicular to the external field for magnetic susceptibility measurements.

5.5. Conductivity Measurements

5.5.1. Sample Mounting

The intercalated crystals are air sensitive so all the manipulations described below were performed in a nitrogen-flushed glove box fitted with a Meiji 5-TRZ trinocular zoom stereo microscope (objective magnification = 0.7→4.5X, eyepiece = 10X, see Figure 5.5). The protruding eyepieces of the microscope are sheathed by a rubber sheet which allows the microscope to be focused over a wide depth of field without compromising the nitrogen atmosphere in the glove box.

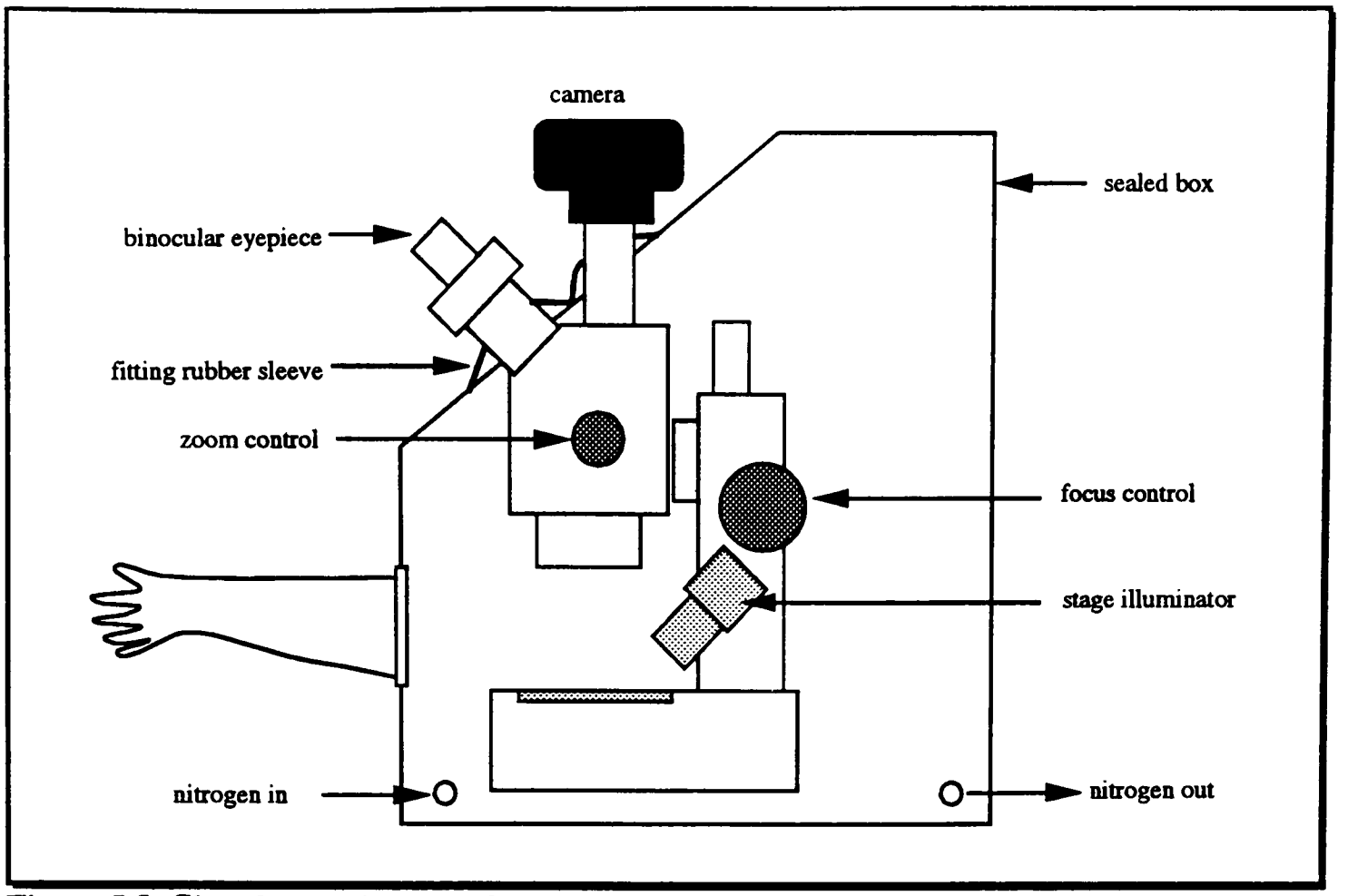

Figure 5.5: Glove box environment for mounting of electrodes onto crystal.

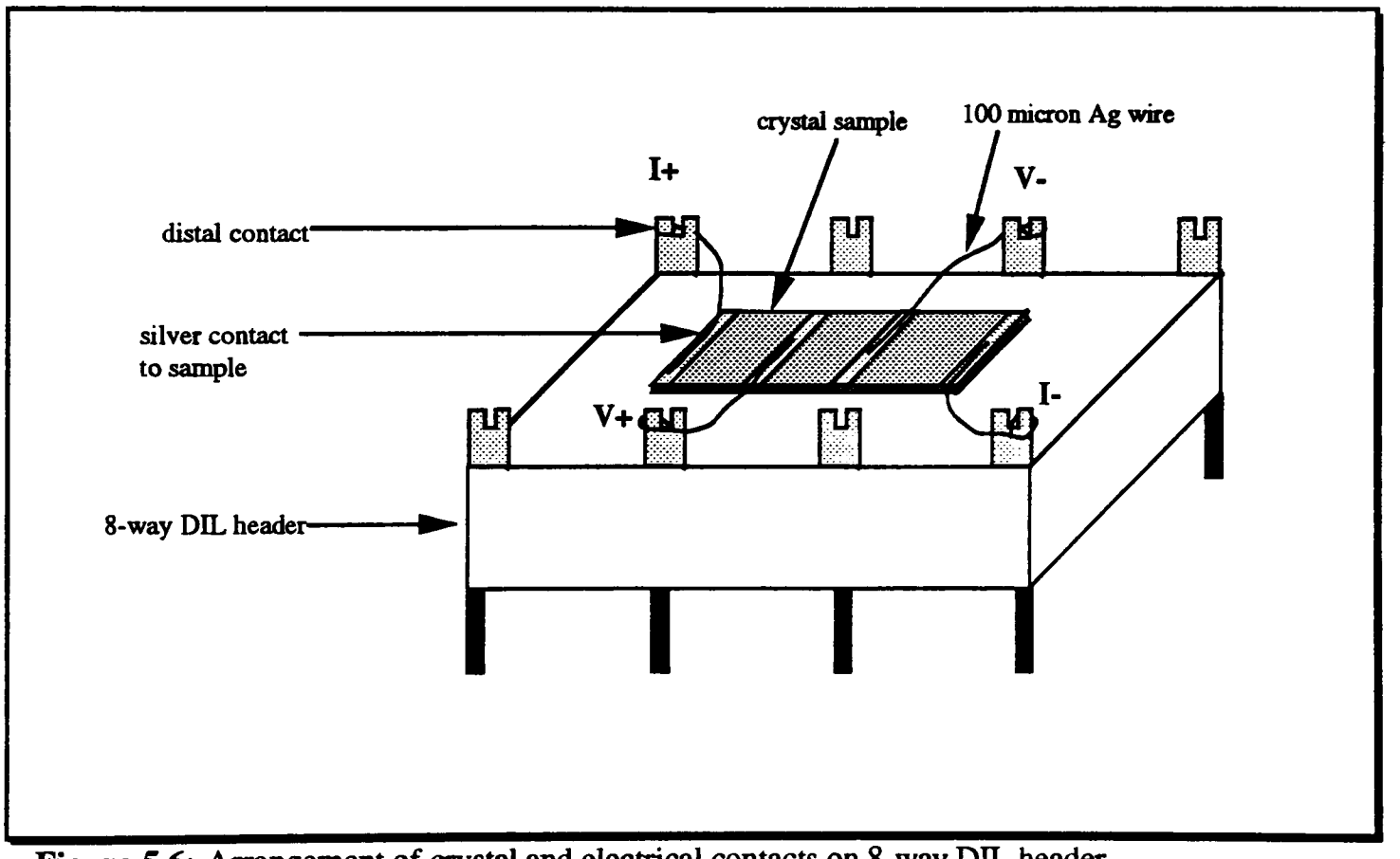

Figure 5.6: Arrangement of crystal and electrical contacts on 8-way DIL header.

The samples were cut into rectangular platelets (3mm x 2mm x 0.1mm) with a sharp scalpel so that the simple 4-electrode arrangement (depicted in Chapter Three) could be employed for measuring resistivities. The crystal was fixed in position within the 8-pin DIL header (Farnell Electronics) with a piece of double-sided sticky tape. With the aid of the microscope, 100μm Ag wire, each secured at its distal end to pin contacts on the chip holder (see Figure 5.6), were then carefully eased into electrical contact with

the crystal using fine tweezers and soldered down with colloidal Ag paint dag (Ag suspension in 2-butylethyl acetate, DuPont). The electrical contacts were then left to dry under a rapid stream of nitrogen before being transferred onto the cryostat probe. Typical contact resistances obtained by this method were between 7 and 10Ω. The sealed probe was removed from the glove box and inserted into the CF1204 continuous flow cryostat in which variable temperature resistivity measurements were performed using the experimental set-up described below.

5.5.2. Measurement apparatus

The apparatus is based on an earlier design by Dr M. Kurmoo and was constructed as part of this work in order to perform the measurements described in Chapter 3. A schematic of the apparatus is shown in Figure 5.7. It is has 3 main components: the *temperature control, measurement* and *data acquisition* systems.

(a) Temperature Control System

The temperature control system was built by Oxford Instruments and utilizes a CF1204 dynamic gas flow cryostat interfaced to an Oxford Instruments ITC-4 temperature controller equipped with a 27Ω Rh-Fe sensor calibrated at 33 points between 1.6K to 300K. The ITC-4, in turn, is interfaced *via* its RS232 serial port to a microcomputer which controls the experimental parameters and logs the data obtained to disk (see below). Accurate temperature control is achieved by using a three-term algorithm consisting of Proportional, Intergral and Derivative terms (P, I, D) respectively. This algorithm allows asymptotic approach of the cryostat temperature to the set point with minimal overshoot (through judicious choice of P, D terms) or residual errors (optimised Integral time). Details of temperature control theory are beyond the scope of this thesis and the interested reader is referred elsewhere[11]. Suffice it to say, each cryostat has its own characteristic P, I, D terms which provide optimal temperature control, and by a series of commissioning experiments, it was determined empirically that for our experimental configuration, P=2%, I=2 min, D=1 min. With these parameters, accurate temperature control of ±1 K/min could be achieved between 4.2 and 300K.

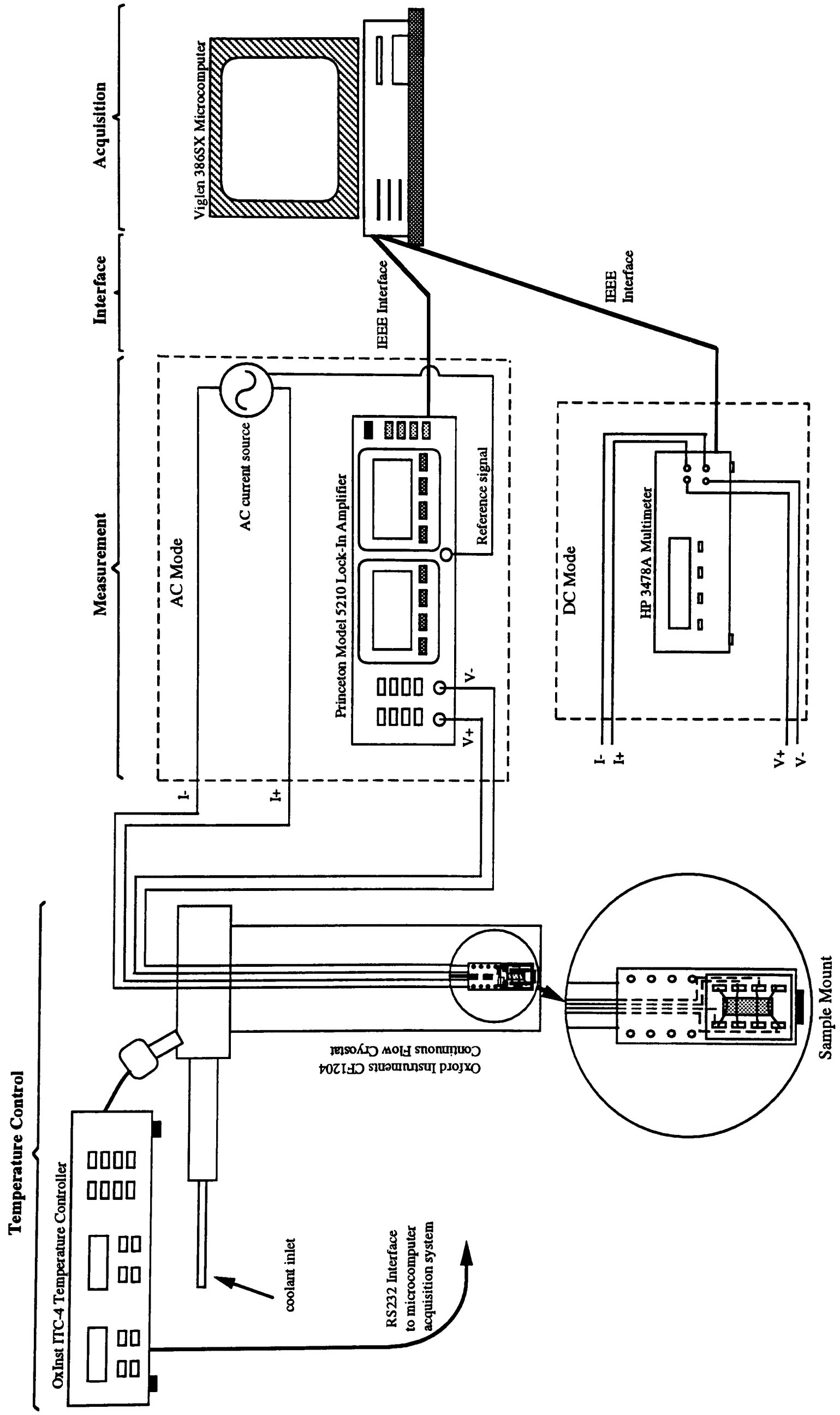

Figure 5.7: Schematic of apparatus used to measure variable-temperature resistivity.

(b) Data Measurement Systems

Two modes of resistivity measurement were incorporated into the design, allowing the user to use either a 2 probe or 4 probe technique. In addition, for the 4 probe method, the user can choose between using direct current (DC) or alternating current (AC) measurements, the former being useful for semiconducting samples with large resistances while the latter allows measurements of the very small resistances characteristic of metallic/semi-metallic samples.

The DC measurement is obtained simply by connecting leads from a Hewlett Packard HP3478A multimeter to the sample (via an interface box which electrically connects the cryostat-mounted sample to the ambient environment). The HP3478A multimeter is in turn interfaced, via HP1B IEEE cable, to the microcomputer acquisition system. Because the automatic ranging function of the multimeter was too slow for our purposes, a software-based subroutine was written by Dr P. Trevellick (Inorganic Chemistry Laboratory, Oxford) to fix the sensitivity range of the multimeter in response to changes in the sample resistance as a function of temperature.

For AC measurements, an oscillatory current source of suitably low frequency and amplitude was commercially unavailable, so was instead designed and built by Iain Ross of the ICL Electronics Laboratory (current range: 1nA to 10mA, frequencies range: 1Hz to 2kHz). Its output current is passed through the sample as well as fed directly into a Princeton Lock-In Amplifier Model 5210. Using the latter signal as a reference, the Lock-In Amplifier is able to measure the potential drops across the sample. The measured potential drop is read, via IEEE interface, by the microcomputer acquisition software which in turn converts it into resistance values for the user.

(c) Data Acquisition System

Data measured in either AC or DC mode were sent to a Viglen 386 microcomputer running Microsoft Windows®-compatible software developed in conjunction with Dr Peter Trevellick (OxSys, ICL). The software is organised in user-friendly GUI-based modules, a summary of which was shown in Chapter 3. The components are described below.

(i) Communications Interfaces (Links Menu)

These connect automatically upon start up of the program, but the user is provided with the option of remotely sending interactively input user commands to each of the devices. This is useful in checking the communications links are physically and electrically intact (ie., no loose connections, damaged cables, etc.).

(ii) Experimental Configuration (Edit/Setup Menu)

All details of the experiment are controlled from this menu, including the exact cooling/heating rates desired, 2 or 4 probe, AC or DC mode parameters (e.g., AC current

amplitude and frequency), frequency of data acquisition and output data filenames and formats.

(iii) Acquisition (Acquire/Control Menu)

Data acquisition can be initiated for up to 8 different experimental set-ups simultaneously, all of these being synchronised relative to a real-time clock running within the program. Each of the experiments can be individually started, terminated or resumed without affecting the data being collected in adjacent experiments, provided the same time reference frame is used (since only one clock is running at any given time).

(iv) Data Display (View Menu)

The collected data can be either displayed in graphical or numerical format (*View* and *Edit* menu options respectively). In addition to resistance data, temperature profiles (set and obtained), heater output (set and obtained) can also be displayed. Since the program is running in a Windows environment, data from several concurrent experiments (or different types of data from the same experiment) can be displayed simultaneously, allowing direct comparison and evaluation of data to be made *during* the course of the experiment.

5.6. ^{2}H NMR

Solid state ^{2}H NMR spectroscopy experiments described in this thesis (Chapters 2 and 4) were performed by Sue Mason (Inorganic Chemistry Laboratory, Oxford) using a Bruker 400 MHz spectrometer, with a high power probe containing a horizontal solenoid insert. The samples were fixed between thin plastic spacers and sealed under nitrogen with a plug of epoxy resin within 5mm diameter silica tubes. $\pi/2$ pulses of 3μs were used. A quadrupolar echo sequence was used, with a spin echo delay of 30μs. Relaxation times of 5 seconds were used. Further details of the spectrometer set-up are described elsewhere[12].

5.7. Energy Dispersive Diffraction (EDD) at Daresbury SRS

5.7.1. Synchrotron Radiation

The SRS at Daresbury consists of 3 accelerators. A 12 MeV linear accelerator injects electrons into a booster synchrotron which accelerates them to an energy of 600MeV before they are extracted into the 2 GeV storage ring. Electrons are injected into the storage ring until a stored current of up to 300mA has been achieved, whereupon the electrons in the ring are "ramped" till they reach an energy of 2000 MeV (2 GeV).

The storage ring is usually operated at 2 GeV with the wiggler at 5T in multibunch mode, that is, with 160 electron bunches of ~180 ps fwhm with a repetition rate of 500 MHz (≡2 ns spacing). The ring contains the superconducting wiggler magnet,

the undulator, pulsed magnets to inject the beam, radio frequency cavities to accelerate and maintain the energy of the beam, beam position monitors, beam steering magnets and beam diagnostic devices. The electrons in the ring decay exponentially with a time constant of 1/e and have to be replaced periodically (every 12 hours at SRS, Daresbury).

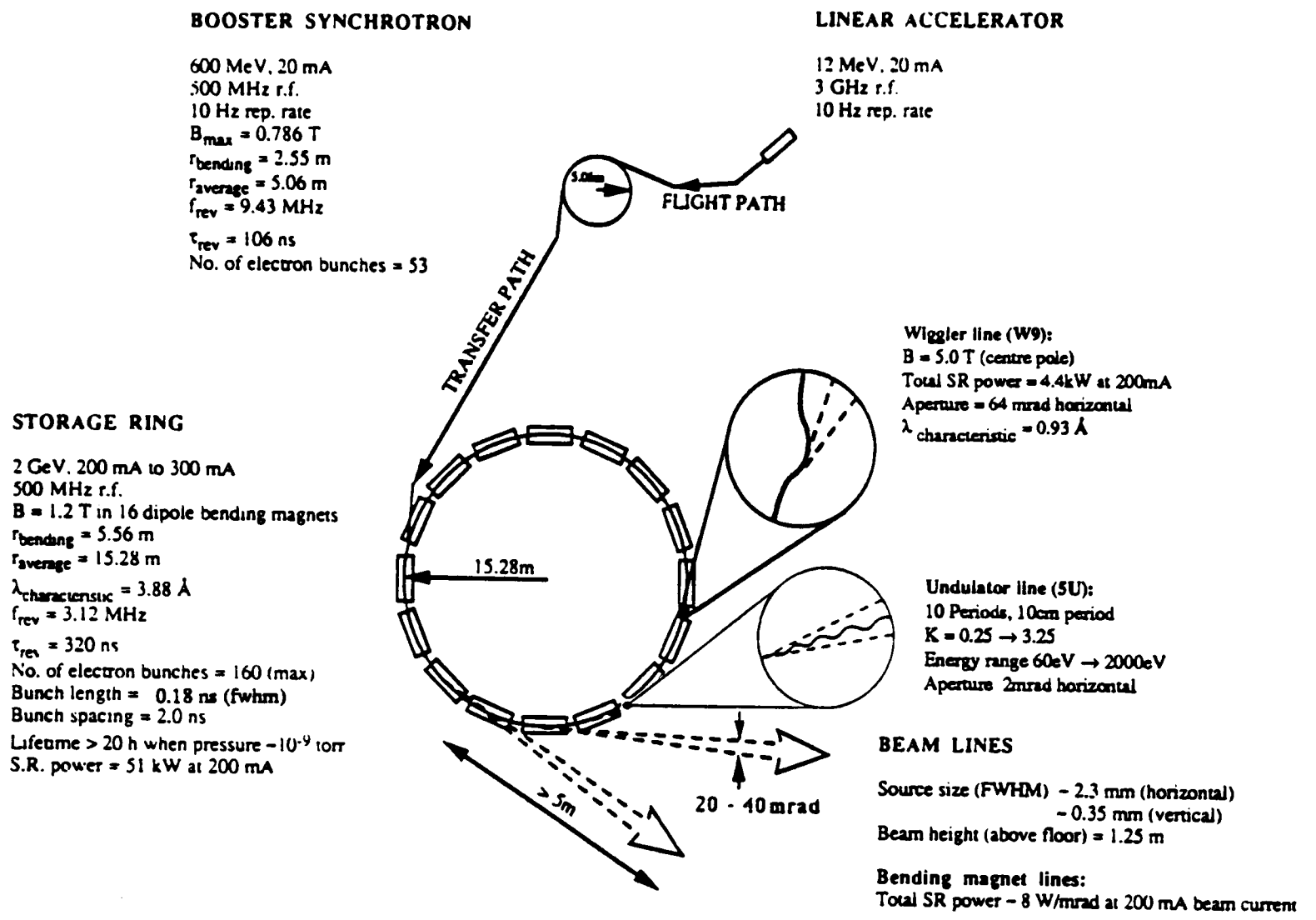

Figure 5.8: Schematic drawing of the Daresbury SRS accelerator complex.

5.7.2. Energy Dispersive Diffraction (General)

As in the time-of-flight neutron experiment described above, the detector angle is fixed at an angle of 2θ with respect to the incoming incident beam. The basic equation of energy dispersive powder diffraction is simply Bragg's law expressed in energy space:

$$Ed_{hkl}\sin\theta = K \qquad (1)$$

where E is the energy of the photons scattered at the fixed angle 2θ by the hkl planes with spacing d in a sample. K is constant equal to hc/2, or 6.19926 keV.Å[13].

All the reflections are recorded simultaneously by a phase sensitive energy detector, the profile being moderated by the detector resolution as well as broadening due to beam divergence. These contributions are approximately Gaussian and the resulting width of a reflection, ΔE, is given by:

$$\Delta E = \{k_1^2 + k_2 E + (k_3 E)^2\}^{1/2} \qquad (2)$$

where k_1, k_2 are detector system constants.
$k_3 = \cot\theta\Delta\theta$
$\Delta\theta$ = total equatorial divergence of the incident and diffracted beams.

On the SRS Station 9.7, for example, incident beam divergence is negligible for all slit dimensions commonly used in EDD. Hence $\Delta\theta$ is simply the diffracted beam equatorial divergence. Expression (2) can be re-written to reflect the relative energy width of a reflection, $\Delta E/E$:

$$\frac{\Delta E}{E} = \left(\frac{k_1^2}{E^2} + \frac{k_2}{E} + k_3^2\right)^{1/2} \qquad (3)$$

That is, the energy width of a reflection decreases with energy for a given set of constants k_1 and k_2. The resolution which is defined roughly as $\Delta E/E$, thus improves with increasing E in a given spectrum and hence better performance can be obtained by shifting reflections to a higher energies as long as k_3 remains constant. Since d-spacing is inversely related to energy (see equation (1)),

$$\Delta E = \frac{d}{\Delta d} E$$

which means that for a given d-spacing difference Δd, a larger energy separation is obtained at higher energies.

5.7.3. Enegry Dispersive Diffraction (Station 9.7)

The set-up on SRS Station 9.7 [14] essentially consists of a heavy duty engineering rotary table supporting the diffracted beam collimation system and a streamline detector, a micro-positioning stage with 3 translational degrees of freedom and a fine slit system ($\pm 5\mu m$) for the incident beam.

The detector is an EG&G ORTEC planar detector with a 5mm thick, 6mm diameter high purity germanium crystal and a preamplifier with a standard feedback resistor. Pulses are processed by an EG&G ORTEC Model 572 amplifier with a $2\mu s$ shaping time.

The beam available on Station 9.7 is the first inner horizontal segment of the radiation fan from a 5 Tesla wiggler (wavelength shifter) which produces usable energies of up to 100keV. The beam is reduced and collimated via an aperture and slit assembly to the minimum required by the experiment.

The diffractometer has a vertical plane of diffraction in order to exploit the horizontal linear polarisation of the radiation. The vertical divergence of the diffracted beam is collimated through the use of multiple slits consisting of molybdenum strips 0.1mm thick and 50cm long separated by 0.1mm spacers.

Since the diffraction angle is fixed for a particular experiment, the diffractometer is aligned by simply adjusting the incident beam pinhole and slits to coincide with the vertical centre of the radiation beam. The sample stage is optimised in the *y* (horizontal, perpendicular to the beam) and *z* (vertical) direction before adjusting the sample position along the *x* direction.

Table 5.3: Characteristics of Dedicated X-ray Diffraction Stations at the SRS, Daresbury.

Station	Distance from tangent point	Incident flux on a 1 mm^2 aperture for a 300 mA beam current (ph/sec/0.1% BW)		X-ray optics	Experimental apparatus
		1.5 Å	0.7 Å		
7.6	80 m	1.5×10^{9}	1.3×10^{8}	Various orientations of single bounce and channel-cut monochromator	Double crystal camera White radiation camera X-ray TV detector
2.3	15 m	3.7×10^{10}	3.3×10^{9}	Si(111) or Ge(111) channel-cut monochromators	High resolution powder diffractometer Cryostat
9.1	15 m	1.5×10^{11}	1.0×10^{11}	Si(111) water-cooled channel-cut or 4-bounce double crystal monochromator	High resolution powder diffractometer Cryostat and furnace Image plate detector
9.4	35 m	1.5×10^{10} (Increased by a factor of 20-30 when focussing mirror in position	1.4×10^{10}	Toroidal Pt-coated 1:1 focussing mirror Si(111) water-cooled channel-cut monochromator	Double crystal camera. Heavy duty single crystal diffractometer with analyzer stage.
9.7	15 m	1.5×10^{11}	1.0×10^{11}	Unfocussed white beam	Energy dispersive powder diffractometer Laue diffractometer
16.3	33 m	2.0×10^{10}	2.3×10^{10}	Si(111) water-cooled channel-cut or 4-bounce double crystal monochromator and/or sagitally focussing monochromator	Six circle stable diffractometer
16.4	26.5 m	5.4×10^{10}	4.4×10^{10}	Unfocussed white beam or focussed with capillary optics	Energy dispersive powder diffractometer High pressure cells and cells for kinetics

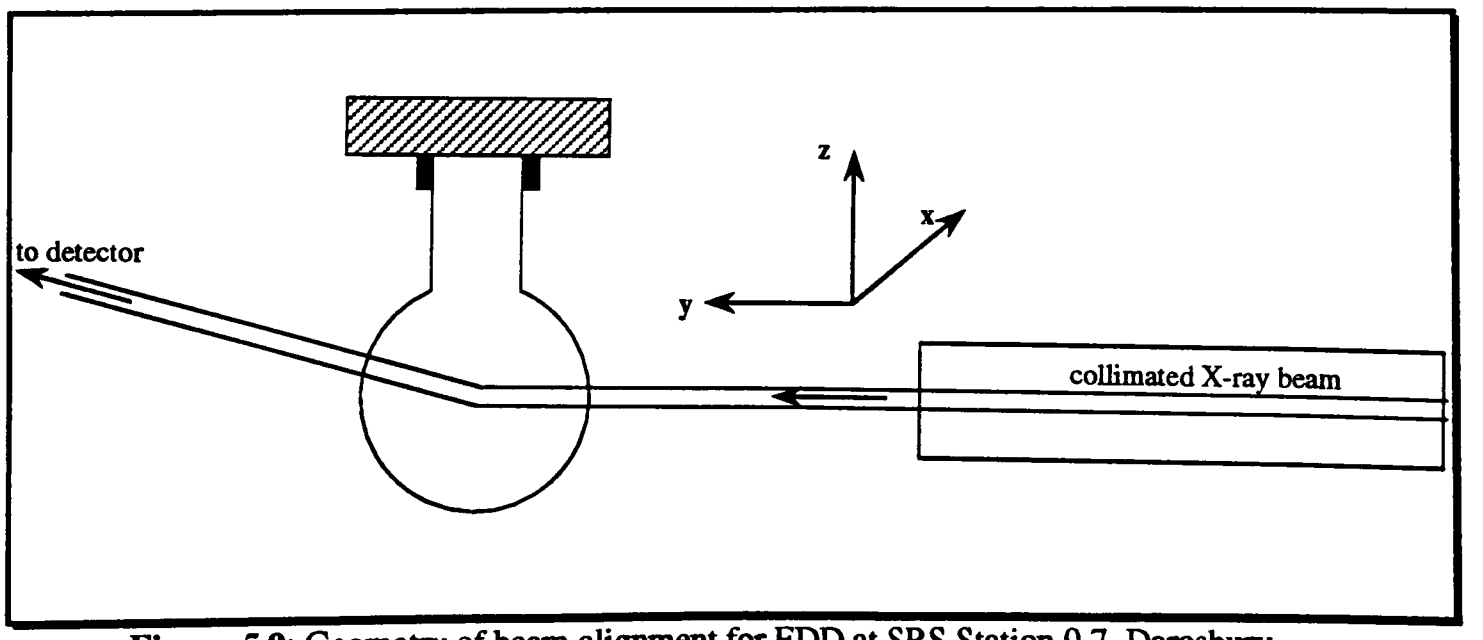

Figure 5.9: Geometry of beam alignment for EDD at SRS Station 9.7, Daresbury.

5.7.4. Apparatus Design

The design and construction of the apparatus used at Daresbury was the result of a

collaborative effort. The people involved are listed in Appendix B, along with their contributions to the project.

The initial chemical system chosen for study was the intercalation of $CoCp_2$ into SnS_2. The main factors which influenced the experimental design are as follows:

(a) The fast speed of this reaction ($t_{0.5}$ ~ 3 minutes at room temperature) makes it essential to mix the reactants *in situ*, while monitoring the reaction.

(b) Since SnS_2 and the intercalate are solids, while the cobaltocene is introduced as a solution in either dimethoxyethane (DME) or toluene, adequate stirring of the mixture is important to prevent settling of the particles which would lead to unrepresentative sampling of the reaction mixture by the X-ray beam.

(c) Cobaltocene is an air-sensitive organometallic compound which oxidises readily upon exposure to air, so that the experiment must be conducted under an inert atmosphere of nitrogen or argon.

To minimise the turn-around time when changing solid samples or liquid feed stocks, the design of the apparatus is based upon a modular concept of having a large number of reaction flasks into which known amounts of the solid reactant can be loaded prior to any on-line measurement. These pre-loaded flasks, in turn, couple easily and rapidly to the liquid injection port and possess adequate stirring capabilities to lift the solid into suspension as well as maintain adequate mixing throughout the course of the reaction.

Initial trials using 5ml round bottomed Pyrex flasks with a 5mm PTFE-coated magnetic flea to provide stirring showed that even the maximum spin speeds attainable on conventional laboratory stirrers (*ca.* 1200 rpm) were insufficient to keep the solid particles fully suspended in the liquid. Moreover, in the fluid vortex created at these spinning speeds, the flea tended to rise and also skip occasionally off the floor of the flask. The flea would then be in the X-ray beam path and interfere with any diffraction spectra collected. By flattening the bottom of the flask so that the diameter of the base is approximately that of the stirrer flea, both these problems were eliminated.

Good temperature stability is required for kinetic measurements. For isothermal kinetic measurements, there is no necessity to be able to change temperature rapidly. As such, a reaction vessel with a large thermal mass was designed to give the best possible temperature stability. Heating was provided by circulating hot fluid (water for temperatures $\leq 30°C$, paraffin oil for for temperatures $> 30°C$) from a thermostatically controlled bath via thermally lagged steel bellows.

The system developed is made up of two modules: a reaction vessel and a liquid feed equipped with gas purge. These are shown schematically in Figure 5.10 (detailed technical drawings of the apparatus are included in Appendix B). The two modules will be described separately, and then in the context of the experiment.

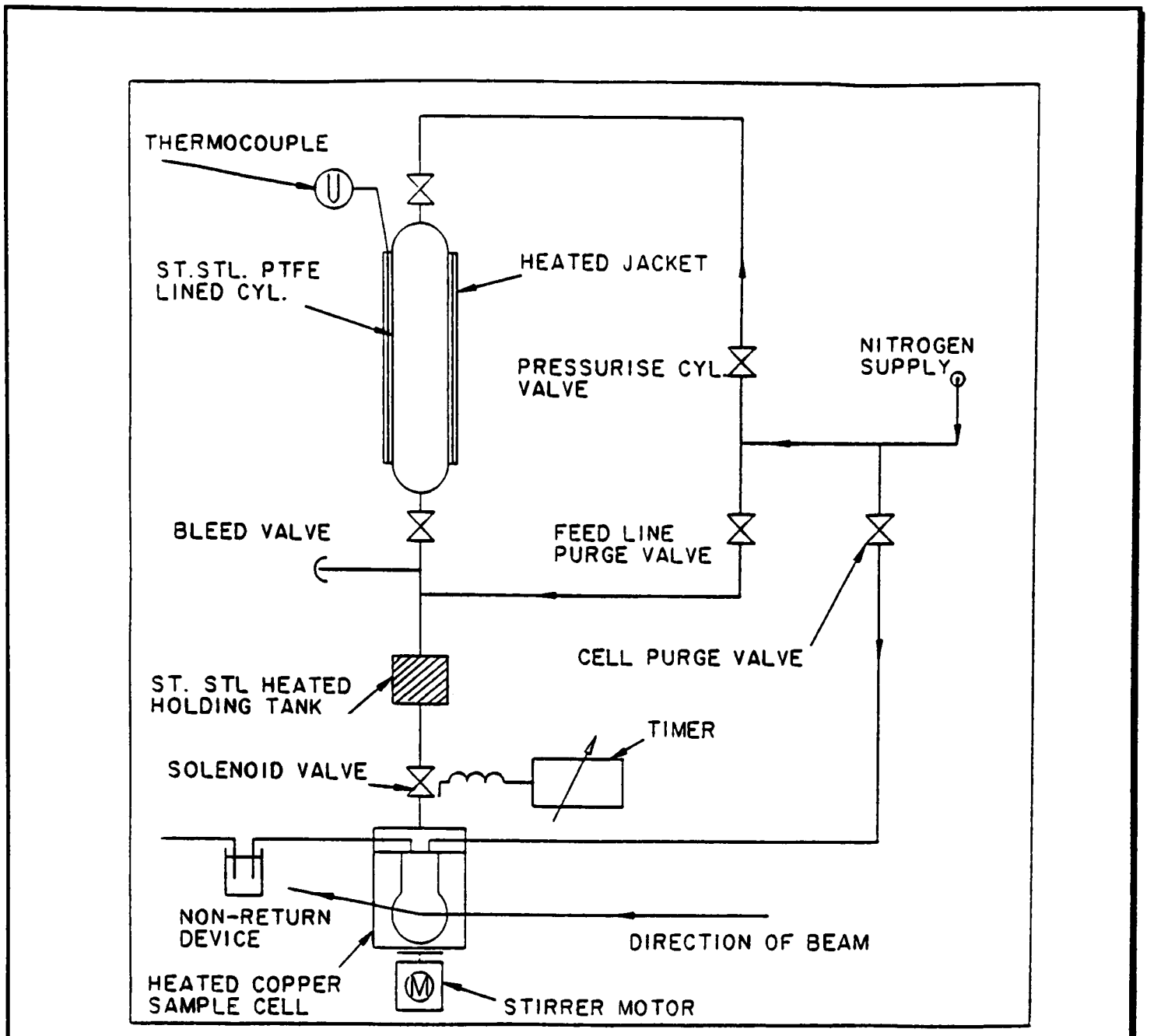

Figure 5.10: Schematic drawing of the apparatus used for *in situ* kinetics experiments.

5.7.4.1. Reaction Vessel

The reaction vessel consists of a heating jacket with lid, inside of which the Pyrex reaction flask fits snuggly (Figure 5.11). The heating jacket was made out of a solid copper block. A hole was machined in the top of the copper block for the reaction flask to sit in, gantries were cut to allow heating fluid to be passed through the block and holes were made to allow the X-ray beam to enter and exit. The block was thermally lagged with a tightly fitting plastic casing. The lid fits closely to the copper block and has a rubber grommet fitted to its underside. Reaction flasks fit into this grommet, forming both a mechanical connection to it and an air-tight seal for the flask. Gas inlet and outlet pipes pass through the lid to allow purging of the reaction flask with dry nitrogen. A small liquid reservoir is mounted on top of the lid; this is connected via a solenoid valve to the reaction flask by 4mm diameter PTFE tubing. The reservoir has a U-shaped heating tube through which warm fluid is passed to maintain the liquid feed at the reaction temperature. The lid is secured by a locking pin and suspended by a counter balance system when open, allowing unencumbered insertion and removal of reaction flasks.

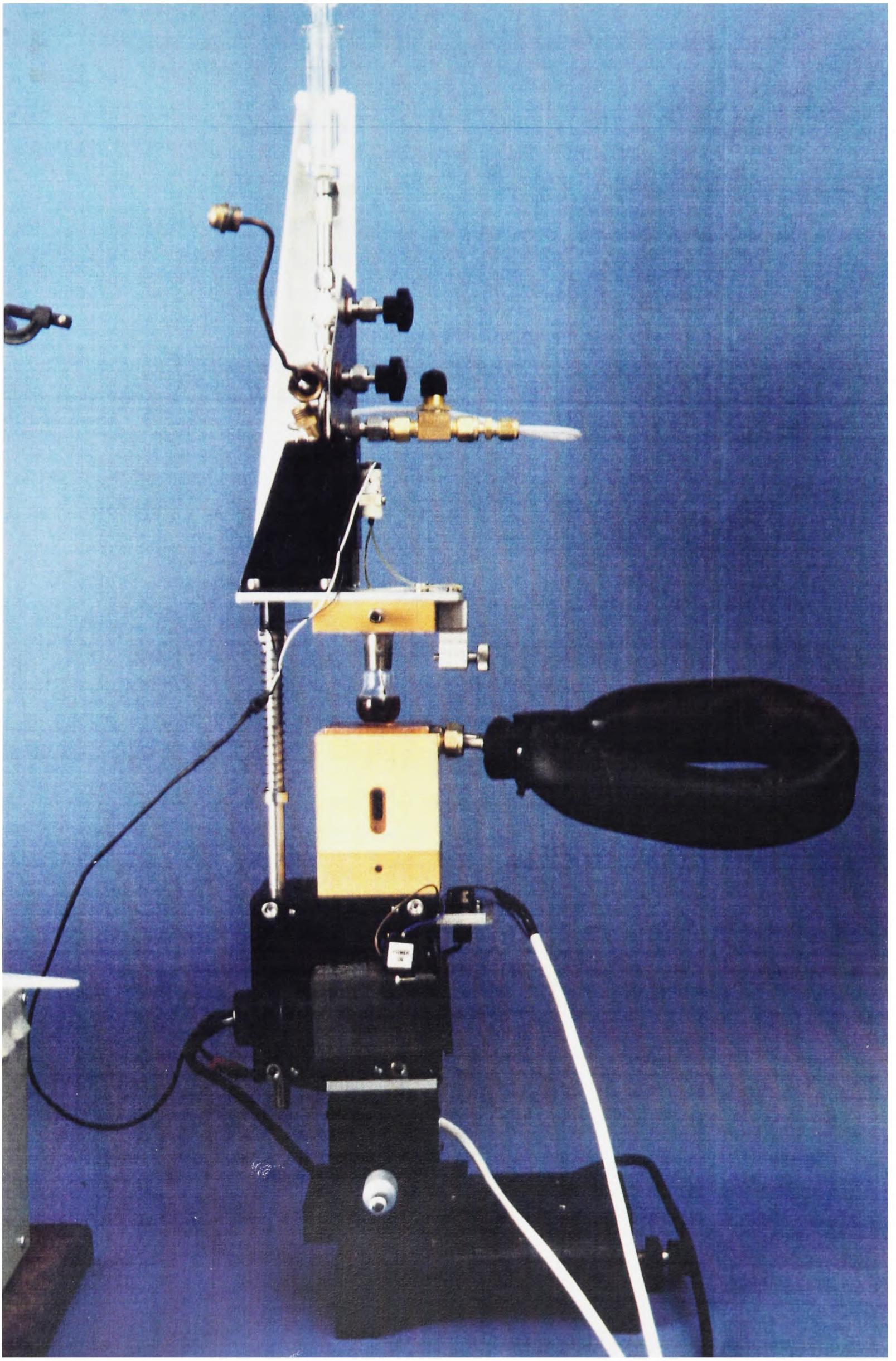

Figure 5.11: Photograph of the reaction vessel and injection system used.

5.7.4.2. Liquid feed and gas purge system

Reaction liquids were prepared prior to the measurements in a glove box and poured into 500ml PTFE-lined stainless steel cylinders. These have an opening at each end, both of which can be sealed using hand valves. They are also fitted with Swagelock fittings to allow them to be rapidly incorporated into the liquid feed system.

The cylinders are held inside a heating jacket in a gas manipulation panel which is mounted on a rack above the reaction vesssel. Gas lines are arranged so that the entire system can be purged with dry nitrogen when the cylinder containing the reaction liquid is changed. An additional line allows the reaction flask to be purged each time it is changed. The system was operated at a nitrogen overpressure of one to two atmospheres. The heating jacket consists of a foil heater (Mincor Products) bonded inside a epoxy laminate hinged jacket held closed by two captive screws. The temperature of the cylinder was maintained using a electronic temperature controller powered by a 24V power supply.

Stainless steel piping and valves were used throughout.

5.7.5. Experimental Protocol

5.7.5.1. Experimental arrangement

The experimental cell was mounted in the EDD facility of the SRS. The incident beam was defined by a 1mm diameter collimator and the diffracted beam was defined using a set of multiple slits. These were 300mm long with an individual slit width of 0.1mm and a total active area of 3mm. The multiple slits were designed so as to optimise the momentum resolution of the system. The detector angle was set at between 2° and 3° to collect spectral energy data corresponding to a *d* spacing of 13Å→4Å.

5.7.5.2. Experimental procedure

Pre-weighed flasks containing a known amount of microcrystalline SnS_2 were mounted onto the sample injection port and purged with dry nitrogen to flush oxygen and moisture from the system. Cobaltocene solution was introduced to the flask by remotely triggering an electronic timer-based solenoid valve. Accurate volumes were dispensed by pre-calibrating the aliquots delivered as a function of both the delivery time and the nitrogen overpressure in the reservoir. Stirring was commenced and acquisition initiated simultaneously to guest injections. Spectral acquisition times were varied according to the time scale of the reaction, ranging from as little as 10 seconds to 5 minutes for slower reactions which lasted several hours.

5.7.5.3. Optimisation of Spectral Signal

The spectral output can be optimised by varying several parameters. These factors are considered below.

(a) Diffraction angle 2θ

Increasing or decreasing 2θ causes the diffraction spectra to be expanded or compressed on the energy scale[13]. The 3 factors which influence the choice of 2θ are absorption, *d* spacing range of interest and spectral resolution. The choice of 2θ is thus often a compromise between these parameters. For the experiments described in Chapter 4, an additional consideration is choosing 2θ such that metal resonance peaks and absorption edges do not interfere with the Bragg peaks of interest.

(b) The diffracting "lozenge"

This is the volume of sample irradiated by the incident beam (defined by the slit system), which can be seen by the detector. For the energy dispersive diffraction geometry, it is the lozenge-shaped volume shown in figure 5.12. There 3 effective ways of increasing the diffracting volume, by adjusting each of the its dimensions in turn. They are (i) increasing W (ii) increasing H (iii) reducing 2θ. The adjustments are normally made in the order (i), (ii) and (iii) as the latter two tend to increase the lozenge length beyond the sample dimensions. Moreover, small values of 2θ decrease the resolution through the cot θ term.

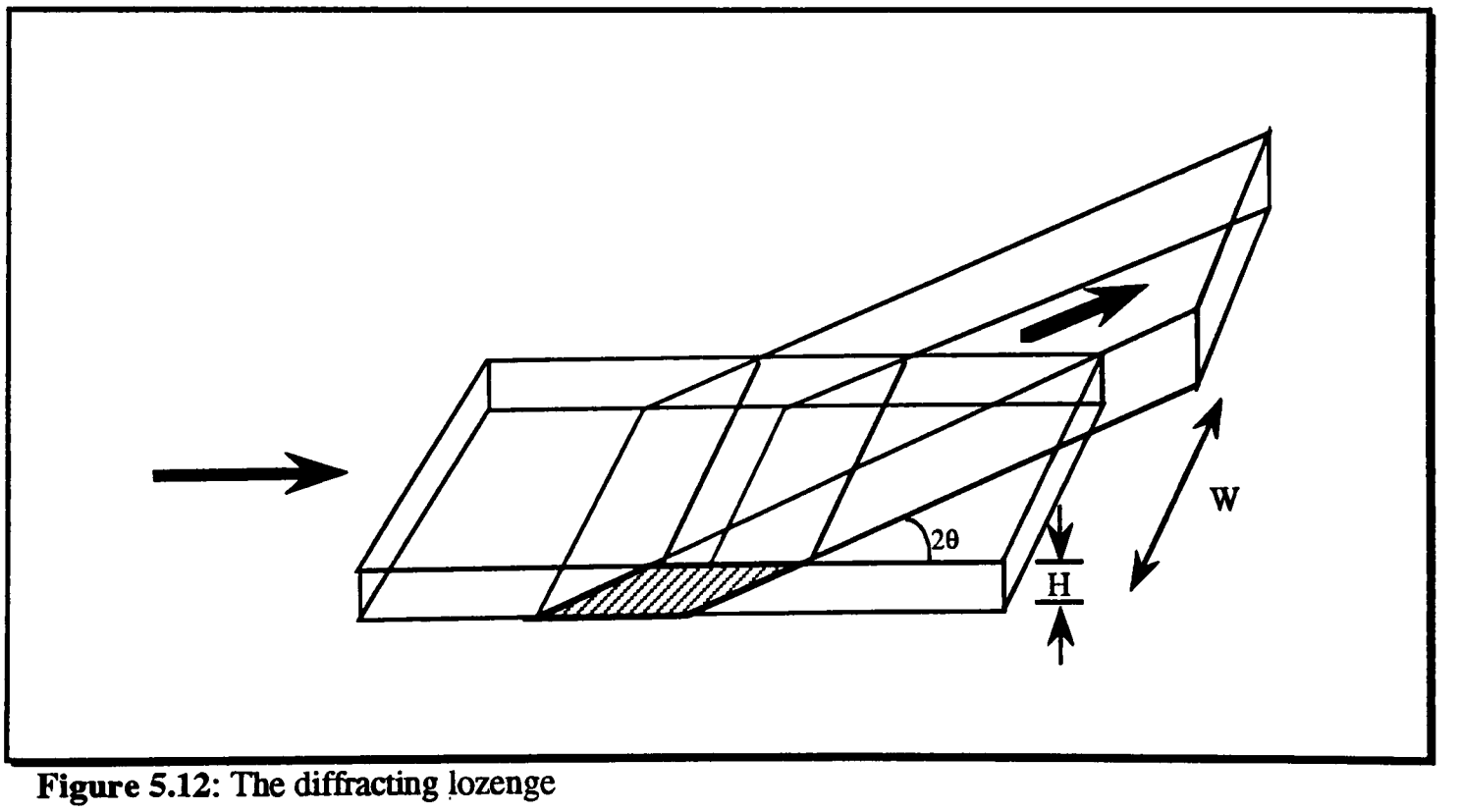

Figure 5.12: The diffracting lozenge

(c) Multiple slits

Multiple slits can be used to increase the diffracting volume without affecting the resolution. The principle is illustrated in Figure 5.13. Each slit can be ascribed to a diffracting lozenge with a beam divergence which is limited by the slit width. The multiple sets of lozenges achieve a corresponding gain in effective diffracting volume without compromising the resolution.

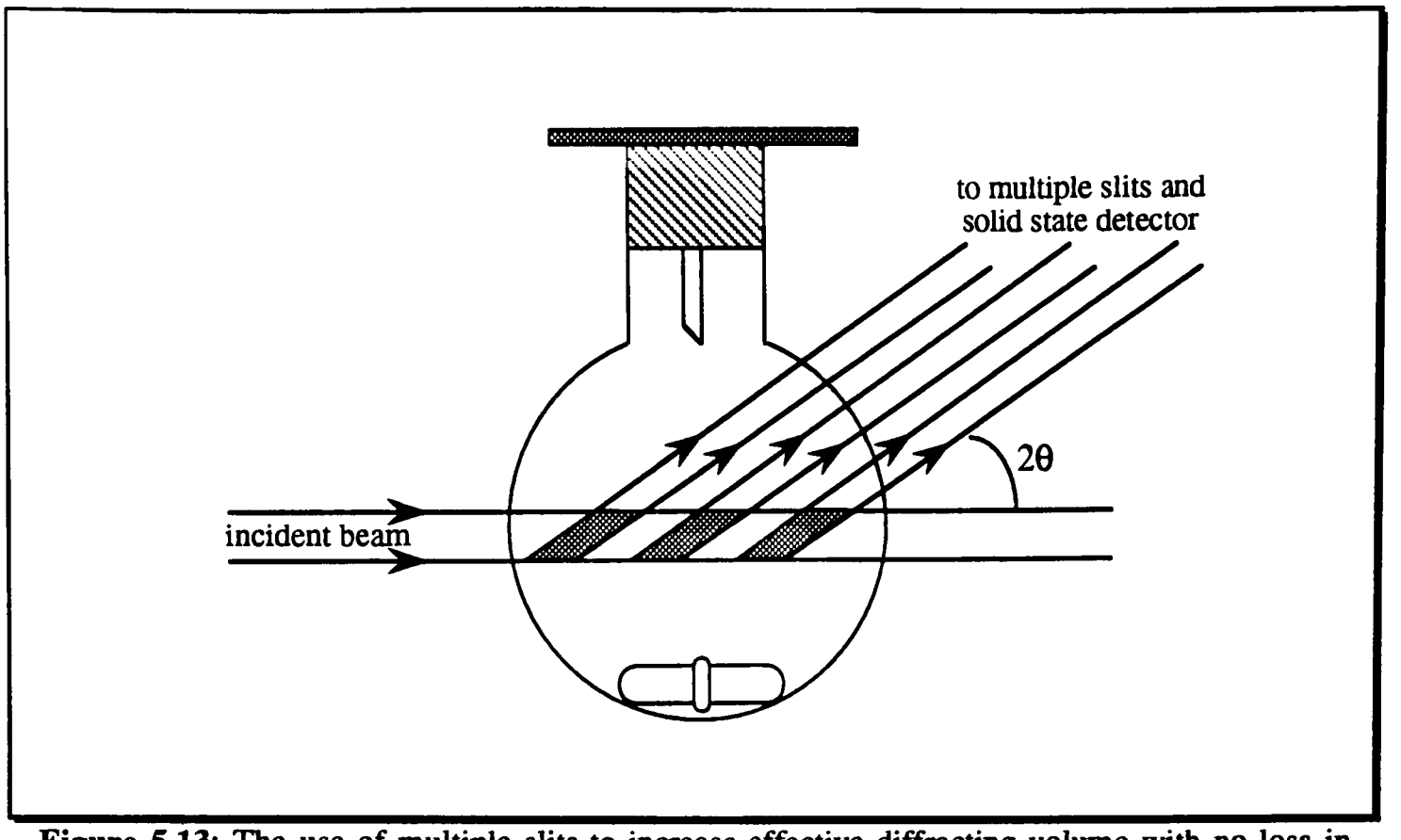

Figure 5.13: The use of multiple slits to increase effective diffracting volume with no loss in resolution.

(d) Sample density

Since the EDD spectra described in this chapter utilise suspensions of microcrystalline samples, an increase in the sample density by using a greater mass of sample will increase the signal-to-noise ratio of the spectra. However, the extent of improvement is limited by the amount of sample which can be effectively stirred into suspension within the diffracting lozenge.

(e) Electronics

Although energy-dispersive diffraction has the advantage of fast data collection arising from an intense radiation source, the speed is eventually limited by the performance of the electronics. Faster circuits with output count rates of up to 40,000 counts per second can be used when only relative intensities are required, but these do not give very reliable peak positions.

Taking the factors (a) through (e) into account, the detector was set at angles between 2° and 3°, where, using a multiple slit arrangement and 200 mg of sample suspended in the reaction flask, spectra could be collected in as little as 10 seconds with minimal overlap from metal absorption edges and no impingement of the surrounding copper block into the diffracting lozenge.

References:

1. A. A. Balchin, in *Crystallography and Crystal Chemistry of Materials with Layered Structures*, ed. F. Levy, D. Reidel Publishing Company: Dordrecht-Holland, 1976, p. 1-50

2. F. A. S. Al-Alamy and A. A. Balchin, *J. Cryst. Growth* (1977), **38**, 221-232.

3. G. Wilkinson, F. A. Cotton and J. M. Birmingham, *J. Inorg. Nucl. Chem.* (1956), **2**, 95.

4. F. H. Kohler and W. Prossdorf, *Z. Natuforsch* (1977), **32b**, 1026-9.

5. E. O. Fischer, *Inorganic Syntheses* **6**, 132-137.

6. E. O. Fischer, F. Scherer and H. O. Stahl, *Chem. Ber.* (1960), **93**, 2065-74.

7. E. O. Fischer and O. Stahl, *Chem. Ber.* (1956), **89**, 1805-8.

8. H. O. Van Oven and H. J. De Liefde Meijer, *J. Organometal. Chem* (1969), **19**, 373-376.

9. D. P. K. Ng, *D. Phil Thesis*. Oxford University, 1993.

10. M. L. H. Green, D. K. P. Ng and R. C. Tovey, *J. Chem. Soc., Chem Comm.* (1992), 918-9.

11. Oxford Instruments, *Temperature Controller ITC-4 Manual*, Oxford, 1989.

12. S. J. Mason, *D. Phil. Thesis*. Oxford University, 1993.

13. H. Cole, *J. Appl. Cryst.* (1970), **3**, 405.

14. S. M. Clark, *Nucl. Instrum. Methods* (1989), **A276**, 381.

Appendix A

This appendix contains supplementary data for the refinements described in Chapter Two. All refinement models assumed centering of the organometallic between the dichalcogenide layers. Carbon-carbon, carbon-hydrogen and metal-ring centroid bond lengths used were based on crystallographically available data. Where unavailable, the closest possible analogue was used (e.g. $CoCp_2$ coordinates for $CrCp_2$). The following radii (Å) were used for the Bessel functions which modelled the rapidly rotating carbocylic rings.

Cp	1.15
Cp'	1.3
Bz	1.4
Cot	1.65
Cht	1.82

Fractional coordinates for the metal along the c axis in the host dichalcogenide were fixed at 0.0 and 1.0 while the chalcogen coordinates were refined (final positions shown in Table 2.3 in Chapter Two).

The following supplementary data table compares the experimentally determined structure factors $|\mathbf{F_{obs}}|$ against those calculated for models in which the organometallic resided *exclusively* in either of two extreme orientations ; that is, either with the metal-ring centroid parallel ($|\mathbf{F_{para}}|$) or perpendicular ($|\mathbf{F_{perp}}|$) with respect to the host layers. Data for samples studied by both X-ray and neutron diffraction are included.

X-Ray Data

	$\|F_{obs}\|$	$\|F_{para}\|$	$\|F_{perp}\|$
$ZrS_2(CoCp_2)_{0.25}$			
002	46.0	46.7	34.1
003	-	-	-
004	12.9	13.3	6.10
005	16.3	16.4	14.7
006	31.3	30.9	37.4
007	30.4	30.7	25.3
008	29.3	29.3	30.5
009	13.6	13.4	15.9
00(10)	9.48	9.70	6.00
$ZrS_2(CrCp_2)_{0.20}$			
002	42.8	43.6	34.1
003	7.13	6.60	16.8
004	12.5	12.6	7.70
005	20.4	20.6	18.9
006	37.8	36.6	41.4
007	40.2	41.4	37.4
008	39.0	38.2	39.1
009	20.7	22.4	23.5
00(10)	13.5	12.3	10.4
$ZrS_2(CoCp'_2)_{0.20}$			
002	42.1	43.7	33.5
003	9.07	7.58	18.2
004	9.50	10.1	5.67
005	17.3	17.5	15.3
006	29.6	28.8	33.7
007	30.2	30.6	27.2
008	27.7	27.6	28.1
009	13.8	13.5	16.1
00(10)	7.70	7.98	6.45
$ZrS_2(MoBz_2)_{0.20}$			
002	55.2	57.3	41.6
003	6.23	3.86	20.0
004	11.9	12.7	6.58
005	5.27	6.03	1.34
006	20.7	19.6	28.2
007	12.7	13.6	8.24
008	20.9	21.0	21.0
009	7.26	6.84	9.98
00(10)	8.49	8.86	5.89

$ZrS_2(TiCotCp)_{0.20}$

002	48.4	49.7	38.7
003	13.7	12.1	25.0
004	7.60	8.58	0.758
005	11.0	11.0	11.6
006	22.0	21.7	25.3
007	23.5	24.1	20.6
008	27.1	27.1	28.1
009	18.4	18.4	19.6
00(10)	11.8	12.1	9.97
00(11)	4.82	4.60	6.26

$ZrS_2(WChtCp')_{0.20}$

002	46.6	49.7	33.8
003	-	-	-
004	11.1	12.5	4.70
005	12.0	11.3	14.2
006	23.5	23.5	22.7
007	21.7	21.6	21.9
008	18.0	18.1	17.7
009	9.63	9.67	9.93
00(10)	4.01	4.11	3.98

$SnS_2(WChtCp')_{0.20}$

002	57.52	64.42	43.03
003	14.16	8.92	25.86
004	17.37	20.07	11.41
005	17.72	16.72	19.62
006	26.80	26.92	26.2
007	24.34	24.30	24.58
008	19.20	19.41	19.22
009	10.98	11.12	11.22
00(10)	5.07	5.20	5.16

Neutron Data

	$\|F_{obs}\|$	$\|F_{para}\|$	$\|F_{perp}\|$
$ZrS_2(CoCp_2)_{0.25}$			
001	1.5500	1.5450	0.89500
002	1.7770	1.8110	0.23400
003	0.57900	0.48000	3.3720
004	0.43900	0.31500	2.4060
005	0.61000	0.47900	0.21500
006	0.83100	0.51900	3.1930
007	1.7530	1.3130	1.9490
008	0.99500	0.68800	2.0900
$ZrS_2(CrCp_2)_{0.20}$			
001	1.0420	1.1370	0.51400
002	1.5700	1.6140	0.029000
003	0.35500	0.39900	2.5910
004	0.15100	0.18400	1.6940
005	0.48800	0.46000	0.27100
006	0.70900	0.67500	2.4170
007	1.3360	1.2920	0.68400
008	0.95500	0.96100	1.7480
$SnSe_2(CoCp_2)_{0.30}$			
001	1.5400	1.6090	0.75500
002	2.1200	1.8930	0.75300
003	0.38100	0.66300	2.9880
004	1.9340	1.4630	4.0100
005	0.10800	0.27800	0.12900
006	0.86400	1.1060	4.4280
007	3.1200	2.3590	1.6570
008	2.4230	1.3000	3.1050

Appendix B

The people who were involved in the development of the work reported in Chapter Four are listed below.

- Simon Clark, Station Scientist
- John Evans and Chris Nuttall, co-workers
- John Flaherty, Project Engineer
- Jim Gordon, Machinist
- Peter Irvine, Project Designer
- Dermot O'Hare, Principal Investigator and Research Supervisor.
- Trevor Rathbone and Alfred Nield, Technical Specialists

I was responsible for the coordination, planning and execution of the experiment, a responsibility shared with my colleague John Evans. Whilst my co-workers helped in the data collection and Simon Clark provided some of the software for data analysis, the actual analysis of the data is entirely my own work.

Technical drawings of the apparatus designed and built at Daresbury are included on the following two pages.

AO- 63/8229

DRG. PRACTICE TO B.S. 308. THIRD ANGLE PROJECTION

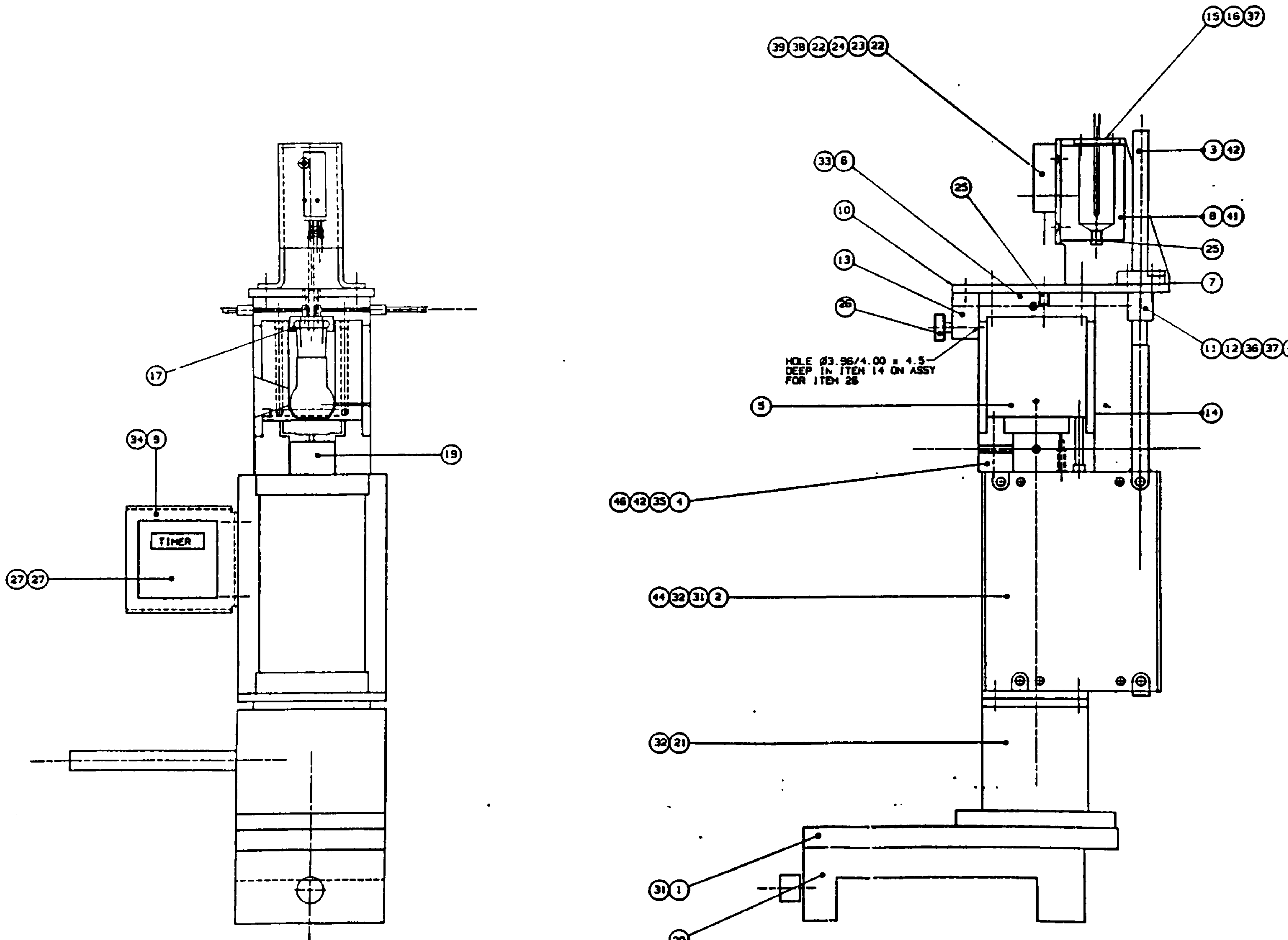

Nº	DRG Nº	DESCRIPTION	QTY	REMARKS
1	A2-63-8236	BASE PLATE	1	
2	A1-63-8237	LOWER M. J. BRKT	1	
3	A2-63-8238	GUIDE BAR	1	
4	A2-63-8239	MOTOR MOUNT	1	
5	A2-63-8240	HEATED CELL	1	
6	A3-63-8241	CELL LID	1	
7	A3-63-8242	GUIDE BRACKET	1	
8	A2-63-8243	FINAL TANK	1	
9	A2-63-8244	TIMER BRKT	1	
10	A3-63-8245	LID PLATE	1	
11	A3-63-8246	GUIDE BUSH	1	
12	A3-63-8247	GUIDE PLATE	1	
13	A3-63-8248	PLUNGER BLOCK	1	
14	A3-63-8249	LAGGING BOX	1	
15	A3-63-8250	FINAL TANK LID	1	
16	A3-63-8251	GASKET	1	
17	A3-63-8252	GRIPPER SEAL	1	
18				
19		STIRRER MOTOR	1	
20	EALING	CARRIER REF 53-0535	1	
21	AREOTECH	VERT POSITIONER VLS-1M	1	
22	LEE	SOL VALVE LFVX0500150A	1	
23	LEE	PIPE ASSY TUTC3216906L	1	60 LONG
24	LEE	PIPE ASSY TUTC3216909L	1	90 LONG
25	LEE	ADAPTOR TMDA3204910Z	2	
26	CARR LANE	PLUNGER 5/16-18 CL-5-HRP-S	1	
27	FARNELL	TIMER REF 177-473	1	
28	FARNELL	PANEL REF 177-179	1	
29				
30	M6 x 20 LG	CAP HD SOC. SCREW	6	ST STL
31	M6 x 16 LG	CAP HD SOC. SCREW	12	ST STL
32	M6 x 12 LG	CAP HD SOC. SCREW	4	ST STL
33	M5 x 12 LG	CAP HD SOC. SCREW	6	ST STL
34	M4 x 8 LG	CAP HD SOC. SCREW	2	ST STL
35	M4 x 35 LG	CAP HD SOC. SCREW	4	ST STL
36	M3 x 18 LG	CAP HD SOC. SCREW	8	ST STL
37	M3 x 6 LG	CAP HD SOC. SCREW	7	ST STL
38	M2.5x16 LG	CAP HD SOC. SCREW	2	ST STL
39	M2.5	HEX NUT	2	ST STL
40	M3	HEX NUT	4	ST STL
41	M3 X 6 LG	CSK HD SCREW	2	ST STL
42	M5x10 LG	SOC GRUB SCREW CONE PT	6	ST STL
43				
44	Ø5 x 25 LG	DOWEL	8	ST STL
45				
46	Ø5 x 6 LG	PLUG (NITRILE 60°-70° SHORE A)	4	RUBBER
		SPRING	1	SPEC

WELDING SPEC

MATERIAL SPEC SEE DETAILS

MATERIAL SEE DETAILS

TOLERANCES UNLESS OTHERWISE STATED

LINEAR DIMENSIONS UP TO ± . OVER ±

ANGULAR DIMENSIONS ±

SCALE 1:1

ALL DIMENSIONS IN mm UNLESS OTHERWISE STATED

SCIENCE & ENGINEERING RESEARCH COUNCIL

DARESBURY LABORATORY

CHESHIRE

DRN. PAI DATE DEC. 92

CHD. FAI DATE JAN 93

APPD. JVF

TITLE HEATED CELL ASSEMBLY

DRAWING Nº AO-63/8229

ISSUE A

USED ON

CONTRACTORS COMPANY

CONTRACTORS DRG Nº

FIRST ISSUE

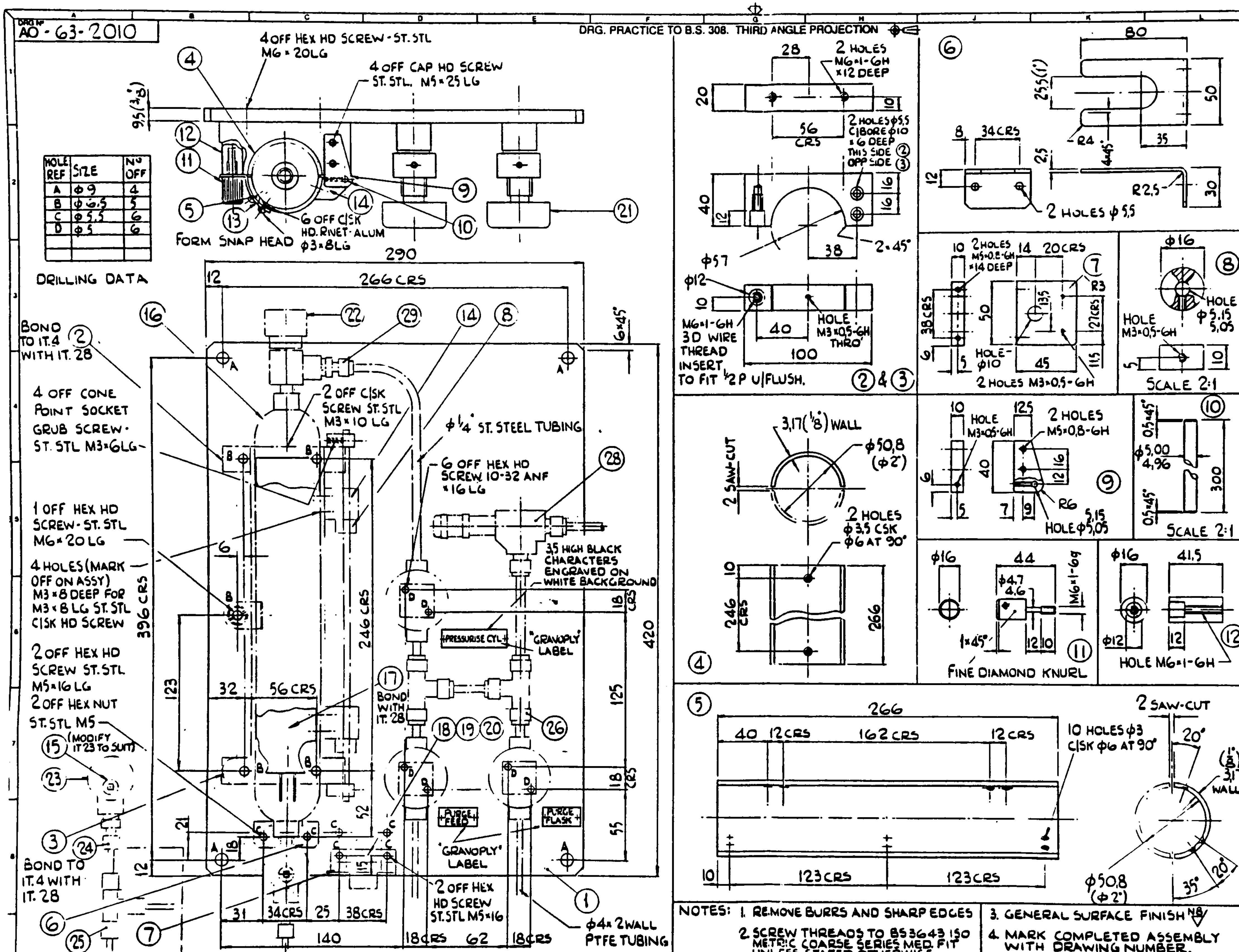

DRG. PRACTICE TO B.S. 308. THIRD ANGLE PROJECTION
4 OFF HEX HD SCREW - ST. STL M6 × 20 LG
4 OFF CAP HD SCREW - ST. STL. M5 × 25 LG
6 OFF C/SK HD. RIVET ALUM φ3 × 8 LG
FORM SNAP HEAD
9,5 (3/8)
290
12
266 CRS
6 × 45°
BOND TO IT.4 WITH IT.28
4 OFF CONE POINT SOCKET GRUB SCREW - ST. STL M3 × 6 LG
2 OFF C/SK SCREW ST. STL M3 × 10 LG
φ 1/4" ST. STEEL TUBING
6 OFF HEX HD SCREW 10-32 ANF × 16 LG
3,5 HIGH BLACK CHARACTERS ENGRAVED ON WHITE BACKGROUND
PRESSURISE CYL.
"GRANOPLY" LABEL
1 OFF HEX HD SCREW - ST. STL M6 × 20 LG
4 HOLES (MARK OFF ON ASSY) M3 × 8 DEEP FOR M3 × 8 LG ST. STL C/SK HD SCREW
396 CRS
246 CRS
420
2 OFF HEX HD SCREW ST. STL M5 × 16 LG
2 OFF HEX NUT ST. STL M5
(MODIFY IT.23 TO SUIT)
BOND WITH IT.28
PURGE FEED
PURGE FLASK
"GRAVOPLY" LABEL
2 OFF HEX HD SCREW ST. STL M5 × 16
BOND TO IT.4 WITH IT.28
φ4 × 2 WALL PTFE TUBING
123
32
56 CRS
125
18 CRS
55
52
21
18
12
31
34 CRS
25
38 CRS
140
18 CRS
62
18 CRS
28
2 HOLES M6 × 1-6H × 12 DEEP
20
56 CRS
10
2 HOLES φ5,5 C/BORE φ10 × 6 DEEP THIS SIDE (2) OPP SIDE (3)
40
38
2 × 45°
φ57
φ12
M6 × 1-6H 3D WIRE THREAD INSERT TO FIT 1/2 P U/FLUSH.
HOLE M3 × 0,5-6H THRO'
100
(2) & (3)
80
25,5 (1")
50
8
34 CRS
R4
4 × 45°
35
2,5
R2,5
30
2 HOLES φ5,5
2 HOLES M5 × 0,8-6H × 14 DEEP
14
20 CRS
R3
38 CRS
13,5
27 CRS
HOLE φ10
45
11,5
2 HOLES M3 × 0,5-6H
φ16
HOLE φ5,15 5,05
HOLE M3 × 0,5-6H
SCALE 2:1
3,17 (1/8) WALL
φ50,8 (φ2")
2 SAW-CUT
2 HOLES φ3,5 CSK φ6 AT 90°
246 CRS
266
HOLE M3 × 0,5-6H
12,5
2 HOLES M5 × 0,8-6H
R6
HOLE φ5,15 5,05
0,5 × 45°
φ5,00 4,96
300
SCALE 2:1
44
φ4,7 4,6
M6 × 1-6g
1 × 45°
FINE DIAMOND KNURL
41,5
φ12
HOLE M6 × 1-6H
40
12 CRS
162 CRS
12 CRS
10 HOLES φ3 C/SK φ6 AT 90°
2 SAW-CUT
20°
(1/8) 3,17 WALL
123 CRS
123 CRS
φ50,8 (φ2")
35°
1,5 THICK
40,5
R1,5
R28,5
HOLE M6 × 1-6H
FULL RAD
2 HOLES φ3
47,5
R6
45°
5,020
HOLE φ 5,004
R28,5
22
25

HOLE REF	SIZE	Nº OFF
A	φ9	4
B	φ6,5	5
C	φ5,5	6
D	φ5	6

DRILLING DATA

No.	MATL.	DESCRIPTION	No. OFF	REMARKS
1	AL ALLOY	PLATE	1	[illegible]
2	[illegible] GF145	END PIECE (UPPER)	1	EPOXY LAMINATE
3	[illegible] GF145	END PIECE (LOWER)	1	EPOXY LAMINATE
4	TUFNOL	FORMER } φ50,1 / DIA	1	WOVEN GLASS
5	ELGH	CLAMP } 3 WALL TUBE		LAMINATE
6	ST. STL.	BRACKET	1	[illegible]
7	AL ALLOY	MOUNTING PAD	1	[illegible]
8	ST. STL.	COLLAR	1	[illegible]
9	ST. STL.	SUPPORT	2	[illegible]
10	ST. STL.	PIN	1	[illegible]
11	ST. STL.	CAPTIVE SCREW	3	[illegible]
12	ST. STL.	STAND-OFF	1	[illegible]
13	ST. STL.	TAB	2	[illegible]
14	DELRIN	BEARING	2	
15	A2-63-2011	M5 AIR TAP	1	
16	WHITEY	SAMPLE CYL [illegible]	1	500 CC
17	[illegible]	FOIL HEATER [illegible]	1	MINCO PRODUCTS
18	HIRSCHMANN	CONN. PLUG 930-814-106	1	
19	HIRSCHMANN	CONN SOCK 931-264-106	1	
20	HIRSCHMANN	CLIP 732-044-000	1	
21	NUPRO	VALVE SS-DSS6MM	3	4mm
22	WHITEY	STEM VALVE SS-16-DKM4-F4A	1	1/4 NPT
23	WHITEY	STEM VALVE SS-16-DKM4-F4	1	1/4 NPT
24	SWAGELOK	CONN SS-4MO-1-4	3	4mm
25	SWAGELOK	TEE CONN SS-4MO3	3	4mm
26	SWAGELOK	TEE CONN SS	2	1/4"
27	NUPRO	RELIEF VALVE SS-RL3S4	1	SET AT 3 PSI
28	NECY	ADHESIVE (ARALDITE 2004)		
29	SWAGELOK	MALE CONN SS-400-1-4	1	

NOTES:
1. REMOVE BURRS AND SHARP EDGES
2. SCREW THREADS TO BS3643 ISO METRIC COARSE SERIES MED FIT UNLESS STATED OTHERWISE
3. GENERAL SURFACE FINISH N8
4. MARK COMPLETED ASSEMBLY WITH DRAWING NUMBER.

WELDING SPEC
MATERIAL SPEC: SEE LIST
MATERIAL: SEE LIST
TOLERANCES UNLESS OTHERWISE STATED
LINEAR DIM'S UP TO 80 ± 0,25 OVER 80 ± 0,5
ANGULAR DIMENSIONS ± 1°
SCALE 1:1
ALL DIMENSIONS IN mm UNLESS OTHERWISE STATED

DRN: PAS FEB '93
CHD: PAS FEB '93
APPD: JVF FEB '93

SCIENCE & ENGINEERING RESEARCH COUNCIL
DARESBURY LABORATORY

TITLE: ASSY & DETAILS OF HEATED CYLINDER PANEL
DRAWING Nº: AO-63-2010
ISSUE: A

USED ON
CONTRACTORS COMPANY
CONTRACTORS DRG Nº

A — FIRST ISSUE

DRG Nº AO-63-2010

Appendix C

The Fortran77 programs used, PJWB (Chapter Two) and INTPEAK (Chapter Four) are listed in the following pages.

Listing of Fortran 77 Program ***PJWB***

```
      PROGRAM PJWPROG
      DOUBLEPRECISION AM,V
       DIMENSION IH(100),IK(100),IL(100),IM(100),IZ(100),SINN(100),
     2 RENZ(100),A(100),FIC(100),SFIO(100),SIOB(100),DELTA(100),F(15),
     3 BR(15),X(15),Y(15),Z(15),O(15),WW(100),KR(25),WT(25,8),KA(25,8),
     4 D(25,100),AB(25),ATA(25,25),AL(25,25),YYY(25),PARA(25),REC(25,
     5 25),EC(25),SIGMA(25),RESID(100),C(3),COSA(6),SINA(6),COSAS(3),
     6 SINAS(6),AS(3),AMAT(24,3,4),SCAL(100)
       DIMENSION B(100),FMOD(100),PHI(100),CPHI(100),SPHI(100),MILL(3),
     2 NPA(25),KAP(25),DERA(100,25),DERB(100,25),NPAR(15,25),KP(15,25),
     3 NA5(25),SINM(100),FF(100,15),FFG(15,18),STL(15,18)
      DIMENSION LABEL(15),TITLE(15),DDLTA(15),IBESS(15),RR(15)
     2,CXPSI(100),SXPSI(100),IRR(15),BAK(15),BAL(15),BAKL(15)
     3,XPER(15),XPAR(15)
       NIN=1
       NOUT=2
       PI=6.2831853
       IB=-1
      READ(NIN,*)FOU
      READ(NIN,*)NX
      READ(NIN,*) ICR,CSTA
       READ(NIN,*)M,N,IS,C(1),C(2),C(3),COSA(1),COSA(2),COSA(3),WAV
       READ(NIN,*)NK,NU,NS
      AZ=1.0/NS
      DO 30 I=1,NS
       READ(NIN,*)((AMAT(I,K,J),J=1,4),K=1,3)
   30 CONTINUE
       READ(NIN,*)SCALE
       DO 40 J=1,N
        READ(NIN,*) IH(J),IK(J),IL(J),IM(J),IZ(J)
       XPA=IL(J)*C(2)
       XPO=IK(J)*C(3)
       XPH=SQRT(XPA**2+XPO**2)
       CXPSI(J)=XPA/XPH
       SXPSI(J)=XPO/XPH
   40 CONTINUE
       DO 50 J=1,IS
       READ(NIN,*) SFIO(J),SIOB(J)
       WW(J)=1./(SIOB(J)**2)
       SFIO(J)=(SFIO(J)**2)/10.0
   50 CONTINUE
       WRITE(NOUT,60)C(1),COSA(1),WAV,M,C(2),COSA(2),N,C(3),COSA(3),IS
    60 FORMAT(//,4X,2HA=,F7.4,4X,6HALPHA=,F7.4,3X,7HLAMBDA=,F8.4,10X,
     2 13HNO. OF ATOMS;,I2,/,4X,2HB=,F7.4,4X,6HBETA =,F7.4,22X,
     3 19HNO. OF REFLECTIONS;,I2,/,4X,2HC=,F7.4,4X,6HGAMMA=,F8.4,21X,
     4 19HNO. OF INTENSITIES;,I2)
       IF(NX)100,70,100
   70 DO 90 J=1,M
       READ(1,80)LABEL(J)
   80 FORMAT(A4)
        READ(NIN,*) F(J),IBESS(J),X(J),Y(J),Z(J),BR(J),O(J)
     2,BAK(J),BAL(J),BAKL(J)
       IF(IBESS(J).EQ.0) GO TO 90
       READ(NIN,*) IRR(J),XPER(J),XPAR(J)
   90 CONTINUE
       GOTO 140
```

```
100 DO 120 J=1,M
  READ(1,110)LABEL(J)
110 FORMAT(A4)
   READ(NIN,*) IBESS(J),X(J),Y(J),Z(J),BR(J),O(J)
  2,BAK(J),BAL(J),BAKL(J)
   F(J)=0.0
   IF(IBESS(J).EQ.0) GO TO 120
   READ(NIN,*) IRR(J),XPER(J),XPAR(J)
120 CONTINUE
2002 DO 130 J=1,M
   READ(NIN,*)(STL(J,ML),FFG(J,ML),ML=1,18)
130 CONTINUE
140 CONTINUE
   READ(NIN,*)IC
   DO 150 K=1,M
150 NPA(K)=0
   IF(IC)220,220,160
160 IP=0
   READ(NIN,*)LL,KK
   IF(IB)170,180,180
170 LLS=LL
180 CONTINUE
   READ(NIN,*)NSCALE
   L1=NSCALE
   DO 210 K0=1,M
   READ(NIN,*)K,NPA(K)
   IF(NPA(K).EQ.0)GOTO 210
   DO 200 J=1,NPA(K)
   L1=L1+1
   READ(NIN,*)KP(K,J),NA5(L1),KA(L1,1)
   NPAR(K,J)=L1
   KAP(L1)=KP(K,J)
   WT(L1,1)=1.00
   KR(L1)=K
   IF(KA(L1,1).GT.0)GOTO 200
   DO 190 L=1,NA5(L1)
   READ(NIN,*)WT(L1,L),KA(L1,L)
190 CONTINUE
200 CONTINUE
210 CONTINUE
220 IF(IB)230,270,270
230 DO 240 J=1,3
   COSA(J)=COS(PI*COSA(J)/360.0)
   SINA(J)=SQRT(1.-COSA(J)**2)
   COSA(J+3)=COSA(J)
240 SINA(J+3)=SINA(J)
   DO 250 J=1,3
   COSAS(J)=(COSA(J+1)*COSA(J+2)-COSA(J))/(SINA(J+1)*SINA(J+2))
   SINAS(J)=SQRT(1.-COSAS(J)**2)
250 SINAS(J+3)=SINAS(J)
   DO 260 J=1,3
260 AS(J)=1./(C(J)*SINA(J+1)*SINAS(J+2))
270 WRITE(NOUT,280)SCALE
280 FORMAT(//,13HSCALE FACTOR;,E12.4,//,2X,1HH,2X,1HK,2X,1HL,7X,
   2 4HFMOD,10X,5HPHASE,10X,5HICALC,11X,4HIOBS,10X,5HSIOBS,10X,
  3 5HDELTA,9X,6HDELTA%)
   I=0
   FNUM=0.
```

```
      DEN=0.
      FFIC=0.
      RES=0.
      IB=IB+1
      DO 620 J=1,N
      IF(IB)290,290,350
  290 AH=IH(J)*AS(1)
      BK=IK(J)*AS(2)
      CL=IL(J)*AS(3)
      Q=AH**2+BK**2+CL**2+2.*(BK*CL*COSAS(1)+CL*AH*COSAS(2)
     2 +AH*BK*COSAS(3))
      SINN(J)=Q/4.
      SSIN=WAV**2*SINN(J)
      RENZ(J)=SSIN*(SQRT(1-SSIN))
      IF(ICR.EQ.0) GO TO 2001
      RENZ(J)=RENZ(J)/(SQRT(SSIN))
 2001 IF(NX.EQ.0) GO TO 350
      RENZ(J)=RENZ(J)/(SQRT(SSIN))
      RENZ(J)=RENZ(J)*1000.0/(1.0+CSTA-4.0*CSTA*SSIN+4.0*CSTA*SSIN**2)
      RENZ(J)=1.0
      SINM(J)=SQRT(SINN(J))
      DO 340 KZ=1,M
      KJ=1
  300 IF(SINM(J)-STL(KZ,KJ))330,320,310
  310 KJ=KJ+1
      GOTO 300
  320 FF(J,KZ)=FFG(KZ,KJ)
      GOTO 340
  330 IF(KJ.EQ.1)KJ=2
      IF(KJ.EQ.18)KJ=17
      FF(J,KZ)=FFG(KZ,KJ-1)*(SINM(J)-STL(KZ,KJ))*(SINM(J)-STL(KZ,KJ+1))
     2 /(STL(KZ,KJ-1)-STL(KZ,KJ))/(STL(KZ,KJ-1)-STL(KZ,KJ+1))+FFG(KZ,
     3 KJ)*(SINM(J)-STL(KZ,KJ-1))*(SINM(J)-STL(KZ,KJ+1))/(STL(KZ,KJ)
     4 -STL(KZ,KJ-1))/(STL(KZ,KJ)-STL(KZ,KJ+1))+FFG(KZ,KJ+1)*(SINM(J)
     5 -STL(KZ,KJ-1))*(SINM(J)-STL(KZ,KJ))/(STL(KZ,KJ+1)-STL(KZ,KJ-1))/
     6 (STL(KZ,KJ+1)-STL(KZ,KJ))
      IF(IBESS(KZ).EQ.1) GO TO 2000
      GO TO 340
 2000 IF(IRR(KZ).EQ.2) GO TO 3912
      IFAIL=1
      X1=XPER(KZ)*2.0*PI*SQRT(SINN(J))*SXPSI(J)
      Y1=S17AEF(X1,IFAIL)
      GO TO 3911
 3912 IFAIL=1
      X1=XPER(KZ)*2.0*PI*SQRT(SINN(J))*CXPSI(J)
      X2=XPAR(KZ)*2.0*PI*SQRT(SINN(J))*SXPSI(J)
      Y1=S17AEF(X1,IFAIL)
      Y2=S17AEF(X2,IFAIL)
      Y1=Y1*Y2
 3911 FF(J,KZ)=FF(J,KZ)*Y1
  340 CONTINUE
  350 RENZ(J)=1.0
      AA=0.0
      BB=0.
      DO 360 JJJ=1,KK
      DERA(J,JJJ)=0.
      DERB(J,JJJ)=0.
  360 CONTINUE
```

```
      DO 500 K=1,M
      DO 500 JJ=1,NS
      DO 370 IA=1,3
      MILL(IA)=AMAT(JJ,1,IA)*IH(J)+AMAT(JJ,2,IA)*IK(J)+AMAT(JJ,3,IA)
     2 *IL(J)
  370 CONTINUE
       IF(NX)380,390,380
  380 T=O(K)*FF(J,K)*EXP(-BR(K)*SINN(J))
      2*EXP(-(IK(J)**2*BAK(K)+IL(J)**2*BAL(K)+IK(J)*IL(J)*BAKL(K)))
      GOTO 400
  390 IF(IBESS(K).EQ.0) GO TO 3902
       IF(IRR(K).EQ.2) GO TO 3932
       IFAIL=1
        X1=XPER(K)*2.0*PI*SQRT(SINN(J))*SXPSI(J)
       Y1=S17AEF(X1,IFAIL)
       GO TO 3901
  3932 IFAIL=1
        X1=XPER(K)*2.0*PI*SQRT(SINN(J))*CXPSI(J)
        X2=XPAR(K)*2.0*PI*SQRT(SINN(J))*SXPSI(J)
       Y1=S17AEF(X1,IFAIL)
       Y2=S17AEF(X2,IFAIL)
       Y1=Y1*Y2
       GO TO 3901
  3902 Y1=1.0
  3901 T=Y1*O(K)*F(K)*EXP(-BR(K)*SINN(J))
      2*EXP(-(IK(J)**2*BAK(K)+IL(J)**2*BAL(K)+IK(J)*IL(J)*BAKL(K)))
  400 ALPA=AZ*T*COS(PI*(MILL(1)*X(K)+MILL(2)*Y(K)+MILL(3)*Z(K)+IH(J)
      2 *AMAT(JJ,1,4)+IK(J)*AMAT(JJ,2,4)+IL(J)*AMAT(JJ,3,4)))
      AA=AA+ALPA
      BET=AZ*T*SIN(PI*(MILL(1)*X(K)+MILL(2)*Y(K)+MILL(3)*Z(K)+IH(J)
     2*AMAT(JJ,1,4)+IK(J)*AMAT(JJ,2,4)+IL(J)*AMAT(JJ,3,4)))
       IF(NU-1) 410,410,420
  410 BB=BB+BET
  420 NNPA=NPA(K)
       IF(NNPA)500,500,430
  430 DO 490 NP=1,NNPA
       KKP=KP(K,NP)
       KNPAR=NPAR(K,NP)
       IF(KKP-3)440,440,470
  440 IF(NU-1)450,450,460
  450 DERB(J,KNPAR)=DERB(J,KNPAR)+PI*MILL(KKP)*ALPA
  460 DERA(J,KNPAR)=DERA(J,KNPAR)-PI*MILL(KKP)*BET
      GOTO 490
  470 DERA(J,KNPAR)=DERA(J,KNPAR)+ALPA
       IF(NK-1)480,480,490
  480 DERB(J,KNPAR)=DERB(J,KNPAR)+BET
  490 CONTINUE
  500 CONTINUE
       A(J)=AA
       B(J)=BB
       FMOD(J)=SQRT(A(J)**2+B(J)**2)
       PHI(J)=ATAN2(B(J),A(J))
       CPHI(J)=A(J)/FMOD(J)
       SPHI(J)=B(J)/FMOD(J)
       IF(AA)510,530,530
  510 IF(BB)550,520,560
  520 PHI(J)=PI/2.
       GOTO 570
```

```
530 IF(BB)570,540,570
540 PHI(J)=0.
  GOTO 570
550 PHI(J)=PHI(J)-PI/2.
  GOTO 570
560 PHI(J)=PHI(J)+PI/2.
570 PHI(J)=360.*PHI(J)/PI
   FFIC=FFIC+(FMOD(J)**2*IM(J))/RENZ(J)
    IF(IZ(J)-1)600,580,600
580 I=I+1
   FIC(I)=FFIC*SCALE
   DELTA(I)=SFIO(I)-FIC(I)
   DDLTA(I)=(DELTA(I)*100.0)/SFIO(I)
   RESID(I)=(SFIO(I)-FIC(I))**2
   FNUM=FNUM+ABS(DELTA(I))
   DEN=DEN+SFIO(I)
   RES=RES+WW(I)*RESID(I)/IS
    WRITE(NOUT,590)IH(J),IK(J),IL(J),FMOD(J),PHI(J),FIC(I),SFIO(I),
  2 SIOB(I),DELTA(I),DDLTA(I)
 590 FORMAT(/,3I3,3X,E12.3,3X,E12.3,3X,E12.3,3X,E12.3,3X,E12.3,3X,
   2 E12.3,3X,E12.3)
   FFIC=0.
   GOTO 620
600 WRITE(NOUT,610)III(J),IK(J),IL(J),FMOD(J),PIII(J)
610 FORMAT(/,3I3,3X,E12.3,3X,E12.3)
620 CONTINUE
   R=(FNUM/DEN)*100
   RES2=SQRT(RES*IS/(IS-LLS))
   WRITE(NOUT,630)R
630 FORMAT(//,9HR-FACTOR;E12.4,//)
   WRITE(NOUT,640)
  640 FORMAT(//,6X,4HATOM,14X,1HF,12X,1HX,12X,1HY,12X,1HZ,10X,6HB
ISO ,
   2 10X,5HOCCUP)
   DO 660 K=1,M
    WRITE(NOUT,*) LABEL(K),F(K),X(K),Y(K),Z(K),BR(K),O(K)
   2,BAK(K),BAL(K),BAKL(K)
 650 FORMAT(1H0,7X,A4,6X,E12.3,8(4X,F9.6))
660 CONTINUE
   IF(IB)670,670,1210
670 IP=IP+1
   WRITE(NOUT,680)IP
680 FORMAT(//,13HCYCLE NUMBER;,I2)
   DO 690 I=1,KK
   AB(I)=0.
   DO 690 L=1,KK
   ATA(I,L)=0.
   DO 690 MM=1,IS
690 D(I,MM)=0.
   IF(NSCALE)720,720,700
700 DO 710 I=1,IS
   D(1,I)=FIC(I)/SCALE
710 AB(1)=AB(1)+D(1,I)*WW(I)*DELTA(I)
720 N1=1+NSCALE
   IF(KK-NSCALE)840,840,730
730 DO 810 KS=N1,KK
   NA5A=NA5(KS)
   KKR=KR(KS)
```

```
      KKP=KAP(KS)
      DO 800 K=1,NA5A
      KKA=KA(KS,K)
      I=1
      DO 790 J=1,N
       GO TO (740,740,740,750,760,7601,7602,7603),KKP
  740 DER=CPHI(J)*DERA(J,KS)+SPHI(J)*DERB(J,KS)
      GOTO 770
  750 DER=-CPHI(J)*SINN(J)*DERA(J,KS)-SPHI(J)*SINN(J)*DERB(J,KS)
      GOTO 770
 7601 DER=-CPHI(J)*IK(J)**2*DERA(J,KS)-SPHI(J)*IK(J)**2*DERB(J,KS)
      GO TO 770
 7602 DER=-CPHI(J)*IL(J)**2*DERA(J,KS)-SPHI(J)*IL(J)**2*DERB(J,KS)
      GO TO 770
 7603 DER=-CPHI(J)*IK(J)*IL(J)*DERA(J,KS)-SPHI(J)*IK(J)*IL(J)*DERB(J,KS)
      GO TO 770
  760 DER=(CPHI(J)*DERA(J,KS))/O(KKR)+(SPHI(J)*DERB(J,KS))/O(KKR)
  770 D(KKA,I)=D(KKA,I)+((DER*2.*FMOD(J)*SCALE*IM(J))/RENZ(J))*WT(KS,K)
       IF(IZ(J))790,790,780
  780 I=I+1
  790 CONTINUE
  800 CONTINUE
  810 CONTINUE
      DO 830 KKA=N1,LL
      DO 820 I=1,IS
  820 AB(KKA)=AB(KKA)+WW(I)*DELTA(I)*D(KKA,I)
  830 CONTINUE
  840 DO 850 J=1,LL
      DO 850 K=1,J
      DO 850 I=1,IS
      ATA(J,K)=ATA(J,K)+WW(I)*D(J,I)*D(K,I)
  850 CONTINUE
      AL(1,1)=SQRT(ATA(1,1))
      IF(LL-1)920,920,860
  860 DO 870 J=2,LL
      AL(J,1)=ATA(J,1)/AL(1,1)
  870 CONTINUE
      DO 910 J=2,LL
      DO 910 I=J,LL
      AM=ATA(I,J)
      NN=J-1
      DO 880 K=1,NN
  880 AM=AM-AL(I,K)*AL(J,K)
       IF(I-J)900,890,900
  890 AL(I,J)=SQRT(AM)
      GOTO 910
  900 AL(I,J)=AM/AL(J,J)
  910 CONTINUE
  920 YYY(1)=AB(1)/AL(1,1)
      IF(LL-1)960,960,930
  930 DO 950 I=2,LL
      V=AB(I)
      NN=I-1
      DO 940 J=1,NN
  940 V=V-AL(I,J)*YYY(J)
      YYY(I)=V/AL(I,I)
  950 CONTINUE
  960 PARA(LL)=YYY(LL)/AL(LL,LL)
```

```
   IF(LL-1)1010,1010,970
970 NN=LL
980 NN=NN-1
   M1=NN+1
   V=YYY(NN)
   DO 990 K=M1,LL
990 V=V-AL(K,NN)*PARA(K)
   PARA(NN)=V/AL(NN,NN)
    IF(NN-1)1000,1000,980
1000 CONTINUE
1010 N1=LL-1
   DO 1020 I=1,LL
   REC(I,I)=1./AL(I,I)
1020 CONTINUE
    IF(LL-1)1080,1080,1030
1030 DO 1070 J=1,N1
    N2=J+1
    DO 1070 I=N2,LL
    N3=I-1
    V=-AL(I,J)*REC(J,J)
    IF(N3-N2)1060,1040,1040
1040 DO 1050 K=N2,N3
1050 V=V-AL(I,K)*REC(K,J)
1060 REC(I,J)=V/AL(I,I)
1070 CONTINUE
1080 DO 1100 I=1,LL
   SUM=0.
   DO 1090 K=I,LL
1090 SUM=SUM+REC(K,I)**2
   EC(I)=SUM
1100 CONTINUE
    IF(NSCALE)1120,1120,1110
1110 SCALE=SCALE+PARA(1)
    IF(KK-NSCALE)1200,1200,1120
1120 KKM=1+NSCALE
   DO 1190 I=KKM,KK
   NA5A=NA5(I)
   KKP=KAP(I)
   KKR=KR(I)
   DO 1180 K=1,NA5A
   KKA=KA(I,K)
    GO TO (1130,1140,1150,1160,1170,1171,1172,1173),KKP
1130 X(KKR)=X(KKR)+WT(I,K)*PARA(KKA)
   GOTO 1180
1140 Y(KKR)=Y(KKR)+WT(I,K)*PARA(KKA)
   GOTO 1180
1150 Z(KKR)=Z(KKR)+WT(I,K)*PARA(KKA)
   GOTO 1180
1160 BR(KKR)=BR(KKR)+WT(I,K)*PARA(KKA)
   GOTO 1180
1171 BAK(KKR)=BAK(KKR)+WT(I,K)*PARA(KKA)
   GO TO 1180
1172 BAL(KKR)=BAL(KKR)+WT(I,K)*PARA(KKA)
   GO TO 1180
1173 BAKL(KKR)=BAKL(KKR)+WT(I,K)*PARA(KKA)
   GO TO 1180
1170 O(KKR)=O(KKR)+WT(I,K)*PARA(KKA)
1180 CONTINUE
```

```
1190 CONTINUE
   LLS=LL
1200 IF(IP+1-IC)270,270,140
1210 DO 1220 I=1,LLS
   SIGMA(I)=SQRT(EC(I)*RES*IS/(IS-LLS))
1220 CONTINUE
   WRITE(NOUT,1230)
1230 FORMAT(//,9HPARAMETER,6X,5HSHIFT,10X,3HESD)
   DO 1250 J=1,LLS
   WRITE(NOUT,1240)J,PARA(J),SIGMA(J)
1240 FORMAT(//,3X,I2,6X,E12.4,6X,E12.4)
1250 CONTINUE
   IF(IC.GT.0)GOTO 670
   IF (FOU) 1280,1280,1260
1260 SCRAL=0.0
   DO 1261 JZ=1,M
   SCRAL=SCRAL+FFG(JZ,1)*O(JZ)
1261 CONTINUE
    WRITE(5,*) C(3),IS,401,SCRAL,1.0
   DO 1270 JZ=1,IS
   WRITE(5,*) JZ,FMOD(JZ),PHI(JZ)
1270 CONTINUE
1280 STOP
   END
```

Listing of Fortran 77 Program INTPEAK

```
c       To fit multiple gaussian peaks to multiple regions in
c       a series of EDPD spectra.

        integer         nsum
        integer         max_points
        parameter       (max_points=4000)
        integer         con_chan,file_chan,data_chan,calib_chan,out_chan
        integer         pos_chan
        parameter       (con_chan=20,file_chan=21,data_chan=22,calib_chan=23)
        parameter       (out_chan=23,pos_chan=49)
        integer         nparm
        parameter       (nparm=3)
        integer         nregions_max,npks_max
        parameter       (nregions_max=20,npks_max=40)
        integer         max_pts,max_gaus
        parameter       (max_pts=1000,max_gaus=30)

        integer         npks(nregions_max),npkst
        real            start(nregions_max),end(nregions_max),pkpos(npks_max)

        real            px(max_pts),py(max_pts)
        real            ppos(max_gaus)
        real            rpos(npks_max),fwhm(npks_max),area(npks_max)
        real            possd(npks_max),fwhmsd(npks_max),areasd(npks_max)
        real            py1(max_points)

        integer         srsrun,srsdat,srstim
        real            dparm(100)
        character*80    srstle
        character*8     srsprj,srsexp,srscn1,srscn2,srscn3
        character*4     srsstn

        real            energy(max_points),intensity(max_points)
        integer         npoints,jrc,isrs,nhead,ixcol,iycol,itype
        integer         iprint,iout,ipos_out
        character*8     convert
        character*80    title,file_name
        character*10    pknames(npks_max)

        real            cal(5),ecal(5),temp

        common/srshed/srsrun,srsdat,srstim,srstle,srsprj,
     +                srsexp,srscn1,srscn2,srscn3
        common/parms/dparm
        common/data/rpos,fwhm,area
        common/err/possd,fwhmsd,areasd

c       Read in control file

        open(unit=con_chan,status='old',readonly)

        read(con_chan,10)title
        read(con_chan,*)nregions,nsum

        ipoint=0
        do i=1,nregions
                read(con_chan,*)start(i),end(i),npks(i)
                do j=1,npks(i)
                        read(con_chan,10)pknames(ipoint+j),pkpos(ipoint+j)
10                      format(a10,f10.0)
                end do
                ipoint=ipoint+npks(i)
        end do
        npkst=ipoint

        close(unit=con_chan)

c       Calculate number of output files required

        if(npkst.le.3)then
                nfilest=1
        else if(npkst.le.9)then
                nfilest=2
        else if(npkst.le.15)then
                nfilest=3
        else if(npkst.le.21)then
                nfilest=4
        else if(npkst.le.27)then
                nfilest=5
        else if(npkst.le.30)then
                nfilest=6
        else
                stop ' Too many peaks for output file'
        end if

        if(npkst.le.8)then
                ipos_out=1
        else if(npkst.le.16)then
                ipos_out=2
        else if(npkst.le.24)then
                ipos_out=3
        else if(npkst.le.30)then
                ipos_out=4
        end if

c       Read in calibration file

        open(unit=calib_chan,status='old',readonly)
                do i=1,5
                        read(calib_chan,*)cal(i),ecal(i)
                end do
        close(unit=calib_chan)

c       Open input and output channels

        open(unit=file_chan,status='old',readonly)
        do i=1,ipos_out
                open(unit=pos_chan+i,status='new',recl=300)
                write(pos_chan+i,20)title
        end do
        do i=1,nfilest
                open(unit=(out_chan+i),status='new',recl=300)
                write(out_chan+i,20)title
20              format(' ',a60,',')
        end do

        if(nfilest.eq.1)then
                write(out_chan+1,30)(pknames(i),i=1,npkst)
```

```
        write(out_chan+1,50)
else if(nfilest.eq.2)then
        write(out_chan+1,30) (pknames(i),i=1,3)
        write(out_chan+1,50)
        write(out_chan+2,40) (pknames(i),i=4,npkst)
        write(out_chan+2,60)
else if(nfilest.eq.3)then
        write(out_chan+1,30) (pknames(i),i=1,3)
        write(out_chan+1,50)
        write(out_chan+2,40) (pknames(i),i=4,9)
        write(out_chan+2,60)
        write(out_chan+3,40) (pknames(i),i=10,npkst)
        write(out_chan+3,60)
else if(nfilest.eq.4)then
        write(out_chan+1,30) (pknames(i),i=1,3)
        write(out_chan+1,50)
        write(out_chan+2,40) (pknames(i),i=4,9)
        write(out_chan+2,60)
        write(out_chan+3,40) (pknames(i),i=10,15)
        write(out_chan+3,60)
        write(out_chan+4,40) (pknames(i),i=16,npkst)
        write(out_chan+4,60)
else if(nfilest.eq.5)then
        write(out_chan+1,30) (pknames(i),i=1,3)
        write(out_chan+1,50)
        write(out_chan+2,40) (pknames(i),i=4,9)
        write(out_chan+2,60)
        write(out_chan+3,40) (pknames(i),i=10,15)
        write(out_chan+2,60)
        write(out_chan+4,40) (pknames(i),i=16,21)
        write(out_chan+4,60)
        write(out_chan+5,40) (pknames(i),i=22,npkst)
        write(out_chan+5,60)
else if(nfilest.eq.6)then
        write(out_chan+1,30) (pknames(i),i=1,3)
        write(out_chan+1,50)
        write(out_chan+2,40) (pknames(i),i=4,9)
        write(out_chan+2,60)
        write(out_chan+3,40) (pknames(i),i=10,15)
        write(out_chan+3,60)
        write(out_chan+4,40) (pknames(i),i=16,21)
        write(out_chan+4,60)
        write(out_chan+5,40) (pknames(i),i=22,27)
        write(out_chan+5,60)
        write(out_chan+6,40) (pknames(i),i=28,npkst)
        write(out_chan+6,60)
end if

if(ipos_out.eq.1)then
        write(pos_chan+1,70) (pknames(i),i=1,npkst)
else if(ipos_out.eq.2)then
        write(pos_chan+1,70) (pknames(i),i=1,8)
        write(pos_chan+2,80) (pknames(i),i=9,npkst)
else if(ipos_out.eq.3)then
        write(pos_chan+1,70) (pknames(i),i=1,8)
        write(pos_chan+2,80) (pknames(i),i=9,16)
        write(pos_chan+3,80) (pknames(i),i=17,npkst)
else if(ipos_out.eq.4)then
        write(pos_chan+1,70) (pknames(i),i=1,8)
        write(pos_chan+2,80) (pknames(i),i=9,16)
        write(pos_chan+2,80) (pknames(i),i=17,24)
        write(pos_chan+3,80) (pknames(i),i=25,npkst)
end if


30      format(' ',' , , , , , ',3(a10,', , ,'))
40      format(' ',6(a10,' , , ,'))
50      format(' ','Number , I1 , I2 , I3 , Temp ,',
     1                     3(' pos , fwhm , area ,'))
60      format(' ',6(' pos , fwhm , area , '))
70      format(' ','Run num',',',8(a10,', ,'))
80      format(' ',8(a10,', ,'))

c       Cycle through progam fitting peaks until the end of the files
c       in the filename dataset

        do ii=1,2000

c       clear pyl(i) before summing spectra
        do i=1,4000
                pyl(i)=0
        end do

c       start loop for summing spectra
        do isum=1,nsum

        do i=1,npkst
                rpos(i)=0.
                fwhm(i)=0.
                area(i)=0.
        end do

        read(file_chan,100,end=999)file_name
100     format(a)

c       Read in data from srs data file.

        open(unit=data_chan,file=file_name,status='old',readonly)

c       Read srs headers

        call srsnml(ijunk,data_chan,jrc)

        if(jrc.eq.1)then
                stop ' End of data file'
        end if

        isrs=jrc

        call srsprm(nparm,data_chan,jrc)

        if(jrc.eq.1)then
                stop ' End of data file'
        end if

        nhead=1
        ixcol=0
        iycol=0
        itype=1
```

```
c       Read data

        if(nhead.gt.0) call srshdr(ijunk,nhead,title,data_chan,isrs)
        npoints=4000

        call srsmca(ijunk,energy,intensity,npoints,ixcol,data_chan,jrc)

        close(unit=data_chan)

        do i=1,npoints
                pyl(i)=pyl(i)+intensity(i)
        end do

c       end loop for summing spectra
        end do

c       Convert from channels to energy

        ncount=0
        do i=1,npoints
                energy(i)=cal(1)+cal(2)*energy(i)
                if(pyl(i).le.0)then
                        pyl(i)=1
                end if
        end do

c       Select regions and fit peaks

        ipoint=0
        do i=1,nregions
                istart=int((start(i)-cal(1))/cal(2))+1
                iend=int((end(i)-cal(1))/cal(2))+1

                ipnts=0
                do j=istart,iend
                        ipnts=ipnts+1
                        px(ipnts)=energy(j)
                        py(ipnts)=pyl(j)
                end do

                do j=1,npks(i)
                        ppos(j)=pkpos(ipoint+j)
                end do

                iipoint=ipoint
                call gauss(px,py,ipnts,ppos,npks(i),iipoint)
                ipoint=ipoint+npks(i)

        end do

c       Correct positional errors for ADC component

        do i=1,npkst
                erradc=ecal(1)+ecal(2)*((rpos(i)-cal(1))/cal(2))
                possd(i)=sqrt((erradc*erradc)+(possd(i)**2))
        end do

c       Write data to output channels

        if(nfilest.eq.1)then
                write(out_chan+1,400)srsrun,(dparm(i),i=1,3),temp,
     1                          (rpos(i),fwhm(i),area(i),i=1,npkst)
        else if(nfilest.eq.2)then
                write(out_chan+1,400)srsrun,(dparm(i),i=1,3),temp,
     1                          (rpos(i),fwhm(i),area(i),i=1,3)
                write(out_chan+2,410)(rpos(i),fwhm(i),area(i),i=4,npkst)
        else if(nfilest.eq.3)then
                write(out_chan+1,400)srsrun,(dparm(i),i=1,3),temp,
     1                          (rpos(i),fwhm(i),area(i),i=1,3)
                write(out_chan+2,410)(rpos(i),fwhm(i),area(i),i=4,9)
                write(out_chan+3,410)(rpos(i),fwhm(i),area(i),
     1                                  i=10,npkst)
        else if(nfilest.eq.4)then
                write(out_chan+1,400)srsrun,(dparm(i),i=1,3),temp,
     1                          (rpos(i),fwhm(i),area(i),i=1,3)
                write(out_chan+2,410)(rpos(i),fwhm(i),area(i),i=4,9)
                write(out_chan+3,410)(rpos(i),fwhm(i),area(i),i=10,15)
                write(out_chan+4,410)(rpos(i),fwhm(i),area(i),
     1                                  i=16,npkst)
        else if(nfilest.eq.5)then
                write(out_chan+1,400)srsrun,(dparm(i),i=1,3),temp,
     1                          (rpos(i),fwhm(i),area(i),i=1,3)
                write(out_chan+2,410)(rpos(i),fwhm(i),area(i),i=4,9)
                write(out_chan+3,410)(rpos(i),fwhm(i),area(i),i=10,15)
                write(out_chan+4,410)(rpos(i),fwhm(i),area(i),i=16,21)
                write(out_chan+5,410)(rpos(i),fwhm(i),area(i),
     1                                  i=22,npkst)
        else if(nfilest.eq.6)then
                write(out_chan+1,400)srsrun,(dparm(i),i=1,3),temp,
     1                          (rpos(i),fwhm(i),area(i),i=1,3)
                write(out_chan+2,410)(rpos(i),fwhm(i),area(i),i=4,9)
                write(out_chan+3,410)(rpos(i),fwhm(i),area(i),i=10,15)
                write(out_chan+4,410)(rpos(i),fwhm(i),area(i),i=16,21)
                write(out_chan+5,410)(rpos(i),fwhm(i),area(i),i=22,27)
                write(out_chan+6,410)(rpos(i),fwhm(i),area(i),
     1                                  i=28,npkst)
        end if

c       if(ipos_out.eq.1)then
                write(pos_chan+1,420)srsrun,(rpos(i),possd(i), i=1,npkst)
c       else if(ipos_out.eq.2)then
c               write(pos_chan+1,420)srsrun,(rpos(i),possd(i), i=1,8)
c               write(pos_chan+2,430)(rpos(i),possd(i), i=9,npkst)
c       else if(ipos_out.eq.3)then
c               write(pos_chan+1,420)srsrun,(rpos(i),possd(i), i=1,8)
c               write(pos_chan+2,430)(rpos(i),possd(i), i=9,16)
c               write(pos_chan+3,430)(rpos(i),possd(i), i=17,npkst)
c       else if(ipos_out.eq.4)then
c               write(pos_chan+1,420)srsrun,(rpos(i),possd(i), i=1,8)
c               write(pos_chan+2,430)(rpos(i),possd(i), i=9,16)
c               write(pos_chan+3,430)(rpos(i),possd(i), i=16,24)
c               write(pos_chan+4,430)(rpos(i),possd(i), i=25,npkst)
c       end if

400     format(' ',i6,',',3(f10.1,','),f10.3,',',3(f8.4,',',f8.2,',',
        1               f8.0,','))
410     format(' ',6(f8.4,',',f8.2,',',f8.0,','))
420     format(' ',i6,',',8(f8.4,',',f8.6,','))
430     format(' ',8(f8.4,',',f8.6,','))
```

```
        end do

c       Close files and finish

999     close(unit=file_chan)
        do i=1,nfilest
                close(unit=out_chan+i)
        end do
        do i=1,ipos_out
                close(unit=pos_chan+i)
        end do

        end
```